

Limits on neutrino oscillations in the CNGS neutrino beam and event classification with the OPERA detector

Dissertation
zur Erlangung des Doktorgrades
des Fachbereichs Physik
der Universität Hamburg

vorgelegt von
Torben Ferber
aus Bonn–Bad Godesberg

Hamburg
2012

Gutachterin/Gutachter der Dissertation: Prof. Dr. Caren Hagner
Prof. Dr. Walter Schmidt-Parzefall

Gutachterinnen der Disputation: Prof. Dr. Caren Hagner
Prof. Dr. Erika Garutti

Datum der Disputation: 28.08.2012

Vorsitzender des Prüfungsausschusses: Prof. Dr. Dieter Horns

Vorsitzender des Promotionsausschusses: Prof. Dr. Peter Hauschildt

Dekan der MIN-Fakultät: Prof. Dr. Heinrich Graener

Limits on neutrino oscillations in the CNGS neutrino beam and event classification with the OPERA detector

Abstract

OPERA, the *oscillation project with emulsion-tracking apparatus*, is a long-baseline neutrino oscillation experiment. It combines an almost pure, high-energy ν_μ beam produced at the SPS accelerator at CERN, Switzerland, with the OPERA neutrino detector located at a distance of about 730 km in the LNGS underground laboratory in Italy. By using a lead/photo emulsion target, ν_τ charged current (CC) interactions of ν_τ from $\nu_\mu \rightarrow \nu_\tau$ oscillations can be observed on an event-by-event basis with very low background rates. Within this thesis, a $\nu_\mu \rightarrow \nu_\mu$ disappearance search is described that uses a flux normalization-independent measurement of the CC event fraction as a function of the hadronic energy as measured by the electronic detectors of OPERA. This allows to derive limits on $\nu_\mu \rightarrow \nu_\mu$ oscillations, complementary to the main ν_τ appearance analysis. For maximal mixing, $|\Delta m_{23}^2| > 4.4 \times 10^{-3} \text{ eV}^2$ is excluded at 90 % C.L. by the disappearance analysis. This thesis represents the first application of this method, including systematic uncertainties, in a long-baseline neutrino oscillation experiment.

Obergrenzen auf Neutrinooszillationen im CNGS-Neutrinostrahl und Ereignisklassifikation mit dem OPERA-Detektor

Zusammenfassung

OPERA ist ein sogenanntes *long-baseline* Neutrinooszillationsexperiment, in welchem ein fast reiner, hochenergetischer ν_μ -Strahl, der am SPS Beschleuniger am CERN in der Schweiz produziert wird, mit dem OPERA-Detektor, der etwa 730 km entfernt im LNGS Untergrundlabor in Italien steht, kombiniert wird. Durch die Nutzung eines Blei/Photoemulsions-*Targets* können individuell Interaktionen via W^\pm Austausch (CC) der in $\nu_\mu \rightarrow \nu_\tau$ Oszillationen entstandenen ν_τ bei gleichzeitig sehr niedrigem Untergrund beobachtet werden. Im Rahmen dieser Arbeit wird eine $\nu_\mu \rightarrow \nu_\mu$ *Disappearance*-Suche beschrieben, welche auf einer flussunabhängigen Messung des CC-Ereignisanteils als Funktion der in den elektronischen Detektoren von OPERA gemessenen hadronischen Energie basiert. Diese erlaubt das Setzen von Obergrenzen auf $\nu_\mu \rightarrow \nu_\mu$ Oszillationen, die komplementär sind zur eigentlichen ν_τ *Appearance* Analyse von OPERA. Für maximale Mischung kann mit der vorliegenden Disappearance-Analyse $|\Delta m_{23}^2| > 4.4 \times 10^{-3} \text{ eV}^2$ (90 % C.L.) ausgeschlossen werden. Diese Analyse ist die erste Anwendung dieser Methode unter Berücksichtigung systematischer Fehler in einem long-baseline Neutrinooszillationsexperiment.

Contents

Introduction	1
1 Neutrino physics	3
1.1 A brief history	3
1.2 Neutrinos in the standard model	5
1.3 Neutrino oscillations	7
1.3.1 Neutrino oscillations in vacuum	7
1.3.2 Sterile neutrinos	13
1.3.3 Neutrino oscillations in matter	18
2 Neutrino interactions	23
2.1 Cross sections	24
2.1.1 Elastic and quasi-elastic scattering	25
2.1.2 Resonant scattering	34
2.1.3 Deep inelastic scattering	38
2.1.4 Inelastic transition region	59
2.1.5 Other types of neutrino interactions	61
2.1.6 Total cross section	62
2.2 Hadronization	66
2.3 Intranuclear rescattering	72
3 The OPERA experiment	74
3.1 The CNGS neutrino beam	77
3.1.1 Neutrino beams in general	77
3.1.2 CNGS design and layout	83
3.1.3 CNGS performance	86
3.2 The OPERA detector	89
3.2.1 Target	90
3.2.2 Target tracker	93
3.2.3 Spectrometer	93
3.2.4 Veto	97
3.2.5 DAQ and overall event trigger	97
3.2.6 Brick extraction and analysis chain	98
3.2.7 τ detection in OPERA	100
3.3 Observation of a first ν_τ candidate	103
3.4 Neutrino velocity measurement	104

4	Monte Carlo simulation	109
4.1	CNGS beam	109
4.2	Geometry description	123
4.3	Neutrino event generator	125
4.4	Cosmic muon generator	127
4.5	Detector simulation	127
4.5.1	OpSim and OpDigit	127
4.5.2	Rock muons	128
4.5.3	Hadronic showers	132
4.5.4	Electromagnetic showers	134
5	Event reconstruction	137
5.1	Official reconstruction software	137
5.2	Shower clustering	138
5.2.1	Track completion	139
5.2.2	Clustering	140
5.3	Preprocessing	142
5.4	Muon removal	143
5.5	Hadron shower axis	145
5.6	Fiducial volume	149
5.7	Vertex reconstruction	150
5.8	Event classification	154
5.9	Energy reconstruction	164
6	Analysis of CNGS beam events	169
6.1	Event selection	169
6.2	Background	176
6.2.1	Beam-induced background	176
6.2.2	Other background	177
6.2.3	Multievents	181
6.3	Beam monitoring	181
6.4	Data/Monte Carlo comparison	185
6.5	Comparison with emulsion data	193
7	Oscillation analysis	196
7.1	Neutrino appearance	197
7.1.1	ν_τ appearance	197
7.1.2	ν_e appearance	201
7.2	Neutrino disappearance	203
7.2.1	ν_μ disappearance	203
7.2.2	Systematic uncertainties	205
7.2.3	Oscillation fit	210
7.3	Accelerator oscillation summary	215
8	Conclusion	217
A	Neutrino oscillation	219

B Relativistic kinematics for neutrino interactions	223
C Integration limits for neutrino interactions	226
D Kinematics of neutrino beams	230
E Systematic uncertainties for the disappearance fit	235
List of tables	237
List of figures	238
Bibliography	244

Introduction

Neutrino oscillations are an experimentally well-established framework to describe the evolution of neutrino flavor states over time. This framework has evolved over many decades, starting with discrepancies of the observed solar neutrino rates with theoretical predictions up to a world-wide experimental neutrino program using natural and artificial neutrino sources.

The OPERA¹ experiment is using a pure muon neutrino beam produced at the CNGS² facility located at CERN³ that is sent over a distance of about 730 km to the LNGS⁴ underground laboratory in Italy. The main goal of OPERA is the search for direct tau appearance from the presumably dominant oscillation $\nu_\mu \rightarrow \nu_\tau$ in the so-called atmospheric neutrino sector. For this purpose, the OPERA detector combines a large target mass of over 1 kt with a very high spatial resolution of about $1 \mu\text{m}$ to detect the short-lived tau leptons produced in charged current ν_τ interactions.

Within this thesis, a complementary $\nu_\mu \rightarrow \nu_\mu$ disappearance search in OPERA is performed, based on a flux normalization-independent measurement of the ratio of charged current event fraction as a function of the hadronic energy as measured by the electronic detectors of OPERA. The analysis is the first application of this method, including systematic uncertainties, in a long-baseline neutrino experiment. For maximal mixing ($\sin^2(2\theta_{23}) = 1$), $|\Delta m_{23}^2| > 4.4 \times 10^{-3} \text{ eV}^2$ is excluded at 90 % C.L..

OPERA has provided a measurement of the muon neutrino velocity, which is compatible with the speed of light within 1σ . A subsample of antimuon events has been analysed within this thesis and used to determine the muon antineutrino velocity. The result $(v_{\bar{\nu}} - c)/c = (7.1 \pm 13.5) \times 10^{-6}$ (68 % C.L.) is compatible with the speed of light within 1σ .

The thesis is organized as follows: Section 1 gives an introduction to neutrinos in the Standard Model and neutrino oscillations. Section 2 describes the various neutrino cross sections and the hadronization processes. The CNGS

¹OPERA: Oscillation project with emulsion-tracking apparatus.

²CNGS: CERN neutrinos to Gran Sasso.

³CERN: Conseil Européen pour la recherche nucléaire.

⁴LNGS: Laboratori Nazionali del Gran Sasso.

neutrino beam, the OPERA detector and the neutrino velocity analysis are described in Section 3. Section 4 provides a detailed description of the Monte Carlo simulation. The event reconstruction and classification is described in Section 5. Section 6 discusses the data selection, comparisons of electronic detector data with Monte Carlo simulations and comparisons of electronic detector data with emulsion data. In Section 7 the oscillation analysis, including the evaluation of systematic uncertainties, is described.

The expressions *uncertainty* and *error* are used interchangeably to denote systematical or statistical uncertainties. All calculations are made in natural units unless noted otherwise. All particle masses and coupling constants are taken from [1] unless noted otherwise. Variables preceded or indexed by the word *true* indicate the known Monte Carlo value, rather than a reconstructed one. Equations, tables or figures preceded by a capital letter (e.g. A.1) can be found in the according appendix (e.g. Appendix A).

Chapter 1

Neutrino physics

1.1 A brief history

The history of the neutrino has begun in 1930 with a famous letter by W. Pauli to the attendees of a meeting on radioactivity, where he postulated electrically neutral particles with spin 1/2 that obey the Pauli exclusion principle [2]. The letter was preceded by decades of unexplained experimental results, one of them being the measured continuous energy spectrum (see Figure 1.1) of *electrons* (e^-) from radioactive β -decays in the assumed process

$$B(A, Z) \rightarrow C(A, Z + 1) + e^-, \quad (1.1)$$

which was in conflict with the expected monoenergetic electron energy $E_e = m_B - m_C$ (neglecting nucleon recoil) from the two-body reaction 1.1.

Another puzzle came along with the β -decays: Quantum mechanical spin statistics, formulated in the late 1920s, divided the fundamental particles into two major classes: Fermions, which are described by an asymmetric wave function and bosons that are characterized by a symmetric wave function. Compound objects like a nucleus are fermions if the number of constituent fermions is odd, and bosons otherwise¹. The total spin of a nucleus, as measured by spectroscopy², was known to depend on the mass number A and not on the charge number Z . Since A does not change in β -decays and electrons are fermions, process 1.1 violates angular momentum conservation. If a hypothetical third particle emitted together with the electron was a fermion, angular momentum would be conserved.

The whole picture became clearer when Chadwick observed the heavy neutron, also a fermion, as constituent of a nucleus and with a mass comparable to the one of the proton in 1932. It explained the similar mass of nucleons, composed of *protons* (p) and *neutrons* (n), before and after a β^- -decay:

$$n \rightarrow p + e^- + \bar{\nu}_e, \quad (1.2)$$

¹The corresponding quantum number is the spin, which is 1/2 for fermions and 1 for bosons.

²The neutron as constituent of the nucleus had not been discovered yet.

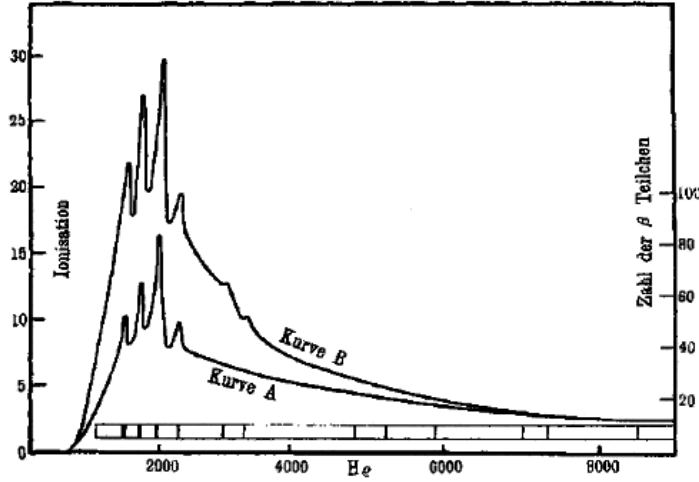


Figure 1.1: β -decay electron energy spectrum of a combined source of ^{214}Pb (Radium B) and ^{214}Bi (Radium C) measured by Chadwick 1914 (Figure reprinted from [3]). The different curves correspond to different experimental methods. The discrete lines above the continuous spectrum are, among others, due to γ -conversion from excited nuclei and Auger electrons.

where the nature of the third particle that we call *electron-antineutrino* ($\bar{\nu}_e$) nowadays, was still unclear.

The name of Pauli's still-hypothetical particle was proposed by the Italian physicist E. Fermi as "the little uncharged one", a "neutrino".

While the β -decay spectrum experiments are an indirect measurement of a neutrino, the first direct detection of a free neutrino took another twenty years, until 1956 when F. Reines and C. L. Cowan detected the inverse β^+ -decay

$$\bar{\nu}_e + p \rightarrow e^+ + n, \quad (1.3)$$

using nuclear reactors as antineutrino source³ [4]. The hypothetical inverse electron-capture

$$\bar{\nu}_e + {}^{37}\text{Cl} \rightarrow e^- + {}^{37}\text{Ar} \quad (1.4)$$

was unsuccessfully searched by R. Davis Jr. [5], also using nuclear reactors as antineutrino source. An explanation for this result was found in the concept of *lepton number* (L) conservation, where all charged leptons are assigned $L = +1$ and all charged antileptons are assigned $L = -1$. The neutrinos are labeled according to their charged partners to ensure lepton number conservation, hence reactor antineutrinos have the lepton number $L = -1$. The process Davis was looking for, would thus be lepton number violating.

³Isotopes used and produced in nuclear reactors typically show neutron excess and hence decay via reaction 1.2.

The neutrino associated with μ -decays, called ν_μ , was found in 1962 at the first accelerator neutrino experiment at the BNL⁴. The expected but still unconfirmed difference to the neutrinos produced in β -decays was established by observation of the reaction $\nu_\mu + n \rightarrow \mu^- + p$ and $\bar{\nu}_\mu + p \rightarrow \mu^+ + n$ while the rate of electron-accompanied events was consistent with the expected background.

It took another almost 40 years to observe the neutrino associated with tau-leptons: It was found in 2000 by the DONUT⁵ experiment, achieving a direct detection of the short-lived tau lepton from ν_τ charged current interactions in an accelerator beam and with a detection technique very similar to the one used in the OPERA experiment. The neutrino beams used in these two experiments are explained in more detail in Section 3.1.1.1.

Finally, the total number of active⁶ neutrinos with a mass $m_\nu < m_{Z^0}/2 \approx 91/2$ GeV is measured to be 3.00 ± 0.06 by combination of the current world data [1]. A very good review about neutrino history up to the results of Reines and Cowan is given by W. Pauli himself [6].

1.2 Neutrinos in the standard model

The theory of modern particle physics is based on the so-called *Standard Model (SM)* that describes all fundamental particles and the forces between them. Since there are many excellent resources available on this topic, it is reviewed only very briefly, phenomenologically and with focus on weak interactions and neutrinos in this section. A general introduction can be found for example in [7], details on weak interactions in [8] and an up-to-date overview, both theoretically and experimentally, on neutrino physics in [9].

The SM is a gauge theory based on the local symmetry group $SU(3) \times SU(2) \times U(1)$ that determines the interactions and all generators of the group⁷. Each generator corresponds to one vector boson (i.e. a spin one particle) that acts as mediator of a corresponding force. The three symmetry groups forming the SM are associated to one type of interaction each. The symmetry group $SU(3)$ is generated by eight massless gluons that mediate the strong interactions, the unbroken symmetry of this group is the color charge. Strong interactions are described by a quantum field theory called *quantum chromodynamics (QCD)*.

Within the SM, weak interactions and electromagnetic interactions are unified into electroweak interactions described by the *Glashow-Salam-Weinberg*

⁴BNL: Brookhaven National Laboratory.

⁵DONUT: Direct Observation of the Nu Tau, (Fermilab E872).

⁶This leaves open the possibility of so-called “sterile neutrinos” that do not couple to the Z^0 and are explained in Section 1.3.2.

⁷ $SU(n)$ denotes the *special unitary group* of $(n \times n)$ matrices with determinant one.

(*GSW*) model [10, 11, 12]. Weak interactions are mediated by three massive bosons, two of them carry an electric charge (W^\pm) while one is electrically neutral (Z^0). The symmetry group of weak interactions is the weak isospin. The massless photon is the mediator of the electromagnetic force and the symmetry group $U(1)$ is the weak hypercharge. While the weak and the electromagnetic gauge bosons mix and thus cannot be described solitarily, the vector bosons of the strong interaction and the electroweak sectors do not mix, which allows to treat the $SU(2) \times U(1)$ group isolated from the $SU(3)$ group. The masses of the W^\pm and Z^0 are explained by the Higgs mechanism in the SM. The Higgs boson itself is the only predicted but not yet discovered boson of the SM⁸.

In addition to the twelve force–mediating particles and the Higgs boson, the SM introduces twelve fermions (i.e. spin 1/2 particles) and the same number of antiparticles⁹. Six of them are so–called leptons (e^- , μ^- , τ^- , ν_e , ν_μ , ν_τ) and six of them are quarks (*up* (u), *down* (d), *charm* (c), *strange* (s), *top* (t), *bottom* (b)).

The heavy bosons of the weak interaction couple only to left–handed fermion fields and right–handed antifermion fields, which is called maximal parity violation by the weak force. The left–handed components of the fermion fields

$$\Psi_L = \begin{pmatrix} \Psi_L(1) \\ \Psi_L(2) \end{pmatrix} \quad (1.5)$$

are

$$\Psi_L = \begin{pmatrix} \nu_l \\ l^- \end{pmatrix} \quad \text{and} \quad \Psi_L = \begin{pmatrix} q_u \\ q'_d \end{pmatrix}, \quad (1.6)$$

where $l = e, \mu, \tau$, $\nu_l = \nu_e, \nu_\mu, \nu_\tau$, $q_u = u, c, t$ and $q'_d = d', s', b'$ are eigenstates of the weak interaction. The charged bosons W^\pm mediate so–called *charged current* (*CC*) interactions between the two components $\Psi_L(1) \leftrightarrow \Psi_L(2)$ and change the I_3 component of the weak isospin by ± 1 , whereas the Z^0 induces *neutral current* (*NC*) interactions $\Psi_L(i) \leftrightarrow \Psi_L(i)$ with $i = (1, 2)$ which conserve the third weak isospin component. The coupling to the gauge bosons is equal for all leptons, known as lepton universality if the weak interaction.

The weak quark eigenstates (q_u, q'_d) are related to the mass eigenstates (q_u, q_d), via the unitary *Cabibbo–Kobayashi–Maskawa* (*CKM*) matrix U_{CKM} [1, 13, 14]:

$$(d', s', b') = U_{CKM} \begin{pmatrix} d \\ s \\ b \end{pmatrix}. \quad (1.7)$$

⁸In summer 2012, the two LHC experiments ATLAS and CMS announced the observation of a boson with a mass of (125–126) GeV that could be the Higgs–boson.

⁹Antiparticles have all their additive quantum numbers (e.g. electrical charge) reversed with respect to the corresponding particle.

1.3 Neutrino oscillations

Even though neutrinos are taken to be massless in the SM, the introduction of neutrino masses does not violate any fundamental gauge symmetry of that theory. Massive neutrinos open up the possibility of a quantum mechanical effect called neutrino oscillation which is an interference phenomenon of different neutrino mass eigenstates that violates flavor lepton number conservation¹⁰: A neutrino is produced in a pure flavor eigenstate ν_α and detected in a pure flavor eigenstate ν_β at a certain distance from the source to the detector. If $\alpha \neq \beta$, the neutrino has changed its flavor and oscillated into a new flavor. The probability of this is called the oscillation probability $P(\nu_\alpha \rightarrow \nu_\beta)$.

1.3.1 Neutrino oscillations in vacuum

Neutrino oscillations can be described by a wave packet treatment for full consistency of the derivation. However, a simpler plane wave approximation yields the same result for the oscillation probability after some reasonable, (often) implicitly made, assumptions [9, 15].

In the SM, neutrinos are only produced and detected in weak interactions as pure weak flavor eigenstates $|\nu_\alpha\rangle$ with $\langle\nu_\beta|\nu_\alpha\rangle = \delta_{\alpha\beta}$. The flavor of a neutrino ν_α is defined in charged current interactions¹¹, where it is determined by the flavor of the associated charged antilepton l_α^+ (for $\nu_\alpha l_\alpha^+$ pair creation, e.g. in β^+ -decays) or by the flavor of the associated charged lepton l_α^- (for $\nu_\alpha \rightarrow l_\alpha^-$ transition, e.g. in neutrino scattering).

Flavor eigenstates and mass eigenstates are related via a $n_m \times n_m$ unitary¹² matrix U :

$$|\nu\rangle = U|\nu'\rangle, \quad (1.8)$$

$$|\nu_\alpha\rangle = \sum_i U_{\alpha i} |\nu'_i\rangle, \quad (1.9)$$

and

$$|\nu'\rangle = U^\dagger |\nu\rangle, \quad (1.10)$$

$$\begin{aligned} |\nu'_i\rangle &= \sum_\alpha U_{i\alpha}^\dagger |\nu_\alpha\rangle \\ &= \sum_\alpha U_{\alpha i}^* |\nu_\alpha\rangle, \end{aligned} \quad (1.11)$$

¹⁰The mechanism of neutrino oscillations, even though not a flavor oscillation but a $\nu \rightarrow \bar{\nu}$ transition, was proposed by Pontecorvo in analogy to neutral kaon oscillations even before the discovery of the muon-neutrino.

¹¹The neutrino flavor in neutral current interactions is undefined, but the interaction is restricted to active neutrinos that couple to the Z^0 boson.

¹²A complex $n \times n$ matrix A is unitary if $A^\dagger A = \mathbb{1}$, where A^\dagger is the conjugate transpose of the matrix A and $\mathbb{1}$ is the identity matrix.

where U^* is the conjugate, but not transpose, of the matrix U . A flavor eigenstate is hence a coherent superposition of mass eigenstates, where the components are weighted by the entries of the mixing matrix U , whereas a mass eigenstate is a coherent superposition of flavor eigenstates with the weights given by the matrix U^\dagger .

In the restframe of a neutrino mass eigenstate, the time evolution is described by the Schrödinger equation:

$$i \frac{\partial}{\partial \tau_i} |\nu'(\tau_i)\rangle = H^{V'} |\nu'(\tau_i)\rangle, \quad (1.12)$$

where $H^{V'}$ is the Hamilton in the mass eigenstate representation in vacuum and τ_i is the neutrino proper time. This equation is solved by

$$|\nu'_i\rangle = e^{-im_i\tau_i} |\nu'_i(0)\rangle, \quad (1.13)$$

which can be expressed in the lab frame by a Lorentz transformation $m_i\tau_i = E_it - p_iL$, where L is the distance traveled in the lab frame and t the elapsed time. Expanding the well-known dispersion relation

$$p_i = \sqrt{E_i^2 - m_i^2} \quad (1.14)$$

around $m_i \approx 0$ and assuming that each eigenstate has the same energy, $E_i = E$ and E is real, gives

$$p_i \approx \sqrt{E_i^2} - \frac{m_i^2 \sqrt{E_i^2}}{2E_i^2} + \mathcal{O}(m_i^3) \quad (1.15)$$

$$= E_i - \frac{m_i^2}{2E_i} + \mathcal{O}(m_i^3) \quad (1.16)$$

$$\approx E - \frac{m_i^2}{2E}. \quad (1.17)$$

The time evolution of a flavor neutrino state can be written as

$$|\nu'_\alpha(t)\rangle = e^{-i\frac{m_i^2}{2E}t} U_{\alpha i} |\nu'_i(0)\rangle. \quad (1.18)$$

The time-dependent transition amplitude for a process $\nu_\alpha \rightarrow \nu_\beta$ is hence given by

$$\mathcal{A}(\nu_\alpha \rightarrow \nu_\beta, t) \equiv \langle \nu_\beta(t) | \nu_\alpha(0) \rangle \quad (1.19)$$

$$= \sum_i U_{\alpha i}^* U_{\beta i} e^{-i\frac{m_i^2}{2E}t}. \quad (1.20)$$

The transition probability between a neutrino with the initial flavor α and the final flavor β is given by

$$P(\nu_\alpha \rightarrow \nu_\beta, t) \equiv |\mathcal{A}(\nu_\alpha \rightarrow \nu_\beta, t)|^2 \quad (1.21)$$

$$= \left| \sum_i U_{\alpha i}^* U_{\beta i} e^{-i \frac{m_i^2}{2E} t} \right|^2 \quad (1.22)$$

$$= \sum_i \sum_j U_{\alpha i}^* U_{\beta i} U_{\alpha j} U_{\beta j}^* e^{-i \frac{(m_i^2 - m_j^2)}{2E} t} \quad (1.23)$$

$$= \sum_i \sum_j U_{\alpha i}^* U_{\beta i} U_{\alpha j} U_{\beta j}^* e^{-i \frac{\Delta m_{ij}^2}{2E} L} \quad (1.24)$$

with $L = t$ for ultrarelativistic¹³ neutrinos (in natural units) and $\Delta m_{ij}^2 = m_i^2 - m_j^2$. This equation describes an oscillation between flavor eigenstates and is hence called oscillation probability. It is convenient to rewrite it by using trigonometric functions and separating the real and imaginary parts:

$$\begin{aligned} P(\nu_\alpha \rightarrow \nu_\beta, L) &= \delta_{\alpha\beta} - 4 \sum_{i>j} \Re(U_{\alpha i}^* U_{\beta i} U_{\alpha j} U_{\beta j}^*) \sin^2 \left(\frac{\Delta m_{ij}^2 L}{4E} \right) \\ &\quad \pm 2 \sum_{i>j} \Im(U_{\alpha i}^* U_{\beta i} U_{\alpha j} U_{\beta j}^*) \sin \left(\frac{\Delta m_{ij}^2 L}{2E} \right), \end{aligned} \quad (1.25)$$

where the minus sign in front of the third term is for the antineutrino oscillation probability $P(\bar{\nu}_\alpha \rightarrow \bar{\nu}_\beta, L)$. If there is no CP violation¹⁴, the imaginary part is zero and $P(\nu_\alpha \rightarrow \nu_\beta, L) = P(\bar{\nu}_\alpha \rightarrow \bar{\nu}_\beta, L)$.

The entries of the mixing matrix U , usually called *Pontecorvo–Maki–Nakagawa–Sakata (PMNS)* matrix, and the squared mass differences Δm_{ij}^2 are physical constants that have to be determined by experiment. The $n_m \times n_m$ PMNS matrix is completely described by n_m^2 complex entries, where n_m is the number of lepton generations. However, the number of independent physical parameters can be reduced by using the unitarity of U and the invariance of the charged lepton fields under global phase shifts [9]. It is common practice to parametrize U by $\frac{n_m(n_m-1)}{2}$ real angles and $\frac{n_m(n_m-1)}{2}$ complex phases. Up to now, all experiments are compatible with the assumption of three light active neutrinos¹⁵. Thus in the remaining part of this section, the number of lepton

¹³This condition is fulfilled in all experiments performed up to now: The lowest energy threshold ever used in neutrino experiments is the inverse β -decay of Gallium ($\nu_e + {}^{71}\text{Ga} \rightarrow e^- + {}^{71}\text{Ge}$) with a threshold energy of $E_t \approx 0.233$ MeV. On the other hand, the electron–neutrino mass and the sum of all neutrino masses are experimentally well constrained below some eV. The kinematic lower limits of ν_μ and ν_τ quasi-elastic CC interactions are 110 MeV and 3.5 GeV, respectively (see Section 2.1.1).

¹⁴CP violation is the violation of the combined charge (C) and parity (P) symmetry conjugation.

¹⁵The only exceptions are accelerator neutrino experiments at a baseline $L/E = \mathcal{O}(1 \text{ km/GeV})$, observing $\bar{\nu}_e$ appearance in a $\bar{\nu}_\mu$ beam, which will be discussed in Section 1.3.2.

generations is set to $n_l = n_m = 3$.

The parametrization of U , while in principle being arbitrary, can be written as product of three rotation matrices around the Euler axes R_{ij} , where the rotation takes place in the ij -plane. The mixing matrix U is usually parametrized by

$$U = \begin{pmatrix} U_{e1} & U_{e2} & U_{e3} \\ U_{\mu1} & U_{\mu2} & U_{\mu3} \\ U_{\tau1} & U_{\tau2} & U_{\tau3} \end{pmatrix} \quad (1.26)$$

$$= R_{23}(\theta_{23})R_{13}(\theta_{13}, \delta)R_{12}(\theta_{12})M_3 \quad (1.27)$$

$$= \underbrace{\begin{pmatrix} 1 & 0 & 0 \\ 0 & c_{23} & s_{23} \\ 0 & -s_{23} & c_{23} \end{pmatrix}}_{\text{atmospheric}} \begin{pmatrix} c_{13} & 0 & s_{13}e^{-i\delta} \\ 0 & 1 & 0 \\ -s_{13}e^{i\delta} & 0 & c_{13} \end{pmatrix} \underbrace{\begin{pmatrix} c_{12} & s_{12} & 0 \\ -s_{12} & c_{12} & 0 \\ 0 & 0 & 1 \end{pmatrix}}_{\text{solar}} \quad (1.28)$$

$$\times \underbrace{\begin{pmatrix} e^{i\alpha_1/2} & 0 & 0 \\ 0 & e^{i\alpha_2/2} & 0 \\ 0 & 0 & 1 \end{pmatrix}}_{\text{Majorana phases}},$$

with $s_{ij} = \sin(\theta_{ij})$ and $c_{ij} = \cos(\theta_{ij})$. δ is the so-called Dirac phase and $\alpha_{1,2}$ are Majorana phases. The latter are nonzero if the neutrinos are Majorana particles, i.e. if $\nu = \bar{\nu}$, and are not measurable in neutrino oscillation experiments (compare Equation 1.21). The Dirac phase is only measurable in neutrino oscillations if none of the real mixing angles is zero. The ν_μ oscillation probabilities $P(\nu_\mu \rightarrow \nu_\beta, L)$, for $\beta = (e, \mu, \tau)$, are given explicitly in Appendix A.

Most aspects of neutrino mixing can be understood in a two-flavor scheme which also is an approximation for experiments where the oscillation probability is dominated by one squared mass difference, $\Delta m_{13} \gg \Delta m_{12}$, and contributions from the rotation matrix R_{13} are small, i.e. $\theta_{13} \approx 0$. The mixing matrix is then given by a unitary 2×2 matrix U_2 , which can be parametrized as a rotation matrix using one single rotation angle θ :

$$U_2(\theta) = \begin{pmatrix} \cos(\theta) & \sin(\theta) \\ -\sin(\theta) & \cos(\theta) \end{pmatrix}. \quad (1.29)$$

The survival probability in the two-flavor approximation is given by

$$P(\nu_\alpha \rightarrow \nu_\alpha, L) = P_{\alpha\alpha} \quad (1.30)$$

$$= P_{\beta\beta} = P_{\bar{\alpha}\bar{\alpha}} = P_{\bar{\beta}\bar{\beta}} \quad (1.31)$$

$$= 1 - P_{\alpha\beta} = 1 - P_{\beta\alpha} = 1 - P_{\bar{\alpha}\bar{\beta}} = 1 - P_{\bar{\beta}\bar{\alpha}} \quad (1.32)$$

$$= 1 - \sin^2(2\theta) \sin^2\left(\frac{\Delta m^2 L}{4E}\right) \quad (1.33)$$

$$= 1 - \sin^2(2\theta) \sin^2\left(\frac{c^3 \Delta m^2 L}{\hbar 4E}\right) \quad (\text{SI units}) \quad (1.34)$$

$$\approx 1 - \sin^2(2\theta) \sin^2\left(1.267 \frac{\Delta m^2 [\text{eV}^2] L [\text{km}]}{E [\text{GeV}]}\right), \quad (1.35)$$

where Δm^2 is the squared mass difference between the two mass eigenstates.

The results for the oscillation parameters from an analysis of global data are shown in Table 1.1. The oscillation frequencies $\Delta m_{ij}^2 L/4E$ measured by solar and atmospheric neutrino oscillation experiments are different, which is attributed to two different squared mass differences, where experiments showed $\Delta m_{\text{solar}}^2 \ll \Delta m_{\text{atmospheric}}^2$. The labeling of the mass eigenstates m_i is arbitrary and chosen such that the observed squared mass difference in solar neutrino oscillations is $\Delta m_{\text{solar}}^2 = \Delta m_{21}^2$ with $m_2^2 > m_1^2$. A value of $\theta_{12} < 45.0^\circ$ allows identifying ν_1 as containing mostly electron flavor, whereas $\theta_{23} > 45.0^\circ$ means a small excess of muon flavor over tau flavor in the mass eigenstate ν_3 . The three squared mass differences are not independent, since $\Delta m_{21}^2 + \Delta m_{32}^2 - \Delta m_{31}^2 = 0$, which leads to the identification $\Delta m_{\text{atmospheric}}^2 \approx |\Delta m_{32}^2| \approx |\Delta m_{31}^2|$. The sign of Δm_{31}^2 is unknown, a question related to the so-called neutrino mass hierarchy that can either be normal ($m_1 < m_2 < m_3$), inverted ($m_3 < m_1 < m_2$) or quasi-degenerate ($m_1 \approx m_2 \approx m_3$) (see Figure 1.2).

Within this work, the three squared mass differences are defined¹⁶ by

$$\Delta m_{21}^2 \equiv \Delta m_{\text{sol}}^2, \quad (1.36)$$

$$\Delta m_{31}^2 \equiv \Delta m_{\text{atm}}^2, \quad (1.37)$$

$$\Delta m_{32}^2 \equiv \Delta m_{31}^2 - \Delta m_{21}^2, \quad (1.38)$$

for the normal neutrino mass hierarchy, and by

$$\Delta m_{21,\text{inv}}^2 \equiv \Delta m_{\text{sol}}^2, \quad (1.39)$$

$$\Delta m_{31,\text{inv}}^2 \equiv -\Delta m_{\text{atm}}^2 + \Delta m_{21,\text{inv}}^2, \quad (1.40)$$

$$\Delta m_{32,\text{inv}}^2 \equiv \Delta m_{31,\text{inv}}^2 - \Delta m_{21,\text{inv}}^2 \quad (1.41)$$

for the inverted neutrino mass hierarchy.

¹⁶Experimental data does not allow to differentiate between Δm_{31}^2 and Δm_{32}^2 yet. However, within three-flavor (or more) oscillations, the two different values lead to two different oscillation frequencies and potentially different results.

Accelerator-based experiments T2K¹⁷ [16] and MINOS¹⁸ [17] gave hint that the least-known third mixing angle θ_{13} is nonzero, looking for subleading electron-neutrino appearance in a muon-neutrino beam. Recent results from different reactor neutrino experiments have established a rather large value of $\theta_{13} \approx 9^\circ$ [18, 19, 20]. Up to now, the magnitude of CP-violation, if any, in the neutrino sector is unknown. The question whether the neutrino mass is due to Dirac or Majorana mass terms is open and currently under study in *neutrinoless double β -decay* ($0\nu\beta\beta$) experiments [1, 21].

Table 1.1: Neutrino oscillation parameters from global data for normal mass hierarchy [22, 23] and from the Daya Bay experiment [20], statistical and systematic errors added in quadrature.

Parameter	Best fit $\pm 1\sigma$	3σ range
$\sin^2(\theta_{12})$	$0.312^{+0.017}_{-0.015}$ ($\theta_{12} \approx 34.0^\circ$)	0.27 - 0.36
$\sin^2(2\theta_{13})$	0.092 ± 0.018 ($\theta_{13} \approx 8.8^\circ$)	0.038 - 0.146
$\sin^2(\theta_{23})$	$0.52^{+0.06}_{-0.07}$ ($\theta_{23} \approx 46.1^\circ$)	0.39 - 0.64
Δm_{21}^2 [10^{-5} eV ²]	$7.59^{+0.20}_{-0.18}$	7.09 - 8.19
$ \Delta m_{31}^2 \approx \Delta m_{32}^2 $ [10^{-3} eV ²]	$2.50^{+0.09}_{-0.16}$	2.14 - 2.76
δ_{CP}	–	0 - 2π

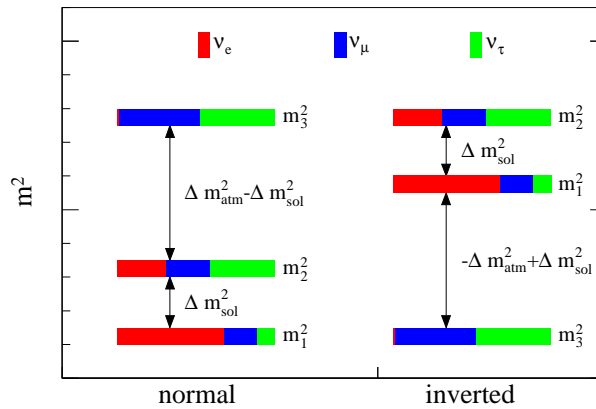


Figure 1.2: Three-neutrino mass spectra (schematic) and flavor composition for normal (left) and inverted (right) mass hierarchy. Flavor composition of the mass eigenstates calculated using the best fit values from Table 1.1.

The current situation can be briefly summarized as follows: All solar and atmospheric neutrino oscillation experiments are compatible within a

¹⁷T2K: Tokai To Kamioka.

¹⁸MINOS: Main Injector Neutrino Oscillation Search.

three–active–neutrino mixing scheme, establishing the two distinct squared mass differences Δm_{sol}^2 and Δm_{atm}^2 . The number of active neutrinos is constrained to $n_a = 3.00 \pm 0.06$ by the invisible Z^0 decay width [1]. The best limits on the total neutrino masses and the total number of neutrinos come from cosmology, where the most stringent limits are placed by the WMAP¹⁹ experiment that constrains the neutrino masses (active and sterile) to $\sum m_\nu < 1.3$ eV (95 % confidence level (CL)) and the number of neutrino generations to $n_l > 2.7$ (95 % CL). Combining these results with other cosmological data yields stronger bounds of $\sum m_\nu < 0.58$ eV (95% CL) and $n_l = 4.34_{-0.88}^{+0.86}$ [24], which is a hint towards the existence of more than three neutrino generations.

1.3.2 Sterile neutrinos

The consistent three–neutrino picture, as outlined in the previous section, is disturbed by the results of the LSND²⁰ experiment. LSND conducted a $\bar{\nu}_\mu \rightarrow \bar{\nu}_e$ appearance search with a baseline of $L/E \approx 1$ m/MeV using antineutrinos with energies of about 50 MeV from pion decays at rest. LSND measured an anti-electron excess of about 3.8σ above the expected background including standard three–flavor neutrino oscillations [25]. If this excess is interpreted in the framework of neutrino oscillations, it suggests a Δm_{LSND}^2 in the range $(0.2 - 20)$ eV² (including constraints from reactor experiments and KARMEN2²¹ [26]).

The MiniBooNE²² experiment was designed to probe the LSND parameter space at the same baseline L/E but with a more than hundred times higher neutrino energy with both neutrinos and antineutrinos. The MiniBooNE results are compatible with LSND in the antineutrino run [27] but exclude the LSND result for neutrinos [28] at 90 % CL. Several accelerator experiments like NOMAD²³ put limits on the LSND CP–conjugate neutrino $\nu_\mu \rightarrow \nu_e$ appearance [29], whereas reactor neutrino experiments limit the allowed region from $\bar{\nu}_e \rightarrow \bar{\nu}_e$ disappearance data. The excluded and allowed regions of several experiments are shown in Figure 1.3. The lower LSND bound of $\Delta m_{LSND}^2 = 0.2$ eV² hints at the existence of at least one massive neutrino with a mass larger than 0.4 eV. This new Δm^2 is much larger than the solar and atmospheric ones, leading to a quasi–degeneration of $\Delta m_{sol}^2 \approx \Delta m_{atm}^2 \ll \Delta m_{LSND}^2$.

A new Δm^2 is directly related to at least one additional light neutrino mass eigenstate. The occurrence of, yet hypothetical, additional mass eigenstates are associated with the existence of so–called “sterile” neutrinos that do not couple to the weak force–mediating bosons within the SM. All sterile neutrinos must hence be electroweak singlets. These sterile neutrinos would be a clear signal of beyond–standard model physics. In the absence of standard model interactions, only indirect observations of sterile neutrinos are possible. Neutrino oscillations

¹⁹WMAP: Wilkinson Microwave Anisotropy Probe.

²⁰LSND: Liquid Scintillator Neutrino Detector.

²²MiniBooNE: Mini Booster Neutrino Experiment.

²³NOMAD: Neutrino Oscillation Magnetic Detector.

provide a tool to discover light sterile neutrinos in the eV mass range²⁴ by looking for active–to–sterile mixing.

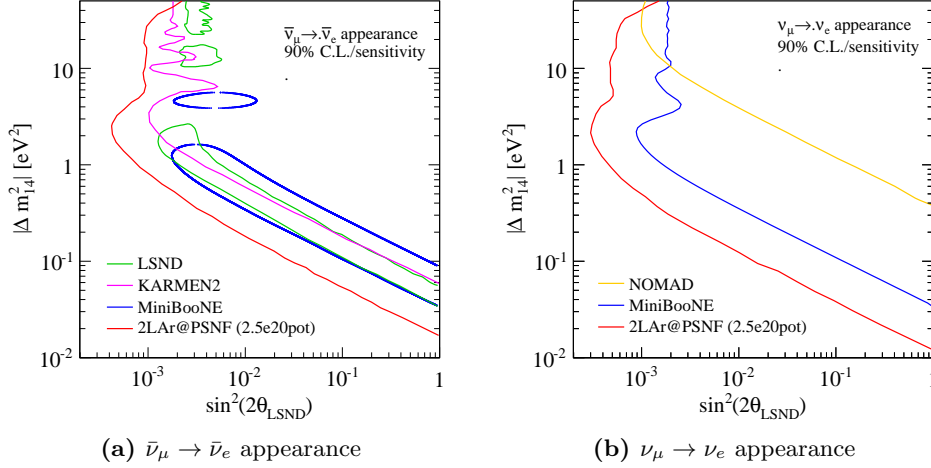


Figure 1.3: Sensitivity (2LAr@PSNF only [30], see end of this section for details) and exclusion plots from various electron–(anti)neutrino appearance experiments [25, 26, 27, 28, 29]. Everything on the right side of the curves is excluded/sensitive.

The extension of the standard neutrino oscillation formalism, as given in the previous section, to more than three generations is straight–forward:

$$\begin{pmatrix} |\nu_e\rangle \\ |\nu_\mu\rangle \\ |\nu_\tau\rangle \\ |\nu_s\rangle \\ |\nu_{s'}\rangle \\ \vdots \end{pmatrix} = \begin{pmatrix} U_{e1} & U_{e2} & U_{e3} & U_{e4} & U_{e5} & \dots \\ U_{\mu1} & U_{\mu2} & U_{\mu3} & U_{\mu4} & U_{\mu5} & \dots \\ U_{\tau1} & U_{\tau2} & U_{\tau3} & U_{\tau4} & U_{\tau5} & \dots \\ U_{s1} & U_{s2} & U_{s3} & U_{s4} & U_{s5} & \dots \\ U_{s'1} & U_{s'2} & U_{s'3} & U_{s'4} & U_{s'5} & \dots \\ \vdots & \vdots & \vdots & \vdots & \vdots & \ddots \end{pmatrix} \begin{pmatrix} |\nu_1\rangle \\ |\nu_2\rangle \\ |\nu_3\rangle \\ |\nu_4\rangle \\ |\nu_5\rangle \\ \vdots \end{pmatrix}, \quad (1.42)$$

where the three–flavor matrix U_{PMNS} is a submatrix of the new mixing matrix.

The minimal extension of the SM with the introduction of one sterile neutrino leads to three additional mixing angles θ_{14} , θ_{24} and θ_{34} , two additional complex Dirac phases δ_2 and δ_3 and an additional mass eigenvalue m_4 . The additional Majorana phase vanishes from the oscillation probabilities as in the standard formalism. The fourth mass eigenstate opens up several different mass hierarchies (see Figure 1.4). The parametrization of the full mixing matrix U_4 can be chosen such that the three–flavor mixing rotation order (see Equation 1.27) is reproduced in case of vanishing active–to–sterile mixing. One of the CP–violating phases, δ_{13} , is chosen in analogy to the three–flavor case, a second phase δ_{12} is put next to θ_{12}

²⁴Some models predict very heavy sterile neutrinos beyond the electroweak scale that are not yet accessible in neutrino experiments.

and hence vanishes if the experiment is not sensitive to this angle, while the third phase δ_{24} is arbitrarily put next to θ_{24} and Majorana phases are omitted. The complete mixing matrix can be written as

$$U_4 = R_{34}(\theta_{34})R_{24}(\theta_{24}, \delta_{24})R_{14}(\theta_{14})R_{23}(\theta_{23})R_{13}(\theta_{13}, \delta_2)R_{12}(\theta_{12}, \delta_1). \quad (1.43)$$

The entries of the mixing matrix are given explicitly in Appendix A and the oscillation probability is calculated using Equation 1.24 as usual.

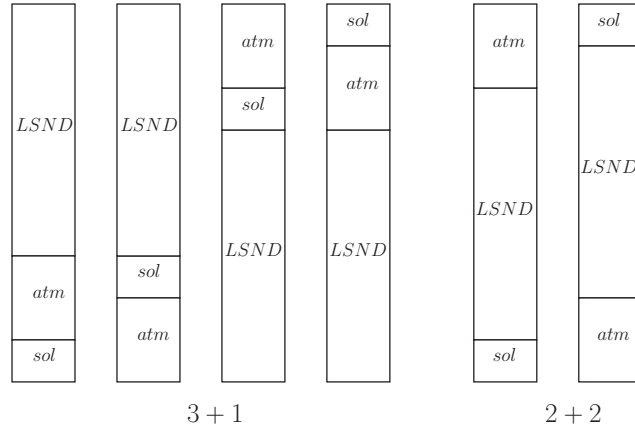


Figure 1.4: Different four–neutrino mass spectra, “3+1” and “2+2”. “LSND”, “sol” and “atm” denote the corresponding squared mass differences. In a “3+1” scenario, the third Δm^2 either separates a heavier or a lighter mass eigenstate from the existing three active neutrinos, whereas in a “2+2” scenario the solar and atmospheric squared mass differences are separated by the additional third Δm^2 .

LSND and MiniBooNE are operated at baselines of $L/E = \mathcal{O}(1 \text{ m/MeV})$, where the solar and atmospheric oscillation frequencies $\Delta m_{sol}^2 \frac{L}{E}$, $\Delta m_{atm}^2 \frac{L}{E}$ are approximately zero and the oscillation is driven by a new $\Delta m_{LSND}^2 \gg \Delta m_{atm}^2 \approx \Delta m_{sol}^2$. The electron–antineutrino appearance probability for LSND–type experiments is given by

$$P(\bar{\nu}_\mu \rightarrow \bar{\nu}_e) = \sin^2(2\theta_{14}) \sin^2(\theta_{24}) \sin^2\left(\frac{\Delta m_{LSND}^2 L}{4E}\right). \quad (1.44)$$

Note that LSND and the other experiments shown in Figure 1.3 are evaluated in the two–flavor approximation 1.30

$$P(\bar{\nu}_\mu \rightarrow \bar{\nu}_e) = \sin^2(2\theta_{LSND}) \sin^2\left(\frac{\Delta m_{LSND}^2 L}{4E}\right). \quad (1.45)$$

Reactor neutrino experiments measuring the mixing angle θ_{13} are operated at $L/E = \mathcal{O}(100 \text{ m/MeV})$ which is far from the first solar oscillation maximum and hence contributions from $\Delta m_{sol}^2 \frac{L}{E}$ are small compared to those from $\Delta m_{atm}^2 \frac{L}{E}$.

On the other hand, a large Δm_{LSND}^2 oscillation averages out and leads to an approximately energy-independent contribution. The electron-antineutrino survival probability is given by

$$P(\bar{\nu}_e \rightarrow \bar{\nu}_e) = 1 - \sin^2(2\theta_{14}) \sin^2\left(\frac{\Delta m_{LSND}^2 L}{4E}\right) - \cos^4(\theta_{14}) \sin^2(2\theta_{13}) \sin^2\left(\frac{\Delta m_{atm}^2 L}{4E}\right) \quad (1.46)$$

$$\approx 1 - \frac{1}{2} \sin^2(2\theta_{14}) - \cos^4(\theta_{14}) \sin^2(2\theta_{13}) \sin^2\left(\frac{\Delta m_{atm}^2 L}{4E}\right). \quad (1.47)$$

Existing null results from reactor experiments limit the size of the mixing angle θ_{14} for all experimentally allowed values²⁵ of Δm_{LSND}^2 .

The three-neutrino “3+0” scheme is not compatible with the LSND and MiniBooNE antineutrino results at about 4σ . The four-neutrino “2+2” scheme is experimentally excluded by both solar and atmospheric disappearance data which favor oscillations between active neutrinos. The “3+1” scheme is not fully consistent with reactor disappearance experiments, whereas “3+2” or “1+3+1” schemes²⁶, including recent re-calculations of reactor fluxes [31], release some of the tension [32].

Using the rotation order defined in Equation 1.43, limits on the three additional mixing angles can be given assuming a “3+1” scheme and normal mass hierarchy (see Figure 1.5) as follows. From Equation 1.46 and existing results from reactor experiments, it follows that θ_{14} cannot be much larger than θ_{13} . The mixing angle θ_{24} is restricted below 10° (90 % CL), where a small value of θ_{24} is a direct consequence of the good compatibility of long-baseline ν_μ disappearance data with the assumption of three-flavor neutrino oscillations. The mixing angle θ_{34} is the least constrained one and can be as large as 60° (90 % CL) for $\theta_{13} = 12^\circ$ and maximal atmospheric mixing [33].

Several, mostly complementary, experiments have been proposed or are under construction to definitely resolve the puzzling LSND anomaly, some of them are briefly mentioned below.

The MiniBooNE detector will be accompanied by the liquid Argon *time projection chamber* (TPC) detector MicroBooNE²⁷ at a similar baseline, which can, among others, help to disentangle contributions from electrons and photons

²⁵The oscillation due to Δm_{LSND}^2 averages out for values above about 0.1eV^2 in reactor experiments.

²⁶“1+3+1” mass spectra involve a sterile neutrino lighter than the three active ones and one heavier neutrino, whereas in the “3+2” mass spectra both sterile neutrinos are heavier than the active neutrinos.

²⁷MicroBooNE: Micro Booster neutrino experiment.

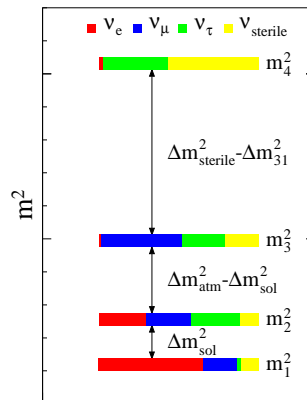


Figure 1.5: Four-neutrino mass spectra (“3+1”, schematic) for the normal mass hierarchy. Flavor composition of the mass eigenstates calculated using the best fit values from Table 1.1 and the set of sterile mixing angles and CP-violating phases minimizing the τ appearance rate in OPERA (see Section 7.1): $\theta_{14} = 6^\circ$, $\theta_{24} = 3^\circ$, $\theta_{34} = 40^\circ$, $\delta_{12} = \delta_{13} = 0$ and $\delta_{24} = 3\pi/2$.

at low energies²⁸. MicroBooNE is already under construction.

The list of proposed experiments cover a wide range of possible neutrino sources and detector concepts [34]. Using liquid Argon TPCs at different distances (2LAr@PSNF²⁹, see Figure 1.3), the existing ICARUS³⁰ detector T600 could be operated in a refurbished CERN-PS³¹ neutrino beam with sensitivity to cover the full LSND parameter space. In combination with OPERA-type iron spectrometers (see Section 3.2.3) downstream of the non-magnetized TPCs, this project is called NESSIE³². Future plans to add a near detector to the MiniBooNE experiment reach similar sensitivity. At much lower neutrino energies of some MeV, strong radioactive sources, similar to those used for the calibration of the GALLEX³³ or SAGE³⁴ experiments, could be placed directly into large liquid scintillator detectors like BOREXINO³⁵, KamLAND³⁶ or SNO+³⁷ to measure full oscillation patterns at $L/E = \mathcal{O}(1 \text{ m/MeV})$. Plans to repeat the LSND experiment with a more powerful spallation source or to perform reactor exper-

²⁸MiniBooNE observes a low-energy excess of electron-neutrinos that is not compatible with the LSND signal. The excess could be due to misidentified final state photons that are difficult to separate from electrons in a scintillation detector like MiniBooNE.

²⁹2LAr@PSNF: Two liquid Argon TPCs at the Proton Synchrotron neutrino facility.

³⁰ICARUS: Imaging Cosmic And Rare Underground Signals.

³¹PS: Proton Synchrotron.

³²NESSIE: Neutrino Experiment with Spectrometers in Europe.

³³GALLEX: Gallium Experiment.

³⁴SAGE: Soviet-American Gallium Experiment.

³⁵BOREXINO: Boron Experiment.

³⁶KamLAND: Kamioka Liquid Scintillator Antineutrino Detector.

³⁷SNO+: Sudbury Neutrino Observatory with liquid scintillator.

iments at a distance of about 10 m from the reactor core are under discussion, too.

Sterile neutrinos in long-baseline experiments are discussed within the OPERA framework in Section 7.1.

1.3.3 Neutrino oscillations in matter

Neutrinos travelling through matter, rather than vacuum, have a different oscillation probability. The impact of matter on the oscillation probability is called matter effect. In general, the Hamiltonian that appears in the description of the time evolution of a system (compare Equation 1.12) is the sum of the kinetic and potential energy. For neutrinos propagating in vacuum, the potential energy contribution is zero. On the other hand, neutrinos in matter are affected by weak interactions and hence have a nonzero potential energy. A modified Hamiltonian yields a modified oscillation probability, as will be shown below.

In the flight path from the source to the detector, only neutrino interactions with a forward (compare Figure B.2 with $\theta = 0$ and Appendix B with $y = 0$) neutrino in the final state contribute to the total neutrino flux at the detector location, all other interactions lead to neutrino deflection off the beam, only reducing the total flux. In order to generate an observable effect, the interactions must produce a constant relative phase shift of the neutrino wave function, which limits the relevant interactions to the elastic ones. Thus, only neutral current elastic neutrino scattering on nucleons or leptons and charged current elastic scattering on like-flavor leptons have nonzero cross sections in the limit $\theta = 0$.

The equation of motion in vacuum (see Equation 1.12),

$$i\frac{\partial}{\partial t}|\nu'\rangle = H^{V'}|\nu'\rangle, \quad (1.48)$$

where $H^{V'}$ is the Hamiltonian in vacuum and $|\nu'\rangle$ is a neutrino mass eigenstate, can be extended (within the same approximations as in the previous section) to include potentials V from the scattering processes mentioned above by modifying the Hamiltonian in the flavor basis:

$$H^V \longrightarrow H^M = H^V + V_n^{NC} + V_p^{NC} + V_{lepton}^{NC} + V_{lepton}^{CC}, \quad (1.49)$$

where H^M is the Hamiltonian in matter in the flavor basis. The explicit expressions for the different potentials in ordinary matter³⁸ are summarized in Table 1.2. Note that radiative corrections (compare Section 2.1.3.7) introduce charged lepton mass-dependent corrections to the matter potentials that resolve the degeneracy of the NC potentials and make the matter effects much more complicated.

³⁸Ordinary matter is composed of neutrons, protons and electrons only. While there are cosmological applications with significant non-electron leptonic matter (muon, tau or neutrinos) or photons, these are negligible for neutrinos travelling through earth.

Table 1.2: Leading-order neutrino matter potentials $V \equiv V(\vec{x})$ in unpolarized ordinary matter at rest (without propagator contributions), where G_F is the Fermi constant, θ_W is the Weinberg angle and $N_t \equiv N_t(\vec{x})$ is the local number density of target t . The upper sign refers to neutrinos, the lower sign to antineutrinos. The hadronic potentials are the sum of up- and down-quark contributions weighted 1:2 (neutron) and 2:1 (proton) [35].

neutrino	target	potential
ν_e, ν_μ, ν_τ	e	$V_e^{NC} = \mp G_F/\sqrt{2}N_e (1 - 4\sin^2\theta_W)$
ν_e	e	$V_e^{CC} = \pm\sqrt{2}G_F N_e$
ν_e, ν_μ, ν_τ	n	$V_n^{NC} = \mp G_F/\sqrt{2}N_n$
ν_e, ν_μ, ν_τ	p	$V_p^{NC} = \pm G_F/\sqrt{2}N_p (1 - 4\sin^2\theta_W)$

In the following, matter effects are derived for the two-flavor approximation of $\nu_e \rightarrow \nu_\mu$ oscillations in matter with constant density ($V(\vec{x}) = V$) in leading order [15].

The equation of motion in the flavor basis is given by

$$i\frac{\partial}{\partial t} \begin{pmatrix} |\nu_e\rangle \\ |\nu_\mu\rangle \end{pmatrix} = H^M \begin{pmatrix} |\nu_e\rangle \\ |\nu_\mu\rangle \end{pmatrix} \quad (1.50)$$

$$= \left[U_2(\theta) \begin{pmatrix} \frac{m_1^2}{2E} & 0 \\ 0 & \frac{m_2^2}{2E} \end{pmatrix} U_2^\dagger(\theta) + \begin{pmatrix} V_e^{NC} + V_e^{CC} + V_p^{NC} + V_n^{NC} & 0 \\ 0 & V_e^{NC} + V_p^{NC} + V_n^{NC} \end{pmatrix} \right] \begin{pmatrix} |\nu_e\rangle \\ |\nu_\mu\rangle \end{pmatrix} \quad (1.51)$$

$$\Rightarrow \left[U_2(\theta) \begin{pmatrix} 0 & 0 \\ 0 & \frac{\Delta m^2}{2E} \end{pmatrix} U_2^\dagger(\theta) + \begin{pmatrix} V_e^{CC} & 0 \\ 0 & 0 \end{pmatrix} + \begin{pmatrix} 1 & 0 \\ 0 & 1 \end{pmatrix} \left(\frac{m_1^2}{2E} + V_e^{NC} + V_p^{NC} + V_n^{NC} \right) \right] \begin{pmatrix} |\nu_e\rangle \\ |\nu_\mu\rangle \end{pmatrix} \quad (1.52)$$

$$= \frac{1}{4E} \left[\begin{pmatrix} A - \Delta m^2 \cos(2\theta) & \Delta m^2 \sin(2\theta) \\ \Delta m^2 \sin(2\theta) & -A + \Delta m^2 \cos(2\theta) \end{pmatrix} + \begin{pmatrix} 1 & 0 \\ 0 & 1 \end{pmatrix} (\Sigma m^2 + A) \right] \begin{pmatrix} |\nu_e\rangle \\ |\nu_\mu\rangle \end{pmatrix}, \quad (1.53)$$

where contributions to the Hamiltonian that are proportional to the identity matrix have been dropped before the last step³⁹. U_2 is given by Equation 1.29,

³⁹Contributions proportional to the identity matrix are equivalent to an unobservable global phase $\delta(t)$ that can be removed by the transformation $\hat{\Psi}(t) \rightarrow e^{i\delta(t)}\Psi(t)$ of the neutrino wavefunction.

$A = 2EV_e^{CC}$, $\Sigma m^2 = m_1^2 + m_2^2$, $\Delta m^2 = m_2^2 - m_1^2$ and the trigonometric identity $\sin^2(\theta) = \frac{1}{2}(1 - \cos(2\theta))$ has been used. Within this two-flavor approximation, the eigenvalues of the (nondiagonal) Hamiltonian

$$H^M = \frac{1}{4E} \begin{pmatrix} A - \Delta m^2 \cos(2\theta) & \Delta m^2 \sin(2\theta) \\ \Delta m^2 \sin(2\theta) & -A + \Delta m^2 \cos(2\theta) \end{pmatrix} \quad (1.54)$$

can be calculated analytically. Since H^M is hermitian, it can be diagonalized by an unitary matrix U^M , giving

$$H_d^M = \begin{pmatrix} (m_1^M)^2 & 0 \\ 0 & (m_2^M)^2 \end{pmatrix} \quad (1.55)$$

$$= (U_2^M)^\dagger H^M U_2^M, \quad (1.56)$$

$$U_2^M(\theta^M) = \begin{pmatrix} \cos(\theta^M) & \sin(\theta^M) \\ -\sin(\theta^M) & \cos(\theta^M) \end{pmatrix}, \quad (1.57)$$

where $\theta^M \neq \theta$ is the mixing angle in matter and m_i^M are the effective mass eigenvalues in matter. As usual, the eigenvalues of H_d^M are the solutions of the quadratic equation system

$$\text{Det} \left(4EH_d^M - \begin{pmatrix} (m^M)^2 & 0 \\ 0 & (m^M)^2 \end{pmatrix} \right) = 0 \quad (1.58)$$

that are given by

$$(m_{1,2}^M)^2 = \frac{1}{2} \left((\Sigma m^2 + A) \pm \sqrt{(A - \Delta m^2 \cos(2\theta))^2 + (\Delta m^2 \sin(2\theta))^2} \right). \quad (1.59)$$

The entries of the unitary matrix can be obtained from

$$\sin(2\theta^M) = \frac{\sin(2\theta)}{\sqrt{\left(\frac{A}{\Delta m^2} - \cos(2\theta)\right)^2 + \sin^2(2\theta)}}. \quad (1.60)$$

Within this simplified two-flavor scheme, the oscillations in matter can be described by the same equations as in vacuum with the two replacements $\Delta m^2 \rightarrow \Delta(m^M)^2$ and $\theta \rightarrow \theta^M$. The additional matter potentials give rise to several phenomena that do not occur in vacuum, among which the *Mikheyev-Smirnov-Wolfenstein (MSW)* effect describes a resonance, where the neutrino mixing in matter gets maximal. This resonance occurs if

$$A = \Delta m^2 \cos(2\theta), \quad (1.61)$$

for which Equation 1.60 becomes maximal. The width of the resonance is proportional to the vacuum mixing angle $\sin(2\theta)$. The mixing angle in matter for different mixing angles in vacuum is shown in Figure 1.6. The numerical value of

the V_e^{CC} can be calculated with $G_F = 1.166 \times 10^{-5} (\hbar c)^3 \text{ GeV}^{-2} = 89.62 \text{ eVfm}^3$ and $N_e = N_A Y_e \rho$, where $N_A = 6.022 \times 10^{23}$ is the Avogadro constant, ρ is the matter density and $Y_e = N_e / (N_n + N_p)$ is the electron fraction per nucleon⁴⁰:

$$V_e^{CC} = 7.63 \times 10^{-14} Y_e \rho \frac{\text{eV}}{(\text{g/cm}^3)}. \quad (1.62)$$

The derivation outlined above can be directly extended to the mixing of three or more neutrinos and solved numerically. Note that, if sterile neutrinos are included or the lepton universality is violated by beyond-SM processes, the NC contributions are no longer proportional to the identity matrix and must not be dropped from the equation of motion.

Matter effects play an important role in the analysis of solar neutrino oscillations, where the so-called *large mixing angle-MSW (LMA-MSW)* solution of the solar neutrino problem (resulting in the values shown in Table 1.1) is favored over vacuum oscillation by data [36]. This solution with $\theta_{12} \leq \pi/4$ is on the so-called “light-side”⁴¹ of the possible parameter space and allows to identify the lightest mass eigenstate, chosen to be $|\nu_1\rangle$ without loss of generality, as the one that contains mainly electron flavor, whereas the second mass eigenstate $|\nu_2\rangle$ contains approximately equal content of electron, muon and tau flavor⁴².

Since the effective mixing angles and the effective squared mass differences in matter depend on the signs of the squared mass differences, matter effects in earth can be used to determine the neutrino mass hierarchy. Looking for ν_e appearance in a ν_μ beam, the NO ν A⁴³ experiment expects to see different oscillation patterns⁴⁴ depending on the sign of Δm_{31}^2 (see Figure 1.7). Experiments like NO ν A and other future neutrino beam experiments will also study possible CP violation in the neutrino sector via measurement of $\Delta P_{\mu e}^{CP} = P_{\mu e} - P_{\bar{\mu} \bar{e}}$, which is enhanced by matter effects.

Matter effects in long-baseline experiments are discussed within the OPERA framework in Section 7.1.

⁴⁰In ordinary matter, typical matter densities are between $\rho \approx 2.7 \text{ g/cm}^3$ (earth crust) and $\rho \approx 150 \text{ g/cm}^3$ (sun core), and typical electron fractions are between $Y_e \approx 0.5$ (Earth) and $Y_e \approx 0.85$ (Sun).

⁴¹Solutions with $\pi/4 < \theta_{12} < \pi/2$ are called the “dark-side”.

⁴²This can be understood qualitatively in the two-flavor approximation as follows. The two mass eigenstates are a coherent superposition of two flavor eigenstates weighted by the entries of a rotation matrix: $|\nu_1\rangle = \cos(\theta)|\nu_e\rangle - \sin(\theta)|\nu_\mu\rangle$ and $|\nu_2\rangle = \sin(\theta)|\nu_e\rangle + \cos(\theta)|\nu_\mu\rangle$. If one arbitrarily chooses $m_1 < m_2$, i.e. $\Delta m^2 > 0$, all physical solutions of these equations are found between $0 \leq \theta \leq \pi/2$. In case of vacuum oscillations, the oscillation probability depends on $\sin^2(2\theta)$ only (see Equation 1.30) which is invariant under $\theta \rightarrow \pi/2 - \theta$, i.e. $|\nu_1\rangle$ and $|\nu_2\rangle$ are interchangeable. This ambiguity disappears in case of matter oscillations, where the denominator of Equation 1.60 destroys the vacuum symmetry around $\theta = \pi/4$, since, by definition, the matter potential $A > 0$ and $\Delta m^2 > 0$ for neutrinos.

⁴³NO ν A: NuMI Off-Axis ν_e Appearance.

⁴⁴NO ν A will also be operated with antineutrinos, where the sign of the matter potential is reversed, enhancing the discovery potential of NO ν A for the mass hierarchy.

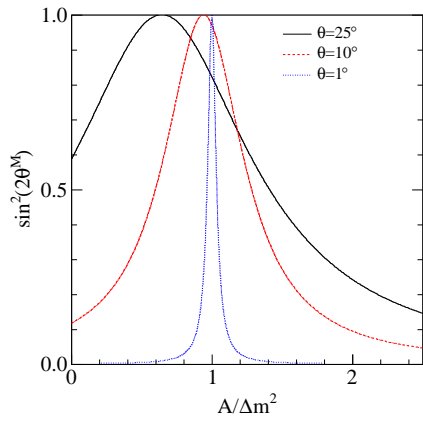


Figure 1.6: Mixing angle $\sin^2(2\theta^M)$ in matter (two-flavor approximation) for different vacuum mixing angles, calculated within the analytical framework outlined in this section.

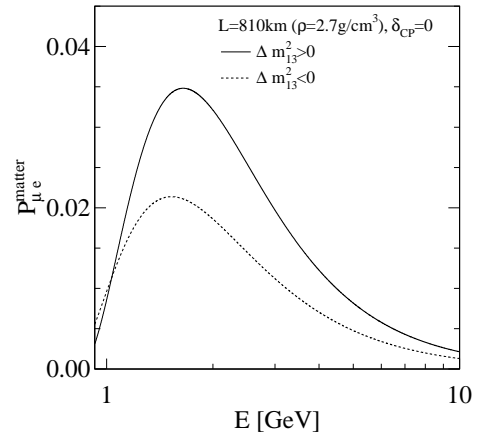


Figure 1.7: Three-flavor oscillation probability $P_{\mu e}$ including matter effects (constant density), $L=810$ km (NO ν A) for normal and inverted hierarchy, calculated numerically.

Chapter 2

Neutrino interactions

Calculating the interactions of neutrinos and understanding the associated uncertainties are a fundamental and challenging part of all neutrino experiments. The analysis of ν_μ disappearance (see Section 7.2) requires a detailed knowledge of neutrino cross sections and the respective hadronic final states for all three neutrino flavors at neutrino energies between 1 GeV and about 200 GeV. Especially in the absence of a near detector of the OPERA experiment, the latter requirement can only be met by detailed Monte Carlo simulations of the neutrino interactions and by evaluating the respective systematical uncertainties. The default OPERA neutrino event generator **NEGN**¹ exhibits several drawbacks like an incomplete documentation, no direct access to the underlying cross section models and an unflexible **FORTTRAN**² software design, making the inclusion of Monte Carlo reweighting schemes in the code difficult. Instead of **NEGN**, the modern and widely used neutrino event generator **GENIE**³ is used within the scope of this thesis [37].

Parts of the neutrino cross section model are theoretically well understood (e.g. deep inelastic scattering on free nucleons), others include phenomenological descriptions (e.g. resonant neutrino scattering) or parametrizations from existing data (e.g. low energy hadronization). Apart from some details where different approaches are used by different experiments, the **GENIE** model described in this section, is the up-to-date, widely used and accepted toolkit for the description of neutrino interactions for the current generation of accelerator neutrino experiments. Within this thesis, the existing **GENIE** cross section model has been extended by radiative corrections for deep inelastic neutrino scattering. The technical implementation of the **GENIE** event generator in the OPERA software framework is explained in Section 4.3. All kinematic variables used within this section are defined in Appendix B.

In order to propagate systematic uncertainties from the event generator and theory level to experiment observables, systematic uncertainties are included as

¹**NEGN**: Neutrino Event Generator for NOMAD.

²**FORTTRAN**: Derived from “The IBM Mathematical Formula Translating System”.

³**GENIE**: Generates Events for Neutrino Interaction Experiments.

fractional uncertainties of input parameters of the **GENIE** model. The parameter uncertainties were estimated from the spread of experimental measurements, the spread of theoretical calculations or generator comparisons with external data [38]. Various comparisons of the model and external data is shown within this section or can be found in [39]. Most of the parameter uncertainties are similar to or taken from MINOS analysis [40, 41, 42] based on the **NEUGEN**⁴ event generator, which is a predecessor of **GENIE**. The higher neutrino energy in the OPERA experiment compared to MINOS, lead to a larger impact of systematic uncertainties of higher energy processes negligible for MINOS. The additional parameter uncertainties included in this thesis are the charm mass, the CKM matrix elements V_{ud} and V_{us} and radiative corrections. Uncertainties of the nuclear corrections in deep inelastic scattering and a possible strange sea asymmetry are included in the discussion.

In general, the change of a single event generator input parameter requires the re-generation of the entire *Monte Carlo (MC)* sample, including the detailed detector simulation and event reconstruction⁵. Instead of re-generating entire MC samples, **GENIE** provides a framework to re-weight simulated events according to a changed input parameter [39, 43]. If an input parameter change affects the distribution of events, it is called a *shape* uncertainty. If it affects the total number of events, it is called a *normalization* uncertainty. Usually a changed input parameter of the cross section model changes both shape and normalization, whereas a changed input parameter of the hadronization model changes the shape only.

2.1 Cross sections

In anticipation of the results derived within this section, the kinematical coverage of the CNGS neutrino beam at OPERA is shown in Figure 2.1, making use of the full cross section model to give an idea of the kinematical regions of interest for the OPERA experiment.

Interactions of the form $\nu + N$ describe the scattering off a hypothetically free isoscalar nucleon N with $\sigma_N = \frac{(\sigma_n + \sigma_p)}{2}$. n and p are a free neutron and proton, respectively, hence nuclear effects are neglected here, if not stated otherwise.

⁴**NEUGEN**: Neutrino Event Generator.

⁵The production of the full OPERA MC sample used within Section 5, Section 6 and Section 7 takes about four weeks on 150 CPUs in parallel.

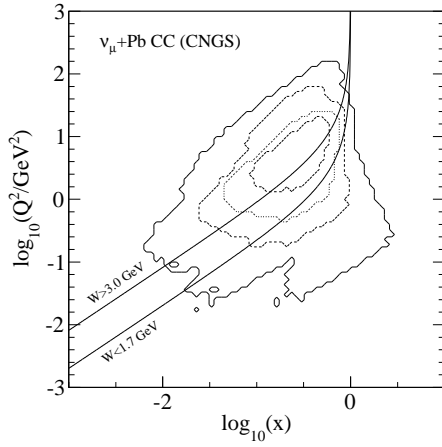
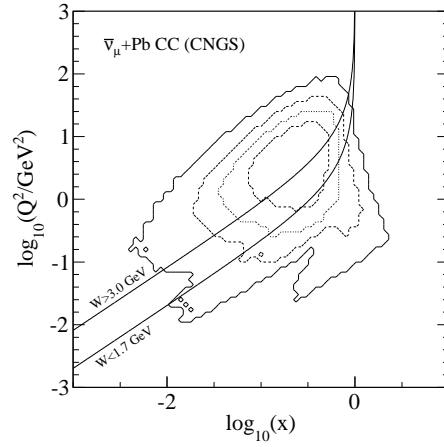
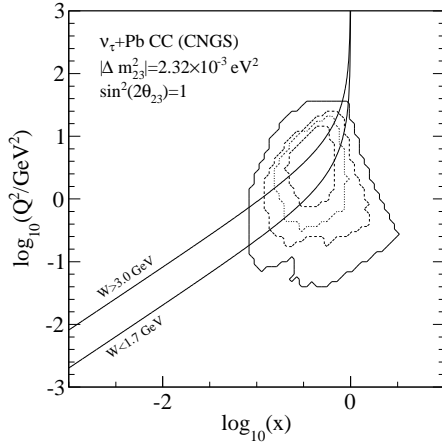
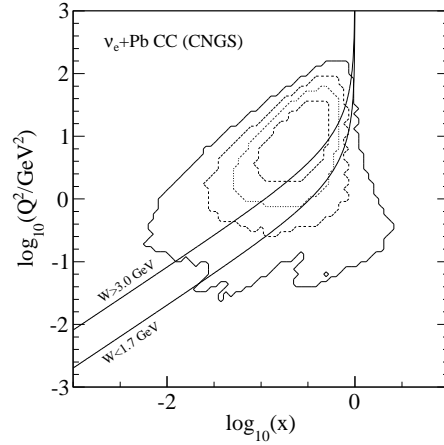
(a) ν_μ (without oscillations).(b) $\bar{\nu}_\mu$ (without oscillations).(c) ν_τ (from $\nu_\mu \rightarrow \nu_\tau$ two-flavor oscillations using Equation 1.30).(d) Intrinsic ν_e (without oscillations).

Figure 2.1: Kinematical coverage of the CNGS neutrino beam for ν +Pb interactions in OPERA. The contour lines show the regions that cover 50 %, 75 %, 90 % and 99 % (from the inside outwards) of all events. Note that x and Q^2 are calculated from final lepton kinematics in the laboratory system (“off-shell”), while W is calculated with so-called “on-shell” kinematics, ignoring any contributions of potential energy. The values of $W = 1.7$ GeV and $W = 3.0$ GeV correspond to two cut values of the cross section model (see Section 2.1.4) and the hadronization model (see Section 2.2), respectively.

2.1.1 Elastic and quasi-elastic scattering

Elastic (*EL*) and *quasi-elastic*⁶ (*QEL*) neutrino scattering are the lowest-multiplicity exclusive ν +N reactions (see Figure 2.2). The following section de-

⁶Both the neutrino and the struck nucleon change their identity under weak CC interactions, contrary to the classical understanding of an elastic reaction.

describes the strong hypercharge⁷-conserving *charged current quasi-elastic (CCQE)* processes

$$\nu_l(k_1) + n(p_1) \rightarrow l^-(k_2) + p(p_2), \quad (2.1)$$

$$\bar{\nu}_l(k_1) + p(p_1) \rightarrow l^+(k_2) + n(p_2) \quad (2.2)$$

and the corresponding *neutral current elastic (NCE)* processes

$$\nu_l(k_1) + n(p_1) \rightarrow \nu_l(k_2) + n(p_2), \quad (2.3)$$

$$\nu_l(k_1) + p(p_1) \rightarrow \nu_l(k_2) + p(p_2), \quad (2.4)$$

$$\bar{\nu}_l(k_1) + n(p_1) \rightarrow \bar{\nu}_l(k_2) + n(p_2), \quad (2.5)$$

$$\bar{\nu}_l(k_1) + p(p_1) \rightarrow \bar{\nu}_l(k_2) + p(p_2), \quad (2.6)$$

where k_1 , k_2 , p_1 and p_2 are the four-momenta of the incoming neutrino ν_l , the outgoing lepton l and the incoming and outgoing nucleons.

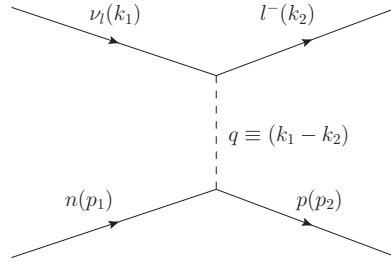


Figure 2.2: $\nu+n$ quasi-elastic scattering, charged current.

Depending on the respective lepton flavor, the CCQE reactions set the energy threshold E_t (see Appendix B.15) for charged current neutrino interactions given by

$$\nu_\mu + n \rightarrow \mu^- + p \quad (E_t = 0.110 \text{ GeV}), \quad (2.7)$$

$$\bar{\nu}_\mu + p \rightarrow \mu^+ + n \quad (E_t = 0.113 \text{ GeV}), \quad (2.8)$$

$$\nu_\tau + n \rightarrow \tau^- + p \quad (E_t = 3.454 \text{ GeV}), \quad (2.9)$$

⁷Strong hypercharge: $Y = 2(Q - I_3)$, where Q is the electrical charge and I_3 is the third component of the isospin I . In weak interactions, the strong hypercharge is generally not conserved.

$$\bar{\nu}_\tau + p \rightarrow \tau^+ + n \quad (E_t = 3.462 \text{ GeV}). \quad (2.10)$$

The energy threshold for ν_e CC interactions is below 10^{-3} GeV and can thus be neglected for all experimental purposes in the OPERA experiment. Note that the CCQE reactions 2.1 for neutrinos are only possible on neutrons, while the CCQE antineutrino reactions 2.2 can only take place on protons.

Following the Feynman rules, the transition matrix element for the CCQE neutrino–neutron interaction is given by

$$\mathcal{M} = \frac{G_F}{\sqrt{2}} \bar{u}_l(k_2) \gamma^\alpha (1 - \gamma_5) u_\nu(k_1) \cdot \langle p(p_2) | J_\alpha^{CCQE} | n(p_1) \rangle \quad (2.11)$$

where γ_i ($i = 0, 1, 2, 3$) are the Dirac matrices with $\gamma_5 = i\gamma_0\gamma_1\gamma_2\gamma_3$ and J_α^{CCQE} is the hadronic current. The lepton current only contains the local weak interaction which can be fully explained within the (V–A) theory⁸ of weak interaction. In contrast to that, the weak interaction of the nucleon is not a pure (V–A) interaction, since the strong coupling between the constituents of the nucleons dirties the pure weak interaction. To calculate the CCQE cross section, one has to introduce an explicit form of the hadronic current J_α^{CCQE} :

$$\langle p(p_2) | J_\alpha^{CCQE} | n(p_1) \rangle = \cos(\theta_C) \bar{u}_p(k_2) \Gamma_\alpha^{CCQE}(Q^2) u_n(k_1) \quad (2.12)$$

with

$$\begin{aligned} \Gamma_\alpha^{CCQE}(Q^2) = & \gamma_\alpha F_V^{(1)}(Q^2) + \frac{i\sigma_{\alpha\beta} q^\beta \xi}{2M} F_V^{(2)}(Q^2) + \frac{q_\alpha}{M} F_S(Q^2) \\ & + \gamma_\alpha \gamma_5 F_A(Q^2) + \frac{q_\alpha \gamma_5}{M} F_P(Q^2) + \frac{\gamma_5 (p_1 + p_2)_\alpha}{M} F_T(Q^2), \end{aligned} \quad (2.13)$$

where θ_C is the Cabibbo angle, $M = \frac{(m_n + m_p)}{2}$, $\xi = \mu_p - \mu_n$ is the difference of the anomalous magnetic moments of proton and neutron, $\sigma_{\alpha\beta} = \frac{i}{2}[\gamma_\alpha, \gamma_\beta]$, $Q^2 = -q^2$ is the squared four–momentum transfer and $F_V^{(1),(2)}$, F_S , F_A , F_P and F_T are the nucleon vector, scalar, axial, pseudo–vector and tensor *form factors* (FF). These FFs describe the strong interaction dynamics which have to be determined by experiment. Using symmetry arguments, the number of FFs is reduced by two: CPT invariance⁹ requires all FFs to be real functions of Q^2 , while the charge symmetry¹⁰ requires F_S and F_T to be imaginary, resulting in $F_S = F_T = 0$.

⁸V–A: Vector minus axial vector.

⁹CPT invariance is the invariance of a system under a combined charge (C), parity (P) and time (T) conjugation.

¹⁰Charge symmetry means the symmetry of up–quark distributions of the proton and down–quark distributions of the neutron and vice–versa.

The differential cross section of CCQE scattering in the *Llewellyn-Smith (LS)* notation [44] is given by

$$\frac{d\sigma}{dQ^2} = \frac{G_F^2 M^2 \cos^2(\theta_C)}{8\pi E_\nu^2 (1 + Q^2/M_W^2)^2} \times \left(A(Q^2) \mp B(Q^2) \frac{(s-u)}{M^2} + C(Q^2) \frac{(s-u)^2}{M^4} \right), \quad (2.14)$$

where M_W is the W boson mass, $s = (k_1 + p_1)^2$ and $u = (k_2 - p_1)^2$ are Mandelstam variables, here $(s - u) = 4ME_\nu + q^2 - m_l^2$. $A(Q^2)$, $B(Q^2)$ and $C(Q^2)$ contain the remaining four FFs and are explicitly given in [44], where the minus sign in Equation 2.14 is for neutrinos and the plus sign for antineutrinos¹¹.

The two vector FFs in neutrino–nucleon scattering are given by

$$F_V^{(1)}(Q^2) = \frac{G_E^V(Q^2) + \frac{Q^2}{4M^2} G_M^V(Q^2)}{1 + \frac{Q^2}{4M^2}} \quad (2.15)$$

and

$$\xi F_V^{(2)}(Q^2) = \frac{G_M^V(Q^2) - G_E^V(Q^2)}{1 + \frac{Q^2}{4M^2}}, \quad (2.16)$$

where $G_E^V(Q^2)$ and $G_M^V(Q^2)$ are the electric and the magnetic vector FFs of the nucleon, related via the *conserved vector current (CVC)* hypothesis with the elastic neutron and proton FFs

$$G_E^V(Q^2) = G_E^p(Q^2) - G_E^n(Q^2), \quad (2.17)$$

$$G_M^V(Q^2) = G_M^p(Q^2) - G_M^n(Q^2). \quad (2.18)$$

These four FFs can be parameterized by

$$G_{(M,E)}^{(n,p)}(Q^2) = \frac{\sum_{k=0}^2 (a_k)_{(M,E)}^{(n,p)} \left(\frac{Q^2}{4M^2}\right)^k}{1 + \sum_{k=1}^4 (b_k)_{(M,E)}^{(n,p)} \left(\frac{Q^2}{4M^2}\right)^k}, \quad (2.19)$$

where a_k and b_k are Q^2 -independent parameters obtained from fits to e+N scattering data (BBBA05 parametrization [45]).

The Q^2 -dependency $F_A(Q^2)$ can only be determined by neutrino experiments. Up to now, the data are too scarce for ruling out deviations from a dipole form

¹¹The term $B(Q^2) \propto F_A(Q^2)$ is negative in the LS notation, resulting in the minus sign in Equation 2.14 for neutrinos and a plus sign for antineutrinos.

$$F_A(Q^2) = F_A(0) \frac{1}{\left(1 + \frac{Q^2}{(m_A^{CCQE})^2}\right)^2}, \quad (2.20)$$

where the axial coupling constant $F_A(0) = g_A$ is known quite well from nuclear β -decay, and m_A^{CCQE} is the so-called axial mass. From the *partially-conserved axial current hypothesis* (PCAC), the pseudo-scalar FF $F_P(Q^2)$ is usually approximated by

$$F_P(Q^2) = F_A(Q^2) \frac{2M^2}{m_\pi^2 + Q^2}, \quad (2.21)$$

where m_π is the mass of the charged pion. While the impact of $F_P(Q^2)$ is almost negligible in ν_μ scattering for E_ν that are not too small, since $F_P(Q^2)$ enters the cross section multiplied by m_l^2/M^2 , the contribution to ν_τ CCQE is in the percent range for all energies.

The formalism used to describe NCE scattering is very similar to CCQE scattering, with some modifications described in the following. The differential cross section is given by Equation 2.14, while the functions $A(Q^2)$, $B(Q^2)$ and $C(Q^2)$ assume a simpler form, since the lepton mass in the final state in this case is approximated as zero. The FFs are modified according to the different coupling of the Z^0 as described by the standard model [46]. In contrast to CCQE scattering, heavy sea quarks may contribute to NCE scattering, where the largest sea contribution is expected from the strange quarks, without being Cabibbo-suppressed. However, experiments have shown that the strange contribution to the nucleon charge and to the nucleon magnetic moment are negligible, hence the vector FFs remain unchanged. Assuming the same Q^2 -dependence of the axial FF for the strange and non-strange part, the strange contribution to the axial FF may be introduced by an additional parameter $F_A(Q^2) \rightarrow F_A(Q^2)(1 + \eta)$, where η is proportional to the strange quark contribution to the total nucleon spin and has to be measured by experiment.

The total NCE and QECC cross sections are given by the integration of Equation 2.14 within the integration limits given in Appendix C.25 (CCQE) and Appendix C.26 (NCE), respectively.

A *relativistic Fermi gas model* (RFG) is used to approximately account for nuclear effects that modify the CCQE and NCE cross section on nuclear targets [47]. In simplified terms, the produced nucleon is required to have a momentum (modified by the effective nucleon binding energy) that exceeds the Fermi momentum k_F of the nucleus¹², or the interaction will be suppressed according to this model. The differential CCQE cross section including Fermi-suppression is shown in Figure 2.3. Fermi-suppression reduces the cross section for small values

¹²The Fermi momentum is different for protons and neutrons in general and amounts to e.g. 0.251 GeV for protons and 0.263 GeV for neutrons in iron.

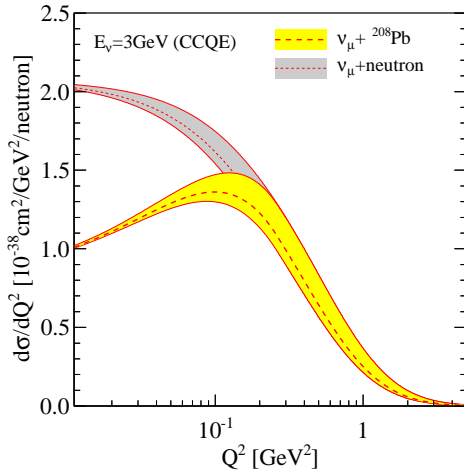


Figure 2.3: Differential CCQE cross section per neutron for $\nu_\mu+^{208}\text{Pb}$ and $\nu_\mu+n$ scattering, including the $\pm 1\sigma$ uncertainty resulting from a variation of m_A^{CCQE} by $^{+25}_{-15}\%$.

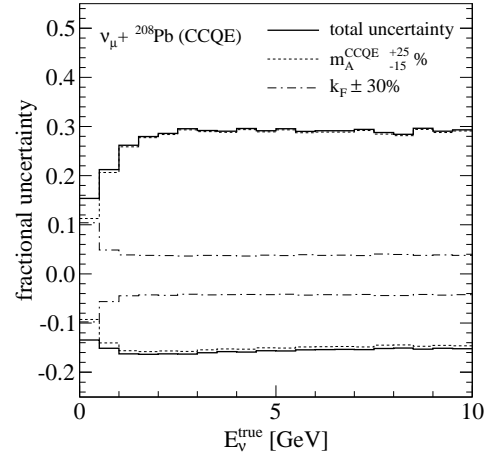


Figure 2.4: Fractional uncertainty of the CCQE cross section (via reweighting 10^5 simulated events).

of Q^2 .

Within this calculation, the default GENIE values are used: $m_A = 0.990$ GeV, $F_A(0) = -1.2670$, $\mu_p = 2.7930$, $\mu_n = -1.9130$, $m_V = 0.840$ GeV and $\eta = 0.12$. BBBA05 parameters and values for k_F are taken from [39].

The following sources of systematic uncertainties are considered for elastic and quasi-elastic interactions at energies above about 0.5 GeV: m_A is varied by $^{+25}_{-15}\%$, k_F is varied by $\pm 30\%$ for nuclear targets, η is varied by $\pm 30\%$ and the vector FFs are changed from BBBA05 to a dipole parametrization with $m_V = 0.840$ GeV (shape-only) [38]¹³. The other parameters only have small experimental uncertainties that may be ignored in the framework of this calculation. The fractional uncertainty of the total CCQE neutrino-lead cross section is shown in Figure 2.4. At all neutrino energies in the OPERA experiment, the total EL and QEL cross section uncertainties are dominated by the uncertainty of m_A .

The high neutrino energies in the CNGS neutrino beam lead to a quite small flux-integrated fraction of CCQE events compared to the total number of CC events on lead of 3.8 % ($\nu_\mu\text{CC}$) and 4.8 % ($\bar{\nu}_\mu\text{CC}$) for neutrino energies up to 100 GeV. The CCQE contribution to the total number of CC events for ν_τ is higher than for ν_μ , where the explicit number depends on the oscillation parameters (see Section 1.3). For all neutrino flavors, though, the ratio CCQE/CC strongly depends on the neutrino energy, as can be seen in Figure 2.5. The total

¹³The large uncertainty on the plus side of m_A is used to include possible contributions from multi-body effects in (quasi-)elastic scattering that may explain the incompatible values of m_A extracted by different experiments.

cross sections for both CCQE and NCE scattering on lead are shown in Figure 2.6.

A comparison of this calculation, including the systematic uncertainties as described above, with data from various experiments is shown in Figure 2.7 and Figure 2.8.

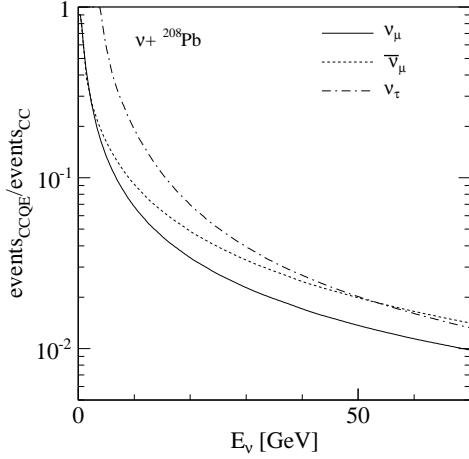


Figure 2.5: Fraction of CCQE events to the total number of CC events for $\nu+^{208}\text{Pb}$ scattering. Below the μ (τ) threshold, the ν_μ (ν_τ) fraction is set to unity.

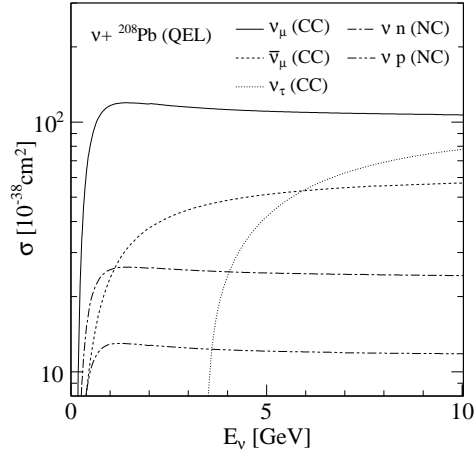


Figure 2.6: Total cross sections for $\nu+^{208}\text{Pb}$ NCE and CCQE scattering. The NCE contributions of neutrons and protons (bound in lead) are shown separately, CCQE ν scattering only takes place on neutrons.

Selection rules ($\Delta Y = \pm 1$, $\Delta Q = \Delta Y$ and $\Delta I = 1/2$) allow the production of Σ^0 , Λ^0 and Σ^- hadrons in quasi-elastic charged current interactions of antineutrinos. Since the cross sections are Cabibbo-suppressed by $\sin^2 \theta_C \approx 0.05$ and because antineutrinos only contribute to about 2 % of the CNGS neutrino flux (see Section 4.1), these processes will be neglected within this work. The quasi-elastic production of even heavier charmed baryons Λ_c^+ , Σ_c^+ and Σ_c^{++} can only be induced by neutrinos and not by antineutrinos. This so-called quasi-elastic charm production is included in the cross section model according to [66, 67].

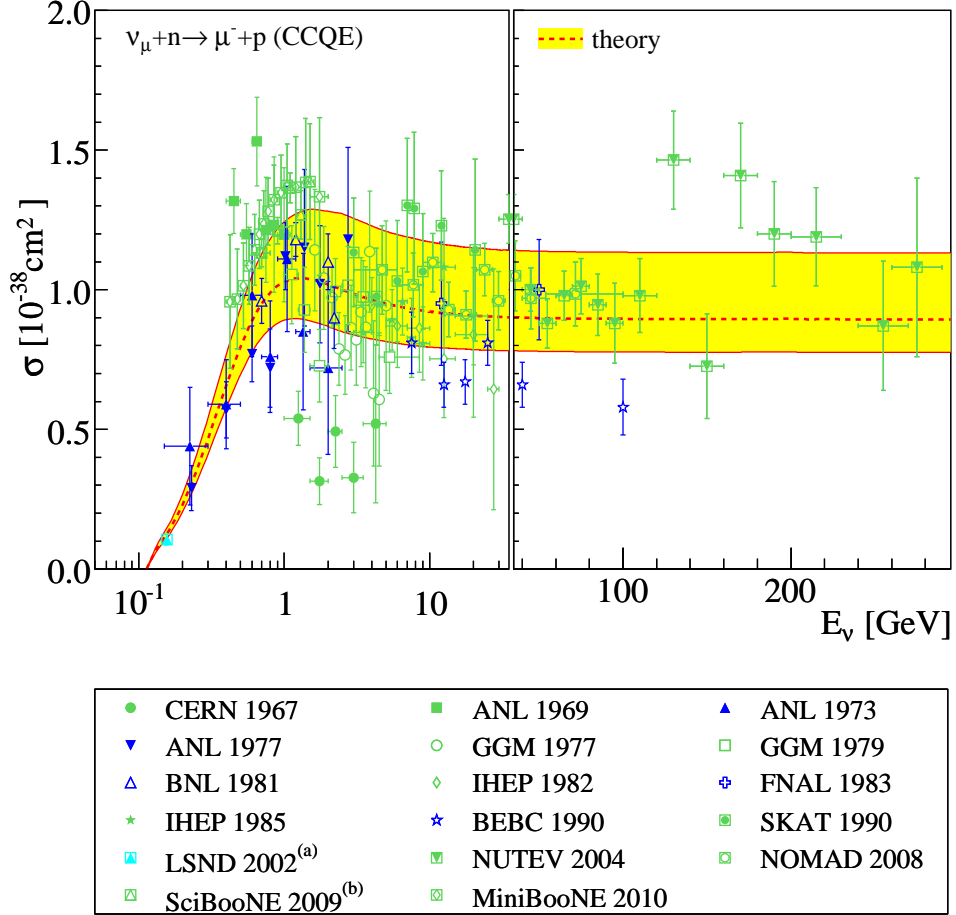


Figure 2.7: Total $\nu_{\mu} + n \rightarrow \mu^{-} + p$ CCQE cross section, comparison of the calculation with data. The dashed line is the theoretical cross section, the shaded band shows the included $\pm 1\sigma$ systematic uncertainty, see text for details. Data are taken from [48] (CERN 1967, CF_3Br), [49] (ANL 1969, Fe), [50] (ANL 1973, D), [51] (ANL 1977, D), [52] (GGM 1977, $\text{CF}_3\text{Br}/\text{C}_3\text{H}_8$), [53] (GGM 1979, $\text{CF}_3\text{Br}/\text{C}_3\text{H}_8$), [54] (BNL 1981, D), [55] (IHEP 1982, Al), [56] (FNAL 1983, D), [57] (IHEP 1985, Al), [58] (BEBC 1990, D), [59] (SKAT 1990, CF_3Br), [60] (LSND 2002, C (mineral oil))^(a), [61] (NUTEV 2004, Fe), [62] (NOMAD 2008, mainly C), [63] (SciBooNE 2009, CH (plastic scintillator))^(b), [64] (MiniBooNE 2010, CH_2 (mineral oil)). All data from heavy targets have been corrected for nuclear effects within the RFG model, data from deuterium have been corrected by the corresponding authors. If given separately, statistical and systematic errors are added in quadrature, correlations are ignored. The x-axis is changed from logarithmic to linear at 35 GeV.

(a) Mentioned for completeness only, additional corrections for nuclear effects needed.

(b) Preliminary.

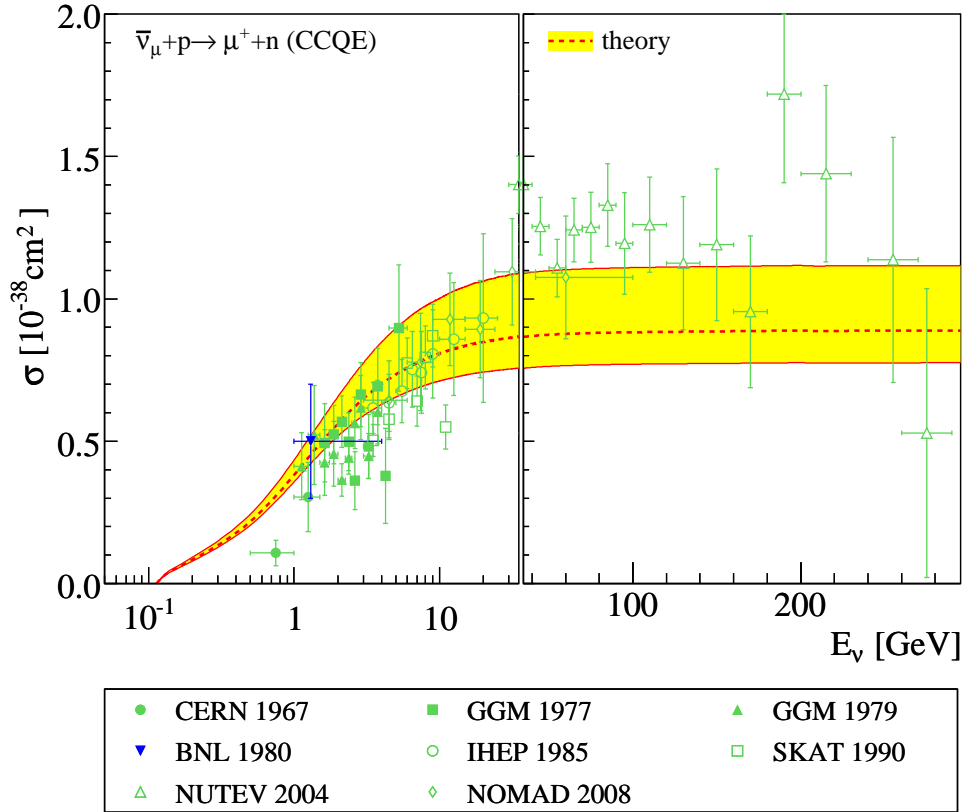


Figure 2.8: Total $\bar{\nu}_\mu + p \rightarrow \mu^+ + n$ CCQE cross section, comparison of the calculation with data. The dashed line is the theoretical cross section, the shaded band shows the included $\pm 1\sigma$ systematic uncertainty, see text for details. Data are taken from [48] (CERN 1967, CF_3Br), [52] (GGM 1977, $\text{CF}_3\text{Br}/\text{C}_3\text{H}_8$), [53] (GGM 1979, $\text{CF}_3\text{Br}/\text{C}_3\text{H}_8$), [65] (BNL 1980, H), [57] (IHEP 1985, Al), [59] (SKAT 1990, CF_3Br), [61] (NUTEV 2004, Fe), [62] (NOMAD 208, mainly C). All data from heavy targets have been corrected for nuclear effects within the RFG model, data from deuterium have been corrected by the corresponding authors. If given separately, statistical and systematic errors are added in quadrature, correlations are ignored. The x-axis is changed from logarithmic to linear at 35 GeV.

2.1.2 Resonant scattering

Resonant (RES) scattering describes the creation of baryon/pion final states through the excitation and the subsequent strong force–decay of the short–lived¹⁴ nucleon resonances N and Δ (see Figure 2.9). The *resonant CC (RESCC)* interactions for neutrinos are given by

$$\nu_l(k_1) + n(p_1) \rightarrow l^-(k_2) + b^*(p_2) \quad \hookrightarrow p + \pi^0, \quad (2.22)$$

$$\hookrightarrow n + \pi^+, \quad (2.23)$$

$$\nu_l(k_1) + p(p_1) \rightarrow l^-(k_2) + b^*(p_2) \quad \hookrightarrow p + \pi^+, \quad (2.24)$$

for antineutrinos by

$$\bar{\nu}_l(k_1) + n(p_1) \rightarrow l^+(k_2) + b^*(p_2) \quad \hookrightarrow n + \pi^-, \quad (2.25)$$

$$\bar{\nu}_l(k_1) + p(p_1) \rightarrow l^+(k_2) + b^*(p_2) \quad \hookrightarrow p + \pi^-, \quad (2.26)$$

$$\hookrightarrow n + \pi^0, \quad (2.27)$$

and the *resonant NC (RESNC)* interactions (with ν_l replaced by $\bar{\nu}_l$ for antineutrinos) are

$$\nu_l(k_1) + n(p_1) \rightarrow \nu_l(k_2) + b^*(p_2) \quad \hookrightarrow p + \pi^-, \quad (2.28)$$

$$\hookrightarrow n + \pi^0, \quad (2.29)$$

$$\nu_l(k_1) + p(p_1) \rightarrow \nu_l(k_2) + b^*(p_2) \quad \hookrightarrow p + \pi^0, \quad (2.30)$$

$$\hookrightarrow n + \pi^+, \quad (2.31)$$

where b^* is a baryon resonance, while the other variables have the usual meanings, as given in the previous sections. Other decay modes of the resonances contribute to less than 1 % of all final states.

Resonant neutrino interactions are calculated in the phenomenological framework proposed by *Rein* and *Sehgal (RS)* [68]. The formalism¹⁵ starts with the

¹⁴The lifetime of these resonances is typically $\tau \sim 10^{-24}$ s.

¹⁵The original notation used in the RS paper has been replaced with a modern one in this thesis. They are related as follows: $Q_{RS} = |\vec{q}_{LAB}|$ and $Q_{RS}^* = |\vec{q}_{RRF}|$ are the absolute three-momentum vector of the exchanged boson, defined by $q = (E_{W/Z}, \vec{q})$, with $E_{W/Z}$ in the laboratory frame given by the invariant ν (see Equation B.21), whereas obviously $\nu_{RS}^* = (E_{W/Z})_{RRF}$ is not invariant. One should keep in mind that the negative squared four-momentum transfer is $Q^2 = -q^2 \neq Q_{RS}^2$.

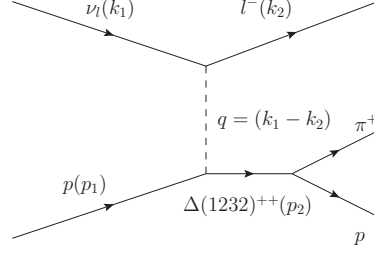


Figure 2.9: $\nu+p$ resonant scattering, charged current, example of the $P_{33}(1232)$ resonance.

general expression of a current–current weak matrix element for an isolated single resonance,

$$\mathcal{M} = \frac{G_F}{\sqrt{2}} \bar{u}_l(k_2) \gamma^\alpha (1 - \gamma_5) u_\nu(k_1) \cdot \langle b^*(p_2) | J_\alpha^{RES} | b(p_1) \rangle, \quad (2.32)$$

where b is a baryon (n or p). The lepton current can be expressed by the polarization four–vector of the exchanged virtual boson. After several transformations, the lepton current in the *resonance rest frame (RRF)* results in

$$\bar{u}_l(k_2) \gamma^\alpha (1 - \gamma_5) u_\nu(k_1) |_{RRF} = -2\sqrt{2} E_\nu \sqrt{\frac{Q^2}{|\vec{q}_{LAB}|^2}} \left(u e_L^\alpha - v e_R^\alpha + \sqrt{2} u v e_S^\alpha \right), \quad (2.33)$$

where

$$e_L^\alpha = \frac{1}{\sqrt{2}} (0, 1, -i, 0), \quad (2.34)$$

$$e_R^\alpha = \frac{1}{\sqrt{2}} (0, -1, -i, 0), \quad (2.35)$$

$$e_S^\alpha = \frac{1}{\sqrt{Q^2}} (|\vec{q}_{RRF}|, 0, 0, (E_{W/Z})_{RRF}), \quad (2.36)$$

are the left–handed, the right–handed and the scalar polarization vectors of the exchanged virtual boson, and

$$u = \frac{(E_\nu)_{LAB} + (E_l)_{LAB} + |\vec{q}_{LAB}|}{2(E_\nu)_{LAB}}, \quad (2.37)$$

$$v = \frac{(E_\nu)_{LAB} + (E_l)_{LAB} - |\vec{q}_{LAB}|}{2(E_\nu)_{LAB}} \quad (2.38)$$

are dimensionless kinematical factors. By factoring out the energy dependence of the hadronic current via $J_\alpha^{RES} = 2M_{b^*}F_\alpha$, and by expressing the remaining hadronic form factor F_α in the same polarization state basis,

$$F_+ = e_R^\alpha F_\alpha, \quad (2.39)$$

$$F_- = e_L^\alpha F_\alpha, \quad (2.40)$$

$$F_0 = \sqrt{\frac{Q^2}{|\vec{q}_{RRF}|^2}} e_S^\alpha F_\alpha, \quad (2.41)$$

the full matrix element for neutrino scattering in the RS model can be written as

$$\begin{aligned} \mathcal{M} = -4G_F M_{b^*} E_\nu & \left(\sqrt{\frac{Q^2}{|\vec{q}_{LAB}|^2}} \langle b^*(p_2) | uF_- - vF_+ | b(p_1) \rangle \right. \\ & \left. + \frac{M}{M_{b^*}} \sqrt{2uv} \langle b^*(p_2) | F_0 | b(p_1) \rangle \right) \end{aligned} \quad (2.42)$$

with the resonance mass M_{b^*} and the nucleon mass M .

The differential cross section for an isolated resonance is given by

$$\frac{d^2\sigma}{dQ^2 d\nu} = \frac{1}{32\pi M (E_\nu)_{LAB}^2} \frac{1}{2} \sum_{\text{spins}} |\mathcal{M}|^2 f_{b^*}(W) \quad (2.43)$$

where the function $f_{b^*}(W)$ is a normalized Breit–Wigner distribution $f_{b^*}(W) = \frac{1}{2\pi} \frac{\Gamma(L)}{(W - M_{b^*})^2 + \Gamma(L)^2/4}$, where L is the orbital momentum of the baryon resonance.

The remaining task is the explicit calculation of the helicity amplitudes $f_\pm = \langle b^*, j_z \pm 1 | F_\pm | b, j_z \rangle$ and $f_0 = \langle b^*, j_z = \pm \frac{1}{2} | F_0 | b, j_z = \pm \frac{1}{2} \rangle$ which is performed within the *Feynman–Kislinger–Ravndal model (FKR)* [69, 70]. A baryon (baryon resonance) in the FKR model is explained as a ground (excited) state of three bound quarks in a harmonic oscillator potential. Within this model, the helicity amplitudes for each resonance are calculated based on seven functions, called the dynamical form factors, that are proportional to a vector and an axial vector transition form factor, each assumed to have dipole-form,

$$F_V(Q^2) \propto \left(1 + \frac{Q^2}{(m_V^{RES})^2} \right)^{-2}, \quad (2.44)$$

$$F_A(Q^2) \propto \left(1 + \frac{Q^2}{(m_A^{RES})^2} \right)^{-2}, \quad (2.45)$$

where the vector mass m_V^{RES} and the axial mass m_A^{RES} have to be determined by experiment. The total resonant cross section is given by combining the

overlapping excited resonances that lead to the same final states.

Within this calculation, the two mass parameters are $m_V^{RES} = 0.840$ GeV and $m_A^{RES} = 1.120$ GeV, the tabulated dynamical form factors¹⁶ are taken from [68]. The total cross section is given by the integration of Equation 2.43 within the integration limits given by [71]. To avoid double counting with contributions from deep inelastic scattering (see Section 2.1.3), resonant scattering is restricted to an invariant mass of less than $W = W_{RES}^{cut} < 1.7$ GeV. The total resonant cross sections for $\nu_\mu + n$ and $\nu_\mu + p$ scattering are shown in Figure 2.10.

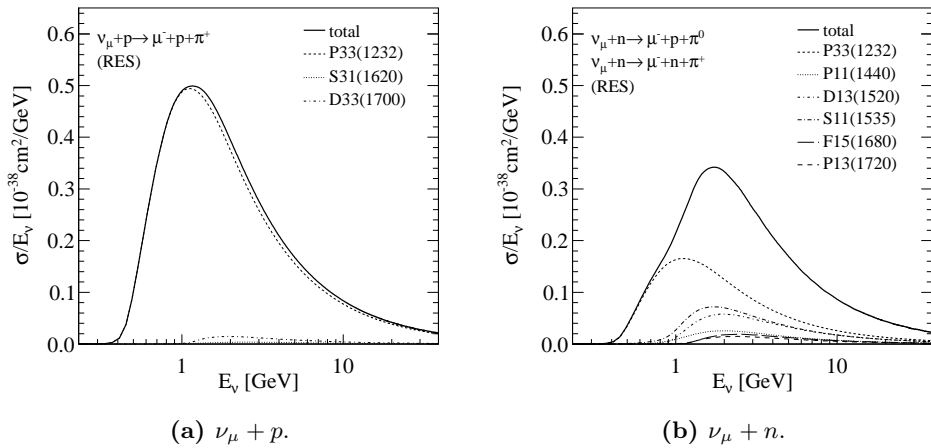


Figure 2.10: Total RESCC cross section divided by neutrino energy, the largest contributions from individual resonances are also shown.

The systematic uncertainties of the RS cross section model are dominated by the uncertainties of the two mass parameters m_V^{RES} and m_A^{RES} . An uncertainty of ± 20 % is assigned to m_A^{RES} whereas m_V^{RES} is varied by ± 5 % (shape only) [38]. The fractional uncertainty of the total RESCC cross section for $\nu_\mu + {}^{208}\text{Pb}$ scattering is shown in Figure 2.11.

Resonant scattering is the dominant cross section contribution at mid-energies around several GeV. For OPERA, the maximum contribution to the total ν_μ CC cross section is about (40 – 50) % at 2 GeV (see Figure 2.12).

¹⁶The resonances P₃₃(1600) and F₁₇(1970) are not included.

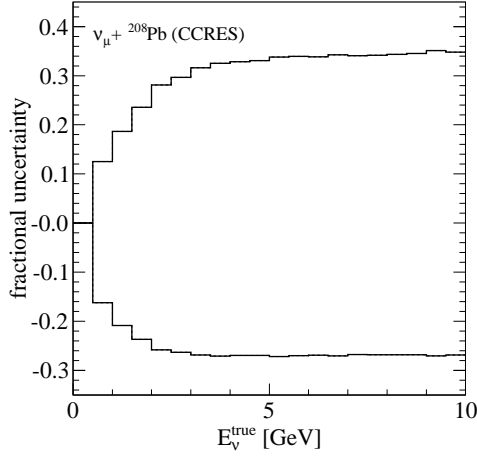


Figure 2.11: Fractional uncertainty of the RESCC cross section, m_A^{RES} only (via reweighting 10^5 simulated events).

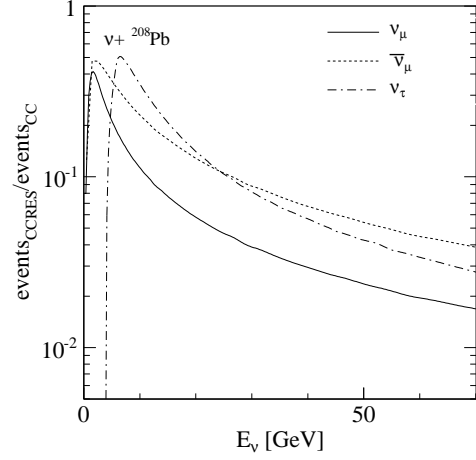


Figure 2.12: Fraction of RESCC events to the total number of CC events for $\nu_\mu+^{208}\text{Pb}$ scattering. The fraction is set to zero below the respective lepton threshold.

2.1.3 Deep inelastic scattering

In contrast to EL or QEL scattering describing the scattering off a compound hadron, *deep inelastic scattering (DIS)* probes the inner hadron structure. Deep inelastic scattering can be understood as an incoherent sum of elastic interactions with the nucleon constituents. The deep inelastic CC neutrino–nucleon and antineutrino–nucleon reactions are given by

$$\nu_l(k_1) + N(p_1) \rightarrow l^-(k_2) + X(p_2), \quad (2.46)$$

$$\bar{\nu}_l(k_1) + N(p_1) \rightarrow l^+(k_2) + X(p_2), \quad (2.47)$$

and the corresponding NC reactions are given by

$$\nu_l(k_1) + N(p_1) \rightarrow \nu_l(k_2) + X(p_2), \quad (2.48)$$

$$\bar{\nu}_l(k_1) + N(p_1) \rightarrow \bar{\nu}_l(k_2) + X(p_2), \quad (2.49)$$

where N is a nucleon, X is a system of outgoing hadrons and the other variables have the usual meanings as given in the previous sections. The pseudo Feynmann diagram of the process described by Equation 2.46 is shown in Figure 2.13.

The double differential cross section for neutrino–nucleon scattering is given by

$$\frac{d^2\sigma}{dxdy} = \frac{G_F^2 y}{16\pi} \kappa_{W,Z}^2 L^{\mu\nu} W_{\mu\nu}, \quad (2.50)$$

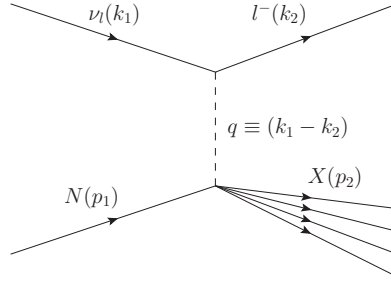


Figure 2.13: ν -N deep inelastic scattering, charged current.

with $\kappa_{W,Z} = \frac{M_{W,Z}^2}{Q^2 + M_{W,Z}^2}$, the Fermi coupling constant G_F and the leptonic tensor $L^{\mu\nu}$ [8, 72]. Expressing the hadronic tensor $W_{\mu\nu}$ in terms of possible four-vector combinations results in

$$W_{\mu\nu} = -g_{\mu\nu}F_1(x, Q^2) + \frac{p_{1\mu}p_{1\nu}}{p_1q}F_2(x, Q^2) - i\epsilon_{\mu\nu\rho\sigma}\frac{p_1^\rho q^\sigma}{2p_1q}F_3(x, Q^2) \quad (2.51)$$

$$+ \frac{q_\mu q_\nu}{p_1q}F_4(x, Q^2) + (p_{1\mu}q_\nu + p_{1\nu}q_\mu)F_5(x, Q^2),$$

where $\epsilon_{\mu\nu\rho\sigma}$ is the total antisymmetric tensor with $\epsilon_{0123} = +1$, $g_{\mu\nu}$ is the metric tensor and F_i ($i = 1..5$) are the dimensionless neutrino–nucleon DIS *structure functions* (*SF*)¹⁷ [73].

Including the final state lepton mass m_l for the case of CC interactions, the explicit DIS Born–level cross section reads

$$\frac{d^2\sigma}{dx dy} = \kappa_{W,Z}^2 \frac{G_F^2 M E_\nu}{\pi} \left[\left[y^2 x + \frac{m_l^2 y}{2E_\nu M} \right] F_1(x, Q^2) \quad (2.52)$$

$$+ \left[\left(1 - \frac{m_l^2}{4E_\nu^2} \right) - \left(1 + \frac{Mx}{2E_\nu} \right) y \right] F_2(x, Q^2)$$

$$\pm \left[xy \left(1 - \frac{y}{2} \right) - \frac{m_l^2 y}{4E_\nu M} \right] F_3(x, Q^2)$$

$$+ \left[\frac{m_l^4}{4E_\nu^2 M^2 x} \right] F_4(x, Q^2)$$

$$- \left[\frac{m_l^2}{2E_\nu M} \right] F_5(x, Q^2) \right],$$

where $+F_3(-F_3)$ corresponds to $\nu(\bar{\nu})$ scattering and M is the mass of the target nucleon. The structure functions F_4 and F_5 appear only multiplied by powers of the final state lepton mass and can be neglected for ν_e and ν_μ scattering

¹⁷After contracting the leptonic and the hadronic tensors, a sixth structure function F_6 vanishes from the cross section and is omitted from further discussions.

in OPERA. However, they are not negligible for ν_τ scattering and thus are included for all lepton flavors, for consistency. In addition to the functional dependence on x and Q^2 , the structure functions $F_i(x, Q^2)$ are different for neutrinos and antineutrinos and depend on the target nucleon and the interaction type: $F_i(x, Q^2) \rightarrow F_{i,NC/CC}(x, Q^2)^{\nu/\bar{\nu},n/p}$.

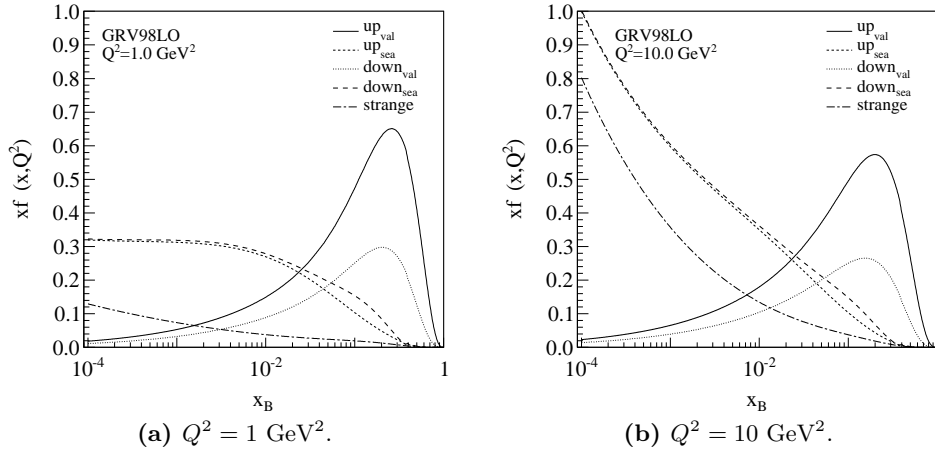


Figure 2.14: Uncorrected GRV98LO parton distributions (GRV98LO: Named after the authors Glück, Reya and Vogt) [74] for fixed values of Q^2 . The subscripts *val* and *sea* denote valence- and sea-quark contributions.

In the *quark-parton model (QPM)*, a nucleon is assumed to consist of non-interacting, point-like constituent partons, namely quarks and gluons. This model is valid in the infinite-momentum frame where the longitudinal momentum of the parton is much larger than its transverse momentum, i.e. the interaction between the quarks may be neglected. Under this assumption of quasi-free partons, the structure functions $F_i(x)$ in the QPM may be expressed as the sums of *parton distribution functions (PDF)* $f(x)$ which describe the probability that a quark of flavor f ($f = up(u)$, $down(d)$, $charm(c)$, $strange(s)$, $top(t)$, $bottom(b)$) carries a longitudinal momentum fraction x of the nucleon momentum (see Figure 2.14). Parton distribution functions cannot be theoretically obtained by QCD and have to be measured experimentally.

Even at *leading order (LO)* QCD, the structure function scaling $F_i(x)$ is violated due to quark-gluon interactions. These effects are described by the DGLAP¹⁸ equations and lead to Q^2 -dependent structure functions $F_i(x) \rightarrow F_i(x, Q^2)$.

The LO structure functions for neutrino-proton interactions below the charm production threshold for charged current interactions, assuming massless quarks (u, d and s only) and neglecting the target mass, are given by

¹⁸DGLAP: Named after the authors Dokshitzer, Gribov, Lipatov, Altarelli and Parisi.

$$F_{2,CC}^{\nu p} = 2x [|V_{ud}|^2 d + |V_{us}|^2 s + (|V_{ud}|^2 + |V_{us}|^2) \bar{u}], \quad (2.53)$$

$$xF_{3,CC}^{\nu p} = 2x [|V_{ud}|^2 d + |V_{us}|^2 s - (|V_{ud}|^2 + |V_{us}|^2) \bar{u}], \quad (2.54)$$

$$F_{2,CC}^{\bar{\nu} p} = 2x [(|V_{ud}|^2 + |V_{us}|^2) u + |V_{ud}|^2 \bar{d} + |V_{us}|^2 \bar{s}], \quad (2.55)$$

$$xF_{3,CC}^{\bar{\nu} p} = 2x [(|V_{ud}|^2 + |V_{us}|^2) u - |V_{ud}|^2 \bar{d} - |V_{us}|^2 \bar{s}], \quad (2.56)$$

where $V_{\alpha\beta}$ are the elements of the unitary CKM quark mixing matrix. The proton PDFs f_p , and the neutron PDFs f_n are related via isospin invariance

$$u_p = d_n \equiv u, \quad (2.57)$$

$$d_p = u_n \equiv d, \quad (2.58)$$

$$\bar{u}_p = \bar{d}_n \equiv \bar{u}, \quad (2.59)$$

$$\bar{d}_p = \bar{u}_n \equiv \bar{d}, \quad (2.60)$$

$$s_p = s_n \equiv s, \quad (2.61)$$

$$\bar{s}_p = \bar{s}_n \equiv \bar{s}, \quad (2.62)$$

which allows to obtain the structure functions $F_i^{\nu n}$ and $F_i^{\bar{\nu} n}$ for neutrino–neutron interactions. The sea quark distributions, as used later in this section, are given by $\bar{u} = u_{sea}$ and $\bar{d} = d_{sea}$.

Under the assumptions described above, the remaining three structure functions are related via the Callan–Gross relation [75]

$$2xF_1(x, Q^2) = F_2(x, Q^2) \quad (2.63)$$

and the Albright–Jarlskog relations [76]

$$F_4(x, Q^2) = 0, \quad (2.64)$$

$$xF_5(x, Q^2) = F_2(x, Q^2). \quad (2.65)$$

The structure functions $F_{i,NC}$ for the neutrino–nucleon neutral current interactions described by Equation 2.48 and Equation 2.49 differ from the equations given above due to the coupling of the Z^0 boson,

$$F_{2,NC}^{\nu p} = 2x [(u_L^2 + u_R^2) (u + \bar{u}) + (d_L^2 + d_R^2) (d + s + \bar{d} + \bar{s})], \quad (2.66)$$

$$xF_{3,NC}^{\nu p} = 2x [(u_L^2 - u_R^2) (u - \bar{u}) + (d_L^2 - d_R^2) (d + s - \bar{d} - \bar{s})], \quad (2.67)$$

where the coupling to the quarks is given by

$$u_L = \frac{1}{2} - \frac{2}{3} \sin^2(\theta_W), \quad (2.68)$$

$$u_R = -\frac{2}{3} \sin^2(\theta_W), \quad (2.69)$$

$$d_L = -\frac{1}{2} + \frac{1}{3} \sin^2(\theta_W), \quad (2.70)$$

$$d_R = \frac{1}{3} \sin^2(\theta_W), \quad (2.71)$$

with the Weinberg angle $\sin^2(\theta_W) = 0.2277 \pm 0.0013 (stat.) \pm 0.0009 (syst.)$ [77]¹⁹. The structure functions for neutrino–neutron interactions can again be obtained by applying isospin invariance, as described above. For NC interactions, the structure functions, but not the cross sections, of neutrinos and antineutrinos are the same: $F_{2,NC}^{\nu p} = F_{2,NC}^{\bar{\nu} p}$ and $x F_{3,NC}^{\nu p} = x F_{3,NC}^{\bar{\nu} p}$. The Callan–Gross relation and the Albright–Jarlskog relation remain valid for NC scattering.

The total DIS cross section is given by the integration of Equation 2.52 within the integration limits derived in Appendix C. To avoid double counting with contributions from resonant scattering, DIS is restricted to an invariant hadronic mass of more than $W = W_{DIS}^{cut} \geq 1.7$ GeV (compare Section 2.1.2).

In the remaining part of this section, several modifications to the basic DIS cross section formula (see Equation 2.52) will be explained that are part of the GENIE model. In addition to them, DIS radiative corrections are added to the default model. Comparisons of the GENIE model with data for the Callan–Gross violation as well as uncertainty discussions for charm production, DIS radiative corrections, nuclear effects and a possible strange sea asymmetry are given.

Some of these modifications describe QCD *next-to-leading order* (NLO) processes, the resulting model is hence called “effective LO” and is mainly based on modifications proposed by *Bodek* and *Yang* (BY) [78]. Within GENIE, DIS cross sections are calculated using the GRV98LO PDF set (see Figure 2.14). While the general idea of the discussed corrections may be adjusted to other PDF sets, the numerical results must not be applied to another PDF set.

2.1.3.1 d/u ratio correction

The GRV98LO PDFs in GENIE are modified according to [78], to match the results of the NMC²⁰ experiment [79]. The corrected quark distribution ratio, with an increased d contribution at high x compared to the original PDF, is given by

$$(d_{val}/u_{val})' = (d_{val}/u_{val}) + \delta(d_{val}/u_{val}) \quad (2.72)$$

¹⁹This value is the so-called on-shell value of the Weinberg angle as measured by the NUTEV experiment.

²⁰NMC: New Muon Collaboration.

with

$$\delta(d_{val}/u_{val}) = -0.00817 + 0.0506x + 0.0798x^2, \quad (2.73)$$

where all ratios and quark distributions are function of x . Since the total valence quark distributions are constrained by QCD sum rules, the integrated u_{val} and d_{val} distributions have to remain unchanged:

$$u'_{val} = \frac{u_{val}}{1 + \delta(d_{val}/u_{val}) \frac{u_{val}}{u_{val} + d_{val}}} \quad (2.74)$$

$$d'_{val} = \frac{d_{val} + u_{val} \delta(d_{val}/u_{val})}{1 + \delta(d_{val}/u_{val}) \frac{u_{val}}{u_{val} + d_{val}}} \quad (2.75)$$

The same corrections are applied to the u_{sea} and d_{sea} distributions, where again the total sea content is conserved. The resulting distributions well describe the E665²¹ measurements of the \bar{u} and \bar{d} distributions [80].

2.1.3.2 Higher twist corrections and target mass corrections

At decreasing Q^2 values, a leading order approach is insufficient to model the structure function and cross section data, since quark–quark interactions via gluon exchange become important (see Figure 2.15). The gluon exchange introduces non-perturbative “higher twist” corrections proportional to powers of $1/Q^2$.

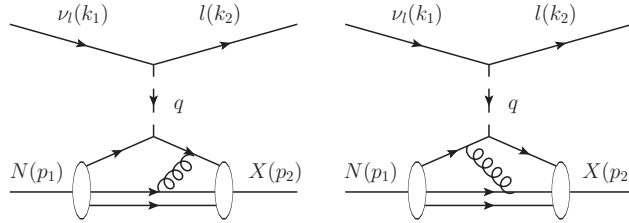


Figure 2.15: Example diagrams contributing to higher twist corrections.

While the dependence of the cross section on the charged lepton masses is explicitly introduced in the leptonic tensor in Equation 2.50, one still has to correct the cross section for hadronic masses entering the structure functions F_i [81]. The mass of the target nucleon is usually taken into account by replacing x with the Nachtmann variable

$$\xi_N = \frac{2x}{1 + \sqrt{1 + 4x^2 M^2/Q^2}}, \quad (2.76)$$

for massless quarks (i.e. u , d and s), where M is the target nucleon mass.

²¹E665 was a fixed target muon scattering experiment at Fermilab.

GENIE uses the DIS model of Bodek and Yang [78] to include both higher twist and target mass corrections in a slow rescaling variable

$$\xi_w = \frac{2x(Q^2 + B)}{Q^2 \left(1 + \sqrt{1 + 4x^2 M^2/Q^2}\right) + 2Ax}, \quad (2.77)$$

for massless quarks, where $A = 0.538$ takes into account both target mass and higher twist corrections. $B = 0.305 \text{ GeV}^2$ is a parameter that accounts for a non-vanishing transverse momentum of the initial quark, allowing the extension of the cross section down to the photo-production limit at $Q^2 = 0$. A and B have to be determined by fits of structure functions to data and are therefore directly tied to the PDF set used in the fit. Both parameters are assigned a systematic uncertainty of 25 % [41] for events in the “safe DIS kinematic range” only (compare Table 2.1).

2.1.3.3 Longitudinal structure function

If the initial quark carries both longitudinal and transverse momentum, the general relation between the structure functions $F_1(x, Q^2)$ and $F_2(x, Q^2)$ is no longer given by the Callan–Gross relation (see Equation 2.63) but by

$$F_2(x, Q^2) = 2x \left(\frac{1 + R(x, Q^2)}{1 + 4M^2 x^2/Q^2} \right) F_1(x, Q^2), \quad (2.78)$$

with the ratio

$$R(x, Q^2) \equiv \frac{\sigma_L(x, Q^2)}{\sigma_T(x, Q^2)}, \quad (2.79)$$

of the cross sections for the absorption of a longitudinally (σ_L) or a transversely (σ_T) polarized boson by the target nucleon [15]. $R(x, Q^2)$ may be understood as a third structure function beside $F_2(x, Q^2)$ and $xF_3(x, Q^2)$ and has to be determined by experiment. A widely used parametrization²² of $R(x, Q^2)$, based on elastic electron scattering data, is given by

$$R_{1990,B}(x, Q^2) = \frac{0.0635}{\log(Q^2/\text{GeV}^2/0.04)} \theta(x, Q^2) + \frac{0.5747}{Q^2/\text{GeV}^2} - \frac{0.3534}{Q^2/\text{GeV}^2 + 0.09} \quad (2.80)$$

with

$$\theta(x, Q^2) = 1 + \left(\frac{12Q^2/\text{GeV}^2}{Q^2/\text{GeV}^2 + 1} \right) \left(\frac{(0.125)^2}{(0.125)^2 + x^2} \right). \quad (2.81)$$

This equation describes charged lepton data above $Q^2 > 0.3 \text{ GeV}^2$, with a fractional uncertainty of less than 15 % [82]. Since this parametrization diverges for

²²The original model includes three different fits (A , B and C) and the suggested parametrization is the unweighted average $R_{1990}(x, Q^2) = (A(x, Q^2) + B(x, Q^2) + C(x, Q^2))/3$. The parametrization used within the scope of this thesis is the fit $B(x, Q^2)$, consequently called $R_{1990,B}(x, Q^2)$.

$Q^2 \rightarrow 0$, $R(x, Q^2)$ is forced down to zero for $Q^2 \rightarrow 0$, as predicted by QCD for charged lepton scattering, using

$$R_{low}(x, Q^2 < 0.35 \text{ GeV}^2) = R_{1990,B}(x, Q^2 = 0.35 \text{ GeV}^2) \cdot 3.207 \left(\frac{Q^2}{Q^4 + 1} \right). \quad (2.82)$$

There are two effects modifying $R(x, Q^2)$ in neutrino interactions which are not accounted for in this model: On the one hand, the axial component of the structure function in neutrino scattering leads to a different expected behavior of $R(x, Q^2) \neq 0$ for $Q^2 \rightarrow 0$. On the other hand, charm production in neutrino interactions gives an additional contribution to $R(x, Q^2)$ which is not present in charged lepton scattering and therefore $R_\nu(x, Q^2) > R_{e,\mu}(x, Q^2)$.

Recent charged lepton data favor a slower decrease for $Q^2 \rightarrow 0$ than the one given by Equation 2.82. A comparison of data with the $R_{1990,B}$ parametrization as well as a modified low- R parametrization is shown in Figure 2.16. However, neutrino data exist at higher Q^2 only and are compatible with the $R_{1990,B}$ parametrization.

Neglecting the transverse momentum of initial quarks, only fully transversely polarized bosons contribute to the cross section. According to Equation 2.79, this means that $R(x, Q^2) = 0$ and $2xF_1(x, Q^2) = F_2(x, Q^2)$ being the well known Callan–Gross relation for spin-1/2 particles in the limit $Q^2 \gg M^2$.

The systematic uncertainty of the Callan–Gross violation is implicitly included in the uncertainty of the parameters A and B of the BY model (see Section 2.1.3.2).

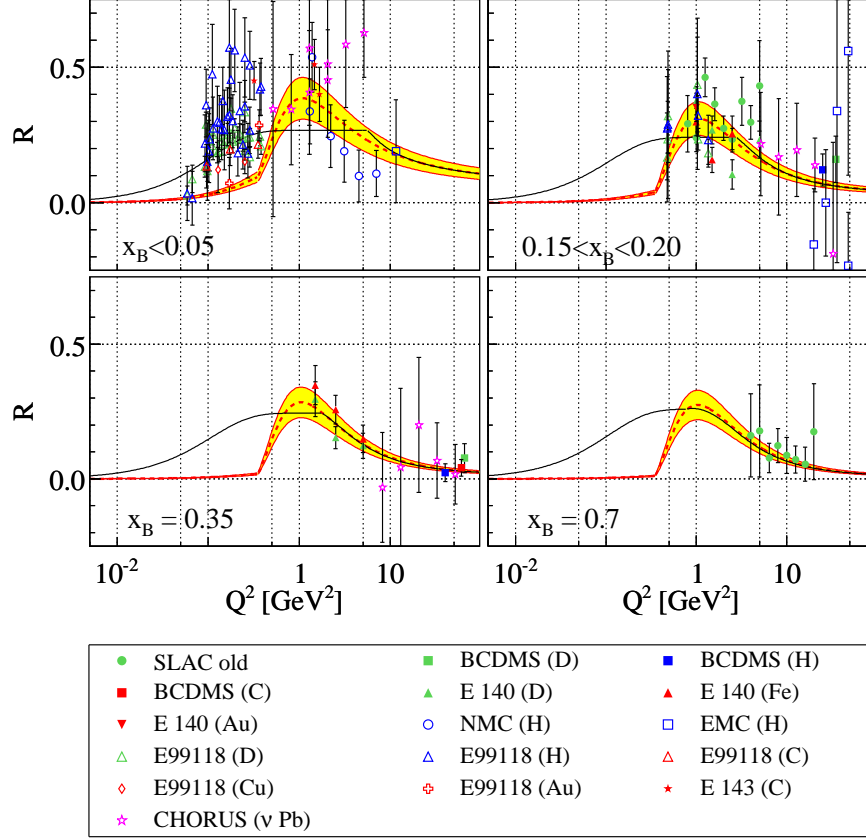


Figure 2.16: Longitudinal structure function, comparison of the calculation with data. The dashed line is the $R_{1990,B}$ parametrization, the shaded band shows a variation of $R_{1990,B}$ by $\pm 15\%$, where the uncertainty estimation is based on charged lepton data. The solid line is a parametrization R_{E99118} from the E99118 experiment, with the high Q^2 part given by R_{1990} . Data taken from [83](CHORUS), [82](SLAC old, E140, BCDMS) and [84](E99118).

2.1.3.4 Low- Q^2 PDF

The GRV98LO PDF set is valid for $Q^2 > 0.8 \text{ GeV}^2$, whereas for Q^2 values below that limit, the PDF are frozen

$$f(Q^2 < 0.8 \text{ GeV}^2) = f(Q^2 = 0.8 \text{ GeV}^2). \quad (2.83)$$

Within the used Bodek–Yang model, the PDF for up and down quarks are multiplied by Q^2 -dependent factors K_f , differing for valence and sea quarks, to describe the data over the full Q^2 -range, down to $Q^2 = 0$

$$K_f^{sea} = \frac{Q^2}{Q^2 + C_f^{sea}}, \quad (2.84)$$

$$K_f^{val} = [1 - G_D^2(Q^2)] \frac{Q^2 + C_f^{val,2}}{Q^2 + C_f^{val,1}}, \quad (2.85)$$

where $G_D(Q^2) = (1 + Q^2/0.71 \text{ GeV}^2)^2$ is the elastic proton form factor, and the sea quarks are defined as $q_f^{sea} = q_f - \bar{q}_f$. The values of the parameters C and the included systematic uncertainties are shown in Table 2.1 [41].

Table 2.1: Parameters used for the low- Q^2 corrections within the BY model. Where no uncertainty is given, the effect of varying the parameters is very small, compared to a change of the C_u^{val} factors. To avoid double counting with other uncertainties, these uncertainties are considered for events with $Q^2 > 1 \text{ GeV}^2$ and $W > 2 \text{ GeV}$ only, known as the “safe DIS kinematic range”.

Parameter	Value [GeV ²]	Uncertainty
C_u^{sea}	0.363	–
C_d^{sea}	0.621	–
$C_u^{val,1}$	0.291	30 %
$C_u^{val,2}$	0.189	40 %
$C_d^{val,1}$	0.202	–
$C_d^{val,2}$	0.255	–

Since these factors change the overall normalization of the PDF, an additional constant correction factor

$$f_{PDF} = 1.015 \quad (2.86)$$

has to be applied to all quark distributions. Within the default GENIE model, this factor is not directly used, but included in an overall factor

$$f_{DIS} = 1.032 \quad (2.87)$$

that is applied to both CC and NC DIS differential cross sections, to match the calculated total ν_μ -N CC cross section to the high-energy average world data. Within the scope of this thesis, however, the original f_{PDF} is retained and applied to both DIS NC and non-charm DIS CC events. The difference between f_{DIS} and f_{PDF} can be fully explained²³ by *quantum electrodynamics (QED)* and weak radiative corrections (see below).

The low- Q^2 PDFs for $x = 0.045$ are shown in Figure 2.17. The simulated Q^2 distribution of $\nu_\mu + {}^{208}\text{Pb}$ CC interactions for the CNGS energy spectrum is shown in Figure 2.18a. About 10 % of all DIS CC events in OPERA have a Q^2 of less than 0.8 GeV^2 .

The current GENIE implementation contains a small inconsistency: Since no reducing K factor is applied to the strange sea quark distributions, the low- Q^2

²³The BY model employed here does not include the axial part of the structure functions and is hence not expected to fully reproduce the experimentally measured neutrino data at low Q^2 . This topic will probably be addressed in a revision of the model [85].

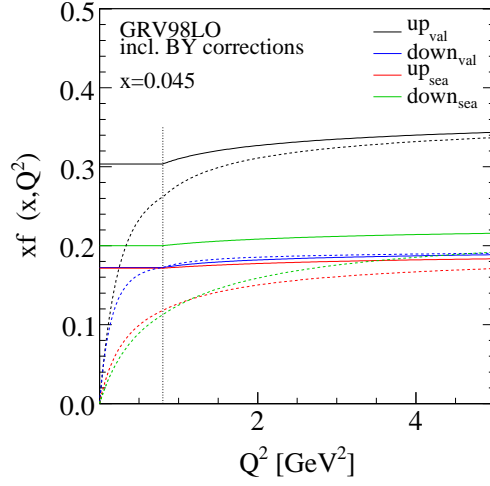
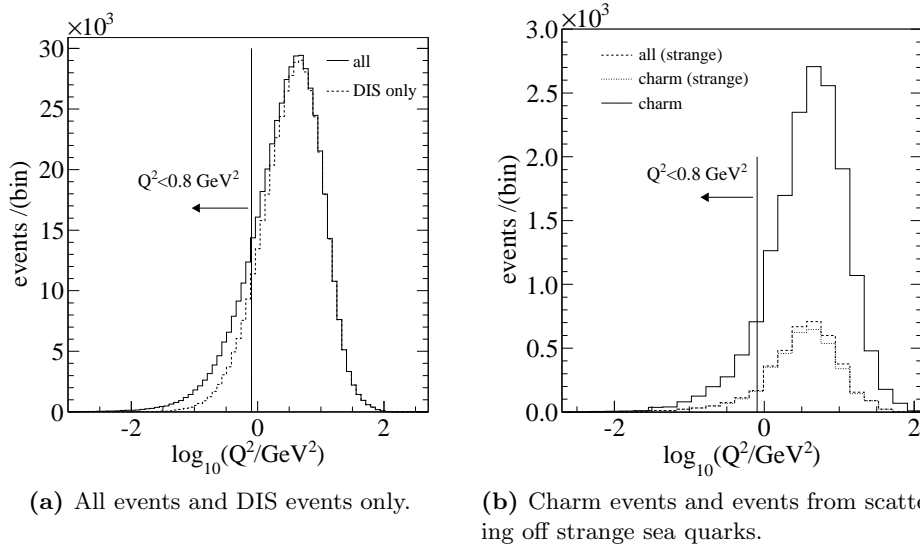


Figure 2.17: Up and down quark distributions from the GRV98LO PDF without (solid) and with BY corrections (dashed) at $x = 0.045$. The vertical dotted line at $Q^2 = 0.8 \text{ GeV}^2$ shows the limit below which the original PDF are frozen.

contribution from the scattering off strange quarks is possibly overestimated. The simulated Q^2 distribution of DIS events from the scattering off strange quarks is shown in Figure 2.18b. These events make up about 0.9 % of all DIS CC events, where about 93 % of these events result in a charm quark in the final state (this is about 23 % of all DIS CC charm events). The fraction of strange events with $Q^2 < 0.8 \text{ GeV}^2$ is again about 10 %.



(a) All events and DIS events only.

(b) Charm events and events from scattering off strange sea quarks.

Figure 2.18: Simulated Q^2 distribution of $5 \times 10^5 \nu_\mu + {}^{208}\text{Pb}$ CC interactions (unoscillated ν_μ CNGS beam spectrum).

A comparison of neutrino data with the structure function model implemented for F_2 and xF_3 , including all corrections mentioned so far, is shown in Figure 2.19.

The PDFs and structure functions are constrained by several QCD sum rules. These can be used to check the consistency of the implementation

$$\text{PDF} \longrightarrow F_i \longrightarrow \frac{d^2\sigma}{dxdy} \quad (2.88)$$

by directly accessing the applied GENIE structure functions and the cross section model. The number of valence quarks in the proton is given by

$$u_{val} = \int_0^1 (u(x) - \bar{u}(x)) dx \quad (2.89)$$

$$= 2 \quad (\text{theory}) \quad (2.90)$$

$$= 1.9962 \quad (\text{GENIE at } Q^2 = 15 \text{ GeV}^2), \quad (2.91)$$

$$d_{val} = \int_0^1 (d(x) - \bar{d}(x)) dx \quad (2.92)$$

$$= 1 \quad (\text{theory}) \quad (2.93)$$

$$= 0.9981 \quad (\text{GENIE at } Q^2 = 15 \text{ GeV}^2). \quad (2.94)$$

At generator level²⁴, the implementation of the inclusive differential cross section model can be tested for consistency using ‘‘Hugh’s trick’’ [89]: The differential cross section (see Equation 2.52) at Born-level (neglecting terms $\propto m^2/M^2$) contains the three unknown structure functions F_1 , F_2 and xF_3 . By evaluation at three different combinations of E_ν and y at fixed values of x and Q^2 , one ends up with a system of linear equations that has a unique solution for the structure functions. Any difference between Hugh’s trick and the structure function model results hints towards a mistake in the implemented algorithm that can be directly tested by comparing the *Gross-Llewellyn-Smith (GLS)* sum rule [90], valid for neutrons, protons and isoscalar targets,

$$S_{GLS} = \frac{1}{2} \int_0^1 (F_3^\nu + F_3^{\bar{\nu}}) dx = 3, \quad (2.95)$$

the *Bjorken (BJ)* sum rule [91]

$$S_{BJ} = \int_0^1 (F_1^{\bar{\nu}p}(x, Q^2) - F_1^{\nu p}(x, Q^2)) dx = 1 - \frac{2\alpha_s(Q^2)}{3\pi}, \quad (2.96)$$

where $\alpha_s(Q^2)$ is the strong coupling constant, and the *Adler (A)* sum rule [92], valid at all orders of QCD,

$$S_A = \frac{1}{2} \int_0^1 \frac{1}{x} (F_2^{\nu n} - F_2^{\nu p}) dx = 1. \quad (2.97)$$

²⁴This is not a generator-specific approach and can be used to compare different event generators with each other.

The results are

$$R_A = \frac{S_A^{Hugh}}{S_A^{SF}} = 1.0004, \quad (2.98)$$

$$R_{BJ} = \frac{S_{BJ}^{Hugh}}{S_{BJ}^{SF}} = 1.0021, \quad (2.99)$$

$$R_{GLS,n} = \frac{S_{GLS,n}^{Hugh}}{S_{GLS,n}^{SF}} = 1.0001, \quad (2.100)$$

$$R_{GLS,p} = \frac{S_{GLS,p}^{Hugh}}{S_{GLS,p}^{SF}} = 0.9997. \quad (2.101)$$

$$(2.102)$$

Since the structure functions get very large for small x , the integration limit was set to the technically lowest possible value of 10^{-6} . The small differences between Hugh's trick and the SF model are due to the missing lepton mass terms and the usage of the simple Callan–Gross relation, especially important for the Bjorken sum rule, assumed by Hugh's trick.

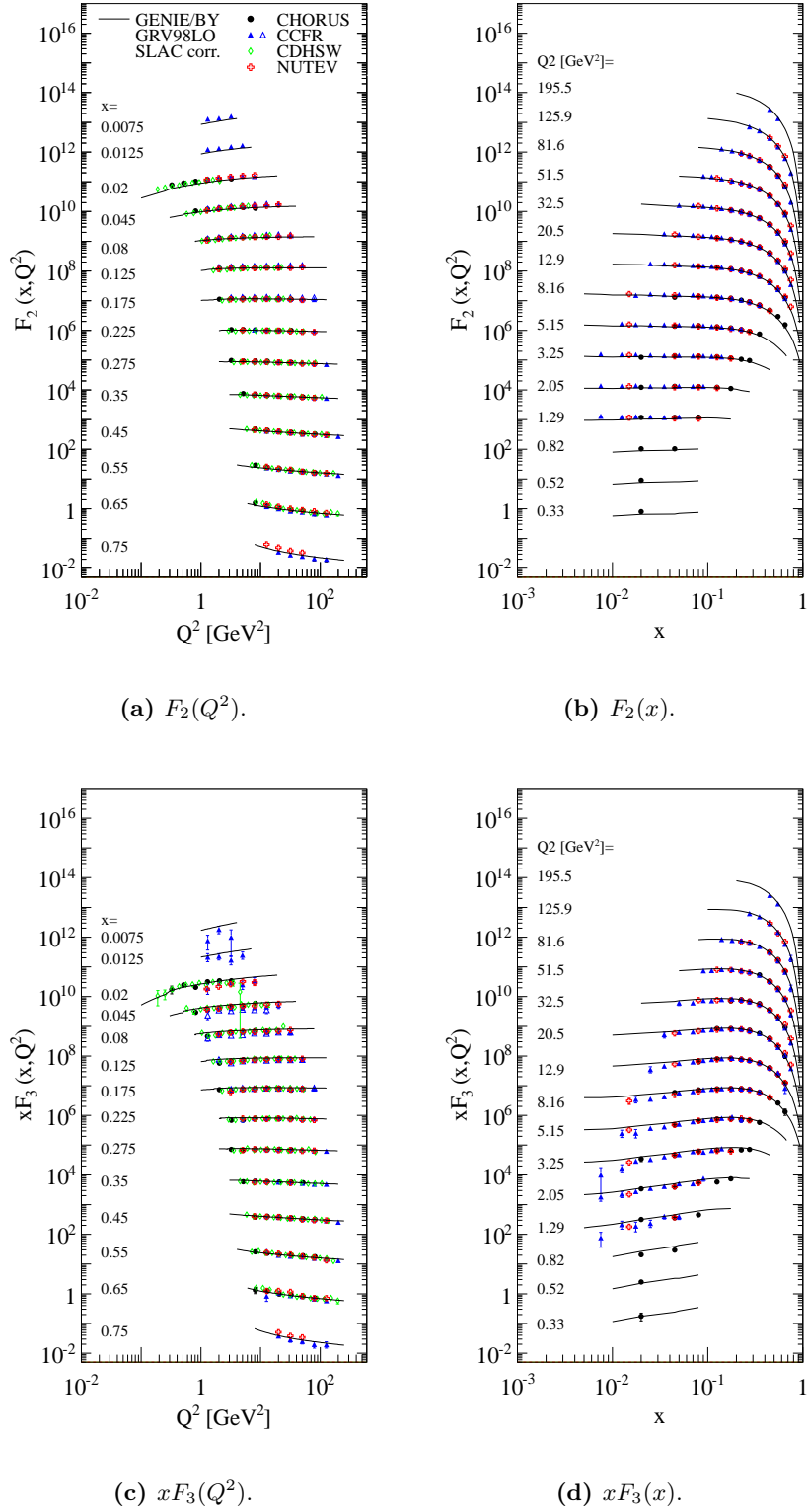


Figure 2.19: Neutrino structure functions, comparison of the **GENIE** model including nuclear corrections with data. Data are taken from [83] (CHORUS, Pb), [86] (CCFR, Fe), [87] (CDHSW, Fe) and [88] (NUTEV, Fe). All data are corrected for isoscalarity by the authors. Data are scaled up by factors of 10, the lowest entries are left unscaled. For display purposes, the (large) errors of the first data point in the xF_3 plot at $x = 0.0075$ are scaled down by 50%.

2.1.3.5 Charm production

The dominant contribution to DIS CC charm production is the $s \rightarrow c$ scattering off strange sea quarks and the Cabibbo-suppressed $d \rightarrow c$ scattering. Since the final state quark cannot be taken to be massless anymore, the LO model described above has to be adjusted with additional modifications. The finite charm quark mass m_c is included by a dimensionless, multiplicative factor to the Nachtmann-variable ξ_N (see Equation 2.76) via

$$\xi_c = \xi_N \left(1 + \frac{m_c^2}{Q^2} \right), \quad (2.103)$$

where the initial quark is assumed to be massless²⁵ [81].

The minimum value of W for DIS CC charm interactions is given by $W > M + m_{D^0}$, where M is the mass of the nucleon and m_{D^0} is the mass of the lightest charmed meson D^0 . The GENIE model implements the DIS CC charm production via a helicity-based approach [93], where the kinematical twist corrections are included naturally. The calculation involves the two CKM matrix elements $V_{cd} = 0.230$ and $V_{cs} = 0.957$ [94] and the charm quark mass $m_c = 1.43$ GeV [95]. Not entering the experimentally and theoretically challenging task to determine and define the charm quark mass, the absolute value of m_c should be understood as input parameter to model charm-production in neutrino interactions and describe the production threshold in combination with LO PDFs.

The dominant charm-production uncertainty for energies up to 30 GeV comes from a variation of the charm mass by ± 10 % as indicated by the world neutrino data [95] (see Figure 2.20). The CKM matrix elements are varied by ± 5 % (V_{cd}) and ± 10 % (V_{cs}), respectively [94]. Since the latter two uncertainties are directly connected to the respective down and strange quark distributions, they are important for different regions of the differential cross section. Near the charm threshold, the total DIS CC charm cross section uncertainty is about ± 20 % and asymptotically approaches values of $\pm(10 - 15)$ % for energies above 30 GeV, where the contributions from these three uncertainties are almost equal (see Figure 2.21). Tweaking the charm mass to lower values increases the available phase space, hence limiting the reliability and possibility of MC reweighting near the charm threshold. A comparison of reweighted and regenerated events shows only negligible effect of the reweighted phase space relevant to the OPERA electronic detector analysis, though. Note that the CKM matrix elements used here are lower than the global fits and the respective uncertainties become much smaller after applying unitary constraints [94]²⁶.

²⁵Equation 2.103 holds for final bottom and top quarks, too, by replacing m_c with m_b and m_t , respectively. It has to be modified if the initial quark is not massless, which is usually negligible in neutrino scattering given the small contribution of kinematically accessible heavy quark PDFs.

²⁶Changing the default values of the CKM matrix elements requires retuning of the generator though, but should be considered if charm production becomes important. The systematic

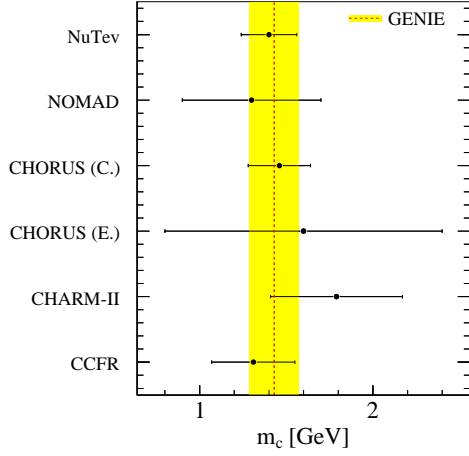


Figure 2.20: Charm mass, comparison of the GENIE value (dashed line) with data from neutrino experiments. The shaded band shows the included $\pm 1\sigma$ systematic uncertainty, see text for details. Data are taken from the compilation in [95]. The two CHORUS data points represent independent measurements from calorimetry (C.) and emulsion analysis (E.).

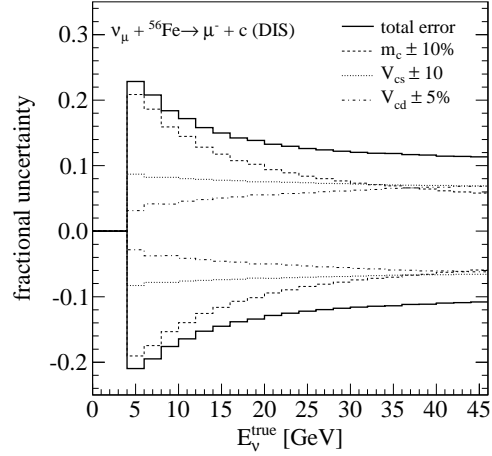


Figure 2.21: DIS CC charm cross section uncertainty, extracted from 10^6 reweighted DIS $\nu_\mu + {}^{56}\text{Fe} \rightarrow \mu^- + c$ (DIS) events. Despite the heavy nuclear target chosen for this simulation, the result is almost the same as for free proton or neutron interactions.

NC charm production, also called “associated charm production“, is a NLO process in boson–gluon fusion [96], where a $c\bar{c}$ pair is produced (see Figure 2.22, while CC boson–gluon fusion is shown in Figure 2.23). The cross section for this reaction has been measured by NUTEV²⁷, yielding $\sigma_{NCcharm} = 0.21_{-0.15}^{+0.18} \times 10^{-39} \text{ cm}^2$ at $\langle E \rangle = 154 \text{ GeV}$, consistent with the theoretical expectation from the boson–gluon fusion model [97, 98]. For the neutrino energies relevant to the OPERA experiment, this contribution is negligible.

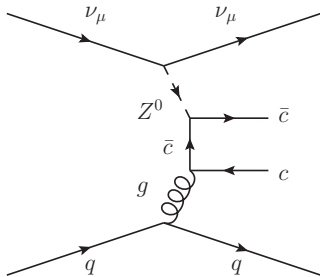


Figure 2.22: NC charm production in boson–gluon fusion.

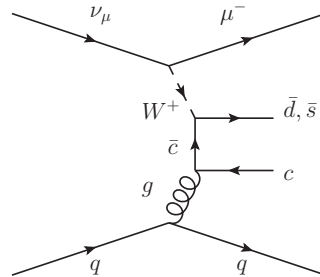


Figure 2.23: CC charm production in boson–gluon fusion.

uncertainty estimation for charm production accounts for this issue by using very conservative values of the CKM uncertainties.

²⁷NUTEV: Neutrinos at the Tevatron.

2.1.3.6 Strange sea asymmetry and charm sea

The GRV98LO PDF set provides a locally symmetric strange sea contribution $s(x) = \bar{s}(x)$, as expected by purely perturbatively generated strange quarks in the nucleon. While sum rules constrain the total nucleon strangeness

$$[s^-] = \int_0^1 s^- dx = \int_0^1 \{s(x) - \bar{s}(x)\} dx = 0 \quad (2.104)$$

for all Q^2 , the integrated momentum density

$$[S^-] = \int_0^1 S^- dx = \int_0^1 \{x(s(x) - \bar{s}(x))\} dx \quad (2.105)$$

is theoretically less constraint. Available experimental data is not conclusive to rule out a small strange sea asymmetry $[S^-] \neq 0$ in the order of -0.001 to +0.004 [95, 99]. A value of $[S^-] \neq 0$ requires at least one zero crossing of s^- , where the area between s^- and the x -axis above and below the x -axis must be equal. The possibility of an asymmetric strange sea is included in the systematic uncertainty discussion in Section 7.2.

The GRV98LO PDF does not include an (anti)charm sea and is hence expected to underestimate the cross sections at high energy transfers ν to the target nucleon. This high-energy effect however is negligible within this analysis. The contribution to the total cross section is included by normalization to data (see below).

2.1.3.7 Radiative corrections

Even though the electrically neutral neutrinos themselves are not subject to QED effects, the scattering off nuclei involves QED radiative corrections. These include photon emission from the initial or final state quark for both NC and CC events (see Figure 2.24), and photon emission from the final state lepton (see Figure 2.25).

Additional weak corrections include self-energy diagrams of the exchanged boson (see Figure 2.26) and can be included approximately by Q^2 -dependent boson-quark coupling. The implementation of these corrections is based on the original FORTRAN code NUDIS2 by Bardin et al. [100] and ZFITTER 6.34 [101] with modifications by G. Zeller [77].

The above-mentioned corrections are included as a correction factor

$$f_{rad}(E, x, y) = \frac{\left(\frac{d^2\sigma}{dxdy}\right)_{Born\ incl.\ rad.\ corrections}}{\left(\frac{d^2\sigma}{dxdy}\right)_{Born}} \quad (2.106)$$

that is applied as a weight to each event. $\frac{d^2\sigma}{dxdy}_{Born}$ is given by Equation 2.52, where terms $\propto m^2/M$ have been neglected. The code is further modified to

use the GRV98LO PDF set, including the low- Q^2 extension and the $R_{1990,B}$ parametrization as described above, while higher-twist corrections and target mass corrections are not applied. Corrections to DIS charm production are evaluated in the QPM including the slow scaling variable ξ_c (see Equation 2.103).

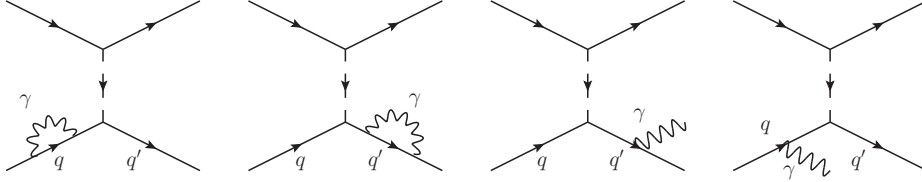


Figure 2.24: QED radiative corrections diagrams, initial and final state quark radiation (both NC and CC).

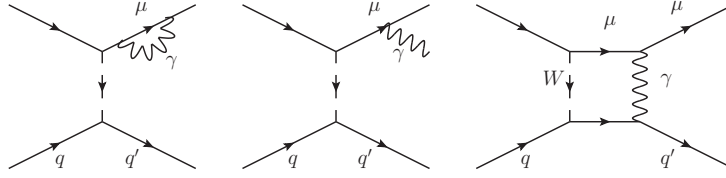


Figure 2.25: QED radiative corrections diagrams, final state lepton radiation (CC only).

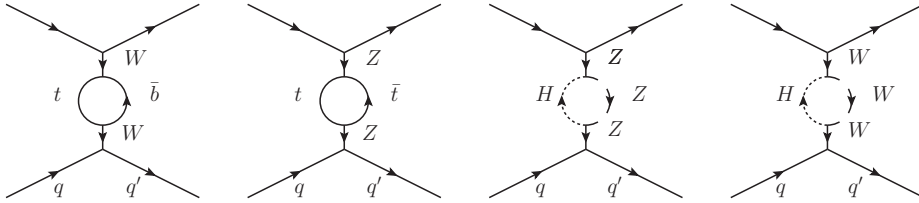


Figure 2.26: Some of the weak corrections diagrams for NC (Z exchange) and CC (W exchange) scattering, involving top quarks (t) and the Higgs boson (H).

To speed up the simulation, the weights are obtained by extrapolation from a set of 24 precalculated tables $T_i(x, y, E)$ using the aforementioned modified code, where i is a combination of neutrino ($\nu_e, \bar{\nu}_e, \nu_\mu$ or $\bar{\nu}_\mu$), target (neutron or proton) and interaction (NC, CC (charm) or CC (no charm)). The tables span a kinematic range of $2.5 \text{ GeV} < E < 500 \text{ GeV}$, $0.0005 < x < 0.9975$ and $0.0005 < y < 0.9975$, while values outside the specified ranges are evaluated at the next available point without extrapolation. This range covers the full phase space of the OPERA experiment. The resulting corrections to the differential cross sections are shown in Figure 2.27. Due to the additional contribution of photon emission from the final state lepton, the effect of radiative corrections is much larger for CC events than for NC events. For CC events in OPERA, the corrections to the differential cross section can be as large as about 25 % for small

(large) y and large (small) x , while they are smallest for intermediate x . The main effect of radiative corrections is the transfer of energy from the outgoing charged lepton to a photon, which appears is measured as hadronic energy in the OPERA calorimeter, resulting in a shift of CC events towards higher hadronic energies. Note that the corrections for antineutrinos are not the same as for neutrinos, even for NC interactions.

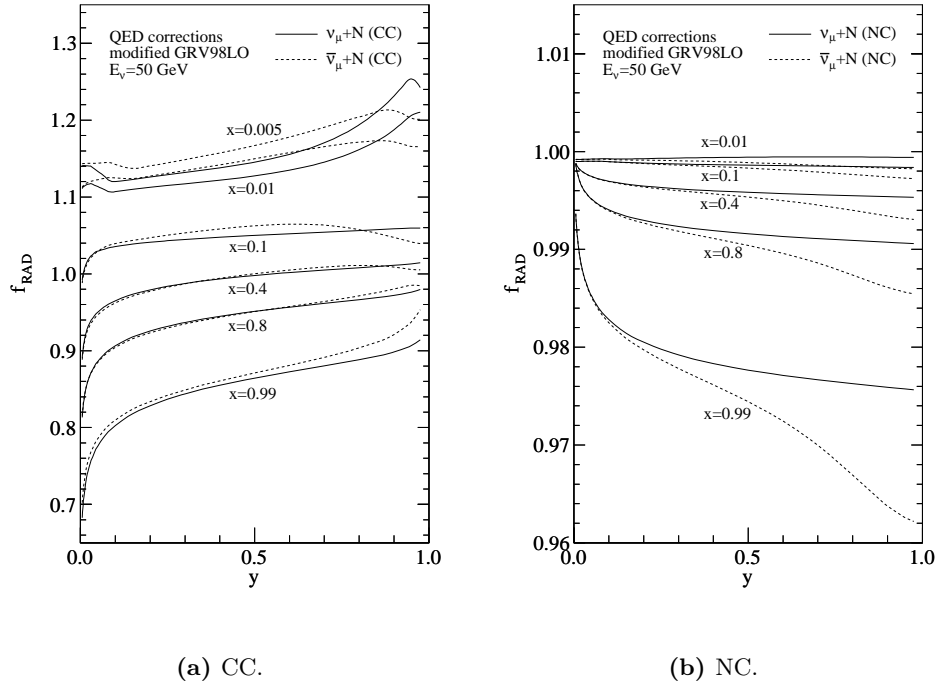


Figure 2.27: Total radiative corrections (QED only) for ν_μ scattering off an isoscalar nucleon, $E_\nu = 50$ GeV.

The radiative corrections also have an impact on the total cross sections (see Figure 2.28). These figures have been obtained following the full Monte Carlo chain, including the simulation of 10^6 interactions each on protons and neutrons for every neutrino flavor, reweighting each single event according to the tables T_i , and smoothing by fitting the resulting distribution with a high-order polynomial. The corrections for ν_e are shown to provide a consistency check of the implementation. The corrections of total cross sections for all neutrino flavors become nearly constant for neutrino energies above 30 GeV, where they amount to about $f_{RAD}^{total\ CC} = 1.021$ (ν_μ CC), $f_{RAD}^{total\ NC} = 0.998$ (ν_μ NC), $f_{RAD}^{total\ CC} = 1.023$ ($\bar{\nu}_\mu$ CC) and $f_{RAD}^{total\ NC} = 1.012$ ($\bar{\nu}_\mu$ NC) for an isoscalar target. While the NC corrections do not depend on the neutrino flavor, the ν_e CC corrections are larger than the ν_μ CC corrections as was expected due to the smaller electron mass.

The modified cross section model, including the PDF correction factor f_{PDF} (see Equation 2.86) and above-mentioned radiative corrections to DIS, very well

reproduces the measured world average slope between (30 – 200) GeV of both the $\nu_\mu+N$ and $\bar{\nu}_\mu+N$ total inclusive CC cross sections for free isoscalar targets [1]:

$$\sigma_{\nu N}^{(experiment)} = (0.677 \pm 0.014) \times 10^{-38} \text{ cm}^2/\text{GeV}, \quad (2.107)$$

$$\sigma_{\nu N}^{(model)} = 0.676 \times 10^{-38} \text{ cm}^2/\text{GeV} \quad (2.108)$$

and

$$\sigma_{\bar{\nu} N}^{(experiment)} = (0.334 \pm 0.008) \times 10^{-38} \text{ cm}^2/\text{GeV}, \quad (2.109)$$

$$\sigma_{\bar{\nu} N}^{(model)} = 0.336 \times 10^{-38} \text{ cm}^2/\text{GeV}. \quad (2.110)$$

Compared to the default GENIE cross section model, the DIS NC cross sections including radiative corrections are lower, since $f_{PDF} f_{RAD}^{total NC} < f_{DIS}$ for all neutrino energies (compare Equation 2.87 and Equation 2.86), whereas the DIS CC cross sections are higher for low neutrino energies. Given the small overall contribution of the DIS cross section at low neutrino energies, the latter effect is very small. Note that no measurements of the total neutrino NC cross section exist.

Radiative corrections for ν_τ CC interactions are smaller than for ν_μ CC interactions due to the high tau-lepton mass. They are also small compared to the total uncertainty of the ν_τ cross section and hence will be neglected within this work.

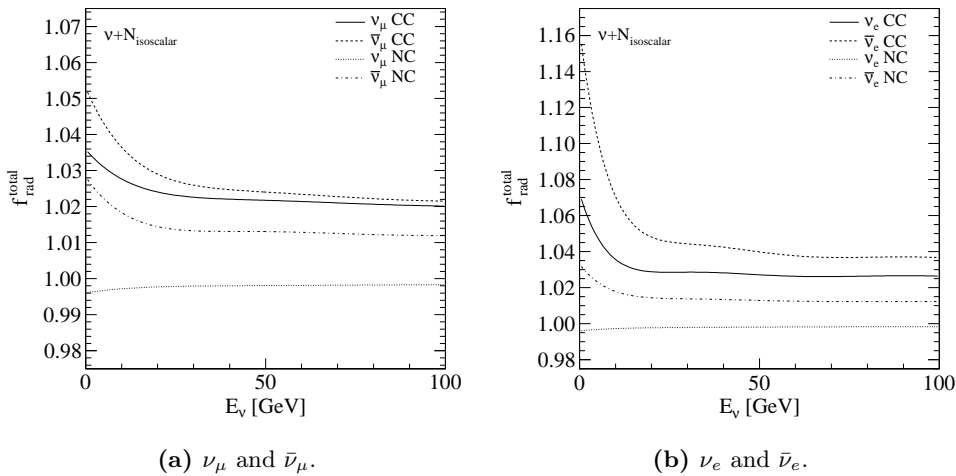


Figure 2.28: Radiative corrections (QED and weak) to the total DIS cross sections for NC and CC interactions.

2.1.3.8 Nuclear corrections

The structure functions measured on nuclear targets differ from the ones obtained on free partons, as becomes evident in the ratio

$$R^A(x, Q^2, A) = F_2^A(x, Q^2)/F_2^{(free)}(x, Q^2) \neq 1, \quad (2.111)$$

where A is the atomic number. This effect has experimentally been well established in charged lepton scattering, where $R^A(x, Q^2, A)$ is commonly divided into four regions approximately given by

- Fermi motion: for $x \gtrsim 0.75$ ($R^A > 1$),
- EMC effect²⁸: for $0.3 \lesssim x \lesssim 0.75$ ($R^A < 1$),
- Anti-shadowing: for $0.1 \lesssim x \lesssim 0.3$ ($R^A > 1$),
- Shadowing: for $x \lesssim 0.1$ ($R^A < 1$).

Recent results show a weak Q^2 -dependence for small x and a scaling with the atomic number A [102]. GENIE uses a parametrization of $F_2^D(x)/F_2^N(x)$ and $F_2^A(x)/F_2^D(x)$ [86, 103], where a Q^2 -dependency is neglected, D is deuterium, N is an isoscalar target and A is a nuclear target:

$$f_{nucl}(x < 0.75, A = 2) = 0.985(1.0 + 0.422x - 2.745x^2 + 7.57x^3 - 10.335x^4 + 5.422x^5), \quad (2.112)$$

$$f_{nucl}(x < 0.75, A > 2) = f_{nucl}(x, A = 2) \cdot (1.096 - 0.364x - 0.278x^{14.417} + 2.722 e^{-21.94x}). \quad (2.113)$$

The GENIE model includes nuclear effects to DIS by applying a correction factor $f_{nucl}(x)$ to all structure functions when calculating the differential cross sections. For $x > 0.75$, most of the nuclear effects are expected to be due to the Fermi motion of the nucleus, which is handled by a dedicated GENIE model. To avoid double counting, no additional nuclear corrections are applied to DIS for $x > 0.75$ within GENIE. A comparison of the GENIE model with charged lepton data is shown in Figure 2.29.

Nuclear effects in neutrino DIS are one of the long standing and yet unsolved questions in neutrino physics. The available data from neutrino scattering is driven by the large data sets of the NUTEV and CHORUS experiments [104], both of them using muon neutrinos and the heavy targets iron and lead, respectively. The situation can be summarized as follows: The NUTEV data is incompatible with the charged lepton data and favors less pronounced shadowing and anti-shadowing effects, whereas the CHORUS data is compatible with both NUTEV and charged lepton data. Since all available neutrino data are based on heavy targets, the influence of the nuclear number A on nuclear effects in $\nu + A$ scattering is unknown²⁹. There are indications that the nuclear corrections for F_2

²⁸Named after being found in the *European Muon Collaboration (EMC)* experiment.

²⁹Additional information could come from the NOMAD experiment. Unfortunately, no differential cross section measurements have been published yet.

and x_F_3 are different, which hints towards different nuclear effects for valence and sea quarks [105]. Notice that the uncertainties in nuclear effects for the analysis conducted in Section 7 largely cancel out as long as nuclear effects are universal for NC and CC interactions. The possibility of non-universal nuclear effects is included in the systematic uncertainty discussion in Section 7.2.

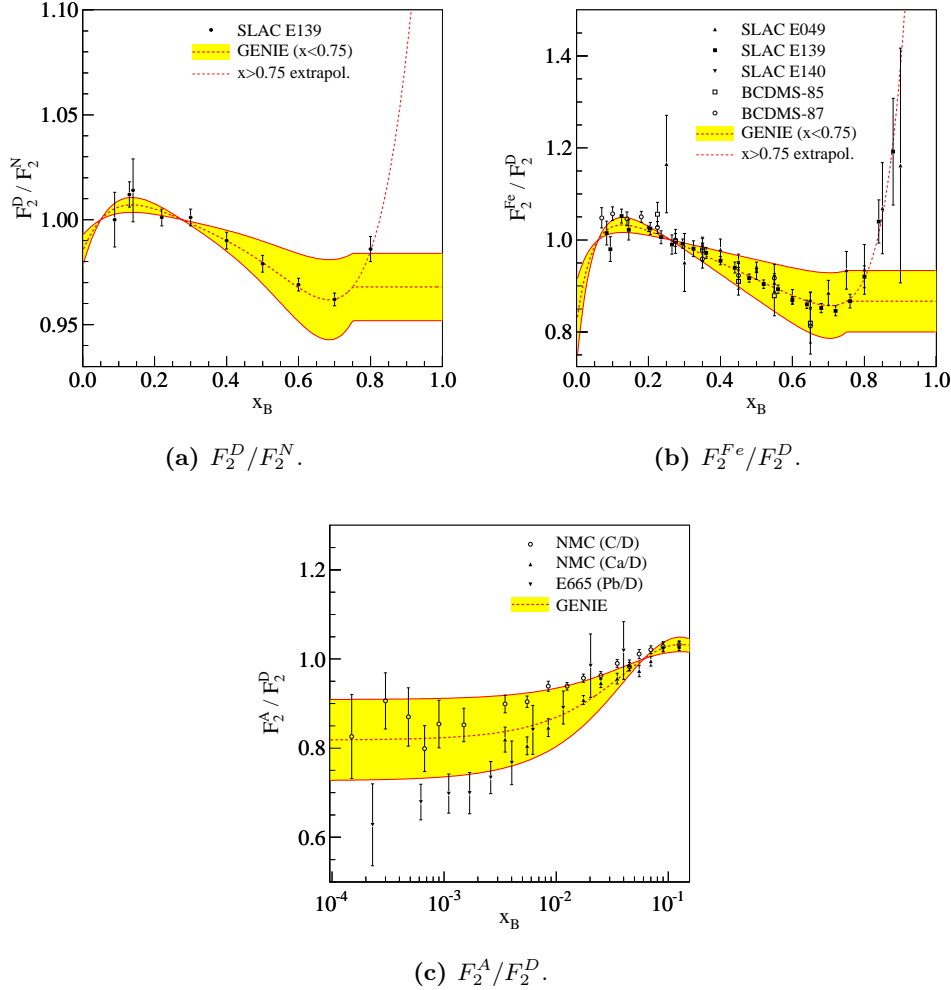


Figure 2.29: Nuclear corrections to F_2 , comparison of the calculation with data from charged lepton experiments. The dashed line is the parametrization used within GENIE, the shaded band shows the systematic uncertainty estimation obtained by replacing f_{nucl} with $(1 + k_{nucl}(f_{nucl} - 1))$ and varying the parameter $k_{nucl} = 1$ by $\pm 50\%$ [106] (not used within this work). Data are taken from [107] (E139), [82] (E140), [108] (E049), [109] (BCDMS-85), [110] (BCDMS-87), [111] (NMC), [112] (E665). The fine-dashed line in (a) and (b) for $x > 0.75$ is an extrapolation of Equation 2.112 and Equation 2.113 and is not used within GENIE (see text for details).

2.1.4 Inelastic transition region

While QEL scattering can theoretically be separated quite clearly, both RES (see Section 2.1.2) and DIS (see Section 2.1.3) scattering contribute to the low-

multiplicity one- and two-pion final states. Neglecting any other small contributions to the cross sections for the moment (see Section 2.1.5), the GENIE event generator composes the inelastic neutrino cross sections by adding up the full RES cross sections plus a weighted DIS contribution below a value $W_{cut} = 1.7$ GeV (evaluated on-shell), and using the full DIS cross section above W_{cut} :

$$\begin{aligned} \left(\frac{d^2\sigma}{dQ^2 dW}\right)^{inelastic} &= \left(\frac{d^2\sigma}{dQ^2 dW}\right)^{RES} H(W_{cut} - W) \\ &+ \left(\frac{d^2\sigma}{dQ^2 dW}\right)^{DIS} H(W_{cut} - W) \sum_M f_M \\ &+ \left(\frac{d^2\sigma}{dQ^2 dW}\right)^{DIS} H(W - W_{cut}), \end{aligned} \quad (2.114)$$

with the Heaviside step function $H(x \leq 0) = 0$ and $H(x > 0) = 1$ otherwise. The crucial input parameters for this model are the coefficients f_M , which are a combination of the probabilities p_M that the DIS final state includes n pions, and the weights w_M that are obtained from fits to the measurements of exclusive pion production and measurements of the total CC cross section. All weights are assigned a 50 % systematic uncertainty and are given in Table 2.2. Note that this approach introduces a dependency on the GENIE DIS hadronization model (see Section 2.2).

Table 2.2: GENIE transition region weight factors for 1π and 2π final states. The same weight factors are applied to NC and CC interactions. For all 2π final states, the weights are one. In principle, all 16 weight factors may be set to individual values in GENIE.

Parameter	Value
$\nu n 1\pi$	0.300
$\bar{\nu} n 1\pi$	0.100
$\nu p 1\pi$	0.100
$\bar{\nu} p 1\pi$	0.300
2π	1.000

The fraction of 1π and 2π events contributing to the total number of events is shown in Figure 2.30. The maximum contribution is reached at about 2 GeV, where more than 50 % of all events have low-multiplicity pion final states.

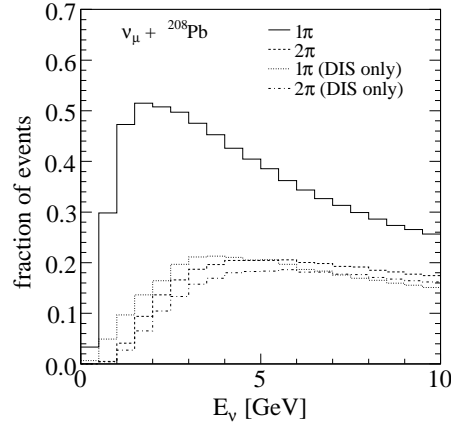


Figure 2.30: Fraction of events with 1π or 2π final hadronic states (CC and NC interactions) for $\nu_\mu + {}^{208}\text{Pb}$ interactions.

2.1.5 Other types of neutrino interactions

While the neutrino interactions described above constitute the largest part of events observable in the OPERA detector, some other processes are also included in the GENIE model.

Coherent scattering (COH)

$$\nu_\mu + N(p) \rightarrow \nu_\mu + N(p') + \pi^0 \quad (\text{NC}), \quad (2.115)$$

$$\nu_\mu + N(p) \rightarrow \mu^- + N(p') + \pi^+ \quad (\text{CC}), \quad (2.116)$$

leaves the entire nucleus intact and results in a single forward pion. It takes place at very low momentum transfers Q^2 and is modeled according to Rein–Sehgal [113, 114], including the final state lepton mass terms.

Inverse muon decay (IMD)

$$\nu_\mu + e^- \rightarrow \mu^- + \nu_e, \quad (2.117)$$

$$(2.118)$$

produces forward–boosted muons with very small transverse momentum. Following Bardin and Dokuchaeva [115], it is calculated including 1–loop radiative corrections. Inverse τ –decay is neglected. Due to the low mass of the target electrons, IMD has a high threshold energy of about 11 GeV.

All neutral current $\nu_l + e$ processes are calculated according to [116].

At all energies of interest for the OPERA experiment, the contribution of these types of neutrino interactions to the total cross section is very low (see Figure 2.31). The associated uncertainties are negligible within the scope of this thesis.

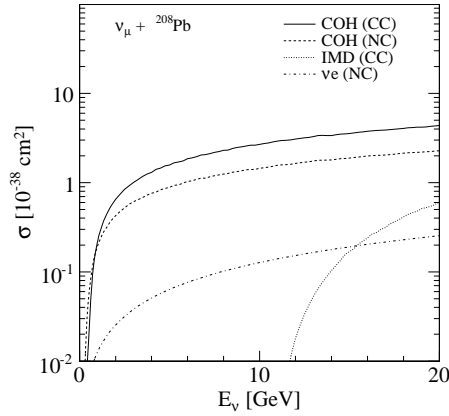


Figure 2.31: Cross sections of ν_μ scattering off lead nuclei for COH scattering, IMD and elastic $\nu + e$ scattering. (For comparison: The total CC cross section at 5 GeV (20 GeV) is about $825 \times 10^{-38} \text{ cm}^2$ ($3100 \times 10^{-38} \text{ cm}^2$)).

2.1.6 Total cross section

In principle, the total neutrino cross sections can be expressed by the sum of all different exclusive cross sections

$$\sigma^{tot} = \sigma^{1\pi} \oplus \sigma^{2\pi} \oplus \dots \oplus \sigma^{1K} \oplus \dots, \quad (2.119)$$

where the exclusive hadronic final state is given in the superscripts. In the absence of any theory that describes neutrino interactions at this level, the usual approach is to incoherently sum up the different aforementioned processes

$$\sigma^{tot} = \sigma^{QEL} \oplus \sigma^{RES} \oplus \sigma^{DIS} \oplus \dots, \quad (2.120)$$

while avoiding double counting of contributions to the same final states in the transition region between RES and DIS.

For the neutrino energies of interest in the OPERA experiment of about $1 \text{ GeV} < E < 200 \text{ GeV}$, the only applicable existent experimental data is from ν_μ and $\bar{\nu}_\mu$ scattering. Data on exclusive processes other than QEL scattering (compare Figure 2.7 and Figure 2.8), are mostly limited to low-multiplicity pion final states taken in low- Z target detectors based on liquid scintillators and bubble chambers. Some data on kaon and charm production exist, where especially the kaon data are not conclusive. Data on neutrino scattering on free nucleons are limited to hydrogen- and deuterium-filled bubble chambers operated at low neutrino energies of $\mathcal{O}(1 \text{ GeV})$ in the 1970s and 1980s, and suffering from low statistics. Other experiments have corrected their results to the free nucleon cross sections on neutrons, protons or isoscalar targets. High statistics data on neutrino DIS scattering exist from several, mostly iron-based, calorimeter experiments. A comparison of the total cross sections, as derived in the previous sections, and experimental data is shown in Figure 2.32 ($\nu_\mu + N$) and Figure 2.33 ($\bar{\nu}_\mu + N$).

Experimental data on ν_τ cross sections are limited to the DONUT experiment (see Figure 2.34).

Apart from NCE and low-multiplicity π^0 production, no data on NC cross sections are available for the processes of interest for OPERA.

The only publication of results on the NC/CC ratio versus hadronic energy was made by NOMAD [117], however with a not yet finally calibrated detector and is thus not expected to exactly reproduce e.g. the GENIE prediction [118].

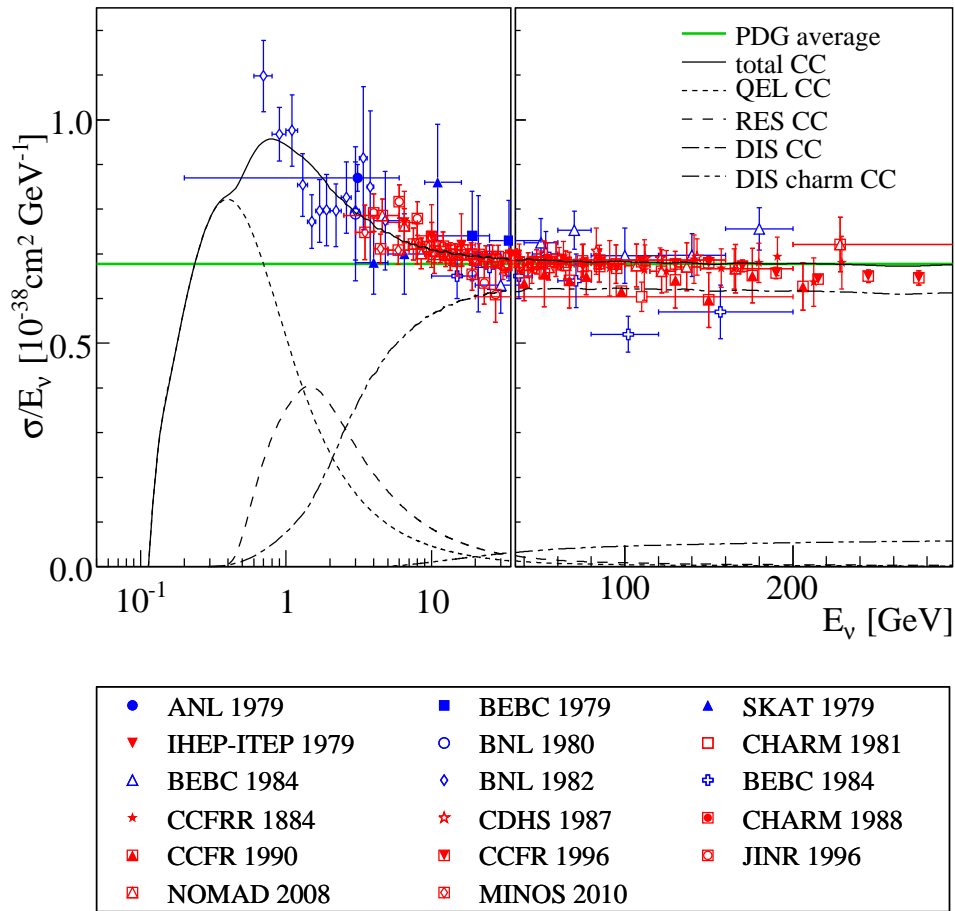


Figure 2.32: Total $\nu_\mu + N$ cross section, comparison of the calculation with data. The solid line is the theoretical total cross section, while the dashed lines are the different contributions to it. Data are taken from [94, 119] and references therein, [120](NOMAD 2008) and [41](MINOS 2010). High-energy data have been corrected for radiative effects by the respective experiments. Note that the theoretical calculation has been normalized to the PDG average value (see Section 2.1.3.4).

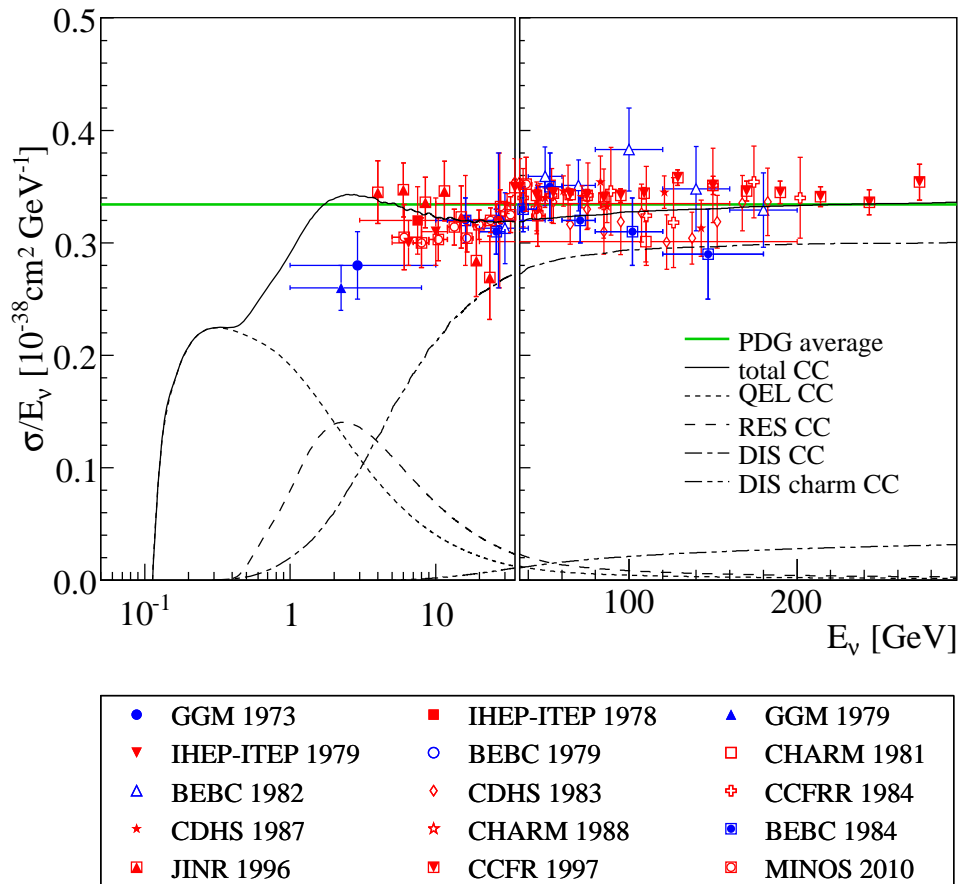


Figure 2.33: Total $\bar{\nu}_\mu + N$ cross section, comparison of the calculation with data. The solid line is the theoretical total cross section, while the dashed lines are the different contributions to it. Data are taken from [94, 119] and references therein and [41](MINOS 2010). High-energy data have been corrected for radiative effects by the respective experiments.

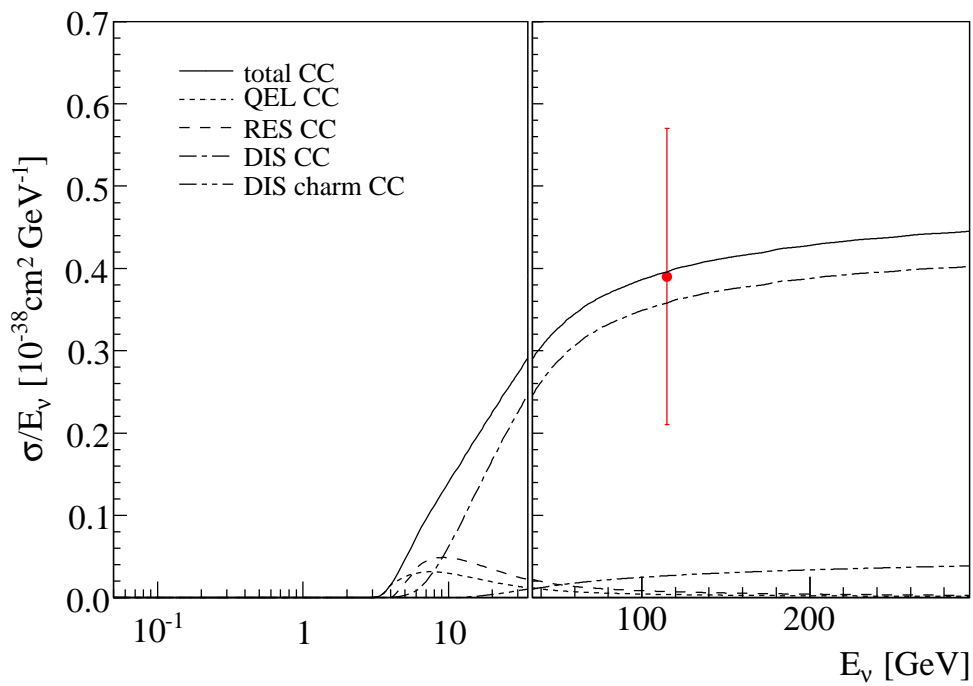


Figure 2.34: Total average $((\nu_\tau + N) + (\bar{\nu}_\tau + N))/2$ cross section, comparison of the calculation with data. The solid line is the theoretical total cross section, while the dashed lines are the different contributions to it. Data are taken from [121] (DONUT 2008).

2.2 Hadronization

Apart from the calculation of the cross sections, the simulation of neutrino interactions requires a hadronization model that describes the formation of hadronic states in DIS depending on the event kinematics, the type of the interaction, the flavor of the incoming neutrino and the hit target. GENIE uses the phenomenological AGKY–KNO³⁰³¹ hadronization model, originally developed for the MINOS experiment and implemented in the NEUGEN event generator [122, 123]. The steps of the AGKY–KNO model are recorded in detail here, to explain the systematic uncertainties included in the final analysis and illustrate limitations of existing hadronization models.

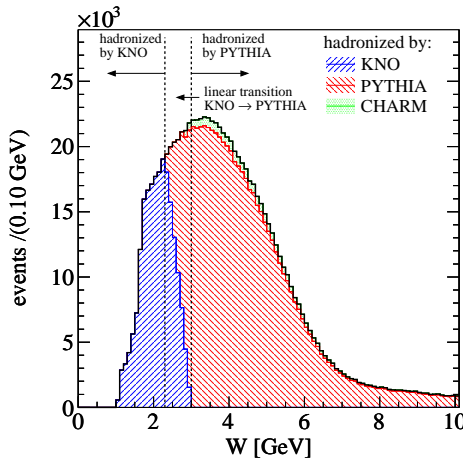


Figure 2.35: W distribution (on-shell) for CNGS beam-induced $\nu_\mu + {}^{208}\text{Pb}$ CC DIS events. Charm events are hadronized by a dedicated hadronization model (labelled CHARM).

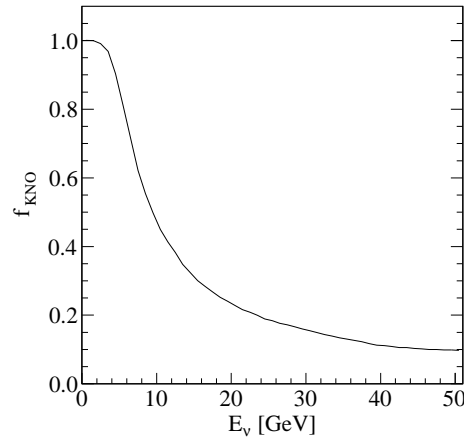


Figure 2.36: Fraction of DIS CC $\nu_\mu + {}^{208}\text{Pb}$ events hadronized by AGKY–KNO to all DIS CC events.

For invariant mass final states with $W > 3$ GeV, the AGKY–KNO model uses PYTHIA 6.4/JETSET³² [124], whereas a phenomenological approach based on KNO–scaling [125] is used to model the low-invariant mass part of $W < 2.3$ GeV. A linear transition between the two models for $2.3 \text{ GeV} \leq W \leq 3 \text{ GeV}$ ensures a smooth W distribution. The W distribution for CNGS beam-induced DIS CC events in OPERA is shown in Figure 2.35, and the fraction f_{KNO} of events hadronized by AGKY–KNO to all DIS CC events is shown in Figure 2.36. All DIS charm events involving a final state charm quark are hadronized by a dedicated model, where the charm fragmentation is described by the Collins–Spiller parametrization [126] and the remaining hadronic system is hadronized by PYTHIA 6.4/JETSET. In the following part, the low- W AGKY–KNO model is

³⁰AGKY: Named after the authors Andreopoulos, Gallagher, Kehayias and Yang.

³¹KNO: Named after the authors Koba, Nielsen and Olesen.

³²PYTHIA 6.4 is a FORTRAN-based code for the generation of complete hadronic final states.

described.

The final state is completely defined by the particle content and the four-momenta of each hadron. The AGKY–KNO model starts by determining the average number of charged particles (charged multiplicity) $\langle n_{ch} \rangle$, assuming a linear dependence on $\ln(W^2)$

$$\langle n_{ch} \rangle = A + B \ln(W^2). \quad (2.121)$$

The parameters A and B depend on the initial state (see Figure 2.37, fit for $W^2 > 4 \text{ GeV}^2$) and are given in Table 2.4. The total hadronic multiplicity is taken to be

$$\langle n_{tot} \rangle = D \langle n_{ch} \rangle, \quad (2.122)$$

with $D = 1.50 \pm 0.05$ for all types of neutrinos and targets³³ [127]. The actual total multiplicity n_{tot} is calculated assuming KNO–scaling for neutrino–nucleon interactions,

$$\langle n \rangle P(n) = f\left(z = \frac{n - \alpha}{\langle n - \alpha \rangle}\right), \quad (2.123)$$

where $P(n)$ is the probability of producing a final state with n hadrons, and, in the case of exact KNO–scaling, $\alpha = 0$. The probability function f is parameterized by a Levy function

$$f(z) = 2e^{-C} \frac{C^{Cz+1}}{\Gamma(Cz+1)}, \quad (2.124)$$

fitted to bubble chamber data (see Figure 2.38). The fit results for the parameter C are also given in Table 2.4. Once the number of final state particles is fixed, the explicit content of the hadronic shower is determined, assuming that it contains exactly one baryon, has no overall strangeness and conserves the electric charge.

The probabilities of obtaining either a proton or a neutron as the final state baryon³⁴ are given in Table 2.3.

³³This value is derived from the experimentally measured fraction $\frac{2\langle\pi^0\rangle}{\langle\pi^+\rangle+\langle\pi^-\rangle} \approx 1$.

³⁴The average probabilities are obtained from rather simple QPM assumptions for valence quark scattering only and by restriction to the lightest two quarks. The target nucleon is split up into a di–quark fragment and the hit quark which changes flavor in CC interactions. The final state baryon is almost always contained in the di–quark–induced jet, and the baryon is assumed to contain one of the two constituents of this di–quark system. The remaining two quarks of the baryon are uu , ud or dd , with identical probabilities. Example: $\nu + p(uud) \rightarrow l^- + X$: The neutrino only interacts with the d –quark, the di–quark is uu . The possible resulting baryon is uuu ($\Delta^{++} \rightarrow$ proton), uud (proton) or udd (neutron). This simple assumption neglects contributions from baryons containing the full di–quark which would further augment the proton probability. Fragmentation models like JETSET/PYTHIA produce about 71 % protons for the given example. This argumentation is less straight–forward for NC interactions, since the neutrinos may couple to all quarks (albeit with different coupling strengths). An approximately equal number of neutrons and protons is expected from the arguments given above.

Table 2.3: Shower charge (including the baryon) and *final state (FS)* baryon selection probabilities for multiplicities > 2 in the AGKY–KNO model. For two–particle final states with a shower charge of +2 (-1), the baryon is always a proton (neutron), to ensure charge conservation, and the proton (neutron) selection probability is shifted from 0.5 to 0.66 (0.33) for a shower charge of +1 and 0.33 (0.66) for a shower charge of 0. In case of hyperon production (see text for details), the corresponding particle and quark content is shown in the right column. The quark content of the hyperons is given by $\Lambda(uds)$, $\Sigma^+(uus)$ and $\Sigma^-(dds)$.

Initial state	Shower charge	FS baryon	FS strange baryon
$\nu_l + p \rightarrow l^- + X$	+2	n (33.33 %)	Λ
		p (66.66 %)	Σ^+
$\nu_l + n \rightarrow l^- + X$	+1	n (50.00 %)	Λ
		p (50.00 %)	Σ^+
$\bar{\nu}_l + p \rightarrow l^+ + X$	0	n (50.00 %)	Σ^-
		p (50.00 %)	Λ
$\bar{\nu}_l + n \rightarrow l^+ + X$	-1	n (66.66 %)	Σ^-
		p (33.33 %)	Λ
$\nu_l + p \rightarrow \nu_l + X$	+1	n (50.00 %)	Λ
		p (50.00 %)	Σ^+
$\nu_l + n \rightarrow \nu_l + X$	0	n (50.00 %)	Λ
		p (50.00 %)	Σ^+
$\bar{\nu}_l + p \rightarrow \bar{\nu}_l + X$	+1	n (50.00 %)	Σ^-
		p (50.00 %)	Λ
$\bar{\nu}_l + n \rightarrow \bar{\nu}_l + X$	0	n (50.00 %)	Σ^-
		p (50.00 %)	Λ

There is also a small probability that the final state baryon contains a strange quark, hence producing a hyperon instead of a neutron or proton (see Table 2.3). This probability, as given by KNO scaling, is parameterized by

$$P_{strange} = A_{strange} + B_{strange} \ln(W^2), \quad (2.125)$$

with $A_{strange} = 0.022$ and $B_{strange} = 0.042$ [123].

The remaining phase space is filled by mesons, starting by balancing the strange content in case of strange baryon production³⁵, then balancing the electric charge by adding single charged pions (π^+ or π^-), and then adding meson–pairs (or a single neutral pion, if otherwise kinematically not possible), with probabilities 31.33 % ($2\pi^0$), 62.66 % (π^+, π^-), 1.5 % (K^0, K^-), 1.5 % (K^+, K^-), 1.5 %

³⁵Note that only $K^+(u\bar{s})$ and $K^0(d\bar{s})$ particles contain anti–strange quarks and can be used to balance the total strangeness, in contrast to $K^-(\bar{u}s)$.

(\bar{K}^0, K^+) and 1.5% (\bar{K}^0, K^0) .

The maximum number of non-baryon final state particles is limited to 18 by the software³⁶, imposing a technical upper limit of about $W_{limit,max} = 3.35$ GeV on the AGKY-KNO model. The AGKY-KNO limit is set to $W_{limit} = 3.0$ GeV within GENIE.

Table 2.4: Parameters used in the AGKY-KNO model for calculating the average charged multiplicity $\langle n_{ch} \rangle$ (see Equation 2.121) and the KNO dispersion (see Equation 2.124), data and uncertainties are taken from [129, 130].

	$\nu+p$	$\nu+n$	$\bar{\nu}+p$	$\bar{\nu}+n$
A	0.40 ± 0.20	-0.20 ± 0.20	0.02 ± 0.20	0.80 ± 0.20
B	1.42 ± 0.05	1.42 ± 0.05	1.28 ± 0.05	0.95 ± 0.05
C	7.93	5.22	5.22	7.93

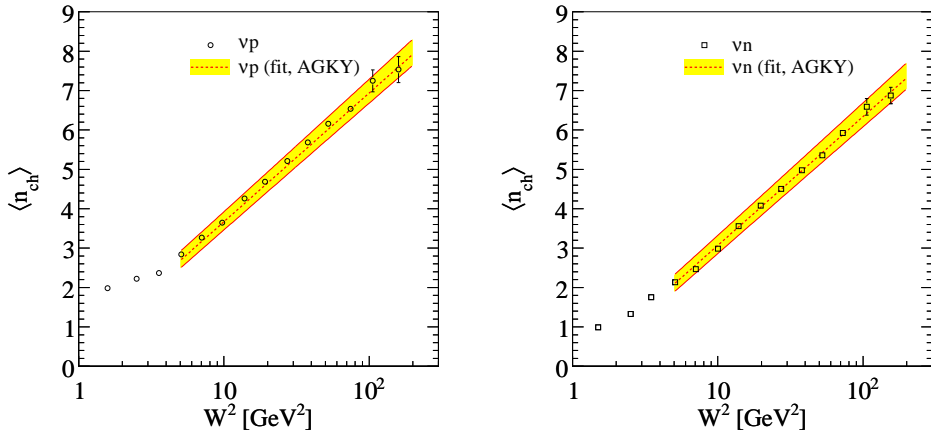


Figure 2.37: Average charged hadron multiplicity (see Equation 2.121), comparison of the parametrization with data. The dashed line is the AGKY-KNO model, the shaded band shows the combined systematic uncertainty from simultaneously varying A and B (see Table 2.4). Data are taken from [129].

Once the hadronic particle content is fixed following the recipe given above, the kinematics of the hadronic final state have to be determined. They are constructed to comply with the properties of the single produced baryon whose direction is preferably the opposite of the transferred momentum $\vec{q} = (0, 0, q)$. The fraction of the total longitudinal momentum is described by the Feynman variable

$$x_F = \frac{p_L^*}{(p_L^*)_{\max}} \approx \frac{2p_z}{W}, \quad (2.126)$$

³⁶The ROOT class TGenPhaseSpace employed here can handle up to 18 particles [128].

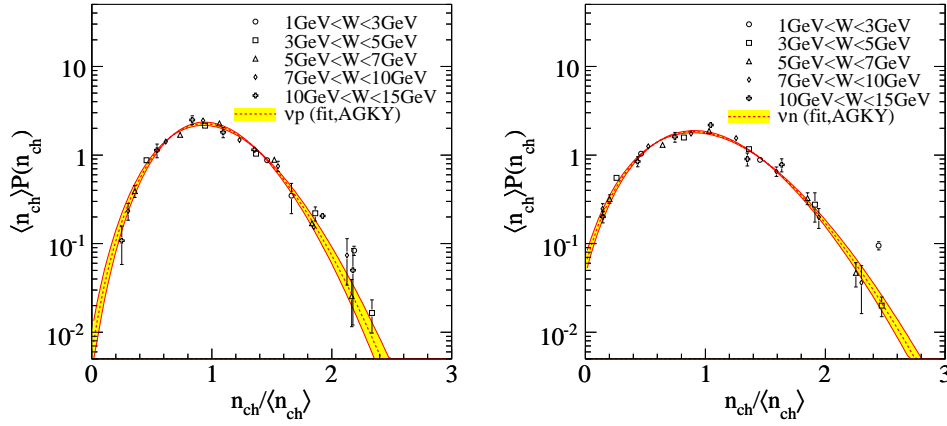


Figure 2.38: KNO-based probability distribution, comparison of the parametrization (see Equation 2.124) with data. The dashed line is the AGKY-KNO model, the shaded band shows the systematic uncertainty gained from varying C by ± 0.7 ($\nu + p$) and ± 0.3 ($\nu + n$). Data are taken from [129] (FNAL).

where p_L^* ($(p_L^*)_{\max}$) are the actual (maximal) longitudinal momentum in the $\nu + \text{target}$ CM frame and p_z is the longitudinal momentum in the lab frame, from a normalized parametrization

$$\frac{1}{N_0} \frac{dN}{dx_F} = 0.083 e^{-0.5(x_F - \langle x_F \rangle)^2 / 0.131} \quad (2.127)$$

of a fit to bubble chamber data (see Figure 2.39), where N_0 is the normalization constant. The transverse momentum of the baryon is sampled from a fit to a normalized p_t^2 distribution (see Figure 2.40) according to

$$\frac{1}{N_0} \frac{dN}{dp_t^2} = e^{-0.214 - \frac{p_t^2}{\langle p_t^2 \rangle}}, \quad (2.128)$$

where p_t is the baryon momentum in the plane transverse to p_L^* and distributed randomly between the p_x and p_y components.

With the four-momentum of the baryon with a mass m_N now determined, the remaining hadronic system is decayed in the phase space $(W - m_N)$, where a p_t -dependent phase space suppression weight

$$w(p_t) = e^{-S\sqrt{p_t^2}} \quad (2.129)$$

with $S = 3.5 \text{ GeV}^{-1}$ is applied in the case of more than one FS meson³⁷ [133].

If the final state contains exactly one meson, this will be produced back-to-back to the baryon in the baryon center-of-mass frame. The whole hadron

³⁷By doing so, the AGKY-KNO model reproduces the so-called “seagull”-dips of the $\langle p_t^2 \rangle$ distributions at $x_F = 0$ quite well [40].

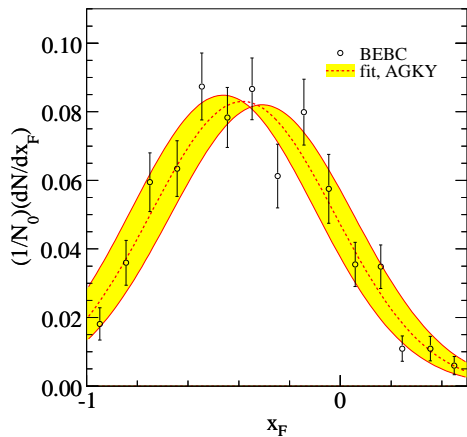


Figure 2.39: Normalized x_F distribution for protons, comparison of the AGKY–KNO model with data. The shaded band indicates the 1σ pseudo–uncertainty band gained by varying the peak x_F by $\pm 20\%$. Data are taken from [131] (BEBC/WA24, $\nu_\mu - p$ scattering).

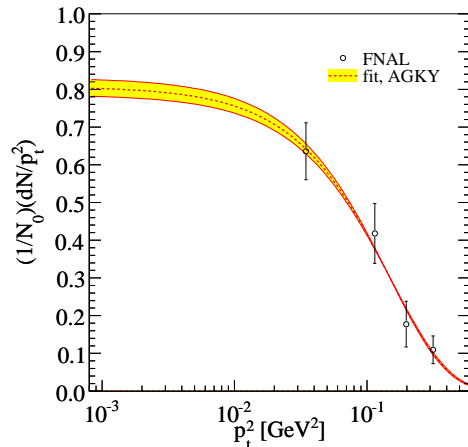


Figure 2.40: Normalized transverse momentum distribution for protons, comparison of the AGKY–KNO model with data. The shaded band indicates the 1σ uncertainty band gained by varying the average $\langle p_t^2 \rangle$ by $\pm 3\%$. Data are taken from [132] (FNAL).

system is boosted and rotated back to the laboratory frame afterwards.

All higher- W events are hadronized by PYTHIA/JETSET, with all but two parameters kept at their default values. The non–default values are changed to the values used in the NUX³⁸–generator [134], tuned to fits to NOMAD data: The average $\langle p_t^2 \rangle$ is changed from 0.36 GeV^2 to 0.44 GeV^2 (PYTHIA parameter PARJ(21)), and the cut–off energy of the fragmentation process is lowered from 0.8 GeV to 0.2 GeV (PARJ(33)). The relative $s\bar{s}$ suppression factor (PARJ(2)) used in NUX and earlier AGKY–KNO versions was 0.21 , while the latest version of the AGKY–KNO model which is applied here uses the default PYTHIA value of 0.30 . Note that neutrino strange production is not very satisfactorily described by either one of these models and also hardly constrained by experiment, especially at low W .

Predictions of the hadronization model are important for many aspects of this analysis. In particular, the event classification and the energy reconstruction depend on the details of the modelled hadronic final state. None of the uncertainties of the hadronization model are allowed to change the total number of events. Thus, they are included as shape–only uncertainties via MC–reweighting. The dominant contributions for energies of interest for OPERA are uncertainties of the peak value of x_F , which is varied by $\pm 20\%$, and of the average value $\langle p_t^2 \rangle$, which is varied by $\pm 3\%$. Details on the hadronization uncertainties are given in [38, 39, 40].

³⁸NUX: Neutrino cross sections, a neutrino event generator.

The existing AGKY–KNO model implements an unphysical correlation in the selection of charged and neutral particles, originating from the determination of an overall multiplicity and later selecting the meson–pairs with fixed probabilities. The aforementioned uncertainties partially account for this shortcoming which will be addressed in future versions of GENIE.

It is difficult to include parameter–based uncertainties into the PYTHIA 6.4/JETSET part of the hadronization model via MC–reweighting. However, the hadronization model for $W \gg 3 \text{ GeV}$ is much better constrained than the low– W AGKY–KNO hadronization. A conservative approach is to extrapolate the overall uncertainties obtained for the AGKY–KNO model to higher mass final states.

2.3 Intranuclear rescattering

All hadrons produced in neutrino–nucleon interactions have to escape the nucleus before they become observable. The relevant process is known as intranuclear rescattering or nuclear reinteractions and can have a large impact on the composition and the kinematics of the outgoing hadron system.

Within GENIE, the transportation of hadrons from their origin at the primary interaction vertex through the inside of the struck nucleus is simulated in two steps, using a hadron transport code named INTRANUKE/hA [135]. After the vertex position inside the nucleus is generated randomly, each hadron takes one step f_z without undergoing any interaction. This so–called “formation zone” is experimentally well established and can be understood as a reduced interaction probability of the quark system before completing the hadronization. In GENIE, the formation zone is modelled by the SKAT³⁹ parametrization [136]

$$f_z = \frac{p_h c \tau_0}{m_h} \quad (2.130)$$

where p_h is hadron momentum, m_h is the hadron mass, c is the speed of light in vacuum and $\tau_0 = 0.342 \text{ fm}/c$ is the formation time determined by experiment. τ_0 is varied by $\pm 50\%$ to account for the rather large experimental uncertainties and the model spread of different formation zone parametrizations⁴⁰ [39, 38].

If this formation zone step f_z does not take the hadron out of the nucleus, the hadron is propagated through the remaining nucleus and may interact with it. The total cross section of the respective hadron is built from the following five

³⁹SKAT: A bubble chamber operated in a neutrino beam at the Serpukhov accelerator.

⁴⁰Reweighting the formation zone is limited by the fact that particles that escaped the nucleus without interaction using the default value of τ_0 , cannot be affected by a tweaked formation time. An additional issue arises from particles with a large non–interaction probability P , that anyhow interacted with the nucleus. These events may receive huge weights due to the rather large systematic uncertainty of τ_0 , which is corrected ad–hoc by leaving all interacting hadrons with a non–interaction probability $P > 0.85$ unweighted. Compare [39] for technical details of intranuclear effect reweighting.

processes: Charge exchange, elastic scattering, inelastic scattering, absorption followed by multi nucleon emission and π production. Both the total cross section and the relative probabilities are different for pions and nucleons. The impact of intranuclear rescattering can be seen when comparing the hadronic state before hadron transportation with the hadronic state after hadron transportation. An example for $\nu_\mu + {}^{208}\text{Pb}$ interactions at $E_\nu = 5$ GeV is shown in Figure 2.41. Based on the uncertainties of external scattering data, uncertainties of both the total interaction probability and the fractional contributions of the different processes are included by tweaking the mean free path by $\pm 20\%$ (total), $\pm 50\%$ (charge exchange), $\pm 10\%$ (pion elastic) and $\pm 30\%$ (nucleon elastic), $\pm 40\%$ (inelastic), $\pm 20\%$ (absorption) and $\pm 20\%$ (π production) for pions and nucleons separately. Elastic scattering is not included as a separate uncertainty but as a cushion term for the other probabilities, to ensure the overall probability of one [38, 39].

$1\pi^+ + 1\pi^-$	0.11	0.00	0.00	0.07	0.00			0.11	0.02	4.01
$1\pi^0 + 1\pi^-$	0.01	0.00		0.00	0.07			0.00	1.08	0.15
$1\pi^0 + 1\pi^+$	0.22	0.95	1.37	0.25	0.16	0.11		6.61	0.04	0.30
$2\pi^-$					0.00		0.00			0.02
$2\pi^+$	0.02	0.00	0.36	0.00	0.00	0.91		0.14	0.00	0.02
$2\pi^0$	0.02	0.00			2.01	0.00		0.22	0.03	0.01
$1\pi^-$	0.03	0.25		3.58	0.02		0.00	0.03	0.32	1.17
$1\pi^+$	0.19	0.33	20.57	0.02	0.02	0.55		1.85	0.00	1.16
$1\pi^0$	0.03	11.96	0.83	0.13	1.15	0.02		1.88	0.32	0.09
0π	20.85	3.96	6.76	1.16	0.18	0.09		0.56	0.10	0.40
	0π	$1\pi^0$	$1\pi^-$	$1\pi^+$	$2\pi^0$	$2\pi^+$	$2\pi^-$	$1\pi^0 + 1\pi^+$	$1\pi^0 + 1\pi^-$	$1\pi^+ + 1\pi^-$

Figure 2.41: Comparison of hadronic final states before (called “initial state” here) and after (called “final state” here) intranuclear rescattering for $\nu_\mu + {}^{208}\text{Pb}$ interactions at $E_\nu = 5$ GeV. Entries are normalized to the total number of 0π , 1π and 2π final states.

Chapter 3

The OPERA experiment

A large number of experiments has been performed within the last decades that have unambiguously verified the disappearance of neutrinos, both in the solar and in the atmospheric sector (see Section 1.3). To complete and establish the picture of neutrino oscillations over other concepts like neutrino decay, decoherence or the oscillation into sterile neutrinos, among other things, a direct measurement of the appearance of the respective neutrino flavor is needed for each possible transition: $\nu_e \leftrightarrow \nu_\mu$, $\nu_\mu \leftrightarrow \nu_\tau$ and $\nu_\tau \leftrightarrow \nu_e$.

The OPERA experiment is designed to search for direct $\nu_\mu \rightarrow \nu_\tau$ appearance [137]. Realized as a long-baseline experiment, it consists of a high-energy pure ν_μ beam which is aimed at a massive detector with very high spatial resolution to observe the final-state τ leptons from ν_τ CC interactions. Neutrino beams in general and the CNGS beam in particular are explained in Section 3.1. The challenging requirements of τ lepton detection demand for a very specialized detector which will be described in Section 3.2. In this chapter, the term “OPERA detector” will be addressing the detector itself, while “OPERA experiment” is going to describe all the components involved, including the CNGS neutrino beam.

The design of the OPERA experiment is constrained by several logistic and physical parameters. The low event rates expected and the resulting need for strong suppression of the background from cosmic muons make an underground location of the detector necessary. Since, during operation, the OPERA detector involves a lot of manpower, easy access for men and material to the laboratory is mandatory. The existing underground and affiliated above-ground infrastructure of the LNGS, equipped with large underground caverns to hold the huge OPERA detector, and the accessibility of the laboratory directly from a highway, satisfies these requirements. At the other end of the beam, the counterpart is CERN, which hosts the only high-energy hadron accelerator in Europe and possesses great experience in the commissioning and operation of neutrino beams, especially with the previous projects at the SPS¹ WANF². With these two locations settled, the flight path of the neutrinos is fixed to

¹SPS: Super Proton Synchrotron.

²WANF: West Area Neutrino Facility.

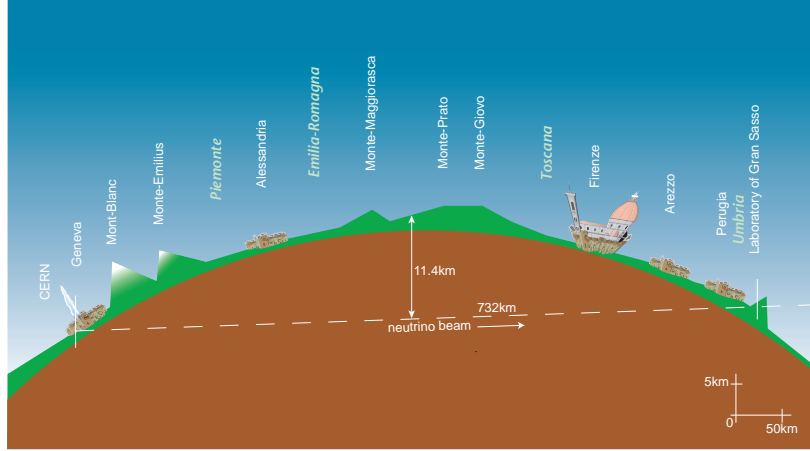


Figure 3.1: Schematic earth profile and neutrino flight path from CERN (left side) to Gran Sasso (right side) (Figure reprinted from [138]).

about 730 km (see Figure 3.1). This kind of experiments are sometimes called “off-peak”, since with an average neutrino energy in the GeV-range, the baseline L/E , with the distance L from the creation of the neutrino to its detection and the neutrino energy E , does not match that of the (first) oscillation maximum.

In a τ -counting ν_τ appearance experiment like OPERA, the value to be maximized is the total number N_τ of observed τ -leptons over background events N_B , with

$$N_\tau \sim M_D \cdot \int_E \Phi_{\nu_\mu}(E) \cdot P(\nu_\mu \rightarrow \nu_\tau, E) \cdot \sigma_{\nu_\tau A, CC}(E) \cdot \epsilon_\tau(E) dE, \quad (3.1)$$

where M_D is the effective detector target mass, $\Phi_{\nu_\mu}(E)$ is the unoscillated ν_μ spectrum at the detector, $P(\nu_\mu \rightarrow \nu_\tau, E)$ is the oscillation probability, $\sigma_{\nu_\tau A, CC}(E)$ is the charged current $\nu_\tau A$ cross section, where A is a target nucleon, and $\epsilon_\tau(E)$ is the total detection efficiency for the τ -lepton.

Two of these impact values are depending on theoretical models and can be analytically optimized with respect to the neutrino energy: At a fixed distance L between source and detector, the oscillation probability $P(\nu_\mu \rightarrow \nu_\tau, E)$ decreases with rising neutrino energy above several GeV. Assuming two-flavor oscillations, $P(\nu_\mu \rightarrow \nu_\tau, E)$ is proportional to $\sin^2(L/E)$ (see Equation 1.30). While the total $\nu_\mu A$ cross section proportionally increases with E for all neutrino energies above several hundred MeV (see Section 2), the large mass of the τ lepton leads to a significantly different behavior of the $\nu_\tau A$ cross section, which rises more than linearly with E , for E below about 100 GeV. The dependency on E^2 of the cross sections for ν_μ and ν_τ CC interactions with neutrons is shown in Figure 3.2 and should be compared with the decreasing oscillation probability proportional to $1/E^2$ if $\Delta m_{23}^2 L/E \ll 1$. For the $\nu_\tau n$ interactions, σ/E^2 shows a maximum around 10 GeV. Since the energy dependence of the

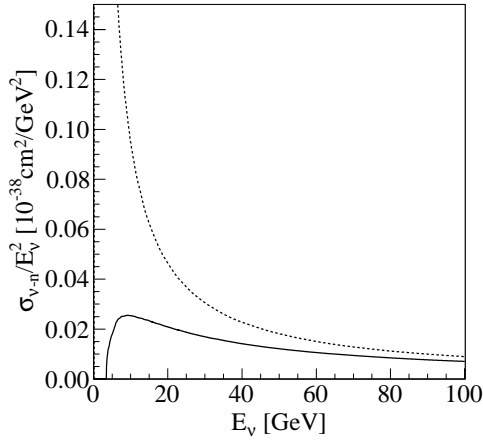


Figure 3.2: $\sigma_{\nu_{\tau n}CC}(E)/E^2$ (solid) and $\sigma_{\nu_{\mu n}CC}(E)/E^2$ (dashed) as functions of the neutrino energy.

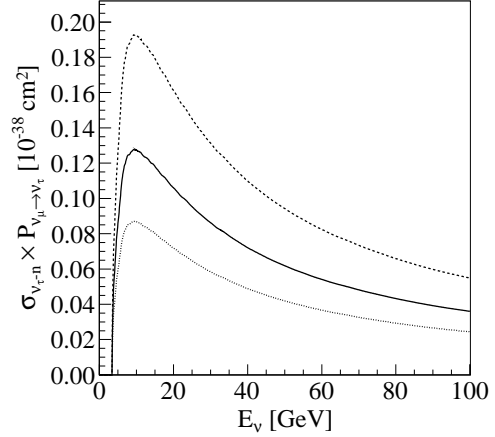


Figure 3.3: $P_{\nu_{\mu} \rightarrow \nu_{\tau}}(E) \times \sigma_{\nu_{\tau n}CC}(E)$ for $\Delta m_{23}^2 = 2.0 \cdot 10^{-3} \text{ eV}^2$ (dotted), $\Delta m_{23}^2 = 2.43 \cdot 10^{-3} \text{ eV}^2$ (solid) and $\Delta m_{23}^2 = 3.0 \cdot 10^{-3} \text{ eV}^2$ (dashed).

ratio $\sigma_{\nu_{\tau n}CC}(E)/\sigma_{\nu_{\tau p}CC}(E) \approx \sigma_{\nu_{\tau n}CC}/\sigma_{\nu_{\tau p}CC}$ is negligible, the position of the maximum value of this product does not depend on the target material.

The product $P_{\nu_{\mu} \rightarrow \nu_{\tau}}(E) \times \sigma_{\nu_{\tau n}CC}(E)$ for different values of Δm_{23}^2 is shown in Figure 3.3, also exhibiting maximum values at about 10 GeV. Fortunately for experiment proposals, the position of this quite sharp maximum does not depend on the actual value of Δm_{23}^2 if $\Delta m_{23}^2 L/E \ll 1$.

The optimal value E_ν strongly depends on the efficiency ϵ_τ , which is a complicated function of the neutrino energy, the detector design and the analysis chain. It has to be determined by Monte Carlo simulations, rather than by analytical calculations. As a rule of thumb, within the range accessible by neutrino beams, ϵ_τ is expected to slowly increase with the neutrino energy.

Due to the different behaviour of $\sigma_{\nu_{\mu A}CC}(E)$ and $\sigma_{\nu_{\tau A}CC}(E)$, it is not possible to optimize a ν_τ appearance experiment also for ν_μ disappearance search. The best energy for a ν_μ disappearance experiment typically lies in the 1–5 GeV range and is thus mostly below the τ production threshold.

The finally realized CNGS beam provides a mean energy of about 18 GeV, which is lower than that of its predecessor neutrino beam at SPS WANF ($\langle E_{\nu_\mu} \rangle \approx 25 \text{ GeV}$) [139], but higher than the ν_μ disappearance search-optimized NuMI³ beam ($\langle E_{\nu_\mu} \rangle \approx 5 \text{ GeV}$ in the low-energy configuration) [140].

³NuMI: Neutrinos at the Main Injector.

3.1 The CNGS neutrino beam

3.1.1 Neutrino beams in general

All accelerator neutrino beams built so far are based on the same principle, going back to Pontecorvo [141] and Schwartz [142] at the end of the 1950s: High-energy protons, in that days around several GeV, are directed onto a massive target. The created secondary particles decay during their flight, resulting in a beam of mainly muon neutrinos and unwanted muons. The latter ones are stopped by massive material before the beam reaches the detector.

For an understanding of the very complex modern neutrino beam facilities, it is useful to get familiar with the fundamental physical properties of neutrino beams, mainly the decay kinematics of the produced secondaries.

The majority of particles emerging from the fixed target struck by protons are charged pions and kaons. Even though positively and negatively charged mesons are produced in very similar fractions, the following discussion focusses on positively charged mesons, without loss of generality. Both pions and kaons predominantly decay into a muon and a muon neutrino

$$\pi^+ \rightarrow \mu^+ + \nu_\mu \quad (\text{branching ratio } (Br) \approx 100 \%), \quad (3.2)$$

$$K^+ \rightarrow \mu^+ + \nu_\mu \quad (Br \approx 63 \%). \quad (3.3)$$

The rest of the kaons decay into one or more charged pions, without the emission of neutrinos ($Br \approx 29 \%$), or via three-body decays into electrons ($Br \approx 5 \%$) or muons ($Br \approx 3 \%$) and an additional π^0 . The general energy dependence of a conventional ν_μ beam is dominated by the two-body decays of pions and kaons, where the pions contribute to the lower part of the ν_μ spectrum, whereas high-energy ν_μ are almost exclusively created in kaon decays. The simplified kinematics of two-body decays are derived in Appendix D, as well as their implications for neutrino beams.

The contamination of a conventional ν_μ beam with neutrinos of wrong sign and wrong flavor⁴ is unavoidable. The main sources of $\bar{\nu}_\mu$ in a ν_μ beam are decays of π^- , K^- and μ^+ , the latter resulting from the previously explained π^+ and K^+ decays (see Equation 3.2 and Equation 3.3). For low energies, the ν_e contamination in a ν_μ beam predominantly originates from μ^+ and, at higher energies, from three-body K^+ decays. Photon-less semi-leptonic decays of K_L^0 are the main source of the $\bar{\nu}_e$ contamination in a ν_μ beam at all neutrino energies, while three-body K^- decays give a significantly smaller contribution. Decays of heavier mesons, mainly D_s , are the main source of ν_τ and $\bar{\nu}_\tau$ in a neutrino beam.

⁴Despite the absence of an electric charge, antineutrinos are considered to be of “wrong sign” if the primary beam is composed of neutrinos, or vice versa. The term “wrong flavor” is used e.g. for all non- ν_μ if a ν_μ beam is desired. In this case, “wrong sign” often means all non- ν_μ .

The maximum energy of the secondary particles itself scales with the incident proton energy, and the number N_π of pions produced per *proton on target (POT)* roughly rises with $E^{0.7}$ [143]. The ratio K/π produced in the target typically amounts to (5–10) %. The actual neutrino energy spectrum of a neutrino beam strongly depends on the treatment of the secondary particles and the layout of the beamline, as will be described in the following.

3.1.1.1 Beam dump beams

The very first accelerator neutrino beam, which led to the discovery of the muon neutrino at BNL [144], was a so-called “beam dump” or “bare target” experiment. This type of experiment reduces the idea of a conventional neutrino beam to its very basics: A proton beam is aimed at a transversely extended solid target, where pions, kaons and other heavier mesons are produced. The contamination with neutrinos of wrong sign and wrong type is high, typically several percent up to several ten percent. This mainly results from the large dimensions of the proton target, which increase not only the overall secondary yield but also the relative contribution of heavy mesons in the secondary beam, due to the high interaction probability of pions and kaons within the target material prior to their decay into neutrinos. The only focusing of the neutrino beam occurs via the Lorentz-boost of the secondaries, requiring short distances of typically less than 100 m between proton target and detector.

The high contamination with other neutrino flavors has very recently been exploited, leading to the discovery of a new kind of neutrino: The DONUT experiment used the high-energy Tevatron⁵ proton beam ($E_p = 800$ GeV), dumped on an expanded (10×10) cm² massive tungsten alloy target to produce a neutrino beam [121]. The resulting beam predominantly contained ν_μ and ν_e but also about 3 % ν_τ , almost exclusively created in the subsequent decays of charmed D_s mesons. Some of these ν_τ have been observed in ν_τ CC interactions in the detector, which was located at a distance of 36 m from the proton target.

3.1.1.2 Wide-band beams

Beam dump experiments are very limited with respect to the total number of neutrinos at the detector site and the contamination of the beam’s main neutrino component with neutrinos of other flavors or signs. A way to optimize both quantities is offered by so-called “wide-band beams”, whose name results from the wide energy range of the produced neutrinos⁶.

⁵The Tevatron accelerator is located at Fermilab near Chicago (USA) and was the highest-energy proton accelerator of the world in the pre-*Large Hadron Collider (LHC)* era, with protons and anti-protons colliding at a center-of-mass energy of 1.96 TeV.

⁶Within this nomenclature, beam dump experiments are also wide-band beams, however they are usually implicitly excluded from wide-band beam discussions.

At the detector site, the neutrino flux is limited by the angular spread of the neutrino beam. For the ideal case of two-body decays, there are two quantities affecting the neutrino flux. The first one is the unavoidable opening angle in pion and kaon decays, which can be estimated by using the “characteristic angle” $\theta'_{\nu,C} = \pi/2$ in the parent rest-frame. In the lab-frame, this angle is given by

$$\theta_{\nu,C} = \frac{1}{\beta_{\pi/K} \cdot \gamma_{\pi/K}} \quad (3.4)$$

$$\approx \frac{1}{\gamma_{\pi/K}} \quad (3.5)$$

if $E_{\pi/K} = p_{\pi/K}$. The second quantity is the transverse momentum of the secondary particles produced in the target, arising mainly from the fermi-motion of the target nucleons, which is of the order of $p_T \approx \hbar c / (1 \text{ fm}) \approx 200 \text{ MeV}$. As the transverse momentum is not subject to Lorentz boost it is expected to remain constant with increasing proton energy, which has also been confirmed by experiment. For 450 GeV protons on carbon, the opening angle of the secondary pion beam can be estimated as

$$\begin{aligned} \theta_{\pi} &= \frac{p_T^{\text{peak}}}{p_L} \\ &\approx \frac{280 \text{ MeV}}{\gamma_{\pi} m_{\pi}} \\ &\approx \frac{2}{\gamma_{\pi}}, \end{aligned} \quad (3.6)$$

with the approximations $E_{\pi} \approx p_{\pi}$, $m_{\pi} \approx 280 \text{ MeV}/2$ and $p_T^{\text{peak}} = 280 \text{ MeV}$ [143]. Inserting the simple approximation $\theta = \theta_{\pi}$ in Equation D.21 will give a flux that is 25 times lower than that of a perfectly focused beam of secondary particles ($\theta = \theta_{\nu,C}$).

The cheapest and technically easiest solution for focussing a fairly wide momenta range of secondary particles is realized by a set of quadrupole magnets following the proton target. Since a single quadrupole magnet will focus a beam of charged particles in one plane perpendicular to the beam axis only and simultaneously defocus it in the other plane, a combination of at least two quadrupole magnets, rotated against each other around the beam axis by $\pi/2$ is needed. To correct aberrations, a third focusing quadrupole magnet, its focal plane being the same as the one of the first quadrupole magnet, is usually added. Quadrupole magnets have a small aperture, limiting their use to high-energy secondary beams, since $\theta_{\nu} \sim 1/\gamma_{\pi/K}$. Arrays of quadrupole magnets will focus both positively and negatively charged particles. To attain extremely low wrong-sign neutrino contaminations (e.g. $\bar{\nu}_{\mu}$) of the beam, the secondary particles are charge-selected prior to the quadrupole focusing. This was done for example in the *sign-selected quadrupole train (SSQT)* by the NUTEV experiment [145].

For focusing lower-energy secondary particle beams of some ten GeV, S. van der Meer proposed the so-called “horns”, able to focus a wide range of

momenta of divergent particle beams [146]⁷.

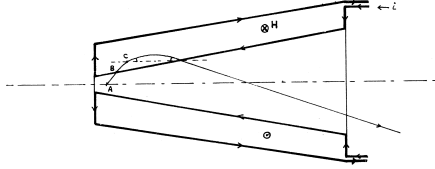


Figure 3.4: Original drawing of a cone-shaped horn. The electrical current is indicated by i , the resulting magnetic field by H (Figure reprinted from [146]).

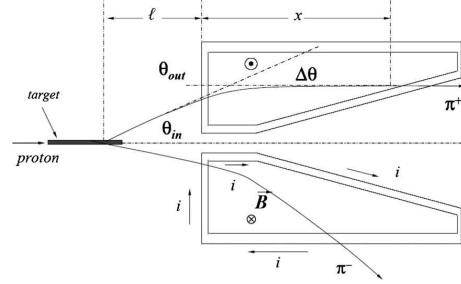


Figure 3.5: Trajectories of charged pions inside a cone-shaped horn (Figure reprinted from [143]).

Horns are designed to be axial symmetric to the secondary beam axis and consist of an inner conductor shell, whose shape determines the horn properties, and an outer conductor shell providing a return path for the electric current (see Figure 3.4). The resulting magnetic field between the inner and the outer conductor is axial symmetric

$$B = \frac{\mu_0 I}{2\pi r}, \quad (3.7)$$

where $\mu_0 = 4\pi \times 10^{-7} \text{ N/A}^2$, I is the electric current and r is the radial distance from the beam axis. The region between the inner conductor shell and the beam axis is field-free. The angular deflection $\Delta\theta$ of the incident particle due to the Lorentz force is given by

$$\Delta\theta = \frac{Bxq}{p}, \quad (3.8)$$

where B is the magnetic field strength, x is the distance traveled in the magnetic field, q is the charge of the particle and p is its incident momentum orthogonal to the magnetic field. The actual shape of a horn has to be optimized by numerical simulation, but simple geometrical considerations yield a good approximation, as will be shown in the following.

The originally proposed cone-shaped horn will focus particles of all given momenta for one angle θ_{in} , where perfect focusing means $\theta_{out} = \theta_{in} - \Delta\theta = 0$. Since $\theta_{in} = \langle p_T \rangle / p$ and $\Delta\theta = Bxq/p \propto x/(pr)$, perfect focusing is obtained for $x \propto r$, i.e. if the distance traveled in the field grows linearly with increasing entry distance from the beam axis, as provided by a cone-shaped geometry (see Figure 3.5).

If the inner conductor is parabolic-shaped ($x \propto r^2$), rather than cone-shaped ($x \propto r$), the horn realizes another special case of focusing: In the limitation that all secondary particles exit the target from one point on the beam axis, the

⁷While quadrupole doublets are working similar to lenses in geometrical optics, the optical analogon of cone-shaped electromagnetic horns is the total reflection on a conical inner surface.

so-called “point-to-parallel-focusing“, the incident angle in the horn is given by $\theta_{in} \approx r/l$, where l describes the distance between the point source and the horn. The condition $\Delta\theta = \theta_{in}$ is fulfilled if $r/l \propto Ix/(rp)$, i.e. if, for fixed l and p , the distance traveled in the magnetic field is $x \propto r^2$. These kinds of horns provide perfect focusing for only one given momentum, but for all possible incident angles. Particles entering at higher momenta will exit under-focused ($\theta_{out} > 0$), while particles with lower momenta will exit over-focused ($\theta_{out} < 0$). Additional horns with larger aperture further downstream the beamline may be used to enhance the overall focusing.

In contrast to quadrupole magnets, horns will defocus particles of opposite charge, and thus do not require charge selection via dipole magnets upstream of the horn to reduce the wrong-sign component of the beam. This permits a position of the horn very close to the proton target to enhance the collection efficiency. As horns require very high electric currents of $I > 100$ kA, their application is limited to short-pulsed proton beams.

It is desirable for most of the secondary particles to decay after focusing and before any re-interactions occur to enhance the neutrino yield. For that reason, the focusing system is usually followed by an extended decay tunnel of up to 1000 m length and with a diameter of up to several meters. To reduce the interaction probability of the secondary particles prior to their decay, this tunnel is usually evacuated or filled with helium at low-pressure.

Downstream of the decay pipe, massive walls of iron or concrete are constructed for stopping any undecayed hadrons. To measure the muon flux and the radial beam displacement, the walls are interspaced with or followed by muon monitors, allowing for online beam monitoring.

3.1.1.3 Narrow-band beams

Some kinds of experiments require a very low number of wrong-signed neutrinos and a better understanding of the neutrino energy spectrum which can be obtained at the expense of a reduced neutrino flux. These “narrow-band beams” get their name from the narrow energy range of the neutrino spectrum at the detector site. There are commonly two different ways to obtain a neutrino energy selection.

By selecting momentum and charge of the secondaries from the proton target with dipole magnets and collimators, an almost monochromatic beam of pions and kaons with a momentum spread of $\Delta p/p \approx 5\text{-}10\%$ can be achieved. For this, thus selected pion or kaon energy, the neutrino energy is given by Equation D.15 and depends only on the neutrino angle θ in the lab frame. If the distance from the meson decay point and the detector is known, the neutrino angle can be obtained by radial position measurement in the detector, without the need for dedicated tracking devices. Equation D.15 has two solutions for any given neutrino angle: One for neutrinos originating from pion decays and

another one for neutrinos from kaon decays. Accordingly, these beams are often called “dichromatic neutrino beams”, as neutrinos of two different energies are produced from a monochromatic beam of secondary particles. By measuring the neutrino angle and the energy deposited in the detector, which, for the same neutrino angle, is higher for neutrinos from kaon decays than for neutrinos from pion decays, the contributions from pions and kaons can be clearly separated and the ambiguity of Equation D.15 is resolved.

The second method involves no rigorous momentum selection of secondaries and goes back to an idea of the E889 experiment [147]. According to Equation D.15, the neutrino energy at any given, nonzero angle θ to the beam axis does not increase linearly with the incident pion energy, as shown in Figure 3.6. For not too small angles, the neutrino energy shows a maximum that moves to lower pion energies with increasing neutrino angle (see Figure 3.7). Since the curve shape in the proximity of the peak is rather flat, pions of a wide energy range result in almost the same neutrino energy, resulting in a narrow-band neutrino beam even for wide-band pion beams.

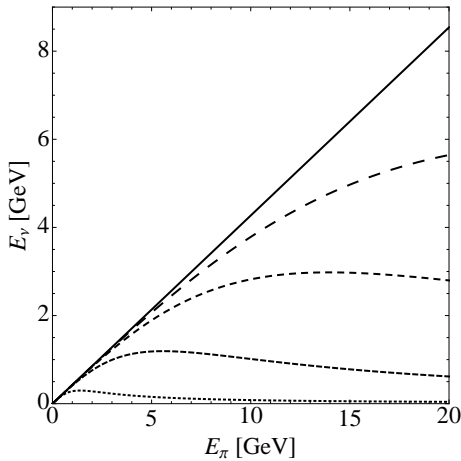


Figure 3.6: Neutrino energy E_ν for different off-axis angles $\theta = 5$ mrad (large dashing), $\theta = 10$ mrad (medium dashing), $\theta = 25$ mrad (small dashing) and $\theta = 100$ mrad (dotted), with respect to the pion energy E_π . The on-axis neutrino energy is also shown (solid).

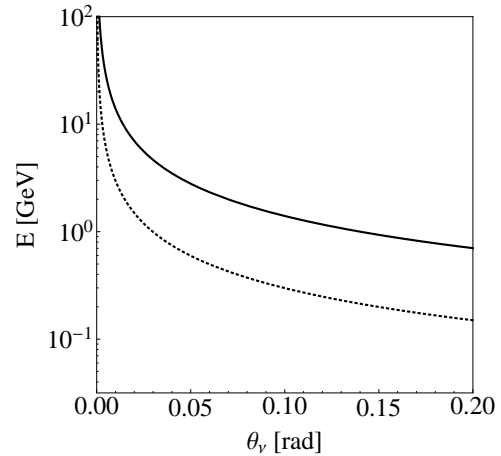


Figure 3.7: Pion energy, corresponding to the maximum neutrino energy (solid) (peak position of E_π in Figure 3.6), and maximum neutrino energy (small dashing) (peak height of E_π in Figure 3.6), both with respect to the off-axis angle θ_ν .

The spectral narrowing of these so-called “off-axis beams” can even lead to a higher flux for specific neutrino energies compared to the on-axis beam spectrum. Furthermore, the high-energy tail of the neutrino spectrum is reduced in off-axis beams. Both these features are convenient for experiments searching for $\nu_\mu \rightarrow \nu_e$ appearance, since the background from π^0 decays, with the π^0 produced in higher-energy NC interactions, and the background from ν_τ CC interactions, where the τ lepton decays into an electron, are reduced for

peak neutrino energies below the τ -lepton production threshold of about 3.5 GeV.

Currently, two off-axis long-baseline neutrino oscillation experiments are under construction or already taking data respectively: NOVA and T2K. The NOVA far detector will be positioned at 14 mrad off the NuMI beam axis, with a baseline of 810 km/ E and a mean neutrino energy of about 2.4 GeV [148], while the MINOS⁸ far detector will continue data taking on-axis. These two large long-baseline detectors are complemented with near detectors for each experiment as well as the MINERVA⁹ detector [149], which are positioned at about 1000 m from the end of the NuMI target. The position of the MiniBooNE detector is also suitable to perform neutrino detection under a very large off-axis angle $\theta \approx 110$ mrad with respect to the NuMI beam axis¹⁰, which is going to improve the knowledge of the kaon contribution to the neutrino beam [150]. The Super Kamiokande detector serves as far detector for the T2K experiment and is positioned 44 mrad off-axis in a 295 km/ E baseline neutrino beam with a mean neutrino energy of about 600 MeV [151], while the near detectors are positioned about 280 m downstream of the target.

3.1.2 CNGS design and layout

The CNGS neutrino beam is characterized as a high-energy conventional neutrino beam. To achieve the required event rates of about ten detected ν_τ CC interactions during the planned five years of data taking (see Section 7), a very high power proton source is required. The SPS accelerator at CERN provides 400 GeV protons, which are fast extracted from the SPS to the CNGS transfer line. The nominal number of protons on target is 4.5×10^{19} per year, at 200 days of running per year. A nominal so-called “CNGS cycle” lasts 6 s and includes two proton extractions on the target, separated by 50 ms, each of them lasting 10.5 μ s. This corresponds to an average beam power of about 0.5 MW. The extracted protons are bent down by about -56.6 mrad by dipole magnets, into the direction of the LNGS in Italy.

The actual creation of the neutrino beam starts when the protons, focused along 120 m by quadrupole and correction magnets, reach the target section of the so-called “secondary CNGS beamline” (see Figure 3.8) [152]. The air-cooled CNGS target consists of 13 consecutively arranged 10 cm long graphite rods, with a diameter of 4 mm and an intervening space of 9 cm to allow pions and kaons to escape the target at small angles θ to the beam axis. To withstand the thermal heat and mechanical shocks generated by the high proton beam intensities, and to increase the containment of the transverse proton beam tails,

⁸MINOS: Main injector neutrino oscillation search.

⁹MINERVA: Main Injector Experiment for ν -A.

¹⁰This detector is also displaced about 35 mrad vertically and, incidentally, placed very close to the NuMI hadron stop, leading to additional neutrinos from secondary interactions in the hadron stop. The detector’s main task is to measure neutrino oscillations at a short baseline in the different Fermilab Booster neutrino beam.

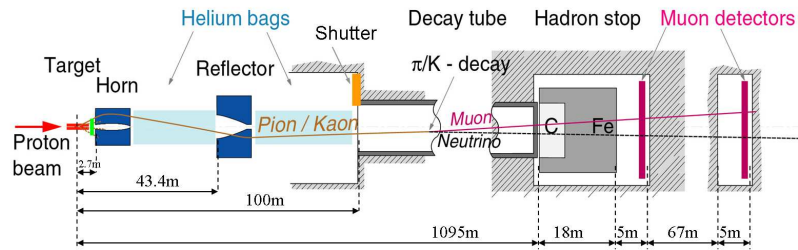


Figure 3.8: Secondary CNGS beamline layout (Figure reprinted from [152]).

the first two target rods have an enlarged diameter¹¹ of 5 mm. To increase the yield of secondaries, the downstream five rods have their distance reduced from 9 cm to 0.2 cm. The total target is about 2 m long with a support structure diameter of about 10 cm. Five similar targets are placed in a revolver and allow for a quick target exchange in case of failure. The proton beam has a spotsize of about $\sigma = 0.5$ mm at the focus point between the third and fourth rod in nominal run conditions. The position and intensity of the proton beam in front of the target is measured by several beam position monitors at various locations along the proton beam pipe. The proton-to-secondary conversion is measured by “secondary emission monitors”, directly downstream of the proton target.

The secondaries are focused by a water-cooled two-horn system, the first horn starting 1.7 m downstream of the target. The opening aperture is about 10 cm, the total length amounts to 7 m. The inner conductor is parabolic-shaped and thus focuses particles regardless of their entry angle, but depending on their momentum (compare Section 3.1.1.2). Since the target is not even approximately point-like for this configuration and the momentum for which perfect focusing is achieved depends on the point of particle creation, most particles end up over- or underfocused. To compensate for this effect, a second horn, called reflector, with a larger aperture of about 50 cm and approximately the same length is added 42 m downstream of the target. This horn/reflector combination effectively focuses particles with momenta between 20 GeV and 50 GeV. The horn and reflector are operated with pulsed currents of about 150 kA. The spaces between the horn and the reflector and between the reflector and the decay pipe are filled with helium to reduce particle interaction and deflection off the beam direction.

The decay tube measures almost 1000 m, with an inner diameter of 2.45 m, and is evacuated to about 1 mbar, the entry window is built of 3 mm titanium. The decay tube is followed by an 18 m thick hadron stop that consists of a water-cooled graphite core and surrounding iron blocks. Muon monitors, the first one positioned directly behind the hadron stop and an additional monitor separated by about 70 m of rock downstream, are used as online neutrino beam

¹¹On the other hand, a larger rod diameter increases the unwanted secondary particle re-interaction probability before their decay into neutrinos.

monitors to measure the position, profile and rate¹² of the tertiary muon beam from pion/kaon decays.

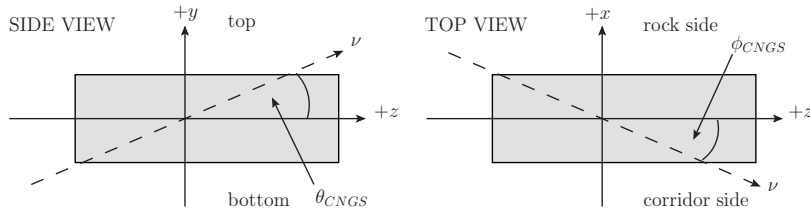


Figure 3.9: OPERA coordinate system (ϕ_{CNGS} and θ_{CNGS} are shown exaggerated here).

The CNGS beam is aligned by GPS¹³ geodesy to reference points in the underground laboratory with a spatial accuracy of about 20 cm. The OPERA GPS coordinate system center is a point called “A1” near the detector center. The OPERA coordinate system is righthanded and cartesian where the $+z$ axis is directed along the neutrino beam axis, the $+y$ axis is pointing upwards and the $+x$ axis is horizontal and pointing from the corridor side to the rock side of LNGS hall C (see Figure 3.9). The distance between the proton target focal point and A1 is 730535 m, whereas the average meson decay point is about 450 m downstream from the proton focal point as determined by MC simulations. The neutrino beam axis is located at $X_{OPERA} = -86.0$ m and $Y_{OPERA} = +2.6$ m, this corresponds to a beam center position in LNGS hall B, about 3 m above ground, which is in excellent agreement with the design beam position (see Figure 3.10). The neutrino beam angles in the OPERA coordinate system are $\theta_{CNGS} = +58.11$ mrad in the YZ-plane, as expected from earth curvature, and $\phi_{CNGS} = -4.48$ mrad in the XZ-plane [153].

¹²The muon intensity is about $10^8/\text{cm}^2/10.5 \mu\text{s}$.

¹³GPS: Global Positioning System.

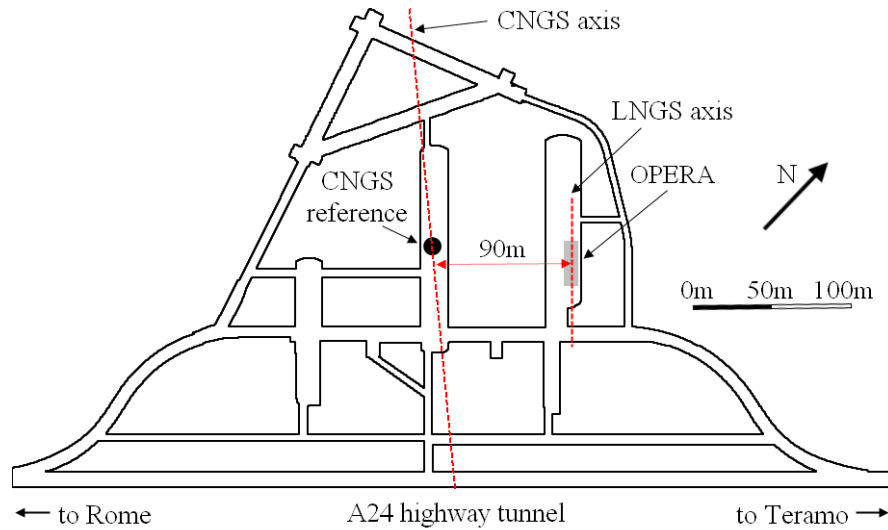


Figure 3.10: LNGS laboratory (schematic, top view), CNGS reference position (black dot), CNGS beam axis (ϕ_{CNGS} is shown exaggerated and with positive sign here), LNGS laboratory axis and the OPERA detector (shaded) in hall C.

3.1.3 CNGS performance

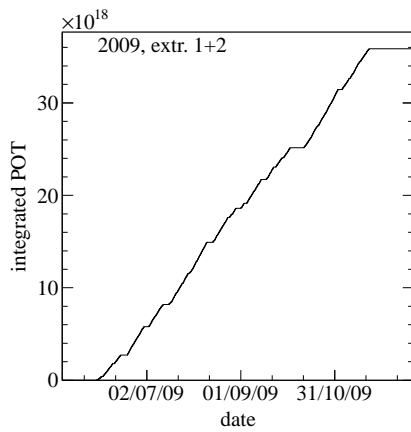
The nominal integrated beam intensity is 4.5×10^{19} POT per year with 2.4×10^{13} POT per extraction. The first neutrinos have been delivered from CERN to Gran Sasso in 2006, the first physics run took place in 2008 with a partially unfilled target section. A total intensity of 1.78×10^{19} POT has been accumulated during the 2008 run. The fully equipped experiment started in 2009 and is expected to run at least until the end of 2012. For the years 2009, 2010 and 2011, the integrated POT are shown in Figure 3.11 and the POT per extraction are shown separately for CNGS extractions one and two in Figure 3.12.

The total integrated POT and the average POT per extraction are summarized in Table 3.1. At the end of the 2011 run, a different extraction mode was chosen in order to perform a dedicated neutrino time-of-flight measurement [154]. The number of average POT per extraction in this so-called “bunched beam” mode was reduced by a factor of 15 to about 0.12×10^{13} POT, the integrated POT during the bunched beam run was reduced by a factor of 60. During the “bunched beam” mode, only the first CNGS extraction was used.

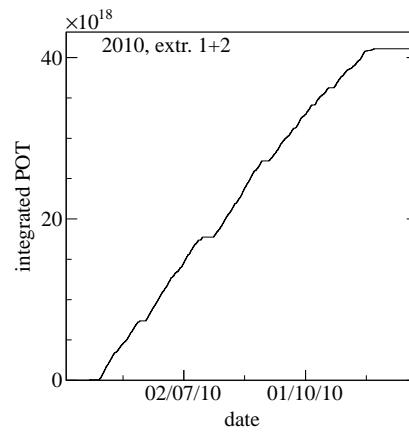
Table 3.1: CNGS performance.

year	integrated POT [10^{19}]			POT per extraction [10^{13}]	
	extr. 1+2	extr. 1	extr. 2	extr. 1	extr. 2
2009	3.59	1.76	1.83	1.94	2.01
2010	4.12	2.04	2.07	1.88	1.96
2011	4.84	2.40	2.43	1.88 ^a	1.91

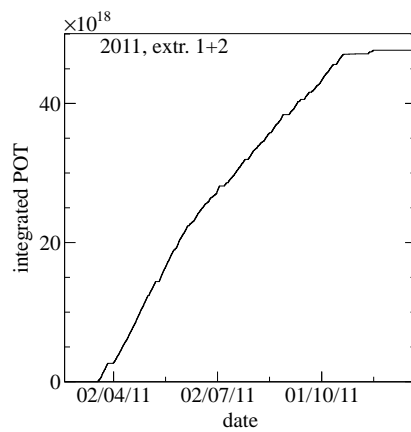
^aWithout bunched beam run, see text for details.



(a) 2009.



(b) 2010.



(c) 2011.

Figure 3.11: Integrated POT over date.

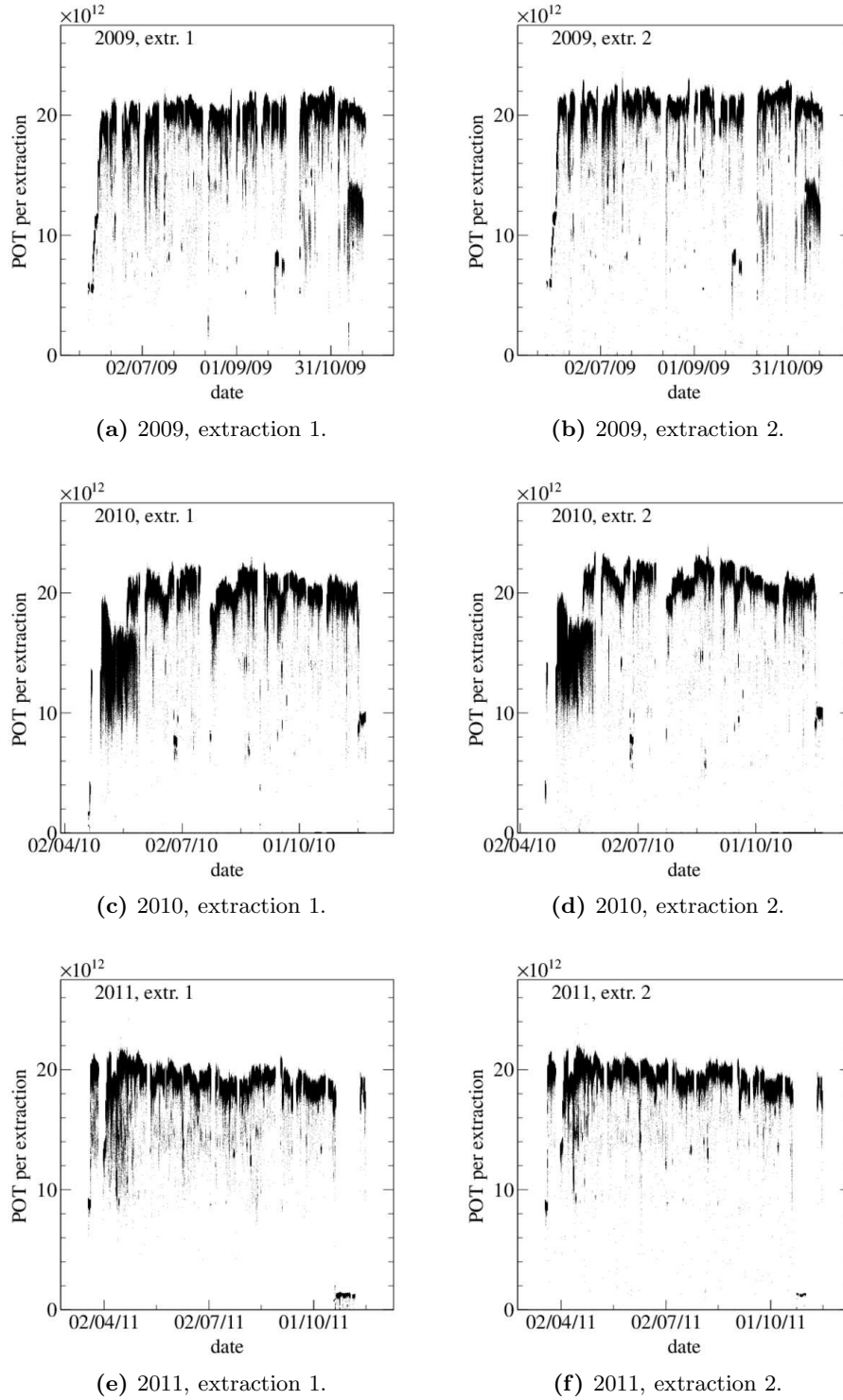


Figure 3.12: Protons on target per extraction over date.

3.2 The OPERA detector

The OPERA experiment has been designed with the goal of detecting charged tau-leptons from neutrino interactions of oscillated neutrinos in a primarily ν_τ -free beam on an event-by-event basis. The short decay length of a τ lepton in the order of millimeters and the very low neutrino cross sections require both a spatial resolution in the μm range and a target mass of the order of kilotons. The only available technique that combines both requirements is a passive photo emulsion/lead sandwich structure that has already been successfully applied to the first detection of the ν_τ in DONUT [121] and in the oscillation experiment CHORUS¹⁴ [155]. “Passive”, in this context, refers to the non-electronical readout of the photo emulsions: These have to be extracted and developed manually, similar to a classical photographic film. The actual reconstruction of the decay kinematics is based on partially automatized CCD¹⁵ camera scans of the developed emulsions.

A crucial part of the OPERA experiment is the scanning speed, which has been significantly increased by several orders of magnitude compared to previous emulsion experiments, making possible the upscaling to more than $100\,000\text{ m}^2$ of emulsion in total. Nevertheless, a preselection of the neutrino events and a prediction of the expected vertex position is mandatory and cannot be performed by the passive emulsions. Therefore, OPERA is realized as a so-called “hybrid detector”, combining the non-electronic offline detection principle of photo emulsions with real-time electronic tracking devices and magnetic spectrometers to measure the charge and momentum of particles.

The OPERA detector is built from two nearly identical *super modules* (*SM1* and *SM2*) that are explained in detail below (see Figure 3.13). Each of them consists of a photo emulsion/lead target section which is interleaved with plastic scintillators (called the *target trackers* (*TT*)). Each target section is followed downstream by a muon spectrometer that contains a large dipole magnet and tracking detectors based on drift tubes (called the *precision tracker* (*PT*)), *resistive plate chambers* (*RPCs*) and *crossed resistive plate chambers* (*XPCs*). An RPC veto upstream of SM1 is used to reject tracks from neutrino interactions taking place in front of the detector.

The OPERA detector measures about $(20 \times 10 \times 10)\text{ m}^3$ and weighs about 4000 t, including support structures. It is built in the southern part of hall C of the LNGS underground laboratory, next to the BOREXINO¹⁶ detector. The maximal vertical rock overburden of the laboratory measures about 1400 m with an average density of 2.71 g/cm^3 (see Section 4.5.2), which corresponds to about 3800 m water equivalent. The total rate of cosmic muons is reduced by a factor of about 10^6 compared to the integrated surface rate.

¹⁴CHORUS: CERN Hybrid Oscillation Research Apparatus.

¹⁵CCD: Charge-Coupled Device.

¹⁶BOREXINO: Boron Experiment.

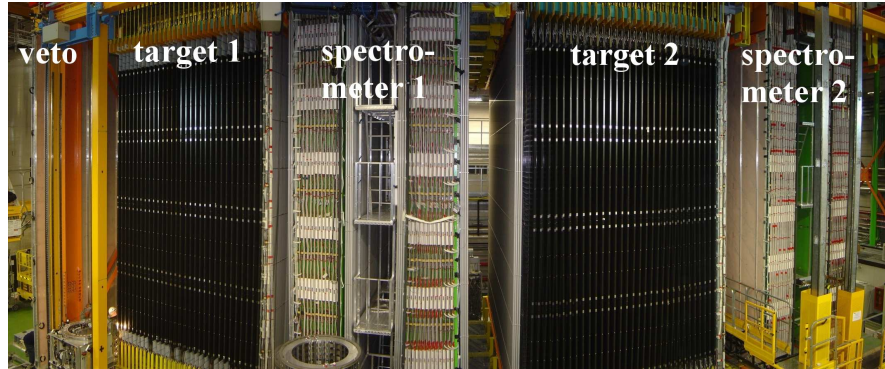


Figure 3.13: Photograph of the OPERA detector, CNGS neutrinos arriving from the left.

3.2.1 Target

The OPERA target is a structure of lead, acting as passive high-density target material, and photo emulsions to detect charged particles originating from the neutrino interactions¹⁷. These two materials are combined to the so-called *emulsion cloud chambers (ECC)* bricks, where 56 lead plates of 1 mm thickness are interleaved with emulsion films: 205 μm thin plastic bases that are coated with 45 μm of photo emulsion on each side. One such double layer emulsion film is added before the first and behind the last lead plate, amounting to a total number of 57 emulsion films per brick. The total sandwich structure is vacuum-sealed and wrapped light-tight in aluminum foil. An additional *changeable sheet doublet (CSd)*, consisting of two tightly packed emulsion films (i.e. four emulsion layers) without an interleaving lead plate, is attached downstream of each brick in a separate plastic box. One ECC brick measures $(128 \times 102 \times 79) \text{ mm}^3$ and weighs 8.3 kg in total (see Figure 3.14).

The emulsion films have been produced in Japan, in collaboration with Fuji-Film, in above-ground industrial facilities. Unfortunately, the photo emulsions begin to record events directly after their fabrication, integrating tracks until the final development. However, if the primary ionization was not too dense, recorded tracks will be erased after some time when the latent images have disappeared again. In a process called “refreshing”, this can be accelerated by high temperature (about 30° C) and high humidity (above 90 %) to take merely several days. This refreshing is done in the Tono mine in Japan about 100 m underground,

¹⁷The OPERA photo emulsions basically consist of silver bromide crystals (about 0.2 μm diameter), embedded in gelatin, with each silver ion Ag^+ surrounded by six bromide ions Br^- , and vice versa. Some silver ions remain unlocalized on interstitial positions in the lattice and can recombine to atomic silver with electrons freed by ionization processes. Together, several silver atoms will form a long-term stable “latent image”. In the presence of a chemical agent, called the “developer”, acting as electron donor, each silver bromide crystal that contains a sufficient number of silver atoms is completely reduced to metallic silver, forming larger grains with a diameter of about 0.6 μm .

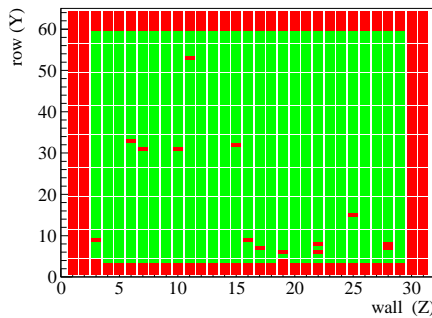


Figure 3.14: Photograph of a partially opened OPERA ECC brick. The detached CSD, separately packed in aluminum, is visible on the right side in the opened white plastic box.

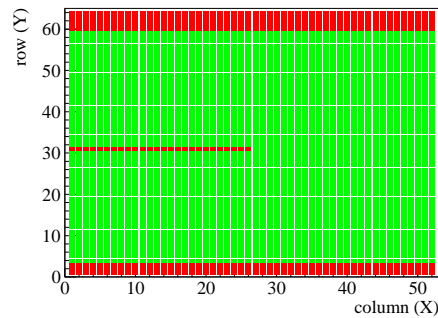


Figure 3.15: Photograph of the empty OPERA brick support structure (side view).

directly before the transportation to Italy by ship¹⁸. After their arrival, the emulsions are stored at low temperature underground at the LNGS to reduce the so-called “fog” from thermal excitation¹⁹. Here, the ECC bricks are assembled in an automatized production line, called the *brick assembly machine (BAM)*.



(a) SM1, column 15 (side view), neutrino flight direction from left to right.



(b) SM1, wall 10 (front view), neutrino flight direction is perpendicular to the projection plane (ingoing).

Figure 3.16: Brick status on 29-06-2009, a green box indicates a present brick, a red box an empty position.

The ECC bricks are arranged in a grid-like structure of 31 walls (front to back) per super module, with 64 rows (bottom to top) and 52 columns (left to right) each, capable of holding a maximum of 103168 bricks per super module

¹⁸Due to the highly ionizing hadronic component of cosmic rays, transportation by plane is not possible.

¹⁹This effect is a continuous, random background of isolated latent images that reduces the track finding efficiency.

(see Figure 3.15). Due to funding difficulties, the OPERA target mass has been reduced by about 25 % compared to the numbers given in the proposal. The maximum total brick count (both super modules) ever reached was 148828, in the evening of 29-06-2009. This number corresponds to a peak target mass (including the emulsion films) of 1235 t. The bricks have been distributed compactly, maximizing the brick finding efficiency²⁰ (see Section 3.2.6) and avoiding an asymmetric load on the brick support structure (see Figure 3.16a and Figure 3.16b). Brick filling into the target section, as well as the extraction of interesting bricks is performed by two robots, one on each side of the detector, constituting the so-called *brick manipulation system (BMS)*. The main filling process of both OPERA super modules was completed in July 2008. However, several thousand bricks of SM1 had been equipped with CSds not fulfilling the required low fog level for the CSd emulsions. These were extracted and reinserted with an exchanged CSd during the CNGS shutdown phase of winter/spring 2009. The total number of bricks during 2008 and 2009 is shown in Figure 3.17.

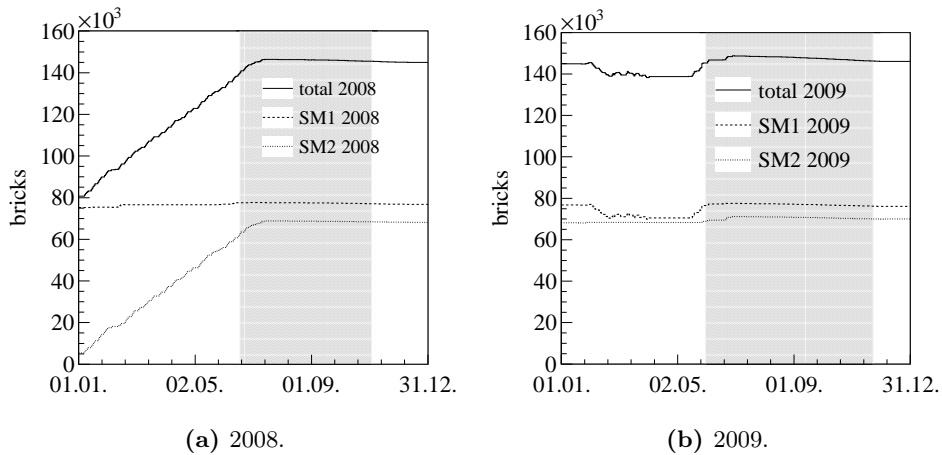


Figure 3.17: Total number of bricks in the OPERA detector (solid), bricks in SM1 (dashed) and bricks in SM2 (dotted), according to the BMS database dumpfiles. The duration of the official 2008 and 2009 run is shaded in gray.

It is not intended to replace extracted and developed bricks with new ones. During the 2009 run, the OPERA target mass has been reduced by about 17 bricks per day on average²¹. To avoid an asymmetric load of the brick support structure, the bricks are rearranged and all rows are filled up again by other bricks rejected from CSd scanning (see Section 3.2.6). If this is not sufficient to fill up all incomplete rows, one brick row from the outermost target region will be

²⁰The outer regions of the target sections are generally less efficient: The last walls of a SM have a lower brick finding efficiency due to the reduced number of subsequent electronic trackers, while the first walls of a SM have a higher contamination of events with vertices that are not contained in the bricks. Due to the slight tilt of the neutrino beam towards the upward direction, it is preferable to fill the detector with a slight bottom-top asymmetry, leaving more top rows empty than bottom rows.

²¹This takes already into account the reinsertion of rejected candidate bricks after CSd scanning.

completely extracted and redistributed among the rows that are not entirely filled.

The position and status including the possible extraction, storage, development and scanning of every brick is saved in a database and known at any time.

3.2.2 Target tracker

The passive brick walls of the OPERA target section are interspaced with plastic scintillators [156]. These consist of 686 cm long, 10.6 mm thick and 26.3 mm wide polystyrene scintillator strips²² that are arranged in planes of 4×64 strips each. Two orthogonally aligned TT planes form one TT wall. Each strip is coated with TiO_2 to enhance light collection and contains a *wavelength-shifting (WLS)* fiber that is read out on both sides by a 64-channel Hamamatsu H7546 photomultiplier.

The TT is mainly used for the localization of neutrino interaction candidate ECC bricks. In addition, it serves as an overall DAQ²³ trigger (see Section 3.2.5). The single-plane trigger efficiency for beam events is greater than 98 % (97 %) for the horizontal (vertical) TT planes [157]²⁴. Each signal in a horizontal (vertical) TT plane corresponds to a YZ (XZ) coordinate, with a single-plane spatial resolution given by the thickness (Z) and width of the strip (X/Y).

Using the number of photoelectrons detected, the energy deposition in the strips can be calculated. In combination with the photo emulsion/lead target walls, the TT thus works as a hadronic calorimeter.

3.2.3 Spectrometer

Each target section is followed by a muon spectrometer. The main component is a large dipole magnet with two magnet arms, perpendicular to the Z axis, that are interspaced with RPC trackers. PTs are positioned before, between and behind the dipole magnet arms, allowing a precise measurement of a particle's charge and momentum. A schematic overview of one OPERA spectrometer is shown in Figure 3.18. A photograph of the spectrometer of SM 1 is shown in Figure 3.19.

3.2.3.1 Dipole magnet

The two arms of the dipole magnet are connected by bottom and top return flux yokes. Each arm consists of 12 steel slabs of 5 cm thickness which are interspaced by 2 cm of air [158] (see Figure 3.20). The magnetized arms cover a surface of (875×820) cm², perpendicular to the Z axis. The steel components, including the return yokes, of one magnet weigh 990 t in total. The magnet is operated at a nominal current of 1600 A. The resulting average nominal magnetic field is

²²p-Terphenyl (2 %) and POPOP (0.02 %) are used as primary and secondary fluor.

²³DAQ: Data acquisition.

²⁴This difference is caused by the effects of dead material between the scintillator strips

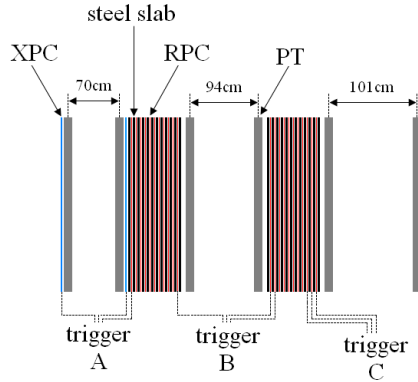


Figure 3.18: Schematic drawing of the OPERA spectrometer of SM1 (side view), including XPCs, RPCs and PTs. The PT trigger stations are labeled A, B and C (D, E and F) in SM1 (SM2).



Figure 3.19: Photograph of the OPERA spectrometer of SM 1. The first target section is visible on the left.

1.53 T. The nominal field polarization²⁵ is pointing up in the first magnet arm and pointing down in the second magnet arm, such that a negatively charged particle flying parallel to the Z axis in beam direction and crossing the first magnet arm will be deflected horizontally to the left (positive X direction).

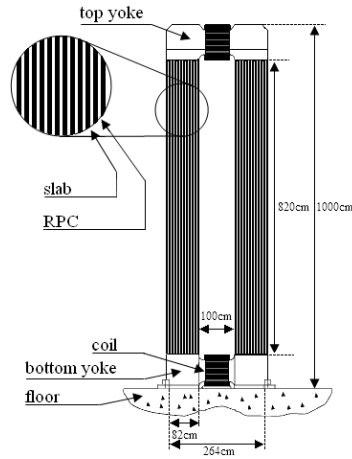


Figure 3.20: Schematic drawing of an OPERA magnet (side view), with the CNGS neutrinos arriving from the left.

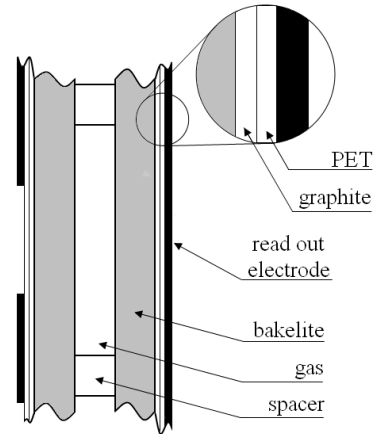


Figure 3.21: Schematic drawing of an OPERA RPC (side view).

3.2.3.2 RPC and XPC

A plane of RPCs is mounted in every air gap between two steel slabs of the magnet, making the RPCs lined up precisely with the magnet dimensions. Every

²⁵This nominal polarization is called “normal” within the OPERA software and publications, while the opposite orientation is called “inverted”.

RPC plane is constructed from 21 RPC modules, with a size of (291×113.4) cm² (width \times height) each. The geometrical acceptance is reduced by about (2-3) % due to steel bolts with a diameter of about 8 cm that hold the magnet slabs at distance. The OPERA RPC modules are made of two 2 mm bakelite plates, arranged parallel to each other at a fixed distance of 2 mm (see Figure 3.21). The remaining distance to the steel slabs is filled with low-density polyester fiber foam. The space between the two bakelite plates is floated with an Ar/C₂H₂F₄/iso-C₄H₁₀/SF₆ (75.4/20.0/4.0/0.6) gas mixture at atmospheric pressure²⁶, with three complete volume exchanges per day. It is operated at a nominal high voltage²⁷ of 5.7 kV, symmetrically split between anode and cathode. The inner sides of the bakelite plates are coated with a thin (several μ m) layer of polymerized linsseed oil to compensate for small surface irregularities, the outer surface is painted with graphite, both serving as high-voltage electrodes. The pick-up electronics are separated by a *polyethylene terephthalate* (PET) insulation painting²⁸ from the graphite electrodes. Copper read-out electrodes are arranged horizontally with a 3.5 cm pitch (870 cm long), and vertically, with a 2.6 cm pitch (800 cm long), one set of strips on each RPC side. The smaller pitch of the vertically-oriented strips provides a better spatial resolution in the horizontal bending plane of the magnet than in the vertical one.

The basic principle of RPCs is similar for all gas amplification detectors: Charged particles passing through gas will ionize atoms and molecules. The primary electrons from these interactions are accelerated along the applied electric field, themselves ionizing further atoms, which leads to an electron avalanche and an amplification²⁹ of the primarily generated electrons, typically by a factor of $10^4 - 10^6$. The expected low event rates of less than 20 Hz/m² per RPC plane make it possible to safely operate them in the “streamer mode”, where the electric field is high enough to induce a permanent discharge between the bakelite plates. The electric signals induced in streamer mode are large (about 100 mV) and do not require additional electronic amplification. The high volume resistivity of more than 10^{11} Ω cm of bakelite locally decreases the electric field in a spot of several millimeters spread, due to the accumulated charge, which stops the streamer. RPCs are cost-effective detectors that provide a good time resolution of several nanoseconds and can be operated safely, even within moderate magnetic fields. The charge induced by passing particles is usually shared among several electrode strips. Neglecting cross talk and electromagnetic showers, this so-called “cluster size” increases logarithmically with the particle energy for tracks perpendicular to the strip orientation. During the 2009 run, an average cluster size of $N_C \approx 1.7$ ($N_C \approx 2.8$) per RPC plane for horizontal

²⁶The underground halls are kept at a slight overpressure, with respect to the highway tunnel at about 900–920 mbar absolute.

²⁷The high voltage at the beginning of the 2008 run had been 5.8 kV. The readout thresholds have been adjusted accordingly.

²⁸Most RPCs have been equipped with an additional PET foil insulation, after the primary PET coating had proven to be insufficient and inducing too much noise on the pick-up electronics.

²⁹The amplification mainly depends on the gas density, gas mixture, electric field strength and the geometry of the detector.

(vertical) strips has been measured for beam events [159].

Each super module is equipped with two XPC planes, in addition to the “inner tracker“ RPCs. Both planes are positioned close to the first PT doublet, the first one is placed 1 cm upstream of the first PT wall, while the second one is placed 1 cm downstream of the second PT wall. The size of the first XPC plane is (806×750) cm², constrained by the dimensions of the OPERA target. The second XPC plane, with a size of (806×873) cm², covers the full magnet surface. The XPCs are technically almost identical to the already described RPCs. The main difference is the orientation of the read-out strips that are rotated with respect to the horizontal by 42.6 degrees.

The main task of the RPCs is the tracking of particles inside the magnet volumes, while the XPCs improve the track merging and reduce the number of ghost tracks by disentangling ambiguities in the XY plane. Per spectrometer, three groups of three XPC and RPC planes each are also used as trigger stations for the PT in a nominal 2-of-3 coincidence (see Figure 3.18) [160]. The trigger signal for all PTs of one spectrometer is generated by an OR signal of all three individual trigger station outputs (called “overall trigger“). The overall PT trigger rate per SM is below 10 Hz for the nominal RPC/XPC thresholds, while the single-plane RPC/XPC trigger rate is several hundred up to several thousand Hz.

3.2.3.3 Precision Tracker

The PT consists of about 10 000 aluminum drift tubes with an outer diameter of 38 mm and a wall thickness of 0.85 mm, a gold-coated tungsten sense wire with a diameter of 45 μ m and a length of about 8 m. The drift tubes are oriented vertically, hence almost perpendicular to the beam axis, and constructed without additional wire support. 48 tubes are combined to form a so-called PT module, arranged in four staggered layers of 12 tubes each (see Figure 3.22a and Figure 3.22b). This layout provides maximal track efficiency and a large geometrical angular acceptance for beam-induced events (mainly forward-going) but also cosmic muons (mainly downgoing). All PT walls that are not directly preceded or followed by a target section are made of 17 modules, while the others are reduced by one module on each side. The PT is filled with an Ar/CO₂ (80/20) gas mixture at 1005 ± 5 mbar absolute pressure that is replaced once every three days [161]. To minimize the number of gas connectors, all tubes of one module at both ends of the drift tubes are interconnected in row by milled channels in the support end plates. Commercial oxygen monitoring devices are used to monitor the gas quality. The PT is operated at 2.45 kV high voltage and equipped with L3 preamplifiers. Signal generation in the drift gas is similar to the RPCs, but the PTs are operated in proportional mode which prevents streamer discharges. The drift time is measured by custom-made temperature- and voltage-compensating *time-to-digital converters (TDCs)*. The maximum drift time is about 1.6 μ s, where the TDC stop is generated by the RPC/XPC trigger stations.

The main task of the PT is the reconstruction of the charge and the momentum of particles passing the dipole magnet. The single-tube spatial resolution is better than $600 \mu\text{m}$ including geometrical misalignment. The momentum resolution $\Delta p/p$ for beam events is about $(20 - 25) \%$ for muon energies up to 30 GeV .

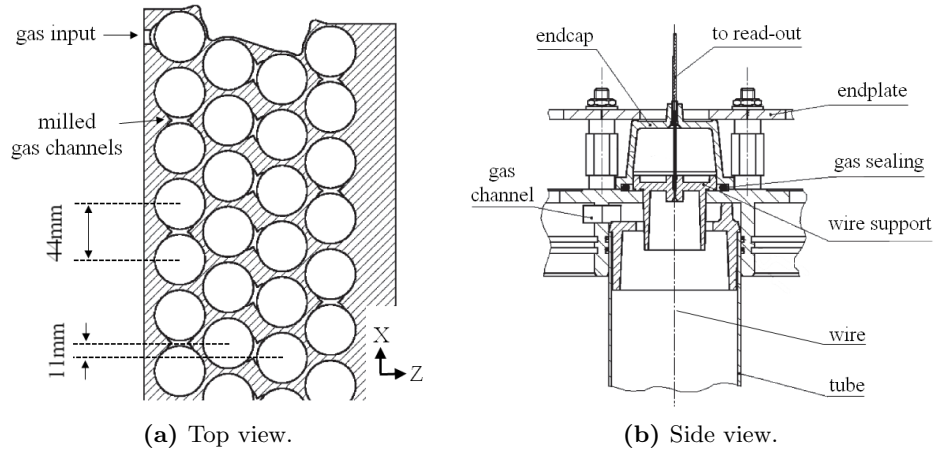


Figure 3.22: Schematic drawing of a PT module.

3.2.4 Veto

An additional veto system is installed upstream of the first SM to reject events with a primary vertex located in front of the detector. It is built of two planes of glass RPCs where the high-resistive plates are made of glass, instead of bakelite. Each plane covers an area of about $(1,000 \times 912) \text{ cm}^2$ (width \times height) and is read out by 2.5 cm -pitch electrodes for both horizontally and vertically oriented strips.

3.2.5 DAQ and overall event trigger

The OPERA DAQ is divided into 1,184 so-called "smart sensors", the overall number of electronic channels is about 105,000. Each sensor serves as an independent node in a 100 MBit ethernet network and is synchronized with a global GPS time signal via a dedicated clock line. The smallest unit of the OPERA DAQ is a sensor that acts as an interface between the customized sub-detector readout boards (TDCs for PTs and ADCs³⁰ for RPCs/XPCs/Veto and TTs) and the global DAQ. The number of electronic channels associated with a sensor depends on the sub-detector type.

A TT sensor is logically mapped to 64 scintillator strips, each TT plane is thus read out by eight sensors, four per plane and side (992 in total). Each RPC sensor is mapped to one complete RPC wall (44 in total), while each XPC is served by two sensors (8 in total). Two PT modules are mapped onto one sensor (108 in total), with nine sensors reserved per PT plane. Since the total

³⁰ADC: Analog to digital converter.

number of PT modules per wall is odd, the last module of each PT wall is singly connected to one sensor. For PT walls with 15 modules only, there is one sensor that is not mapped to any PT modules. Several RPC/XPC channels used as PT trigger inputs are also connected to *timing boards (TB)* that are read out by spare PT TDCs and mapped to the otherwise empty sensors. The Veto is read out by 16 sensors per plane (32 in total). None of the sensors of any sub-detector is connected to readout channels of different planes/walls.

All OPERA sensors are read out asynchronously and timestamped with a 10 ns clock signal. Both the TT and the RPC/XPC sub-detector readout boards are self-triggered: They provide a trigger output signal to the sensor if a logic OR-signal from all strips connected to one TT PMT or an OR-signal from all strips of an RPC/XPC plane is above a set threshold ("L0 trigger"). As described above, the PT receives an external RPC/XPC trigger signal, where no signal filtering is performed on-board.

Sensor information is grouped into one event until no further hits arrive within a 500 ns window³¹. To reduce detector noise, a minimum bias filter is applied that selects events with at least ten hits and that have

- TT hits in at least two adjacent TT planes (i.e. in the two orthogonally oriented planes that form a TT wall), or
- at least one TT plane (horizontal or vertical) with a combined ADC count³² in the left and right *photomultiplier tubes (PMTs)* of above 1500, or
- a three-of-all majority of all RPC/XPC planes in either the horizontal (U for XPC) or the vertical (V for XPC) projection.

3.2.6 Brick extraction and analysis chain

In order to minimize the load of the photo emulsion scanning stations, a multi-step procedure using the electronic detector data is applied to each event before a candidate brick is extracted and additional cross-checks are done before the respective extracted brick is finally scanned, demonstrating the full potential of a hybrid detector like OPERA.

All events that have passed the global DAQ trigger and that are in coincidence with the CNGS extraction (see Section 6.1) are reconstructed within the electronic detectors. All events with a reconstructed vertex in the target section, are searched by an algorithm that predicts a weighted list of the bricks most probable to contain the respective neutrino vertex.

³¹Since drifttube hits are delayed in time, an offset of 1,800 ns is subtracted from PT hits before this operation and added again afterwards.

³²This value has been lowered in 2010 to 500 to increase the trigger efficiency for QEL ν_τ interactions. The original value of 1500 is re-applied to data and MC within this analysis thought.

The most probable brick is extracted by the BMS, and the CSd is aligned to the ECC brick by applying four $100\ \mu\text{m}$ wide frontal x-ray marks. The CSd is then detached from the ECC brick and developed. Both the x-ray marking and the CSd development are performed underground. The remaining undeveloped CSd-less ECC brick also stays underground, inside an additionally shielded area.



Figure 3.23: Photograph of a European photo emulsion scanning station.

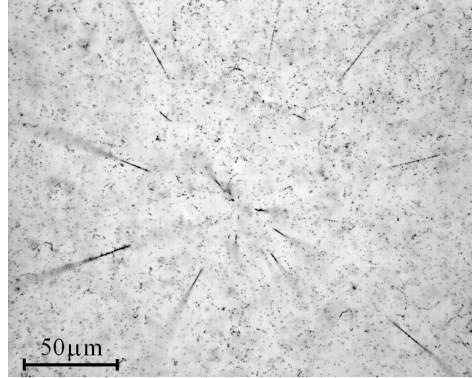


Figure 3.24: Scanned photo emulsion, where the thick black tracks are from nucleon remnants flying almost parallel to the emulsion layer. Charged particles from the primary neutrino interaction are expected to propagate perpendicular to the emulsion layer and in this view are thus only visible as black dots.

The developed CSds are then scanned in 16 different focal depths by optical CCD-based microscopes, at above-ground facilities at LNGS (Italy) or Nagoya (Japan) (see Figure 3.23). The average emulsion area to be scanned for each CSd is about $35\ \text{cm}^2$ for CC events and $160\ \text{cm}^2$ for NC events. In case of a negative CSd scanning result, the ECC brick is equipped with a new CSd and reinserted into the detector (see Section 3.2.1). If at least one track predicted by the electronic detector is found in the CSd, the corresponding ECC brick is taken to the surface and exposed to cosmic ray muons for several hours in the cosmic ray pit³³, providing inter-emulsion alignment. Additional lateral x-ray marks are also applied to the brick sides to allow an unambiguous identification of each emulsion position and its orientation inside the brick. Afterwards, the brick is unpacked and developed in a partially automatized development line at LNGS before it is sent to one of the several scanning laboratories in Europe or Japan. A photograph of a scanned emulsion is shown in Figure 3.24.

During the scanning, three-dimensional "microtracks", consisting of a straight sequence of grain clusters within one emulsion layer, are reconstructed online. If two corresponding microtracks are found in the adjacent emulsions of one plastic base and can be interconnected, these are forming a "basetrack". Each

³³The cosmic ray pit is a shaft of several meters depth, reducing the non-vertical muon flux. The bricks to be developed are positioned on the floor of this shaft.

track predicted by the electronic detectors and found as a basetrack in the CSd is followed upstream in the brick, starting with the emulsion layer closest to the CSd. This so-called "scan-back" procedure continues until the track could not be found in at least three subsequent emulsion films. Since each disappearing track indicates a possible (decay) vertex, a transverse area of about 1 cm^2 is scanned around the track stopping point, covering five films upstream and ten films downstream. If secondary vertices are found, a kinematical analysis of the scanned event is performed, based on measurements of angular deflection via multiple scattering in the lead sheets of the brick. For momenta up to 6 GeV, the momentum resolution is better than 22 %.

3.2.7 τ detection in OPERA

The OPERA detector aims for the direct detection of tau leptons from ν_τ CC interactions by observation of their characteristic decay topology within the ECC bricks. The mean lifetime of a tau lepton is only $cT = 87.1 \mu\text{m}$, while T being the eigentime. The expected decay length for energies in the GeV-range is up to several millimeters. The experimental signature of a heavy particle decay is that of a track with a large *impact parameter (IP)*, where the IP is the distance between the extrapolated track and the reconstructed primary vertex, or a characteristic kink angle. These events appear in two different scenarios: "Short decays", in which the heavy particle decays in the lead plate that also contains the primary vertex (see Figure 3.25a) and "long decays", where the secondary decay vertex is found one or, rarely, more plates downstream of the primary vertex, both leading to the characteristic kink in the reconstructed particle track (see Figure 3.25b).

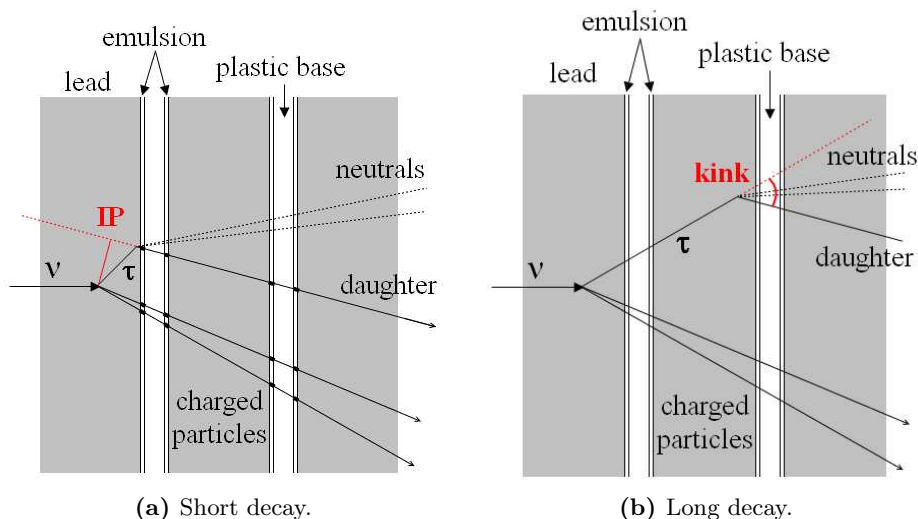


Figure 3.25: τ decay topologies (schematic).

Even though the kink angle or the IP is the most important part of the τ detection, at lot more selection cuts have to be applied to each event that shows a

decay topology. The cut parameters³⁴ and their values depend on the respective τ decay mode and are given in [137].

In the standard model, each τ^- decays into a ν_τ under virtual W^- boson emission. The W^- decays into a negatively charged lepton (and the corresponding lepton antineutrino) or into a pair of \bar{u}/d -like quarks. In contrast to real W , the virtual W from τ decays have a very limited available phase space, prohibiting decays into charm or bottom quarks. Decays into a strange quark (i.e. $\bar{u}s$) are suppressed by the small CKM matrix element V_{us} . Neglecting decays into strange quarks, phase space effects and QCD corrections, the universality of the weak interaction predicts probabilities of the τ^- decaying into an electron, muon or $\bar{u}d$ (hadron) of 20 %, 20 % and 60 %, respectively. Taking all corrections into account, the τ^- decay probabilities are 17.4 % for

$$\tau^- \rightarrow \mu^- + \nu_\tau + \bar{\nu}_\mu \quad (3.9)$$

and 17.9 % for

$$\tau^- \rightarrow e^- + \nu_\tau + \bar{\nu}_e, \quad (3.10)$$

where a small subset of these decays is accompanied by an additional photon. The remaining 64.7 % of all τ^- decays are into quark pairs. Among these, direct π^- production

$$\tau^- \rightarrow \pi^- + \nu_\tau \quad (3.11)$$

occurs in only about 11 % of all τ^- decays, while the direct Cabibbo-suppressed K^- production amounts to about 0.7 %. Most hadronic τ^- decays occur into intermediate states $\rho^-(770)$ (about 25 %) and $a_1^-(1260)$ (about 18 %), which subsequently decay mostly into one π^- and neutrinos. About 15 % of all τ^- decays result in three charged particles (almost always $\pi^- \pi^+ \pi^-$), whereas decay modes with five or more charged hadrons or three charged leptons in the final state are very rare (< 0.1 %) and can thus be neglected. According to the number of charged particles in the final state, the decays are categorized as "one-prong" or "three-prong" decays. The decay modes of the τ^+ are the charge-conjugates of the ones described above.

Since the number of expected τ events (see Section 7.1) in the OPERA detector is very low, a precise knowledge of the expected backgrounds³⁵ is important for the success of the experiment. The numbers given below for the different background channels are used to estimate the overall background rates in OPERA. The actual background of τ candidates is calculated on an event-by-event basis and strongly depends on the type of the decay, the event topology (long or short decay) and the applied analysis cuts. Compared to the OPERA proposal [137], contributions from different background channels to the

³⁴These are the missing transverse momentum at the primary vertex, the angle of the decay parent with respect to the other charged particles in the event, the transverse momentum of the decay daughter with respect to the parent, and the angle between the daughter particle and the decay parent.

³⁵The backgrounds for τ detection are all events that can fake the decay topology of a τ .

total background have changed significantly, mostly due to adjusted efficiency estimations, improved reconstruction methods and additional external data, as described below.

The number of background events is normalized to a fiducial target mass of 1.29 kt and the nominal exposure of 22.5×10^{19} POT [162]. In the following, the backgrounds will also be given as the approximate fraction of ν_μ charged current (N_{CC}) or ν_μ deep inelastic (N_{DIS}) events (NC and CC) to make them comparable to the numbers given in the proposal.

If not explicitly stated, the contribution of $\bar{\nu}_\mu$ and other flavors is small compared to the uncertainty of the background. The τ decay channels affected by the respective backgrounds will be specified in the brackets of the following section titles. The small background contributions to the $\tau \rightarrow e$ channel in addition to the ones described in detail below, due to pion conversion, γ conversion and prompt electrons from ν_e in the CNGS beam are expected to be below $2.0 \times 10^{-6} \times N_{CC}$.

3.2.7.1 Charm production (all τ decay modes)

A background for all τ decay modes is the production of charmed particles in ν_μ NC and CC interactions:

$$\nu_\mu + N \rightarrow \mu^- + c \quad (\text{CC}), \quad (3.12)$$

$$\nu_\mu + N \rightarrow \mu^- + c + \bar{c} + X \quad (\text{CC}), \quad (3.13)$$

$$\nu_\mu + N \rightarrow \nu_\mu + c + \bar{c} + X \quad (\text{NC}), \quad (3.14)$$

where N is a nucleus, c (\bar{c}) are charm (anticharm) quarks and X is a system of outgoing hadrons. Charmed particles show a decay topology similar to the τ due to their comparable lifetimes. The three processes given above will only contribute to the τ background if the primary muon (CC) or the charmed particle (NC and CC) remains undetected³⁶. Of the charm decay modes given above, the contribution from single charm production (Process 3.12) in neutrino CC interactions is the largest source of background. Associated charm production (Process 3.13 and Process 3.14) via boson–gluon fusion (NC) or gluon bremsstrahlung (NC and CC) are rare processes that will result in two charmed hadrons in the final state. The corresponding background contribution is conservatively estimated to be at least one order of magnitude lower than the background from Process 3.12 (see Section 2.1.3.5).

The total number of background events from charm production is 0.55 ($27.5 \times 10^{-6} \times N_{CC}$). This number is significantly higher than the one given in the proposal, due to the higher total charm cross section and the higher relative fragmentation fraction into D^+ final states which is only partially countered by an improved particle identification. Charm production mostly constitutes a

³⁶If the charmed particle decays into a μ^+ , this will lead to the so-called different-sign "dimuon" (Process 3.12) or "trimuon" events (Process 3.13).

background for long, non-muonic τ decays. The charm background is assigned a systematic uncertainty of $\pm 25\%$.

3.2.7.2 Hadronic re-interactions ($\tau \rightarrow h$)

All hadronic decay modes of the τ suffer from background due to so-called "hadronic re-interactions" in NC interactions or CC interactions where the primary muon is not identified. A hadron can interact via deep inelastic scattering and produce a one-prong hadronic final state, possibly faking the decay topology of a τ . Hadronic activity can be detected in the emulsion films by searching for highly ionizing nuclear remnants from the re-interaction. This background is estimated to result in total in about 0.11 events ($4.6 \times 10^{-6} \times N_{DIS}$). This number is significantly lower than the one given in the proposal due to tighter rejection cuts and better particle identification. The hadronic re-interaction background is assigned a systematic uncertainty of $\pm 50\%$.

3.2.7.3 Muon scattering ($\tau \rightarrow \mu$)

Large-angle Coulomb scattering of muons from ν_μ CC interactions can mimic the decay of a τ into a muon if this scattering takes places in the first lead plates downstream of the primary vertex. OPERA expects about 0.07 ($3.8 \times 10^{-6} \times N_{\nu_\mu CC}$) background events from muon scattering, a number which is slightly smaller than the one given in the proposal due to the reduced vertex finding efficiency. The muon scattering background is assigned a systematic uncertainty of $\pm 50\%$.

3.2.7.4 Prompt tau neutrinos (all τ decay modes)

The background from primary ν_τ and $\bar{\nu}_\tau$ in the CNGS beam is negligible for all τ decay modes. The energy-integrated beam contamination $N_{\nu_\tau + \bar{\nu}_\tau} / N_{\nu_\mu}$ is below 10^{-6} , where $N_{\nu_i} = \int_E \Phi_{\nu_i}(E) dE$. Since $\sigma_{\nu_\tau N} < \sigma_{\nu_\mu N}$ and taking into account the low τ detection efficiency, the expected background is less than $1.0 \times 10^{-6} \times N_{\nu_\mu CC}$.

3.3 Observation of a first ν_τ candidate

One τ candidate was found in the analyzed subsample of the 2008/2009 run data that corresponds to 4.88×10^{19} POT [162, 163]. This event passes all criteria defined for a τ signal event. The reconstructed τ decay mode is $\tau \rightarrow \rho\nu$, where the ρ^\pm decays into a π^\pm . This is the most-probable τ decay, with a branching ratio of about 25.8 %.

The total background for this event in the single-prong hadron decay channel is 0.05 ± 0.001 (syst.), where 0.03 background events are expected from possible charm decays and 0.02 due to hadronic re-interactions. The probability that this event arises from statistical background fluctuation is 5.0 % in the single-prong hadron decay channel. Considering all decay channels, the total

expected background is 0.16 ± 0.03 (syst.), the probability of the event to be background is 15 %. The scanning result is shown in Figure 3.26a and Figure 3.26b.

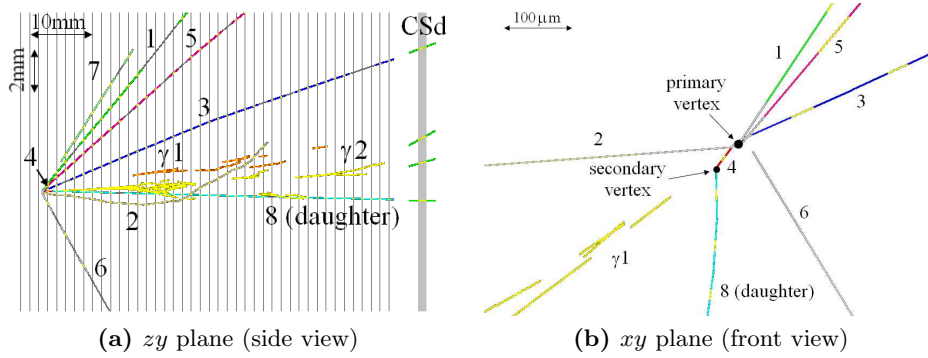


Figure 3.26: Scanning result of the first τ candidate event (Figure reprinted from [162]). The tracks labeled 1 to 8 are associated with the particles given in the following: 1, 3 and 5 are hadrons with energies of (1-2) GeV. 2 is most likely a proton track, identified by its high ionization and range. 6 is assumed to be a low-energy charged pion, while 7 originates most likely from a neutral particle. The τ candidate is associated with track 4 which shows a kink angle of (41 ± 2) mrad after a track length of (1335 ± 35) μm and decays into one charged particle (8) with a momentum of about (12_{-3}^{+6}) GeV. $\gamma 1$ and $\gamma 2$ are electromagnetic showers, with high probabilities of pointing to the secondary vertex.

3.4 Neutrino velocity measurement

The OPERA experiment reported results of a neutrino *time-of-flight* (*TOF*) measurement of neutrinos from the CNGS beam over a distance of about 730 km in 2011 using about 16,000 neutrino interactions collected during the runs 2009, 2010 and 2011 [153, 154]. This measurement is based on a comparison of the approximately $10.5 \mu\text{s}$ long time distribution of protons hitting the CNGS target (see Section 3.1), as measured by *beam-current transformers* (*BCT*) and the corresponding arrival times at the OPERA detector as given by the first hit recorded by a TT. After correcting the timestamps of the respective proton waveform and the neutrino arrival time, a best fit δt_k is obtained by minimizing the *negative log-likelihood* (*NLL*)

$$-\mathcal{L}(\delta t_k) = \prod_j w_k(t_j + \delta t_k), \quad (3.15)$$

where $k = 1, 2$ denotes either the first or the second CNGS extraction³⁷, $w_k = \sum_j w_k^j$ is the sum of all proton time distributions, one sum for each extraction, that resulted in a hit in the OPERA detector and t_j is the arrival time of the j -th neutrino event.

³⁷The two extractions have different delays with respect to the trigger signal of the TOF measurement, given by a kicker magnet, due to their different positions within the SPS cycle.

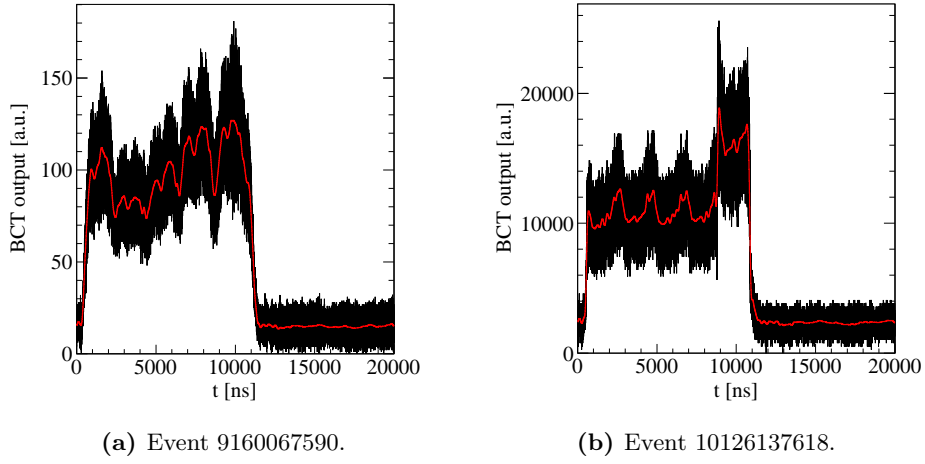


Figure 3.27: BCT measurements of the proton time distributions for two arbitrarily selected events. The filtered waveforms, using a 5 MHz low-pass filter (see text for details), are shown by a red line.

By this summing over all proton time distributions, the individual neutrino arrival times are compared to an average waveform. This removes most noise from the proton waveforms, but also reduces their individual characteristics, which exhibit large variations, as shown in Figure 3.27. A comparison of the neutrino arrival time distributions and the average proton waveforms is shown in Figure 3.28.

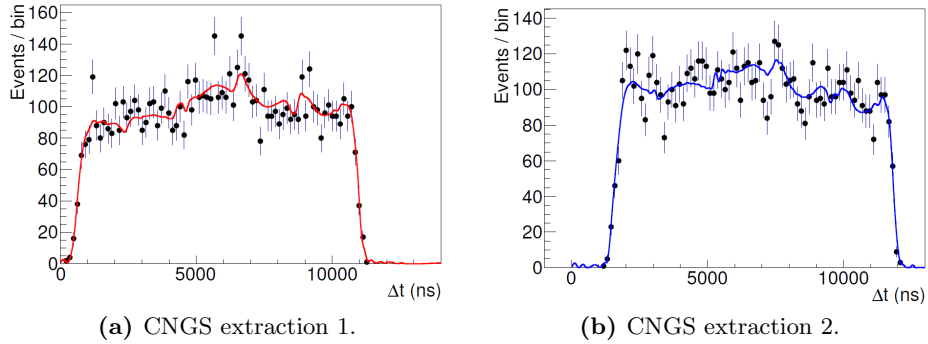


Figure 3.28: Comparison of the neutrino arrival time distributions (black markers) and the average proton waveforms (red and blue lines) after fit for both CNGS extractions (Figures reprinted from [154]). These plots are for visualization only, the actual fit is unbinned.

An alternative method compares each neutrino arrival time to its corresponding waveform, resulting in a modified likelihood

$$-\mathcal{L}(\delta t) = \prod_j w_j(t_j + \delta t). \quad (3.16)$$

This alternative method produces smaller statistical errors by exploiting the full proton waveform information, but on the other hand needs an individual wave-

form filtering to reduce the electronic noise on the waveforms³⁸ and a correction of the waveform baseline for each event which introduces an additional systematic uncertainty³⁹. Using a *fast Fourier transformation (FFT)* and removing Fourier components with frequencies higher than 5 MHz turned out to be optimal in MC studies. The 68 % C.L. for the fitted δt for both methods are given by $\mathcal{L}_{min} + 0.5$ [94], where \mathcal{L}_{min} is the global minimal NLL value.

Additional cross-checks, performed after the initial result was published, revealed a different measured delay of the 8.3 km optical cable between the GPS⁴⁰ output (above-ground) and the OPERA Master Clock (underground) as well as a drift of the OPERA Master Clock itself. Under the assumption that these effects were stable during the original measurement, as confirmed by a joint LVD-OPERA analysis [164], the recorded timestamps have been corrected and the result has been revised. The revised result of the original method is

$$\delta t_{original} = TOF_c - TOF_\nu = (6.5 \pm 7.4 (stat.) \pm_{-8.0}^{+8.3} (syst.)) \text{ ns.} \quad (3.17)$$

Using the effective distance L' between the average meson decay point as determined by simulations and the OPERA detector, the relative difference of the muon neutrino velocity with respect to speed of light is

$$\frac{(v_\nu - c)}{c} = \frac{\delta t}{(TOF'_c - \delta t)} = (2.7 \pm 3.1 (stat.) \pm_{-3.3}^{+3.4} (syst.)) \times 10^{-6} \quad (3.18)$$

where $TOF'_c = L'/c$.

The alternative method⁴¹ gives

$$\delta t_{alternative} = (3.5 \pm 5.6 (stat.) \pm_{-9.1}^{+9.4} (syst.)) \text{ ns.} \quad (3.19)$$

The NLL distribution⁴² is shown in Figure 3.29a. The result is compatible with $v_\nu = c$ and is the most precise measurement of the ν_μ velocity.

The magnetic spectrometers of the OPERA detector can be used to prepare a sample of events with a reconstructed μ^+ track, which originate predominantly from $\bar{\nu}_\mu$ CC interactions. The resulting sub-selection contains 411 events, and a fit using the alternative method yields a time difference of⁴³

$$\bar{\delta t}_{alternative} = (17.4 \pm 33.0 (stat.)) \text{ ns.} \quad (3.20)$$

³⁸Without this filtering, the NLL fit does not produce stable results.

³⁹The original waveforms need filtering and pedestal correction, too. Different filters have no significant effect on the fit result, though.

⁴⁰GPS: Global Positioning System.

⁴¹This value is the average of several independent fits with different waveform treatments, resulting in an additional contribution of ± 4.4 ns to the systematic error, that is included in the quoted values.

⁴²This NLL distribution corresponds to one of the independent fits used in the computation of the average alternative methods value.

⁴³The statistical error is taken symmetric in the following, $\mathcal{L} + 0.5$ yields -30.8 ns and +33.0 ns respectively.

The relative difference of the muon antineutrino velocity with respect to speed of light is

$$\frac{(v_{\bar{\nu}} - c)}{c} = \frac{\bar{\delta}t}{(TOF'_c - \bar{\delta}t)} = (7.1 \pm 13.5 (stat.)) \times 10^{-6}. \quad (3.21)$$

The NLL distribution of the μ^+ fit is shown in Figure 3.29b. Systematic uncertainties related to the muon antineutrino measurement are similar than those affecting the result for muon neutrinos, where the total uncertainty is dominated by statistical error anyhow⁴⁴. This result is compatible with $v_{\bar{\nu}} = c$ and is the first measurement of the $\bar{\nu}_\mu$ velocity.

The full sample was furthermore divided into low-energy/high-energy, day/night, spring/autumn and internal/external event samples. None of these sub-sample analyses revealed any significant deviation from $\delta t = 0$ ns.

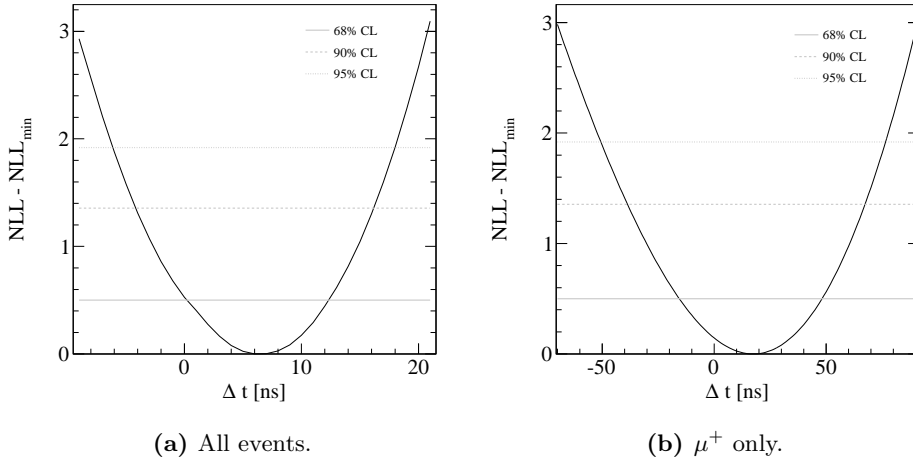


Figure 3.29: NLL distribution for the alternative method for all events (left) and for events with a reconstructed μ^+ only (right).

The TOF measurements have been repeated in November 2011 using a short-bunch wide-spacing neutrino beam produced in a dedicated SPS operation mode. This so-called *bunched beam* (*bb*)⁴⁵ consists of several isolated proton bunches, separated by about 500 ns and each lasting about 3 ns (full width half maximum). During about two weeks of operation, 35 events were collected. Out of these, 20 events were selected to determine an event-by-event neutrino TOF resulting in

$$\delta t^{bb} = (1.9 \pm 3.7(stat.)) \text{ ns}, \quad (3.22)$$

which is compatible with the original result and excludes possible systematic effects related to the proton waveform measurement, the CNGS target or the likelihood

⁴⁴The μ^+ event sample has a background contamination in the percent range from ν_μ CC interactions that produced a charm which decayed into a μ^+ as well as from misidentified true ν_μ CC and ν_μ NC interactions (compare Figure 6.17).

⁴⁵The beam intensity in this mode is about a factor of 60 lower than during nominal CNGS operation and thus not compatible with the CNGS oscillation physics program.

fit. Systematic uncertainties related to the bunched beam are expected to be equal or smaller than for the nominal CNGS operation.

Chapter 4

Monte Carlo simulation

Like all modern experiments, OPERA relies on a simulation framework for modeling the detector response and correcting the experimental data. This allows the comparison to theoretical expectations and the estimation of systematic uncertainties arising from theoretical uncertainties of the underlying physics or parameterizations. The OPERA simulation chain includes a *Monte Carlo (MC)* simulation of the neutrino beam (see Section 4.1), the neutrino event generator (see Section 4.3), the cosmic muon event generator (see Section 4.4) and the detector simulation and digitization (see Section 4.5). Many parts of the analysis require a software description of the experiment geometry which is explained in Section 4.2. All aspects of the MC described within this section are used for the electronic detector simulation and reconstruction only, and not for emulsion simulation.

4.1 CNGS beam

The prediction of the neutrino flux at the detector site is always a crucial part of neutrino experiments. Disappearance experiments usually employ a near detector to measure the neutrino spectrum and use extrapolation methods to predict the expected spectrum in the far detector. The OPERA experiment lacks a near detector, since, contrary to disappearance experiments, the uncertainties due to the expected very low statistics for τ -appearance detection dominate over the uncertainties from the flux prediction. This limits the OPERA options for investigating non-appearance beam physics, though.

The neutrino flux prediction at the OPERA detector is performed by a FLUKA¹ simulation [165, 166]. The FLUKA CNGS beam simulation framework has been successfully benchmarked with the data obtained by the NOMAD experiment in the SPS WANF² neutrino beam [139] and the hadron production experiment NA56/SPY³ [167].

¹FLUKA: Fluktuierende Kaskade.

²WANF: CERN West Area Neutrino Facility.

³SPY: Secondary Particle Yield.

Within this thesis, simulated neutrinos from the latest *2006 CNGS-FLUKA (CF06)* MC production have been used. The details of the simulated CNGS layout can be found in [152]. The full available sample contains 10^7 neutrinos at Gran Sasso. This number is a trade-off between the required simulation time and the statistical uncertainty of the simulation for the different neutrino flavors ν_μ , $\bar{\nu}_\mu$, ν_e and $\bar{\nu}_e$, as will be explained later. All neutrinos are propagated, starting from their creation in the secondary beamline at CERN to the LNGS site, in vacuum to within a 400 m radius at the LNGS site, resulting in unoscillated neutrino spectra. Prompt ν_τ are fully negligible: The contamination $N_{\nu_\tau+\bar{\nu}_\tau}/N_{\nu_\mu}$ of the beam is below 10^{-6} and has thus not been simulated.

Due to the long distance to CERN, all neutrinos arriving at the OPERA detector site are assumed to propagate parallel to the beam axis. This allows to reduce the double differential neutrino distribution $\Phi_\nu(E, \theta)$ by one dimension via integration over the respective angular range, ending up with the neutrino flux $\Phi_\nu(E)$, normalized to a given number of POT and a given area. For practical reasons, the angle θ is expressed as a lateral displacement r from the beam center (given in meters).

The total number of neutrinos $\Phi(r)$, integrated over all energies, with respect to the lateral displacement r is shown for the different neutrino flavors in Figure 4.1, Figure 4.3, Figure 4.5 and Figure 4.6. The gray bands indicate the statistical bin width-dependent uncertainty of the simulation. The statistical uncertainties within this chapter are approximated using Jackknife-resampling [168].

The flux decreases approximately proportionally to r^{-2} (see Figure D.1 and Figure D.2), as derived from pion decay kinematics. The beam is radial symmetric, therefore the statistics in each bin increases proportionally to r^2 , resulting in smaller errors at larger radii. $\Phi(r)$ gets maximal for $r \rightarrow 0$, as expected. Within the statistical errors, the total flux is approximately constant within the inner 150 m for ν_μ and $\bar{\nu}_\mu$ and within the inner 400 m for ν_e and $\bar{\nu}_e$. For a 400 m off-axis position, the total ν_μ and $\bar{\nu}_\mu$ flux is reduced by about 3–4 %.

Apart from the total flux reduction, some parts of the neutrino energy spectrum get distorted even for small off-axis positions of less than 1 mrad. The effect on the ν_μ and $\bar{\nu}_\mu$ energy spectra for a small displacement of the OPERA detector is shown in Figure 4.2 and Figure 4.4. For ν_μ , in the innermost region, an excess of about 30 % can be seen around 25 GeV while for neutrino energies around 40 GeV a 45 % deficit and for energies around 20 GeV a 5 % deficit is visible. The $\Phi_{\bar{\nu}_\mu}(E)$ spectrum shows a deficit of approximately 10 % at 18 GeV and an excess of about 20 % for neutrino energies around 25 GeV when comparing the innermost to the outermost regions. This distortion is less distinctive than for the $\Phi_{\nu_\mu}(E)$ spectrum. The smaller number of simulated events does not permit to create these plots for ν_e and $\bar{\nu}_e$. ν_e and $\bar{\nu}_e$ are less subject to this kind of energy spectrum distortion anyway, since their creation is dominated by three-body

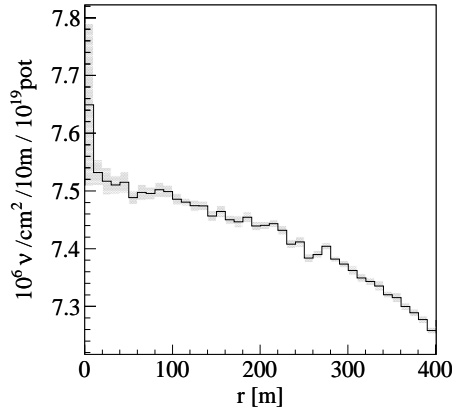


Figure 4.1: $\Phi_{\nu_\mu}(r)$ at LNGS and statistical uncertainties of the simulation (gray), where r is the distance from the beam center. The OPERA detector center is located at $r = 90$ m.

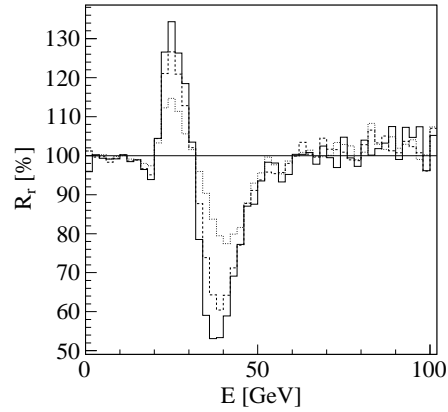


Figure 4.2: Comparison $R_r = \Phi_{\nu_\mu}(E)|_r / \Phi_{\nu_\mu}(E)|_{(300-400)\text{m}}$ of $\Phi_{\nu_\mu}(E)$ for three concentric 100-m-wide rings with outer radii of 100 m (solid), 200 m (dashed) and 300 m (dotted), relative to a forth ring with an outer radius of 400 m.

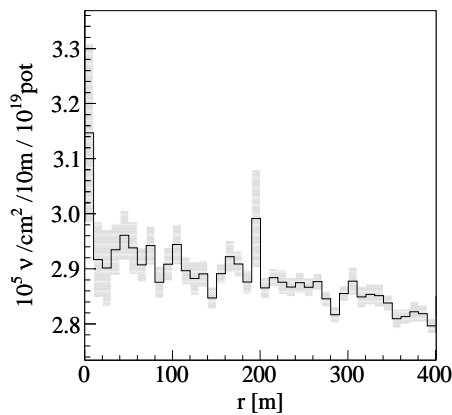


Figure 4.3: $\Phi_{\bar{\nu}_\mu}(r)$ at LNGS and statistical uncertainties of the simulation (gray), where r is the distance from the beam center.

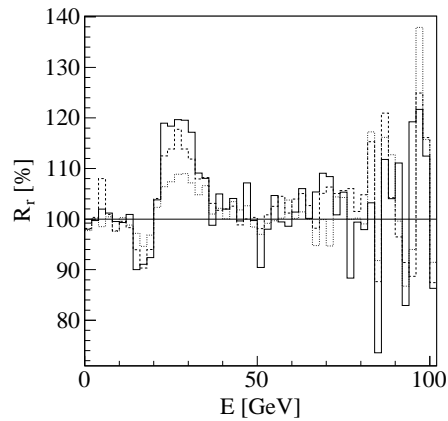


Figure 4.4: Comparison $R_r = \Phi_{\bar{\nu}_\mu}(E)|_r / \Phi_{\bar{\nu}_\mu}(E)|_{(300-400)\text{m}}$ of $\Phi_{\bar{\nu}_\mu}(E)$ for three concentric 100-m-wide rings with outer radii of 100 m (solid), 200 m (dashed) and 300 m (dotted), relative to a forth ring with an outer radius of 400 m.

decays that show only a weak angular dependency.

The CNGS default integration limits are [169]:

$$r_{limit} = \begin{cases} (0 - 120) \text{ m} & \text{for } \nu_\mu \text{ and } \bar{\nu}_\mu, \\ (0 - 400) \text{ m} & \text{for } \nu_e \text{ and } \bar{\nu}_e. \end{cases} \quad (4.1)$$

The resulting default neutrino fluxes $\Phi_\nu(E)$ for all four simulated flavors are shown in Figure 4.8a, Figure 4.10a, Figure 4.12a and Figure 4.13a, along with contributions from the main decay parents. The mean neutrino energy $\langle E \rangle$, the energy-integrated flux Φ and the integrated flux fraction ν_α/ν_μ of each neutrino flavor α with respect to the integrated ν_μ flux are given in Table 4.1.

Table 4.1: Average CNGS beam composition for all four simulated flavors within the OPERA default radial integration limits (0–120) m, integrated over neutrino energies of (0–40) GeV, (0–100) GeV and (0–400) GeV. The integrated beam flux Φ is given in $\nu/\text{cm}^2/10^{19}$ POT, the mean neutrino energy $\langle E \rangle$ is given in GeV. The contamination ν_α/ν_μ is given in % and calculated relative to the OPERA default ν_μ spectrum. The two lines marked with an asterisk (*) correspond to a (0–400) m-integration, provided for comparison. See text for systematic uncertainties.

ν_α	$E < 40$ GeV			$E < 100$ GeV			$E < 400$ GeV		
	Φ	$\langle E \rangle$	ν_α/ν_μ	Φ	$\langle E \rangle$	ν_α/ν_μ	Φ	$\langle E \rangle$	ν_α/ν_μ
ν_μ	7.26×10^6	16.8	–	7.45×10^6	17.9	–	7.50×10^6	18.6	–
ν_μ^*	7.14×10^6	16.6	–	7.34×10^6	17.9	–	7.38×10^6	18.5	–
$\bar{\nu}_\mu$	2.51×10^5	16.7	3.4	2.89×10^5	22.0	3.9	2.92×10^5	23.0	3.9
$\bar{\nu}_\mu^*$	2.46×10^5	16.5	3.4	2.83×10^5	21.9	3.9	2.86×10^5	22.8	3.9
ν_e	3.96×10^4	17.7	0.6	4.76×10^4	24.6	0.6	4.83×10^4	26.1	0.7
$\bar{\nu}_e$	4.94×10^3	16.3	0.07	6.06×10^3	24.5	0.08	6.19×10^3	26.7	0.08

The CNGS beam axis is about 90 m horizontally displaced from the OPERA detector center, as measured by geodesy (see Section 3.1.2). Therefore, an alternative flux integration has been performed to avoid a possible bias in the OPERA simulation. The revised CNGS integration limit for OPERA is centered around the 90 m off-axis position

$$r_{limit, revised} = (50 - 130) \text{ m for } \nu_\mu \text{ and } \bar{\nu}_\mu, \quad (4.2)$$

while the (0–400) m-integration for ν_e and $\bar{\nu}_e$ remains. Within the statistical uncertainties of the simulation, the new limit provides the same beam composition as the CNGS default limit sample⁴. While the $\bar{\nu}_\mu$ flux does not change notably (see Figure 4.7b), the revised ν_μ flux is lowered by 3 % at about 35 GeV (see Figure 4.7a).

⁴The revised sample is a bit smaller than the default sample for the same covered area, since the flux is reduced for growing r .

The relative contribution

$$R_P = \frac{N_{P \rightarrow \nu_\alpha + \text{others}}(E)}{N_{\nu_\alpha}(E)} \quad (4.3)$$

of neutrinos $\nu_\alpha = (\nu_\mu, \bar{\nu}_\mu, \nu_e, \bar{\nu}_e)$ from different decay parents P is shown in Figure 4.8b, Figure 4.10b, Figure 4.12b and Figure 4.13b, where only parents that contribute to at least 1 % in at least one energy bin up to 150 GeV are shown, hence the summed-up contribution in the figures might not reach 100 %. No discrimination between different decay modes is made.

In the following, the default integration limits and $E_\nu < 100$ GeV will be used.

The ν_μ originate almost exclusively from the decays of π^+ (96.9 %) and K^+ (3.0 %), where π^+ decays dominate up to about 45 GeV and K^+ above (see Figure 4.8). Contributions from other parents are very rare. Due to the long distance, the neutrino spectrum at LNGS is dominated by neutrinos from decays with very small opening angles. Thus, the relative contribution of K^+ decays is reduced compared to the otherwise similar SPS WANF spectrum in the NOMAD detector, where these parents were contributing about 10 % to the ν_μ flux. The longitudinal and radial positions of π^+ and K^+ decays that result in a ν_μ reaching LNGS are shown in Figure 4.9.

Most of the $\bar{\nu}_\mu$ flux originates from the decay of (wrong-sign) π^- (84.9 %) and K^- (6.6 %) (see Figure 4.10). These are mainly high-energy particles that have remained underdeflected or that entered the horn/reflector combination in the field-free region close to the beam axis. The average $\bar{\nu}_\mu$ energy is thus notably higher than the average ν_μ energy. π^- decays dominate up to about 100 GeV, and K^- above. Three-body μ^+ decays contribute to low neutrino energies up to 35 GeV (7.5 %), maximally amounting to 16 % at about 15 GeV. A 0.9 % background from K^0 exists and remains almost constant for all investigated energies. The position of π^- and K^- decays that result in a $\bar{\nu}_\mu$ at LNGS is shown in Figure 4.11. The defocusing of the horn/reflector is clearly visible in that figure: Most decays are close to the beam axis, and a large contribution comes from decays that happen before the actual focusing takes place.

The ν_e flux is mainly due to the decays of μ^+ (47.1 %) which dominate the energy spectrum up to about 25 GeV (see Figure 4.12). K^+ decays contribute at higher neutrino energies (39.2 %). A relative contribution of about 9.5 %, weakly increasing with energy, arises from K^0 decays. A small fraction of ν_e originates from the helicity-suppressed $\pi^+ \rightarrow e^+ \nu_e$ decays (4 %).

The by far largest amount of $\bar{\nu}_e$ in the beam is due to K^0 decays (68.8 %) (see Figure 4.13) which remain unaffected by secondary beam focusing and thus are an unavoidable contamination of the beam. The long distance geometrically reduces the $\bar{\nu}_e$ contamination to almost a factor of five lower than in the SPS WANF beam. K^- decays (21.6 %) contribute to all neutrino energies with a quite

constant fraction and the fraction of μ^- decays (8.3 %) decreases slowly with energy. In contrast to the ν_e case, the contribution from π^- decays is negligible due to the small number of (wrong-sign) π^- in the secondary beam.

The relative contributions from the main decay parents, as well as the resulting mean neutrino energies for the different neutrino flavors present in the CNGS beam are summarized in Table 4.2. The contamination of the CNGS beam with wrong-sign and wrong-flavor neutrinos is much lower than in the SPS WANF beam, because prompt unfocused neutrinos and neutrinos from proton re-interactions downstream the focusing elements (mainly in the beam dump) are negligible at long distances.

Table 4.2: Decay parent contribution of the various neutrino flavors in the CNGS beam for $E < 100$ GeV. The mean neutrino energy $\langle E \rangle$ is given in GeV. The two lines marked with an asterisk (*) correspond to a (0–400) m-integration provided for comparison.

ν_α	π^\pm		K^\pm		μ^\pm		K^0	
	%	$\langle E \rangle$	%	$\langle E \rangle$	%	$\langle E \rangle$	%	$\langle E \rangle$
ν_μ	96.9	17.0	3.0	48.4	< 0.1	–	< 0.1	–
ν_μ^*	96.8	16.9	3.1	48.3	< 0.1	–	< 0.1	–
$\bar{\nu}_\mu$	84.9	21.7	6.6	33.6	7.5	17.6	0.9	24.8
$\bar{\nu}_\mu^*$	85.0	21.4	6.3	33.2	7.5	17.6	1.1	22.1
ν_e	4.0	30.7	39.2	33.6	47.1	16.4	9.5	25.6
$\bar{\nu}_e$	< 0.1	–	21.6	23.3	8.3	16.9	68.8	25.9

A crucial part of the CNGS beam simulation is a solid understanding of the systematic uncertainties. These are divided into a neutrino energy-independent part and energy-dependent uncertainties. The CNGS beam uncertainties are mainly estimated by rescaling the uncertainties of the SPS WANF simulation to the different design and the different secondary particle energies of the CNGS beam. The main source of systematic uncertainty in the CNGS beam is the yield of secondary particles from the target, including the scaling from the SPS WANF target material (Beryllium) to the CNGS target material (Carbon). The effect of the secondary beam alignment, horn/reflector fields and material budget is very small (0.8 %) compared to the corresponding uncertainties for the SPS WANF short-distance beam (about 5.5 % for ν_μ). The total energy-independent uncertainty is estimated to be about 5 % for all neutrino species and 3.1 % for the ν_e/ν_μ ratio [170]. The quite large uncertainty of the SPS WANF flux prediction for $\bar{\nu}_\mu$ was dominated by the reinteractions of secondary particles. These are reduced for the CNGS beam due to the long distance, making the systematic uncertainties of ν_μ and $\bar{\nu}_\mu$ comparable. Since both ν_μ and ν_e originate, to a large part, from the same parents (π^+), several sources of errors cancel out and the uncertainty of the ratio ν_e/ν_μ is smaller than the uncertainties of the primary

fluxes.

The energy-dependent uncertainties are evaluated in [170] for ν_μ , ν_e and the ratio ν_e/ν_μ , but not for $\bar{\nu}_\mu$ and $\bar{\nu}_e$. They are shown in Figure 4.14a, Figure 4.14b and Figure 4.14c. For the energy-dependent uncertainties of the $\bar{\nu}_\mu$ and the $\bar{\nu}_e$ flux, the following linear approximations of the SPS WANF results are used:

$$\sigma_{\bar{\nu}_\mu} = \begin{cases} 0.055 - (0.035/40)E/\text{GeV} & \text{for } E \leq 40 \text{ GeV}, \\ 0.02 & \text{for } 40 \text{ GeV} < E \leq 75 \text{ GeV}, \\ -0.005 + (0.025/75)E/\text{GeV} & \text{for } 75 \text{ GeV} < E, \end{cases} \quad (4.4)$$

and

$$\sigma_{\bar{\nu}_e} = \begin{cases} 0.08 - (0.04/20)E/\text{GeV} & \text{for } E \leq 20 \text{ GeV}, \\ 0.04 & \text{for } 20 \text{ GeV} < E \leq 100 \text{ GeV}, \\ (0.02/50)E/\text{GeV} & \text{for } 100 \text{ GeV} < E. \end{cases} \quad (4.5)$$

The limited size of the simulated neutrino sample introduces a statistical uncertainty to the final simulated neutrino spectrum that depends on the chosen bin-width. The bin-width is set to 0.25 GeV for ν_μ , 1.0 GeV for $\bar{\nu}_\mu$, 2 GeV for ν_e and 5 GeV for $\bar{\nu}_e$, which is the smallest fixed-size binning⁵ that fulfills the requirement $\sigma_{stat} < \sigma_{syst}$ for neutrino energies below 40 GeV. This requirement is partially violated for the $\bar{\nu}_e$ spectrum, where the statistical and systematic uncertainties are approximately equal. An additional uncertainty arises from the chosen radial integration limits of the neutrino spectra (compare Figure 4.2 and Figure 4.4) that affects mainly the ν_μ spectrum. It amounts to about 0.5 % for ν_μ and energies below 40 GeV, obtained by variation of the integration limits by ± 25 %, while keeping the mean value fixed. This uncertainty is comparable to the statistical uncertainty for the 0.25 GeV-binning. For the other neutrino species, the statistical uncertainty for the respective chosen binning is larger than the effect of the exact choice of the radial limits.

The energy-dependent statistical uncertainties for these binnings are shown in Figure 4.15a, Figure 4.15b, Figure 4.16a and Figure 4.16b. The obtained statistical uncertainties are averaged over 5 GeV (ν_μ and $\bar{\nu}_\mu$) and 10 GeV (ν_e and $\bar{\nu}_e$), respectively. For neutrino energies above around 150 GeV, the Jackknife method fails, since the statistics per sub-sample are too small (or zero). The statistical uncertainty is approximated by an extrapolation of a second-order polynomial fit to the (50 – 150) GeV energy range uncertainty and truncated at a maximum uncertainty of 100 %.

To obtain the total uncertainties of the simulated neutrino spectrum, the systematic energy-independent uncertainties, the systematic energy-dependent uncertainties and the statistical energy-dependent uncertainties have to be added

⁵The plots shown previously in this section have their binning optimized for display purposes.

in quadrature. For a neutrino energy of 20 GeV, the total uncertainty is 5.5 % for ν_μ , 6.2 % for $\bar{\nu}_\mu$, 6.3 % for ν_e and 8.5 % for $\bar{\nu}_e$.

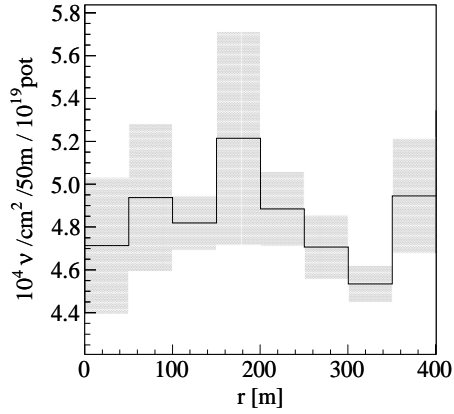


Figure 4.5: $\Phi_{\nu_e}(r)$ at LNGS and statistical uncertainties of the simulation (gray), where r is the distance from the beam center.

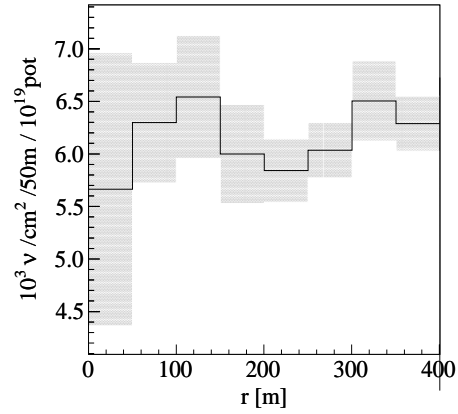


Figure 4.6: $\Phi_{\bar{\nu}_e}(r)$ at LNGS and statistical uncertainties of the simulation (gray), where r is the distance from the beam center.

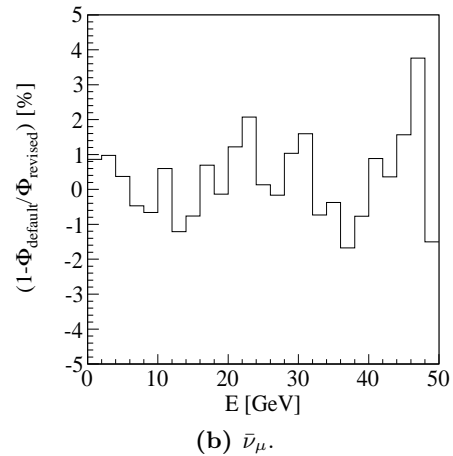
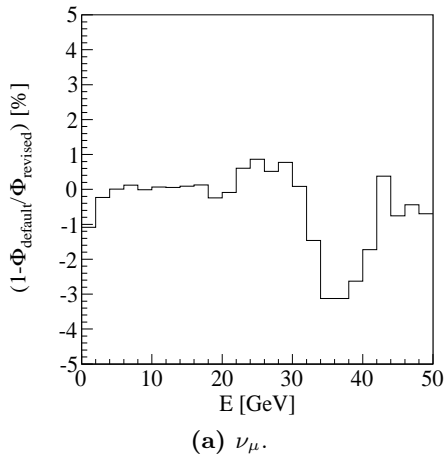


Figure 4.7: Comparison of default and revised neutrino fluxes $\Phi_{\text{default}}(E)$ and $\Phi_{\text{revised}}(E)$ at LNGS for ν_μ and $\bar{\nu}_\mu$.

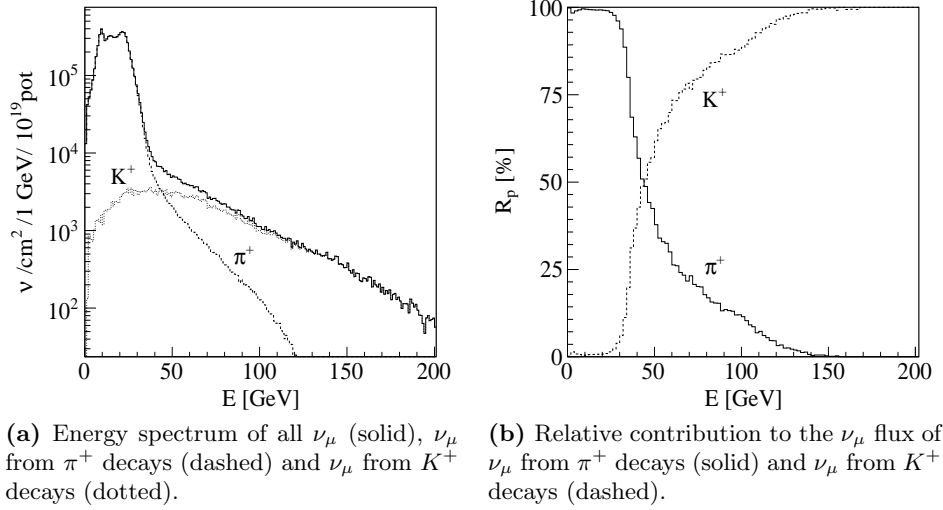


Figure 4.8: ν_μ flux $\Phi_{\nu_\mu}(E)$ at LNGS, $r < 120$ m.

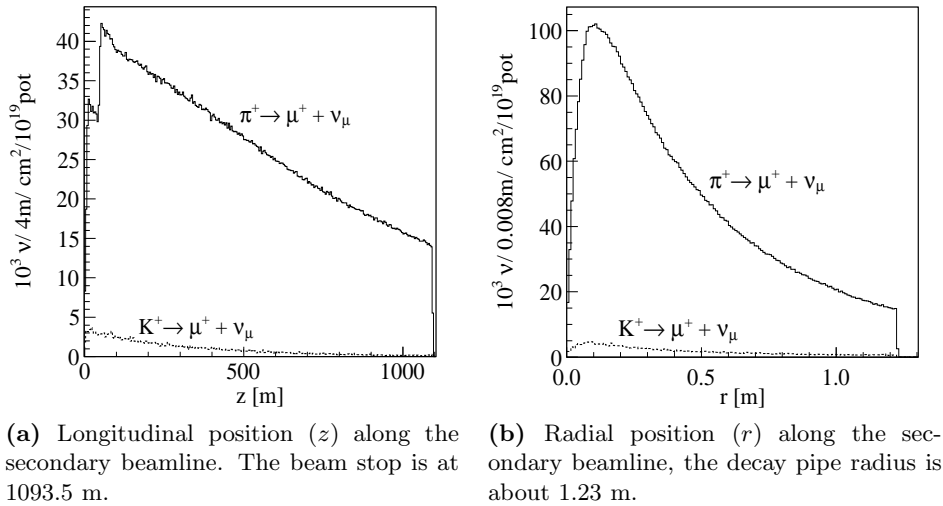


Figure 4.9: Decay position of the ν_μ parent with respect to the proton target center. All ν_μ within the default integration limits are considered.

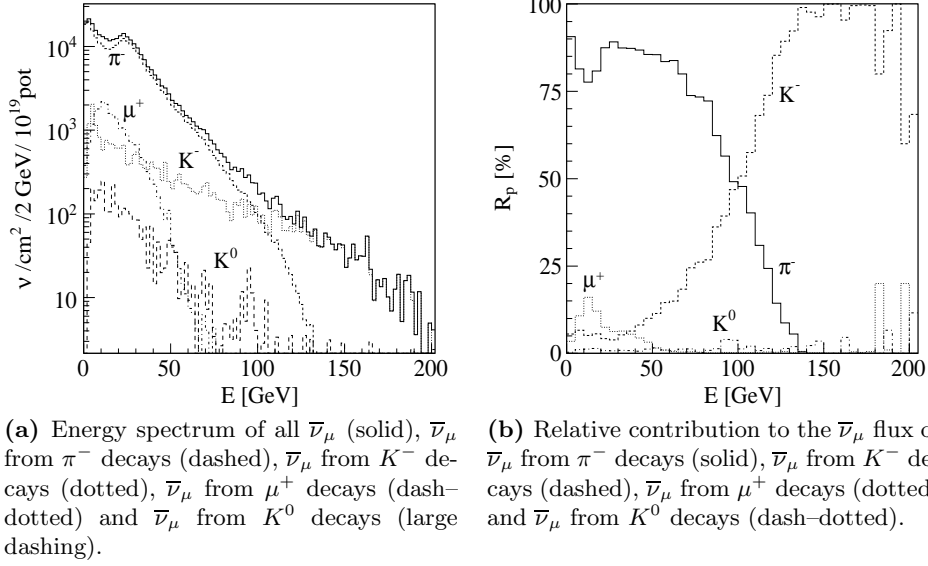


Figure 4.10: $\bar{\nu}_\mu$ flux $\Phi_{\bar{\nu}_\mu}(E)$ at LNGS, $r < 120$ m.

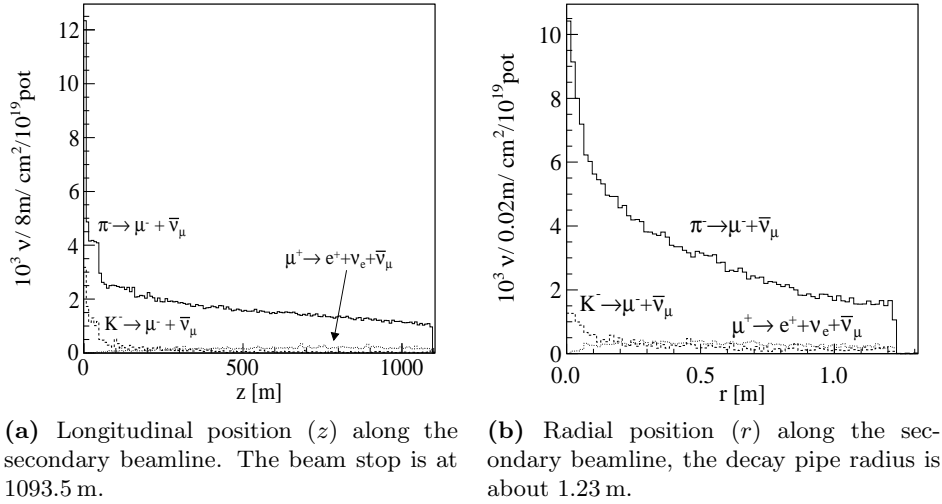


Figure 4.11: Decay position of the $\bar{\nu}_\mu$ parent with respect to the proton target center. All $\bar{\nu}_\mu$ within the default integration limits are considered.

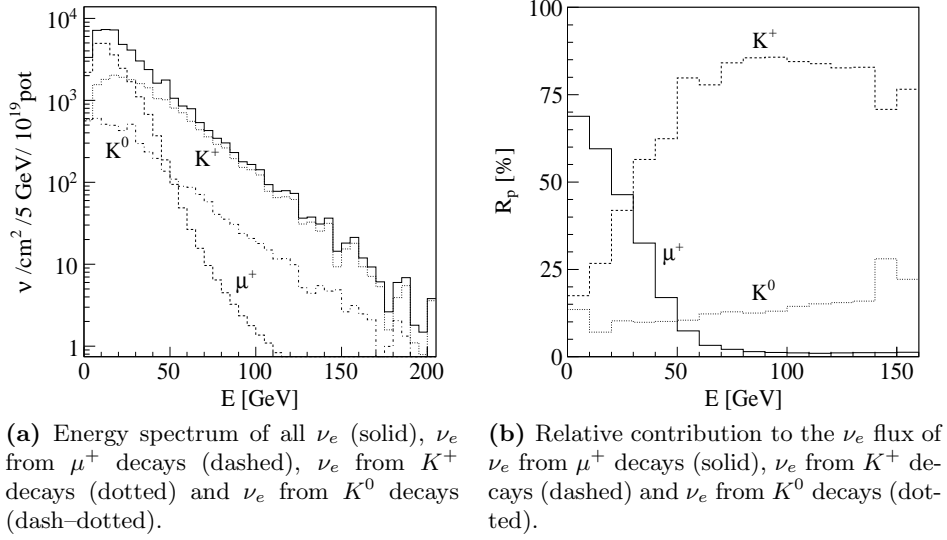


Figure 4.12: ν_e flux $\Phi_{\nu_e}(E)$ at LNGS, $r < 400$ m.

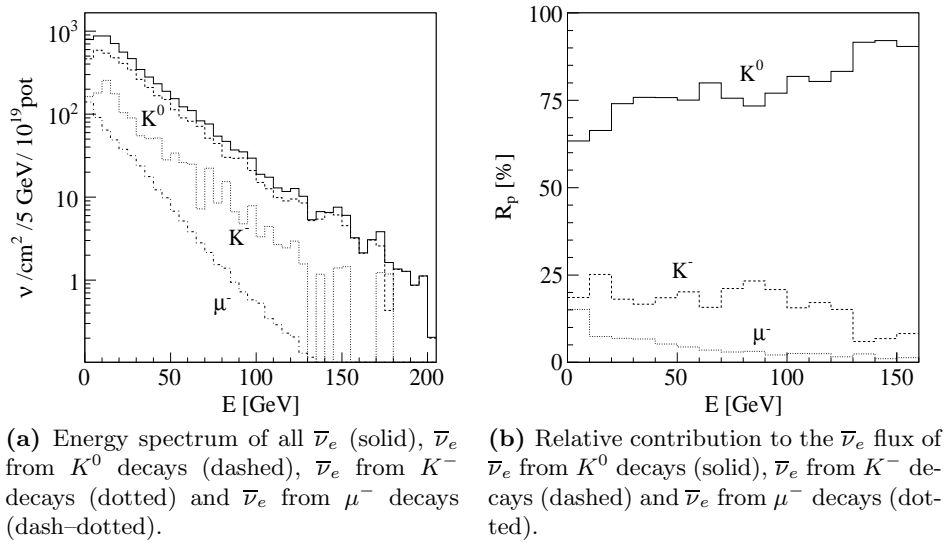


Figure 4.13: $\bar{\nu}_e$ flux $\Phi_{\bar{\nu}_e}$ at LNGS, $r < 400$ m.

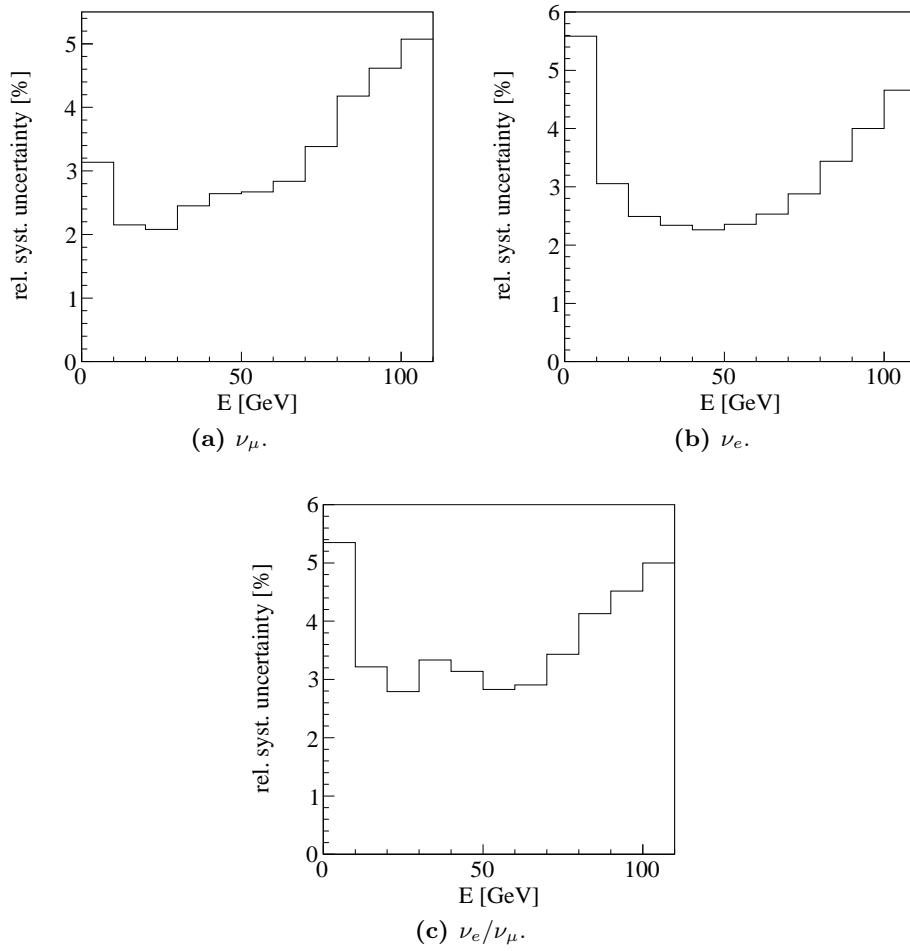


Figure 4.14: Systematic energy dependent uncertainty of the FLUKA neutrino beam simulation (values digitized from [152]).

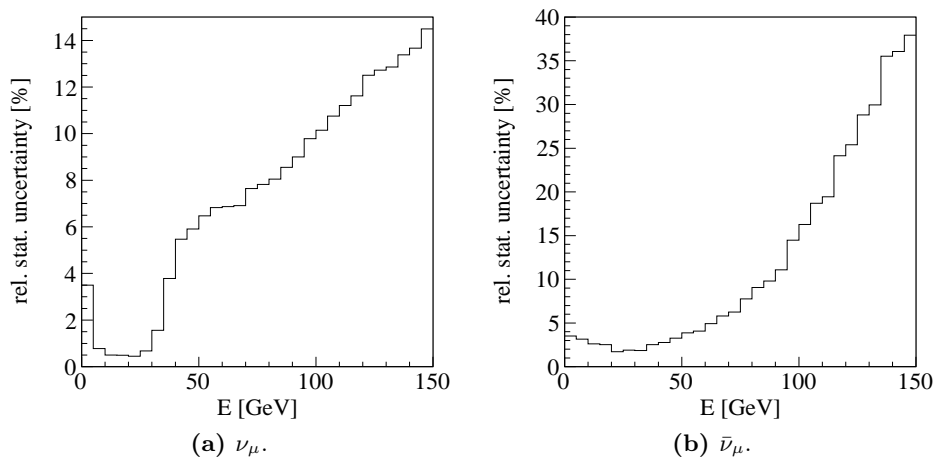


Figure 4.15: Statistical uncertainty of the FLUKA ν_μ and $\bar{\nu}_\mu$ neutrino beam simulation, $r < 120$ m.

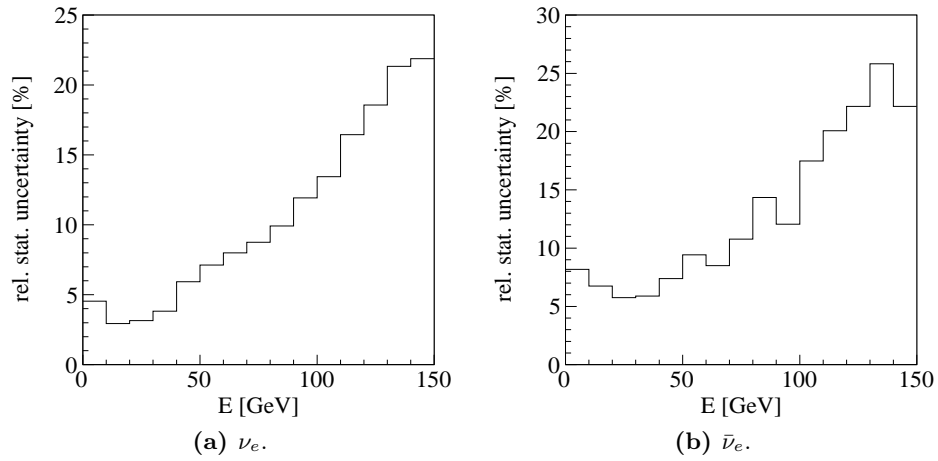


Figure 4.16: Statistical uncertainty of the FLUKA ν_e and $\bar{\nu}_e$ neutrino beam simulation, $r < 400$ m.

4.2 Geometry description

The OPERA geometry model, called `OpGeom`, as used in both the simulation and the reconstruction algorithms, is based on a `ROOT`⁶ `TGeoManager` description that is included in the `OpRelease`⁷ software framework. The geometry model includes a detailed description of the detector, a variable brick configuration and an approximate description of the support structure (see Figure 4.17, the mother volume containing these structures is called `OPDY` in `OpGeom`), the main volumes of the BOREXINO experiment and the surrounding rock (see Figure 4.18, the mother volume containing all structures is called `WRLD` in `OpGeom`) [171].

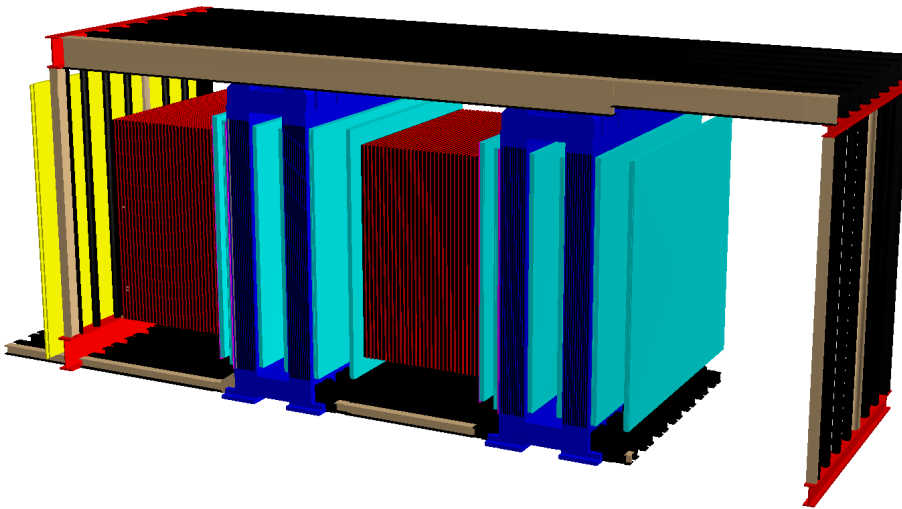


Figure 4.17: 3D view of the OPERA detector as implemented in `OpGeom`.

Within this work, several modifications of the default geometry model have been implemented to comply with the `GENIE` geometry driver during event generation (see Section 4.3). Small adjustments of material compositions have been made if new information was available, and some parts of the non-`OPDY` geometry have been corrected according to new position measurements.

All material definitions have been changed from the default average element mixtures to isotope mixtures. However, these changes have only negligible impact on other parts of the simulation or reconstruction. The composition of the emulsions and the steel of the magnet spectrometers have been updated [172, 173] and the material of the magnets' concrete base has been changed to standard reinforced concrete. The position of the four BOREXINO storage tanks, located directly upstream of the OPERA detector, has been corrected. The filling level

⁶`ROOT` is a data analysis and library package developed by CERN.

⁷`OpRelease` is the name of the official OPERA software package.

with *pseudocumene* (*PSCU*), the main component of the BOREXINO scintillator, of these storage tanks has been adjusted to the value measured at the beginning of 2009. The concrete walls surrounding the storage tanks have been added to the geometry model.

The composition of the rock surrounding hall C has been changed from the average Gran Sasso rock mixture, as used by MACRO⁸ [174], to a carbonate rock mixture of $\text{CaCO}_3/\text{SiO}_2$ (90/10) [175], while the rock density of 2.71 g/cm^3 remains unchanged [176]. The shielding of hall C has been changed from standard concrete to a dry concrete mixture⁹ with a density of 2.30 g/cm^3 , as measured for hall C [177].

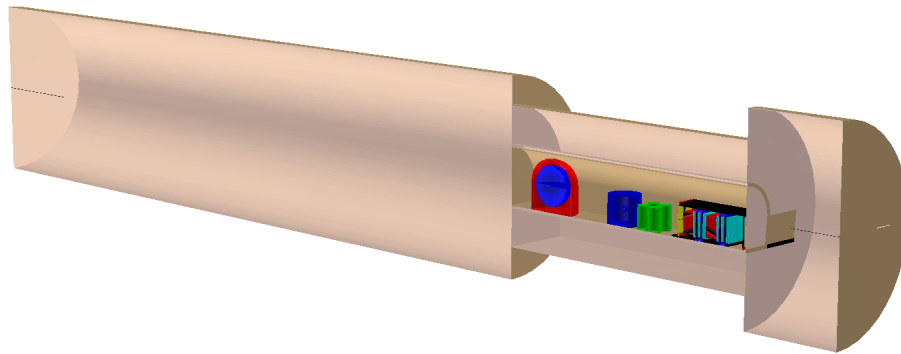


Figure 4.18: 3D view of the total geometry, as implemented in `OpGeom` (lateral cut). The walls around the BOREXINO storage tanks (green) are not shown.

The material composition of the `OPDY` geometry is given in Table 4.3. Note that the material composition does not directly reflect the MC neutrino vertex distributions which depend on the different nuclear cross sections.

⁸MACRO: Monopole, Astrophysics and Cosmic Ray Observatory.

⁹For ionization energy loss calculations, this mixture is assigned the parameters of CaCO_3 , for simplicity.

Table 4.3: Material composition of the OPDY geometry using the maximal realistic brick filling of 29–06–2009.

material	mass [kt]
Iron ^a	2.202
Lead	1.156
Aluminum ^b	0.066
Plastic scintillator	0.058
Brick components	
Plastic base	0.032
Emulsion	0.029
Nylon	0.020
Bakelite	0.021
other together ^c	< 0.035

^aMainly the magnetic spectrometers, smaller contributions from support structures surrounding the detector.

^bMainly outer scintillator boxes, drift tubes and ECC brick packaging.

^cGlass (veto), concrete (magnet base), TiO₂ (scintillator coating), adhesive tape (scintillator coating), air.

4.3 Neutrino event generator

In the scope of this thesis, the C++/ROOT–based neutrino event generator **GENIE** (version 2.6.2) is used. All physics parameters are set to the **GENIE** default values, and the default set of interactions is used (see Chapter 2). **GENIE** does not yet offer an interface to, e.g., **TAUOLA** [178] for handling polarized τ decays, nor does it create a displaced secondary decay vertex for unstable particles, like charmed hadrons or tau–leptons, decaying at generator level. This, of course, is not sufficient for the OPERA emulsion analysis, but a reasonable approximation for the electronic detector analysis. In addition to the default set of decays, within this analysis all charmed particles and neutral pions are also decayed by **GENIE**. Hence, all outgoing particles emerge from the same primary pseudo–vertex position¹⁰. All possible decay channels are open.

To make use of the full potential of **GENIE**, adjustments to the OPERA software, as well as an OPERA–specific **GENIE** event generator, named `gevgen_opera`, have been developed. The input neutrino flux from the CF06 simulation (see Section 4.1) is converted to one–dimensional ROOT histograms with a uniform bin–normalization of 0.25 GeV^{-1} for all four neutrino species and a standardized total normalization of $(\text{cm}^2 10^{19}\text{POT})^{-1}$. The input histograms are derived from

¹⁰This decision is technically motivated: All decayed particles have lifetimes $c\tau$ of less than some mm at most, which is far below the spatial resolution of the electronic detector.

the coarsely binned, statistically optimized histograms described in Section 4.1. Non-primary beam neutrinos, like ν_τ , may be specified by choosing an arbitrary input flux histogram for these neutrino species and weighting them later according to the respective physics model (e.g. neutrino flavor oscillation). Neutrinos, such as ν_e , which may originate from both the primary neutrino beam and from possible other sources like $\nu_\mu \rightarrow \nu_e$ neutrino flavor oscillations, require separate MC runs.

`gevgen_opera` uses the GENIE ROOT geometry analyzer, which propagates each thrown flux neutrino through a given ROOT geometry defined by a `TGeoManager` and calculates then the interaction probability

$$P_{int} \propto \int_{\vec{x}_0}^{\vec{x}_1} \sigma(\vec{x}) \rho(\vec{x}) \vec{x} d\vec{x} \quad (4.6)$$

along each neutrino flight path, where σ is the cross section, ρ is the material density and \vec{x} is the position within the geometry. The starting point \vec{x}_0 of each flux neutrino is generated randomly on the surface of a disc with radius R (see Figure 4.19), using the GENIE flux driver `GCylindTH1Flux`, where $(0, 0, 0)$ is the ROOT geometry origin¹¹ and $(0', 0', 0')$ is the center of the disc which is displaced by \vec{s} with respect to geometry origin. The endpoint \vec{x}_1 is the outer border of the specified ROOT geometry for a neutrino propagating along the direction $\vec{d} = (\tan(\phi_{CNGS}), \tan(\theta_{CNGS}), 1)$ (see Section 3.1.2).

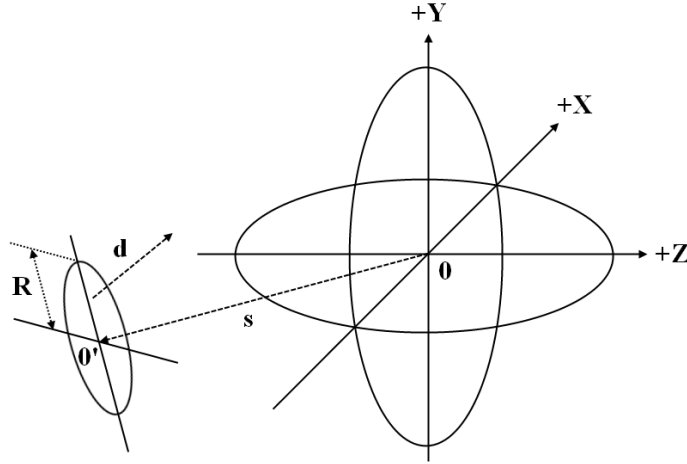


Figure 4.19: GENIE flux driver geometry used by `gevgen_opera`.

The number n_p of protons on target, corresponding to a requested number n_r of events, is calculated via

$$n_p = n_r f_s^{-1} \frac{n_n}{S}, \quad (4.7)$$

¹¹The ROOT geometry origin in `OpGeom` is placed near the center of the second magnet arm of the first OPERA spectrometer.

where $S = \pi R^2$ is the generation disc surface, f_s is a geometry- and input flux-dependent scale factor used to speed up the simulation and

$$n_n = \sum_i \int_{E_\nu} \Phi_{\nu_i}(E_\nu) dE_\nu \quad (4.8)$$

is the sum of the respective energy-integrated neutrino fluxes $\Phi_{\nu_\alpha}(E_\nu)$ specified as the generator input.

The parameters of the Monte Carlo simulations used in Section 5, Section 6 and Section 7 are $\theta_{CNGS} = +58.11$ mrad, $\phi_{CNGS} = -4.48$ mrad, $\vec{s}^{OPDY} = (0, 0, -20.0)$ m, $R^{OPDY} = 20.0$ m, $\vec{s}^{WRLD} = (0, 0, -400.0)$ m and $R^{WRLD} = 125.0$ m.

4.4 Cosmic muon generator

Cosmic muons are simulated using the `OpMult` event generator which is an adaption of a MACRO simulation code [179, 180] to the OPERA experiment [181]. It is a parametrized muon generator based on the primary cosmic ray model used in the MACRO experiment. `OpMult` is not only capable of reproducing single muons but also high-multiplicity cosmic muon events. The atmospheric charge ratio is set to $R = 1.4$. A comparison of data and the `OpMult` MC is shown in [181].

Within the scope of this thesis, all muons are generated on the boundaries of an imaginary box that is at least 13 m larger than the hall C dimensions (see Section 4.2), this value corresponds to about 35 hadronic interaction lengths in rock¹². The generated muons are then passed to the detector simulation which includes the propagation through the remaining rock and the generation of possible secondary muon-induced particles.

4.5 Detector simulation

4.5.1 OpSim and OpDigit

The OPERA detector simulation is based on `GEANT3.21` [182] and interfaced with the `GEANT3.21 VMC`¹³. The detector simulation is included in the official `OpRelease` package `OpSim`. `OpSim` has been modified to accept vertex positions generated by the event generator (see Section 4.3), instead of than placing the vertices randomly in the specified target material¹⁴.

¹²No difference of the non-muon component is observed for further increases of this value.

¹³VMC: Virtual Monte Carlo.

¹⁴For a long-distance experiment like OPERA it is mathematically equivalent to generate a neutrino interaction at a point geometry like a specified target nucleus and place the whole event into the specific geometry at a later simulation step. This approach is used when using the default OPERA event generator `NEGN`. However, this method involves extensive bookkeeping of all target materials and neutrino flavors and a non-trivial normalization factor when combining different target materials into a full sample.

During the investigation of external events, it became obvious that the muon ionization energy loss routine `GDRELX.f` needed to be modified (see Section 4.5.2). In addition to that, a long-standing issue in the OPERA collaboration has been the choice of the `GEANT3.21` hadronic event generator. A comparison of the different options is given in Section 4.5.3.

The digitization of the detector signals is performed by `OpDigit`, using parametrized response functions and the efficiencies of the subdetectors tuned to cosmic muon data [183]. Electronic noise is simulated for the PT and the TT and crosstalk of the multi-channel PMTs used in the TT, is included in the simulation.

4.5.2 Rock muons

Muons (antimuons) from ν_μ ($\bar{\nu}_\mu$) interactions in non-OPERA volumes provide the largest fraction of events detected in the OPERA detector, which requires a good understanding of the expected energy spectra. These external events, vaguely called rock muons, offer an opportunity to cross-check and understand the respective Monte Carlo simulations without using any explicit detector description. Several different physics groups have been working on this subject: Both the LVD¹⁵ [184, 185] experiment and the CNGS-FLUKA project [186] reported results comparable within the statistical errors. Previous work for the OPERA collaboration [187], using the default `OpSim/GEANT3.21`, showed a muon deficit of about 6 % for the rate of muons/m²/10¹⁹POT for both muons and antimuons when compared to the FLUKA prediction. In order to resolve this discrepancy, different Monte Carlo codes have been employed: The default `OpSim/GEANT3.21` [182], a revised `GEANT3.21` code and the MUSIC¹⁶ Monte Carlo [188].

The CNGS-FLUKA group used FLUKA to propagate the muons through a “realistic” rock composition without giving any further specifications. Neutrino interactions are generated on a nucleus with $Z = 10$ and $A = 21$, using the FLUKA-NUX event generator, the rock density is 2.765 g/cm³ and the neutrinos are directed upwards by $\theta_{CNGS} = +57$ mrad. The n-tuples provided contain about 16000 μ^- (900 μ^+), resulting in statistical errors of about 1 % (3 %) for the exiting muon (antimuon) rate.

The other simulations use the revised default CaCO₃/SiO₂ (90/10) rock composition and a density of 2.71 g/cm³ (see Section 4.2). Neutrinos are generated using GENIE with a realistic target mix and the revised neutrino fluxes (see Section 4.1). Only ν CC interactions are used as input, incoming neutrinos are directed upwards by $\theta_{CNGS} = +58$ mrad.

¹⁵LVD: Large Volume Detector.

¹⁶MUSIC: Muon Simulation Code.

It turned out that the default `GEANT3.21` implementation is not correct when used with a (pseudo)isotope-based `ROOT` geometry model¹⁷, since the ionization potential and density corrections δ used in the Bethe–Bloch equation are depending on the electron configuration of the compound, rather than on the pure physical composition of nuclei in a mixture. A modified `GDRELX.F` routine has been implemented in the revised `GEANT3.21` code, following the ionization energy loss and material property calculations given in [189].

The `MUSIC` cutoff for stochastic energy loss is set to the minimal value of $MINV = -49$ [188]. In contrast to `FLUKA` and `GEANT3.21`, `MUSIC` does not propagate any secondary particles. The secondary production of muons is very small, though, making this effect negligible for this rock muon Monte Carlo comparison. The results are corrected for wrong-sign (anti)muons produced in the primary neutrino interaction. `MUSIC`, optimized for very high energy muons of $\mathcal{O}(\text{TeV})$ and long distances of $\mathcal{O}(\text{km})$, is not expected to give very accurate results for low-energy muons¹⁸ and short distances of less than 1 m, where the sampling distance may be too small. V. Kudryavtsev has provided a modified `MUSIC` code optimized for thin layers of material [190]. However, the effect on the total event rate and the exiting muon distribution is negligible, compared to the statistical error of the simulation.

For providing a rate prediction with a statistical uncertainty of less than 0.25 %, 2×10^6 ν interactions per MC configuration have been simulated in an isotropic rock volume of 400 m length with randomly distributed vertices along an axis perpendicular to the exit plane. All distributions are normalized to an interaction rate of $r_\mu = 585.1$ events/kton/ 10^{19} POT (ν_μ CC) and $r_{\bar{\mu}} = 13.0$ events/kton/ 10^{19} POT ($\bar{\nu}_\mu$ CC) for energies $0 \text{ GeV} < E_\nu < 200 \text{ GeV}$. The `FLUKA` results have been adjusted to match the definitions used in the other simulations: The contribution of μ^- from non- ν_μ CC interactions is negligible, but the requirement $E_\nu < 200 \text{ GeV}$ reduces the μ^- -rate by 2.3 %. Applying the corresponding corrections to the antimuon result yields a reduction of 4.3 % when removing events from non- $\bar{\nu}_\mu$ CC interactions¹⁹ and an additional 3.0 % reduction from the restriction $E_\nu < 200 \text{ GeV}$.

The final corrected rates are shown in Table 4.4, where the `FLUKA` results are normalized to the `GENIE` interaction rates. The results from `FLUKA`, `MUSIC` and the revised `GEANT3.21` are compatible for both muons and antimuons, while the default `GEANT3.21` result is compatible with the previous result [187], as expected, but with none of the others. Even though the default `GEANT3.21` rate also is smaller for antimuons, the discrepancy is much weaker than for the muon result. Simulations using `MUSIC` taking into account a variation of $\Delta\theta_{CNGS} = \pm 1$ mrad show no effect of this on the muon rate. The small

¹⁷`GEANT3.21` uses tabulated values for chemical elements in the Bethe–Bloch equation.

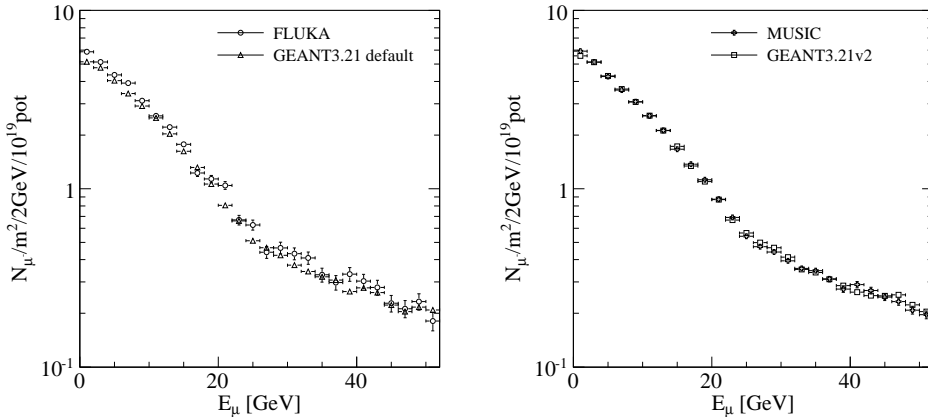
¹⁸In `MUSIC`, muons with an energy below 1 GeV purely suffer continuous ionization energy loss

¹⁹The largest fraction of antimuons results from the subsequent decays of charmed mesons produced in DIS ν_μ CC interactions.

Table 4.4: Rock muon rate for different Monte Carlo codes, statistical uncertainties only, see text for details. The fractional deviation of the different **GEANT3.21** and the **MUSIC** simulations from the **FLUKA** simulation is defined as $\Delta\mu^\pm = \frac{\mu_{\text{FLUKA}}^\pm}{\mu^\pm} - 1$.

Simulation	μ^-	μ^+	$\Delta\mu^-$	$\Delta\mu^+$
	[1/m ² /10 ¹⁹ POT]			
FLUKA	40.8±0.8	1.61±0.03	–	–
GEANT3.21 default	37.7±0.1	1.57±0.01	0.082±0.021	0.025±0.020
GEANT3.21 revised	39.8±0.1	1.64±0.01	0.025±0.020	-0.018±0.019
MUSIC	40.0±0.1	1.64±0.01	0.020±0.020	-0.018±0.019

difference in density between **FLUKA** and the other simulations introduces an additional systematic uncertainty of about 0.5 % (see below). Since exiting rock muons originate mainly from higher-energy neutrinos ($E_\nu > 5$ GeV), the difference between the **FLUKA-NUX** and **GENIE** total cross sections is small, and the leading muon energy calculation is quite similar among the different generators for these neutrino energies. Tweaking the target nucleon $A = 21$ by ± 3 does not lead to a visible change of the muon energy spectrum or the muon rate.



(a) FLUKA and default OpSim/GEANT3.21.

(b) MUSIC and revised GEANT3.21.

Figure 4.20: Comparison of different rock muon simulations, statistical errors only.

The difference between the **FLUKA** and the default **GEANT3.21** predictions is clearly visible, e.g. in the energy distribution (see Figure 4.20a), while there is excellent agreement between the **MUSIC** and the revised **GEANT3.21** simulations (see Figure 4.20b). The inconsistency observed in [187] is now fully understood and resolved by the correct implementation of ionization muon energy loss in **GEANT3.21/GDRELX.F**, as described before.

To estimate the systematic uncertainties of the muon rate and the muon energy spectrum originating from the uncertainty of the rock composition and rock density upstream of the OPERA detector, the simulations are repeated for a variety of materials and different rock densities. The uncertainty of the muon energy spectrum has been obtained by determination of

$$\Delta b(E) = \frac{\max(|N_i(E) - \langle N(E) \rangle|)_{i=1..n}}{\langle N \rangle(E)} \quad (4.9)$$

per energy bin for all n configurations, where N_i are the entries per energy bin for configuration i and $\langle N \rangle(E)$ is the mean energy bin content of all configurations.

The rock composition is varied within reasonable fractional weights and components: The fractional weights of CaCO_3 , SiO_2 and MgCO_3 have been varied from 0% to 100%, in steps of 20%, for all possible combinations. The Z/A ratio for all three materials is very close to 0.5 (the maximal deviation from 0.5 is -0.4% for pure MgCO_3), and the differences of the density corrections and ionization potentials used in the Bethe–Bloch equation are small. There is a larger variation of the Z^2/A ratio which determines the contribution from radiative energy loss processes: It varies from 4.41 (pure MgCO_3) over 5.59 (pure SiO_2) to 6.27 (pure CaCO_3).

The total muon event rates are compatible within the statistical uncertainties of the simulations, while the antimuon rate is about 5% higher for pure MgCO_3 than for pure CaCO_3 due to the higher average neutrino energy of antineutrinos in the CNGS beam and the resulting higher contribution of radiative energy loss for these events.

The uncertainties of the energy spectrum are smaller than the statistical uncertainties of the simulation when restricting²⁰ the variation to compositions that contain at least 60% CaCO_3 . Since the interaction rate ($\propto \rho$) and the muon energy loss ($\propto \rho^{-1}$) are anticorrelated, the effect of a varied density is expected to be small, and in fact no difference is visible for density variations of $\pm 5\%$.

The total systematic uncertainties of the particle energy spectrum for all external events due to uncertainties of the material composition and density are hence estimated to be 1% for muons and 2% for antimuons, where the largest effect arises from the uncertainties of the rock composition.

The distance between the production vertex and the exit plane for exiting muons is shown in Figure 4.21, and the lateral displacement is shown in Figure 4.22 (MUSIC simulation). According to this result, it is necessary to simulate at least 250 m of rock in front of the OPERA detector, while in the transverse direction, particles rarely travel more than 8 m (compare Figure 4.18).

²⁰The systematic uncertainties are larger than the statistical uncertainties only for energies above 100 GeV and mixtures that contain more than 60% MgCO_3 .

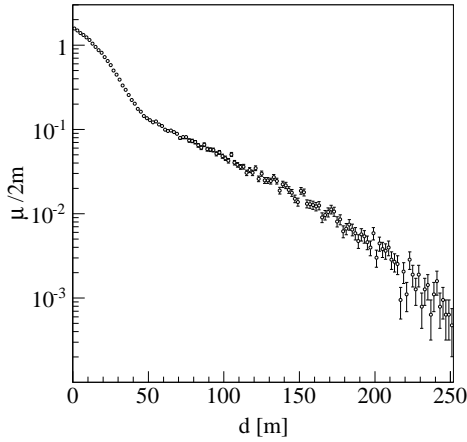


Figure 4.21: Distance between production vertex and exit plane for rock muons (MUSIC simulation).

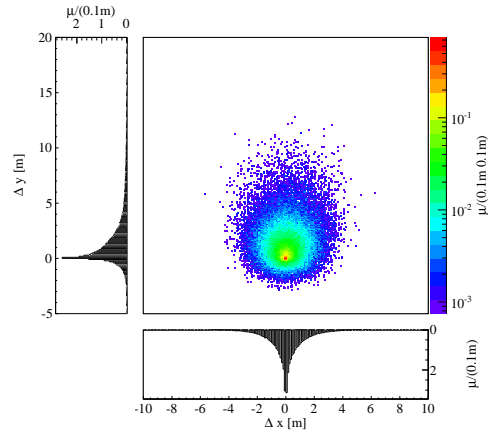


Figure 4.22: Lateral displacement of rock muons due to the neutrino beam angle and multiple Coulomb scattering (MUSIC simulation).

4.5.3 Hadronic showers

The simulation of hadronic interactions in GEANT3.21 is handled by one of three possible generators: GHEISHA [191] (the default GEANT3.21 option), GFLUKA²¹ [192] (the default OPERA option) and GCALOR [193].

In calibration measurements with the MINOS–CalDet detector in a CERN–PS test beam [42], the MINOS experiment observed the best compatibility of the detector response to charged hadrons with the GCALOR simulation. The MINOS calorimeter consists of 2.54 cm thick steel absorbers interspaced with 1 cm thick plastic scintillators, whereas the OPERA target section is built from 7.9 cm thick lead/emulsion ECCs and two layers of crossed plastic scintillators, each of them 1 cm thick. In terms of hadronic interaction lengths λ_A , the MINOS absorbers measure about $d_{MINOS} \approx 0.15\lambda_A$, whereas the OPERA brick walls amounts to $d_{OPERA} \approx 0.4\lambda_A$.

The largest part of the visible energy in neutrino interactions is produced as neutral or charged pion pairs and single baryons, where the average energy of these particles only slowly rises with the energy of the incident neutrino. The energy distributions of outgoing π^+ and protons from $\nu_\mu + {}^{208}\text{Pb}$ NC interactions for different neutrino energies are shown in Figure 4.23. The energies of hadrons produced in neutrino interactions are comparable for neutrino interactions in both MINOS and OPERA. In the absence of a dedicated calibration measurement with the OPERA detector, it is assumed to behave qualitatively similar to MINOS.

²¹GFLUKA is an old adaption of the FLUKA code from around 1993 that has little in common with the recent FLUKA simulation package.

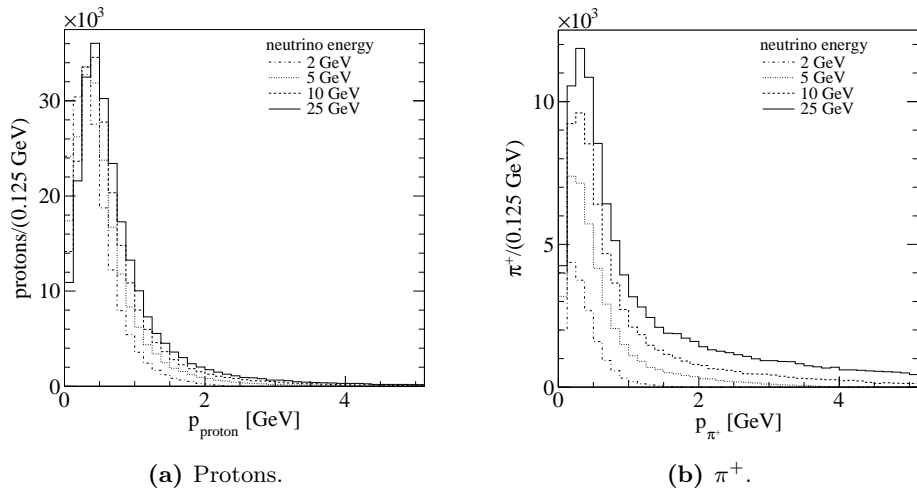
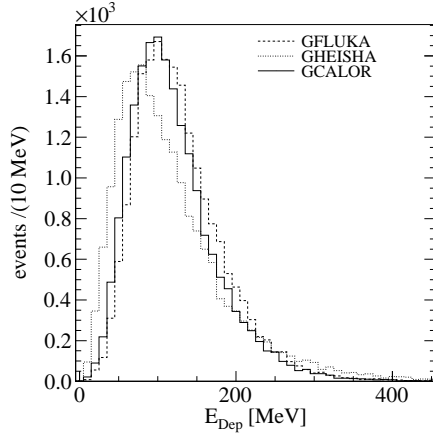


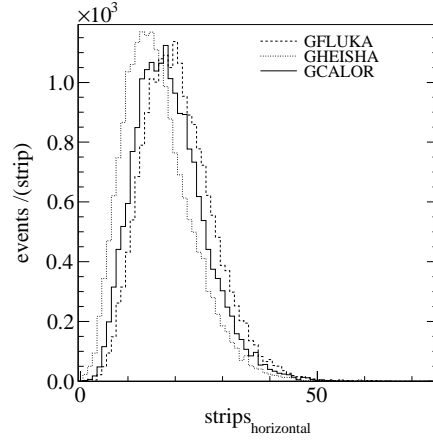
Figure 4.23: Momentum distributions of different outgoing hadrons (after final state interactions (FSI)) from $\nu_\mu + {}^{208}\text{Pb}$ NC interactions (GENIE simulation). Most of the protons emerging from the target nucleus are produced in the intranuclear cascade following the initial neutrino interaction. The neutron spectrum is similar to the proton one, whereas the energy spectrum of π^- is similar to the π^+ spectrum, with an initial excess of π^+ over π^- , as expected for NC interactions on proton targets (see Table 2.3).

The choice of the hadronic interactions generator has a direct impact on the energy reconstruction and event classification for MC data and hence indirectly also for real data that relies on MC input (see Section 5). The effect on the deposited energy, the longitudinal shower profile, the shower length and the number of hit scintillator strips is shown by the example of 3 GeV π^+ in Figure 4.24. The differences can be summarized as follows: Among the three generators, GHEISHA produces the weakest hadronic activity, manifesting in the smallest deposited energy, the smallest number of hit strips and the shortest shower lengths. GFLUKA, on the other hand, simulates the largest energy deposition and the largest number of hit strips, whereas the GCALOR result is between these two. The shower length and the longitudinal shower profile are very similar for GFLUKA and GCALOR. Above kinetic energies of about 1 GeV, the differences between these generators remain qualitatively the same for charged pions, protons and neutrons. Lower-energy protons lose most of their energy within one or two brick-walls due to generator choice-independent ionization processes, leading to only small differences between the three generators. While neutrons above about 1 GeV typically interact inelastically and create a hadronic shower, lower-energy neutrons may be absorbed or will travel long distances without losing visible amounts of energy, and the event-to-event differences are too large for the generated sample size to discern any generator differences.

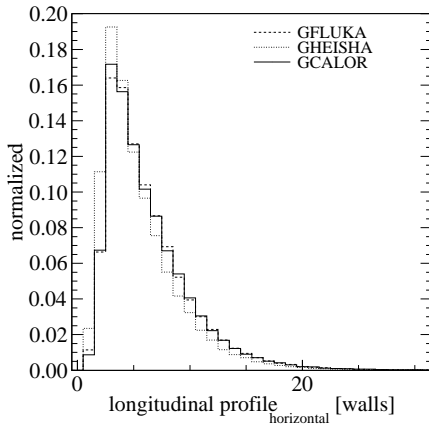
The good agreement with the MINOS measurements and the reasonable results obtained in the study described above, identify GCALOR as the preferred generator for hadronic interactions in OPERA. Unfortunately, the use of GCALOR is limited to 32-bit environments, which are not running stable within the OpRelease framework. As a result, GFLUKA is chosen as the default generator, and the differ-



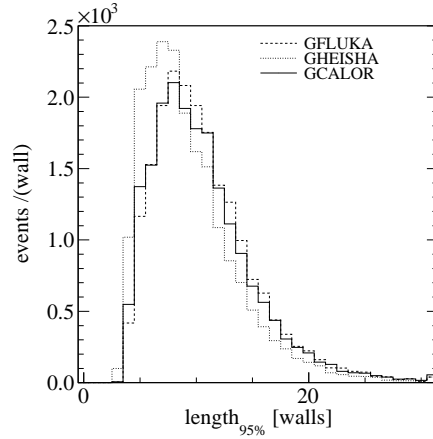
(a) True deposited energy in TT strips.



(b) Number of hit TT strips (horizontal projection).



(c) Longitudinal shower profile, defined as the fraction of the true deposited energy in each wall to the true total deposited energy in all walls (horizontal projection), averaged over all events.



(d) Shower length, defined as the number of hit walls that contain 95 % of the true total deposited energy.

Figure 4.24: Detector response to π^+ with $p = 3$ GeV in the OPERA target. Based on 20000 simulated particles with $p_T = 0$, a realistic brick configuration and a starting vertex in the center of the first target wall. The first and second target wall are not filled with bricks.

ence to GHEISHA is taken as the systematic uncertainty of the simulation. Both GFLUKA and GHEISHA have been tested to produce the same results when compiled and run on 32-bit and 64-bit systems. However, it should be noted that the OPERA brick and emulsion simulation is performed using standalone FLUKA, and not the adapted GEANT3.21/GFLUKA.

4.5.4 Electromagnetic showers

Electromagnetic cascades in neutrino interactions are mostly started by photons from π^0 decays, while the contribution of all other photon production mechanisms

from the primary neutrino interaction is almost an order of magnitude smaller (see Figure 4.25). Electrons and positrons in OPERA usually have low energies around 1 GeV and originate from short-lived particle decays. Only about 1 % of all CC events in OPERA are due to ν_e and $\bar{\nu}_e$ in the CNGS beam that result in a high-energy electron or positron in the final state, initiating an electromagnetic shower.

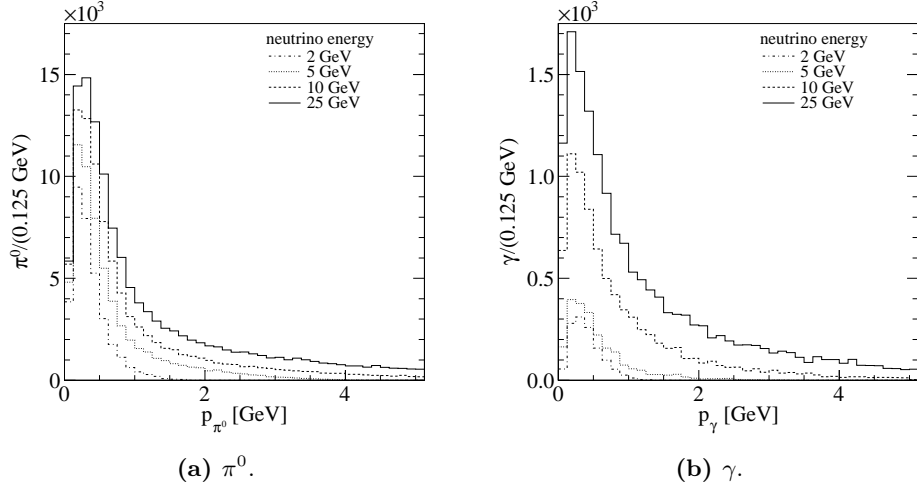


Figure 4.25: Energy distributions of outgoing π^0 and γ (after FSI) from $\nu_\mu + {}^{208}\text{Pb}$ NC interactions. Note the different scale of the two figures.

The `GEANT3.21` simulation of electromagnetic interactions is based on commonly accepted models whose theories are much better understood than the hadronic interactions. The thickness of about ten radiation lengths of each brick wall severely limits the use of the OPERA electronic detectors for the reconstruction of electromagnetic showers. Most showers from, e.g., 3 GeV π^0 or electrons are stopped within three target walls (see Figure 4.26, note that the first two target walls are empty). As was expected, for electromagnetic showers the differences of the detector response for the three different hadronic interactions generators tested Section 4.5.3 are negligible.

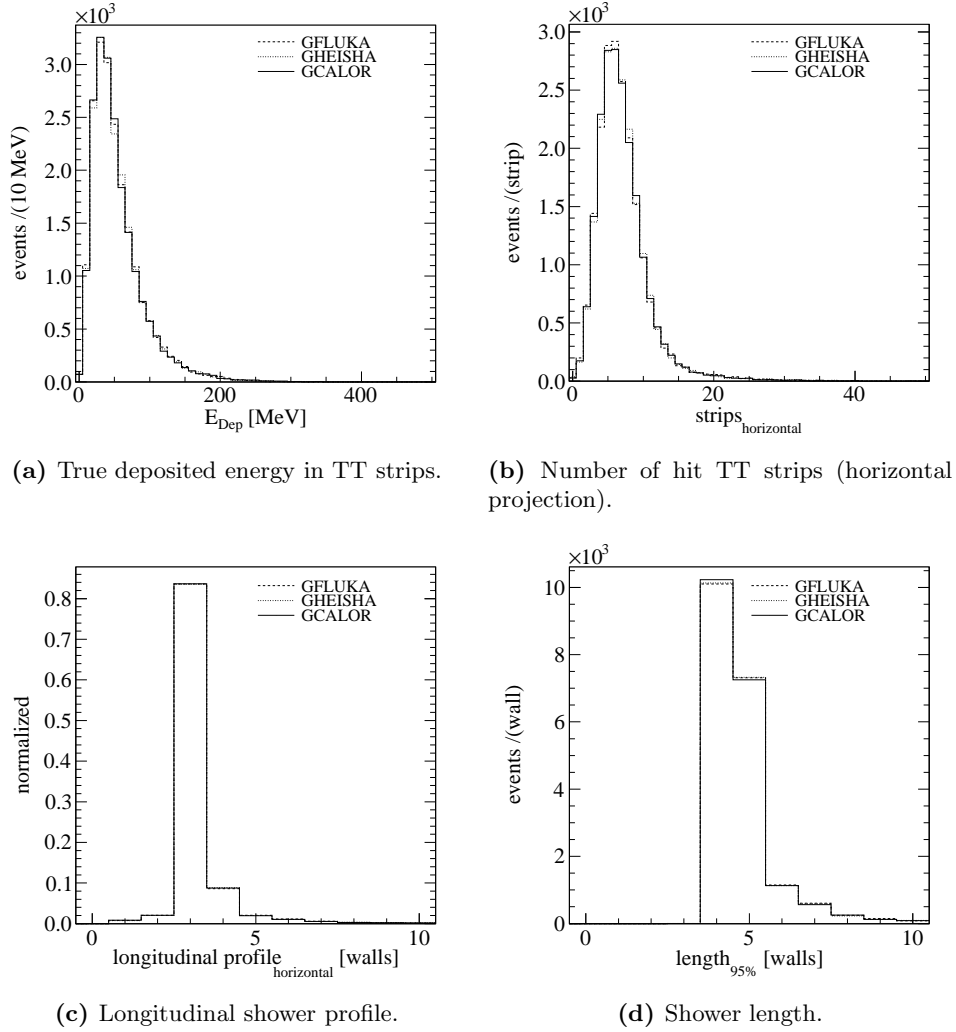


Figure 4.26: Detector response to π^0 with $p = 3$ GeV in the OPERA target. Based on 2×10^4 simulated particles with $p_T = 0$ each, a realistic brick configuration and a starting vertex in the center of the first target wall, using the same definitions as in Figure 4.24. The first and second target wall are not filled with bricks.

Chapter 5

Event reconstruction

The $\nu_\mu \rightarrow \nu_\mu$ disappearance search in OPERA is based on a measurement of the ratio of charged current events to all events in dependency of the reconstructed hadronic energy as described in detail in Section 7. This analysis requires a classification of events into either NC-like or CC-like interactions and a good hadronic energy reconstruction, especially for energies below about 10 GeV. Since NC-like interactions of neutrons and photons in the border regions of the detectors impose the largest source of background for this analysis, a good vertex reconstruction is mandatory. The data flow for Monte Carlo and real data is shown in Figure 5.1, where all reconstruction steps described within this section, in addition to the official reconstruction, are included in `MyAna`.

5.1 Official reconstruction software

The official OPERA reconstruction software for the electronic detectors is contained within the `OpRec` package that is part of the `OpRelease` framework. The highest-level output of `OpRec` is the result of a Kalman algorithm [194] yielding energy, charge and track slopes at the beginning of tracks found by a pattern reconstruction and merging in both detector projections, so-called *3D-tracks*.

The `OpCarac` [195] package categorizes events according to the event position, where *contained* is the flag for events that originate from the lead/emulsion target section and *spectro* are events originating from the spectrometers. Muons entering from the front or side are categorized accordingly. Low-energy NC-like interactions in the border regions of the target sections are categorized as *bordersoftnc*.

The `BrickFinder` package is used to predict the most probable brick for each *contained* event, for the later brick extraction by the BMM.

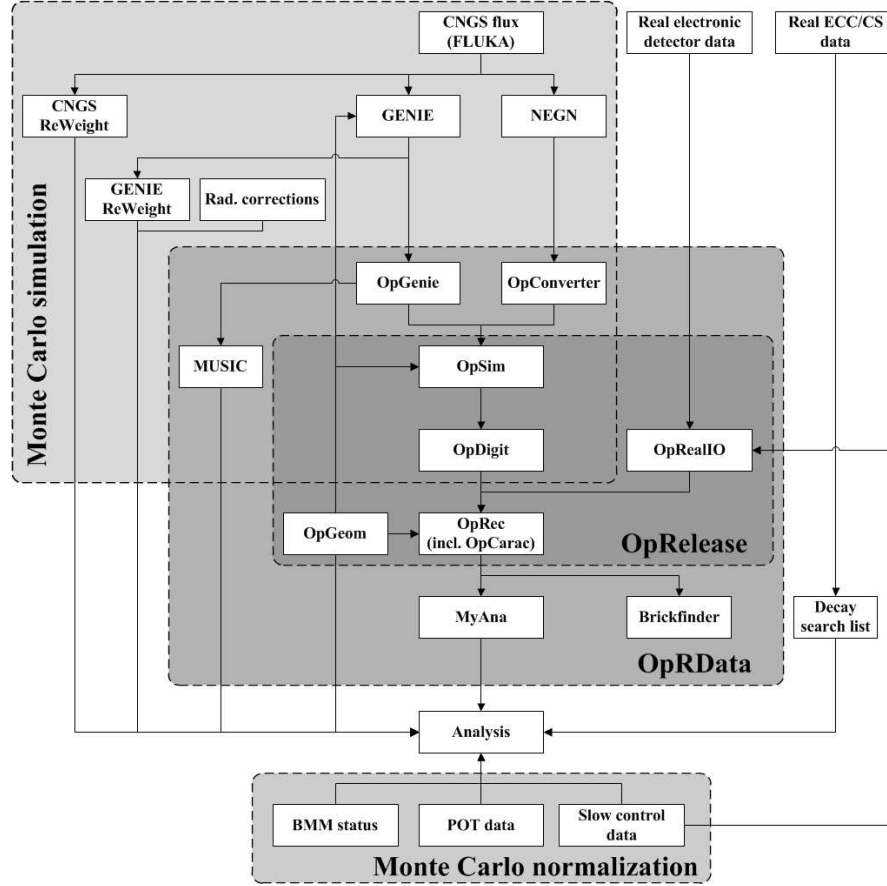


Figure 5.1: Monte Carlo and real data flow in the OPERA experiment, as used within this thesis.

5.2 Shower clustering

The coarsely segmented calorimeter of the OPERA detector is not suited to track single particles apart from muons or, rarely, pions or kaons. The outgoing particles from the primary neutrino interactions usually produce a shower-like structure composed of several overlapping initial hadronic or electromagnetic showers (compare Section 4.5.3 and Section 4.5.4).

A typical ν_μ -induced event in OPERA consists of an identified 3D-track from the charged muon (CC) and/or a shower-like structure (NC and CC), where both the track and the shower are attached to a common vertex. Ideally, the vertex is located within the target section, the track has crossed at least one spectrometer and the shower is fully contained within one target. An example of such an event is shown in Figure 5.2. The separation of hits belonging to the primary shower and to secondary showers (e.g. from neutral hadrons), the removal of uncorrelated energy depositions (e.g. from electronic noise or natural radioactivity) and the recognition of hits that are shared between the 3D-track and a shower in the

track–shower overlap region, are the main motivation for the use of a shower pattern recognition, also called clustering algorithm.

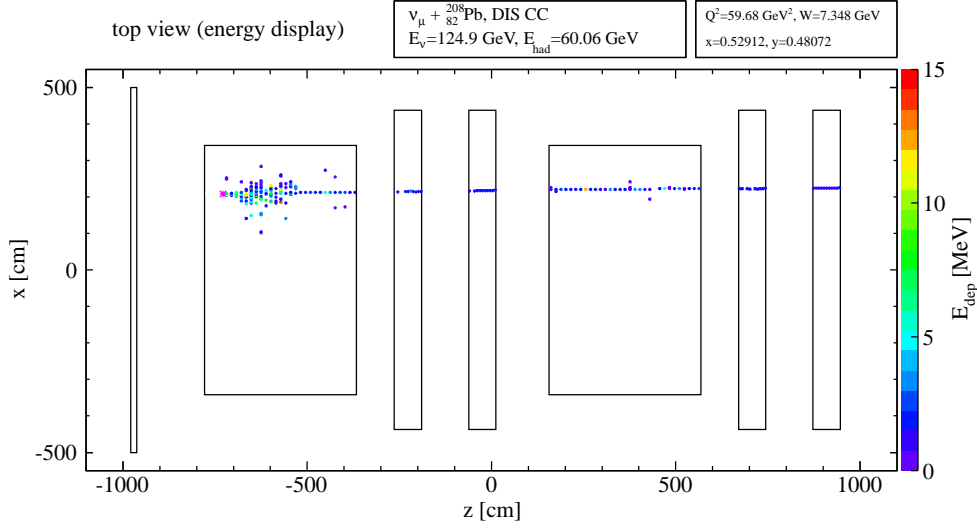


Figure 5.2: Example of a ν_μ CC interaction (MC) in the electronic detector. The color shows the reconstructed deposited energy (TT only). The true vertex position is marked by a magenta star.

5.2.1 Track completion

Each event is processed by a pattern recognition included in `OpRec` to find particle tracks. These tracks consists of a list of detector digits¹ that are connected to form a track. Inefficiencies, missing DAQ sensors or digits removed from the track by the Kalman algorithm may lead to missing TT or RPC planes in a track. The clustering algorithm described below shows a more stable behavior if the primary track is gap-less, hence a *track completion* algorithm is performed for the longest 3D-track of an event to recover those missing digits. The longest track of an event is also called leading track or first track in the following.

Every gap of three or fewer planes inside a track is checked in every missing plane for recorded digits at a distance of maximally two times the respective strip width from the expected digit position. The digit that is closest to the ideal position is added to the track. If no digit fulfills this requirement, a so-called *fake digit* is added at the ideal position. Fake digits have zero deposited energy, but behave like regular track digits in all other regards of the clustering described below. The same procedure is repeated at both ends of the track. A thus completed track is not reprocessed for the track kinematics but used within shower clustering and track removal only.

¹A digit is the smallest digitized readout unit of the OPERA detector.

5.2.2 Clustering

The task of assigning each hit detector strip to a certain cluster is partially solved by means of a two-dimensional cellular automaton. A cellular automaton consists of cells that are arranged on a (usually regular) grid, where each cell is in one of a finite number of states. A cellular automaton evolves iteratively, where the state of each cell c at iteration $(n + 1)$ is determined by the states s of all neighbor cells at iteration n and a set of rules that act on the states s . The neighbors and the set of *evolution rules* thus define the behavior of the cellular automaton.

Cells are represented by TT and RPC readout strips² that are arranged on a gapless cartesian grid with (planes×strips) positions for each orientation (horizontal and vertical)³. The grid is divided into six sub-grids for each orientation, one grid for each target section and for each spectrometer arm.

The following set of evolution rules has been found to be only weakly dependent on the explicit choice of the Monte Carlo implementation of hadronic interactions and detector response. It requires a *two-dimensional connected* definition of neighborhood to result in a steady state with all cells tagged after a finite number of steps. A neighborhood is defined as *connected* if all neighbors share at least one corner or side with another neighbor or the center cell. A neighborhood of a center cell at position (i', j') is defined as *two-dimensional* if there is at least one neighbor at the positions $(i_1 > i', j_1)$, $(i_2 < i', j_2)$, $(i_3, j_3 > j')$ and $(i_4, j_4 < j')$. A *mirror-neighbor* is given by the point reflection of a neighbor's coordinates across the center cell.

All cells that belong to the longest 3D-track (if any) after track completion, are marked as belonging to a track. The following set of rules is then applied to each cell, starting at a random cell at the grid and proceeding through all cells in an arbitrary pattern. If the algorithm has processed all cells, it is executed again with a random starting cell, until all cells are either tagged or marked or tagged and marked.

Rule 1: If the cell is already tagged or the cell has no deposited energy, do nothing and continue to the next cell.

Rule 2: If the cell is not marked and the cell is a local maximum of energy deposition within its neighborhood, tag the cell as *seed*. If there is already a cell tagged as *seed* in the neighborhood, remove the *seed*-tag from the cell with the smaller energy deposition and continue to the next cell.

²The RPC strips used here are not the physical readout strips but the reconstructed position, which can be either a physical strip or a position between two readout strips, thus roughly doubling the options of possible positions.

³A cartesian grid allows the usage of efficient and simple computer operations, since every cell may be addressed by two integer numbers i and j , but includes a mapping function $f_{x/y,z \rightarrow i,j}$ from the physical coordinates $(x/y, z)$ of the strips to the cartesian grid coordinates (i, j) .

- Rule 3: Remove neighbors with $j(i) > j_{track}(i)$ from the mirror-neighborhood if $j' < j_{track}(i')$ and neighbors with $j(i) < j_{track}(i)$ from the mirror-neighborhood if $j' > j_{track}(i')$, respectively, and continue with the next rule. $j_{track}(i)$ is a tagged cell belonging to a track at the position $j_{track}(i)$.
- Rule 4: If the cell has one or more tagged but not marked mirror-neighbors with the same tag, tag the cell with the not-marked mirror-neighbors tag and continue to the next cell.
- Rule 5: If the cell has more than one tagged but not marked mirror-neighbors with different tags, tag the cell with all tags of the not-marked mirror-neighbors.

An intuitive choice of a connected two-dimensional neighborhood are all cells that share either a side or a corner with the central cell (see Figure 5.3a). The used neighbor definitions are shown in Figure 5.3b (RPC) and Figure 5.3c (TT). These shapes approximate the intuitive neighborhood definitions (see Figure 5.3a (TT)) for the OPERA geometry. Including one additional neighbor in the center position (TT only) increase the performance of the muon-removal algorithm as described below.

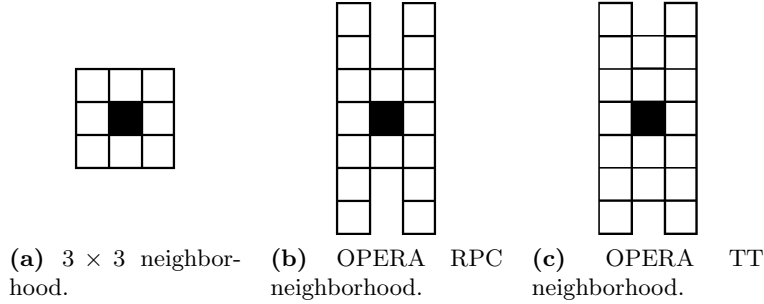


Figure 5.3: Different neighbor definitions.

All clusters obtained by the evolution rules described above are combined into superclusters if the minimal distance⁴

$$d_{c_1 c_2} = \Delta j + |(\Delta i - k_1)|k_2 + \Delta i k_3, \quad (5.1)$$

$$\Delta j = |j_{c_1} - j_{c_2}|, \quad (5.2)$$

$$\Delta i = |i_{c_1} - i_{c_2}|, \quad (5.3)$$

between two cells c_1 and c_2 of clusters C_1 and C_2 is equal to or less than d' , with $k_1 = 2$, $k_2 = 2$, $k_3 = 0$, $d' = 6$ and $\Delta z \leq 2$. Note that different combinations of neighbor and distance definitions may reach the same final configuration.

Finally, superclusters in the different sub-detectors (but not different orientations) are merged if their respective starting and ending plane do not differ

⁴The distance definition is intentionally not simplified to enhance comprehensibility.

by more than three planes, the upstream supercluster has more than one cell, and the minimum angle between the connection line between any two cells of the different clusters and the z -axis is less than 45° . After completion of clustering, each cell belongs to a track or exactly one supercluster and each cell belonging to a supercluster belongs to at least one cluster.

An example of an event after clustering is shown in Figure 5.4.

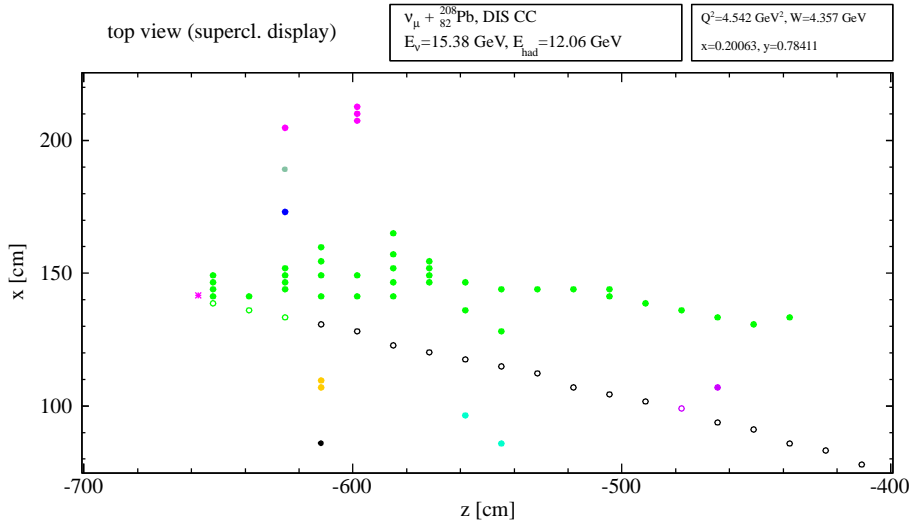


Figure 5.4: Example of a ν_μ CC interaction (MC) in the electronic detector after clustering. The color shows the different superclusters, empty circles are cells belonging to the leading 3D-track. The true vertex position is marked by a magenta star.

5.3 Preprocessing

Events without TT digits in both projections of either the first or the second super module are removed from the analysis⁵. Furthermore, the result of the clustering algorithm is used to preprocess every event before passing it to the subsequent reconstruction steps. All superclusters with no more than two cells and superclusters with a length of one wall and equal or no more than three cells are removed from an event. If such superclusters contain marked track cells, these cells are re-added to the event.

The first plane p_1 of an event is defined as the first plane in z that contains a TT digit (if any) after the removal of small superclusters as explained above. The first plane of an event is usually but not necessarily the first plane of the leading 3D-track (if any) and usually but not necessarily the plane downstream of the neutrino vertex (see Section 5.7). The downstream two planes p_2 and p_3 of the first plane are checked for possible TT digits, where the plane-ID p_i is set to -1

⁵Technically, these events are assigned to the non-fiducial volume category (see Section 5.6).

if no digit was found. This information is used to classify the events in different walltypes:

Type 1: $p_1 = p_2 = p_3 = -1$ (no TT digits),

Type 2: $p_2 = p_3 = -1$ (only one plane),

Type 3: $p_3 = -1$ (two adjacent planes),

Type 4: $p_2 = -1$ or all $\neq -1$ (three planes).

The largest supercluster in terms of reconstructed deposited energy that starts within the six planes downstream of the first plane, is called the primary shower of an event.

An example of an event after preprocessing is shown in Figure 5.5.

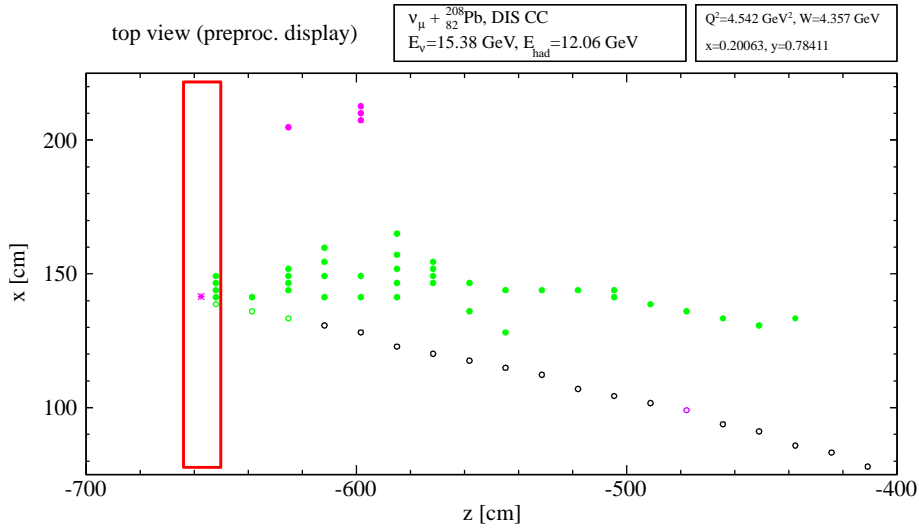


Figure 5.5: Example of a ν_μ CC interaction (MC) in the electronic detector after preprocessing (same event as shown in Figure 5.4). Different colors indicate different superclusters, where the primary shower is marked green and the red box outlines the first plane of the event. The true vertex position is marked by a magenta star.

5.4 Muon removal

If an event contains a reconstructed 3D-track, all energy depositions associated with this track are removed from any cluster or adjusted under the assumption that the track is produced by a muon. This procedure is called *muon removal (MR)* and aims at a separation of the track and the hadronic shower.

All digits associated with the completed leading 3D track (see Section 5.2.1) are removed completely from the event if they do not belong to any supercluster.

Delta-rays and inelastic photonuclear interactions of the muon may lead to energy depositions that are connected to the muon and not the hadronic system of the event. The former typically lead to small superclusters that contain three track cells and one or two attached non-track cells. Non-track cells of superclusters with no more than five cells in total and a fraction of track cells above 0.6 are removed completely if the first plane of that supercluster is more than four planes away from the first plane of the event. If the first plane of a supercluster that contains at least one track cell is more than six planes away from the first plane of the event, all cells of that supercluster are removed.

The treatment of the remaining track digits is different for TT and RPC. TT digits are adjusted by subtracting the energy deposition of a *minimum ionizing particle (MIP)* in a scintillator strip⁶ (see Section 3.2.2) from the measured energy E_0 of the respective digit. The distance travelled in the strip is corrected by the reconstructed 3D track slope at the strip center using the adjacent track digits, resulting in an expected E_{loss} . If $E_0 < (1.3 \times E_{loss})$, the digit is removed completely, otherwise the strip energy E_0 is replaced by $(E_0 - E_{loss})$. The number of photoelectrons in both PMTs is adjusted accordingly using the reconstructed position in the strip.

RPC digits are adjusted by lowering the cluster size by two (three) for vertical (horizontal) oriented strips and removing the strip completely if the remaining cluster size is equal to or less than zero. This correction is less important than the one for the TT since the RPC strips contribute only to a lesser extent to the vertex and energy reconstruction.

An example of an event after muon removal is shown in Figure 5.6. If not stated otherwise, all reconstructed variables that depend on the hadronic shower are based on the muon-removed events as outlined above.

⁶Using pure polystyrene with $(dE/dx)_{MIP} = 1.938 \text{ MeV cm}^2/\text{g}$ and $\rho = 1.060 \text{ g/cm}^3$ [196].

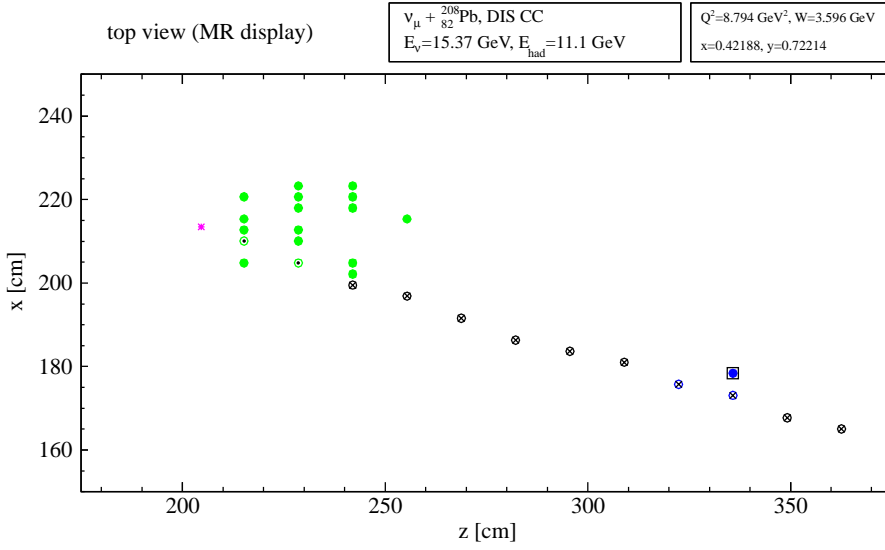


Figure 5.6: Example of a ν_μ CC interaction (MC) in the electronic detector after muon removal. Removed digits are marked by a black cross (track digits) or a black box (detached clusters). Energy-adjusted digits are indicated by a black dot inside the circle. The true vertex position is marked by a magenta star.

5.5 Hadron shower axis

The spatial resolution of the TT is about 2.6 cm and hence not suited for the reconstruction of single particle tracks in the close proximity of the primary vertex. However, the shower axis of the hadronic shower is expected to point to the neutrino vertex (see Section 5.7). The direction of the hadronic shower, which is expected to point in the opposite direction of the outgoing lepton in the projection to the plane perpendicular to the incident neutrino direction, is used to distinguish between NC-like and CC-like events (see Section 5.8).

The hadronic shower axis is reconstructed as a straight line, separately for both detector projections. Apart from detector noise, which does not belong to the physical event by definition, hadronic showers exhibit large fluctuations and outliers that violate the requirement of (approximately) normally distributed residuals of a *least squares fit (LSF)*. Instead of minimizing the sum of squares

$$\sigma^2 = \frac{\sum_{i=1}^n r_i^2}{n} \quad (5.4)$$

of the residuals r_i , an *iteratively reweighted least squares fit (IRLF)* is used, as outlined below [197].

The fit is initialized by a weighted straight line fit parallel to the z axis⁷, where the weights are given by $w_i = A_i$ (see below). The residuals r_i obtained in the initialization step, are *adjusted* by

$$a_i = \frac{r_i}{\sqrt{1 - h_i}}, \quad (5.5)$$

where

$$h_i = \frac{1}{n} + \frac{(z_i - \bar{z})^2}{\sum_i (z_i - \bar{z})^2} \quad (5.6)$$

are so called *leverages* that de-weight the influence of points far away from the bulk of detector hits. The adjusted residuals are furthermore standardized via

$$s_i = \frac{a_i}{1.4826m}, \quad (5.7)$$

where m is the *median absolute deviation (MAD)* of the residuals r_i . The numerical factor 1.4826 is introduced to recover the standard deviation from the MAD in case of normal distributed residuals.

This robust fit uses Tukey's bi-weights [197]

$$w_i = \begin{cases} A_i \left(1 - \frac{s_i^2}{K_T^2}\right)^2 & |s_i/K_T| < 1, \\ 0 & |s_i/K_T| \geq 1 \end{cases} \quad (5.8)$$

with a tuning constant $K_T = 4.685$. A_i depends on the detector subtype and is given by

$$A_i^{TT} = \left(\frac{E_i}{E_{max}}\right)^k \quad (5.9)$$

for TT cells, where i is the cell index and E_i is the deposited energy in the i -th cell and

$$A_i^{RPC,v} = \left(f_v \frac{C_i}{C_{max}}\right)^k \quad (5.10)$$

for RPC cells, where C_i is the RPC cluster size (see Section 3.2.3) of the i -th cell and in both cases $k = 0.25$. f_v is an approximate normalization factor to account for the difference of deposited energy and RPC cluster size, set to $f_v = 1.1$ and $f_h = 0.7$ for vertical and horizontal strips, respectively. All fits are performed using MINUIT.

After the track has been identified by a pattern recognition, the direction of the outgoing lepton is reconstructed by a Kalman algorithm. Since the outgoing lepton is not subject to intranuclear rescattering and usually produces straight tracks, the leading track can be reconstructed with much higher accuracy than the shower axis. Even if the leading track does not belong to the primary lepton

⁷This initialization makes short showers more robust against a wrongly reconstructed shower axis that is almost parallel to the x (or y) axis.

but another high-energy particle, it is likely to point towards the vertex.

The residual distance between the reconstructed hadronic shower axis and the true neutrino vertex is shown in Figure 5.7a, and the residual distance between the leading track and the true neutrino vertex is shown in Figure 5.7b. The difference between the reconstructed shower axis direction⁸ and the true hadron direction is shown in Figure 5.8a, and the difference between the reconstructed track direction and the true lepton direction is shown in Figure 5.8b.

The robustness of the shower axis reconstruction can be enhanced by lowering the tuning constant K_T or by removing non-primary superclusters from the event. A comparison of different methods is shown in Table 5.1. The best performance is given by IRLS using the primary showers only for determining the distance to the vertex, called nominal vertex method, and by robust fitting, i.e. without iteration, using all showers for determining the shower direction, called nominal direction method. Using an iterative fit slightly improves the vertex reconstruction but worsens the shower direction reconstruction.

If both a 3D-track and a hadronic shower are reconstructed, the 3D-track information is weighted by 0.6 and the shower information by 0.4. These weights have been found by minimization of the RMS_{50} of the vertex reconstruction for the nominal vertex method.

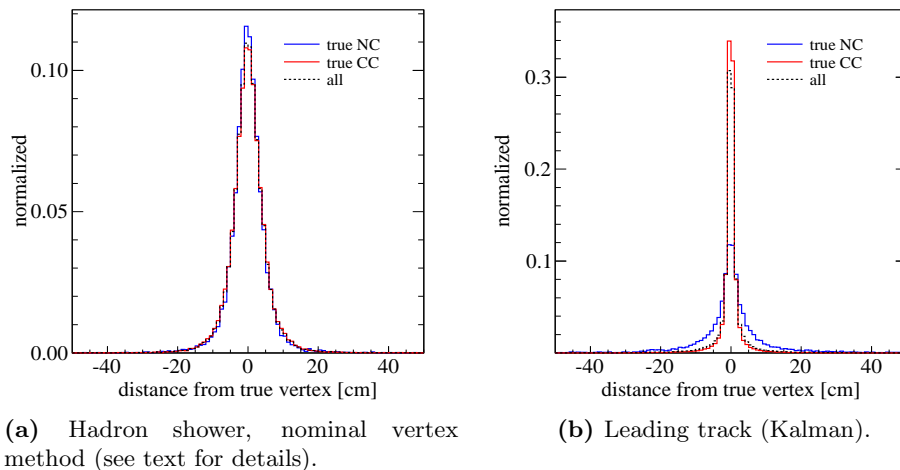


Figure 5.7: Distance between the reconstructed shower axis (a) or the leading track (b) and the true vertex in the xz -plane for ν_μ events generated in both target sections. The resolution and mean are very similar in the yz -plane. The leading track distance for true NC events usually is not associated with a lepton but with a high-energy pion, while for true CC events it usually belongs to the primary muon, explaining the difference in the distributions.

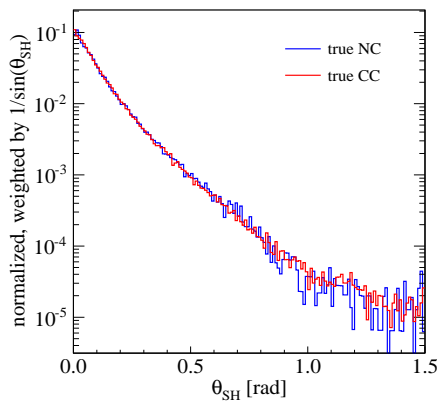
⁸Note that the shower direction reconstruction is intrinsically limited by intranuclear rescattering, absorption of low-energy particles in the passive material, particles exiting under large angles with respect to the beam direction and escape of neutral particles.

Table 5.1: Comparison of different shower axis reconstruction methods in the horizontal plane (i.e. xz plane) for the primary shower (PS) or all showers (All) of the respective event. The resolutions in the vertical projection are about 0.1 cm worse, due to the larger RPC strip distance in that projection. RMS_x is the RMS of the distribution including distances d in the range $-x < d < x$. $f_{0.1}$ ($f_{0.5}$) is the fraction of events with an angle between the reconstructed shower axis and the true hadron direction of less than 0.1 rad (0.5 rad). Ordinary, non-robust LSFs use the energy/cluster size weights A_i only. The best values are indicated by bold letters.

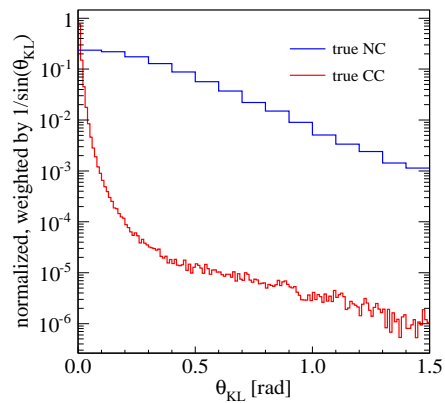
method	RMS_{10} [cm]	RMS_{25} [cm]	RMS_{50} [cm]	$f_{0.1}$	$f_{0.5}$
^a PS, $K_T = 4.685$, iter., $k = 0.25$	3.6	4.7	5.1	20.8	87.1
All, $K_T = 4.685$, iter., $k = 0.25$	3.8	5.2	6.0	27.3	89.9
PS, $K_T = 4.685$, $k = 0.25$	3.8	4.9	5.3	21.1	88.2
^b All, $K_T = 4.685$, $k = 0.25$	4.0	5.6	6.4	27.6	90.5
PS, $K_T = 2.685$, $k = 0.25$	3.7	4.8	5.3	21.7	88.8
PS, $K_T = 6.685$, $k = 0.25$	3.9	5.1	5.5	20.3	88.1
PS, ordinary LSF, $k = 0.25$	4.3	5.8	6.3	–	–
All, ordinary LSF, $k = 0.25$	4.6	6.8	7.9	–	–
PS, $K_T = 4.685$, $k = 0.5$	3.8	5.2	5.8	20.3	86.2
All, $K_T = 4.685$, $k = 0.5$	3.9	5.8	6.9	27.2	89.4
PS, $K_T = 4.685$, $k = 1.0$	3.8	6.1	7.4	17.8	81.2
All, $K_T = 4.685$, $k = 1.0$	4.0	6.4	8.4	24.9	86.6

^aNominal vertex method.

^bNominal direction method.



(a) Hadron shower, nominal direction method (see text for details).



(b) Leading track (Kalman).

Figure 5.8: Angle between the reconstructed shower axis and the true hadron direction (a) and angle between the leading track and the true lepton direction (b) for ν_μ events generated in both target sections. The entries have been scaled by $1/\sin(\theta)$ to account for the solid angle.

5.6 Fiducial volume

The OPERA detector exhibits several features that are uncommon for massive neutrino detectors⁹. Firstly, the OPERA detector is not designed for high uniformity but it is divided into two super modules built from both two different target materials and detector types: lead/TTs and magnetized iron/RPCs. The TTs offer a direct energy measurement, whereas the RPCs provide only a coarse information about the deposited energy given by the electric discharge cluster size, which is approximately proportional to $\log(E_{dep})$. Contrary to the TTs, no calibration system exists for the RPCs making them thus sensitive to changes of operation parameters¹⁰. The agreement between simulation and real data for the RPC cluster size is poor [159], making the introduction of normalization factors between deposited energy (TT) and cluster size (RPC) impossible. Hence, only the strip count and not an energy-related quantity is used for RPC-based calorimetry within this thesis.

The second issue affects the target section. About 25% of the target are instrumented with TTs but not filled with ECC bricks. Treating the targets as a homogeneous sampling calorimeter will thus lead to an overestimation of the hadronic energy and related variables for events leaking into the non-filled target sections. This issue is partially addressed during the reconstruction of 3D-tracks, since the Kalman algorithm uses the initialized MC detector geometry including the actual brick positions. Given the typical event kinematics in OPERA, the largest impact is expected for low-energy events occurring in the downstream parts of the target section, where two completely unfilled and not accounted for target walls will bias any energy reconstruction.

The third difficulty is a unique property of the OPERA detector: The OPERA target mass decreased by about 3% per year, due to extracted and not re-inserted bricks¹¹. This brick reduction mostly affects the border regions of the targets, since the target section is intentionally kept as compact as possible and in approximately cuboid shape.

Both target-related difficulties can be addressed by the introduction of a super module-dependent *compact target volume (CTV)*, defined as the largest cuboid shaped volume that is to at least 99% filled with bricks. Within the CTV, the brick configuration is approximately stable and thus the assumption of a homogeneous sampling calorimeter is valid. While the CTV definition, in principle, varies each day, no significant difference in the distributions of CTV-dependent event variables can be observed when the CTVs are defined on a yearly-

⁹Uniform tracking calorimeters, mostly build from magnetized iron, have a long tradition in neutrino physics with experiments like CDHS, CHARM, CCFR/NUTEV or MINOS (compare Section 2 for details).

¹⁰In addition, spatial inhomogeneities have been observed in proximity to the gas connectors, causing a decrease of efficiency.

¹¹This effect is not included in the Kalman algorithm per default, as it does not load a time-dependent brick configuration.

average basis, as given in Table 5.2 and used within this thesis. In addition to the CTV, which defines the applied target calorimeter dimensions, further *fiducial volumes (FVs)* are defined relative to the CTVs as given in Table 5.3.

Table 5.2: Compact target definitions of the first and second SM during the different CNGS run periods. The given numbers indicate the first filled position of the target, where columns are counted from 1 to 52 (rock to corridor), rows from 1 to 64 (bottom to top), and walls from 1 to 31 (front to back).

	column		row		wall	
	rock	corridor	bottom	top	front	back
2009 ^a	1/1	52/52	5/5	58/56	3/4	29/29
2010	1/1	52/52	5/5	58/55	3/5	29/29
2011	1/1	52/52	5/5	58/55	4/6	29/29
MC reference ^b	1/1	52/52	4/4	58/56	3/4	29/29

^aThe target of the first SM (rock side) was partially unfilled during the first days of the CNGS run 2009.

^bTarget configuration of 29-06-2009.

Table 5.3: Fiducial volume definitions of the first and second SM during the different run periods (see Table 5.2 for definitions).

	column		row		wall	
	rock	corridor	bottom	top	front	back
2009	3/3	50/50	7/7	56/54	4/5	24/24
2010	3/3	50/50	7/7	56/53	4/6	24/24
2011	3/3	50/50	7/7	56/53	5/7	24/24
MC reference	3/3	50/50	6/6	56/54	4/5	24/24

5.7 Vertex reconstruction

The reconstruction of the neutrino vertex is a crucial part of the OPERA experiment, since the whole emulsion reconstruction relies on the prediction of the so-called candidate brick that contains the primary interaction vertex. The electronic detector vertex reconstruction is limited by a process called *backscattering (BS)*, where final state hadrons are emitted in the backward direction with respect to the neutrino momentum. Backscattering is only possible on nuclear targets and scales with neutrino momentum and nuclear number A . An example event with BS is shown in Figure 5.9. Vertex reconstruction along the z -direction, i.e. parallel to the neutrino momentum, reduces to the identification of the interaction brick wall, hence called *brickfinding (BF)*.

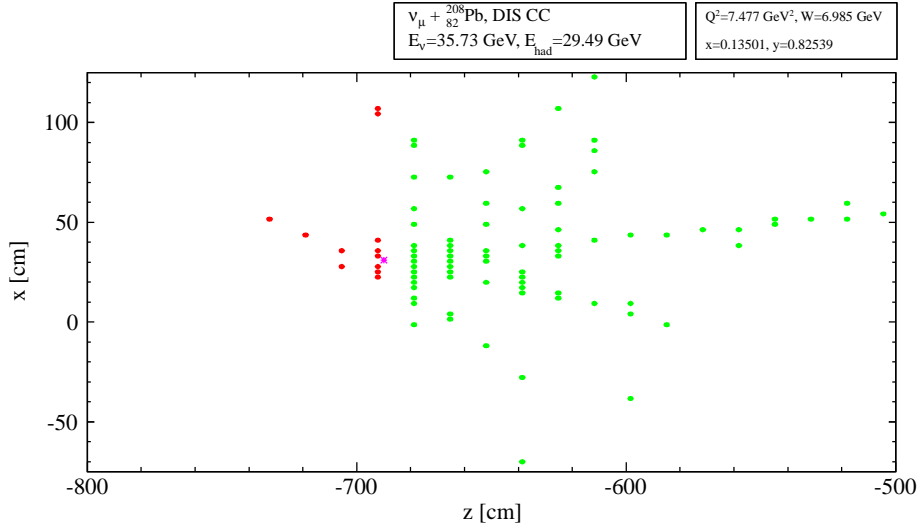


Figure 5.9: Example of a ν_μ CC interaction (MC) with backscattering in the electronic detector. Digits from backward-propagating particles are red, digits from forward particles are green. The true vertex position is marked by a magenta star.

For the analysis conducted within this thesis, the well-tested idea, but not the actual implementation of the existing `WallFinder`, as part of the `BrickFinder`, is used. It applies a *multivariate analysis (MVA)* using a *artificial neural network (ANN)* with up to 19 input variables and results in a ranked list of most probable target walls. The input variable definitions used within this thesis are the same, but there are differences in the data preprocessing, the hadronic shower reconstruction and, especially, the Monte Carlo training sample¹². In contrast to the existing vertex reconstruction, all events and not only those tagged *contained* by `OpCarac` are processed.

Within this thesis, the algorithm is implemented as a multi-target classification based on a back-propagation-trained TMVA-MLP¹³ ANN [198, 199]. Events are classified according to their relative wall position within the selected up to three first walls of the event (see Section 5.3). The different input variables for the ANN aim to cover the full event kinematics close to the vertex, using information from both the 3D-track and the hadronic shower. All variables described below include track digits and make no use of the CTV definition but use all TT digits.

Number of digits The first set of variables (up to three) are the numbers of digits N_w per wall $w = (1, 2, 3)$, where the number of digits in the horizontal and vertical projections $p = (h, v)$ are added: $N_w = \sum_p N_w^p$.

¹²The existing `BrickFinder` uses a NEGN-based simulation of neutrino interactions in lead, whereas `GENIE` interactions in the whole target section (lead, emulsion, TTs, ...) are used in this thesis.

¹³This is the recommended and fastest ANN implementation available in `TMVA4.1.2`.

Number of photoelectrons The second set of variables (up to three) are the numbers of photo electrons $(N_{pe})_w$ per wall: $(N_{pe})_w = \sum_p (N_{pe})_w^p$.

Spatial dispersion The third set of variables (up to three) are the spatial dispersions D_w of digits per wall: $D_w = \sqrt{\sum_p (D_w^p)^2}$, where $D_w^p = (\sum (x_w^p)^2 - N_w^p (\bar{x}_w^p)^2) / (N_w^p - 1)$. \bar{x}_w^p is the mean value of all digit positions in the w -th wall and $D_w^p = 0$ for $N_w^p = 1$.

Track digits The 4th set of variables (up to three) are the presence or absence of digits (including track digits) within $\pm(1.5 \times \text{strip width})$ around the reconstructed 3D track direction (if any) per wall.

Distance to shower axis The 5th set of variables (up to three) are the adjusted mean distances \bar{d}_w between all digits and the shower axis (if any) per wall: $\bar{d}_w = \sqrt{\sum_p (d_w^p / N_w^p)^2}$, where $\bar{d}_w^p = \sum (x_w^p - S_w^p) / (\sqrt{(m_S^p)^2 + 1})$ and m_S is the slope of the shower axis.

Ratio of digits The 6th set of variables (up to two) are the ratios of digits $N_{2/1} = N_2 / N_1$ and $N_{3/2} = N_3 / N_2$ per wall, with N_w as defined above.

Ratio of energies The 7th set of variables (up to two) are the ratios of energies $E_{2/1} = E_2 / E_1$ and $E_{3/2} = E_3 / E_2$ per wall, with the energy E_w defined analogously to N_w .

Maximum digit number The 8th variable is the distance between the first wall and the wall with the highest number N_w of digits.

Maximum energy deposition The 9th variable is the distance between the first wall and the wall with the maximal energy deposition E_w .

The training sample is composed of about 2.2×10^5 ν_μ events (all interactions, both true NC and true CC) with a true vertex in the fiducial volume¹⁴. The ANN training is performed for events of walltype 3 and walltype 4 separately, where the first type uses 9 input variables for the ANN and the latter one 19. The first ANN consists of two hidden layers of nine neurons each, whereas the second one uses two layers of 19 neurons each. These parameters have been varied within reasonable range to find the optimum number of hidden layers and neurons.

Events of walltype 2 are assumed to have a vertex in the wall of activity, whereas walltype 1 events are assigned to the non-fiducial volume category. Walltype 3 events do not make use of the variables *track digits* and *distance to shower axis*, since these have been found to have only little impact on this kind of events. By doing so, the required training sample is reduced significantly, since

¹⁴This does explicitly include non-brick volumes like the TTs and non-lead targets.

walltype 3 events only account for about 1% of all events. The ANN has also been trained with more output targets to account for a vertex position outside the first three walls without changing the number of input variables. While some improvement was found for events with a very large amount of backscattering, the performance for events with a small fraction of backscattering decreased. Using the information from the first four or more walls of an event and thus requiring more than 19 input variables exceeded the available MC statistics for the training of the ANN.

The vertex is finally reconstructed by combining the hadronic shower axis (if any) using the vertex method and the leading track (if any) with the output wall of the ANN. If neither a 3D-track nor a shower axis is reconstructed or the event is of walltype 2, the x/y position of the vertex is placed in the mean x/y position of the digits of the first wall. The z position of the vertex is placed in the most probable vertex position of the most probable wall. This position is determined by MC to be 5.1 cm downstream of the beginning of the brick (see Figure 5.10). The distance between the reconstructed wall and the true wall containing the vertex is shown in Figure 5.11. The vertex residuals in x and y are shown in Figure 5.12. The residuals can be fitted by the sum of two Gaussians, where the more narrow one accounts for the intrinsic resolution and the wider one for non-Gaussian tails from, e.g., misidentified tracks or shower axes. The fits show no indication for a bias and yield very similar fit parameters.

Using the algorithm outlined above, 81% of all (both true NC and true CC) true fiducial volume events are reconstructed in the correct wall, and 96% within ± 1 wall. Limiting the selection to events with interactions in the ECC bricks, 83% of the true FV events are reconstructed in the correct wall¹⁵. Finding the vertex wall for true NC events is more challenging due to the absence of a muon track: 75% of all true fiducial volume true NC events are reconstructed in the correct wall and 95% within ± 1 wall, while the corresponding values for true CC events are 82% and 97%, respectively.

¹⁵Interactions in the low-density TT strips deposit only little energy in the respective TT strip, while events originating from the high-density ECC bricks usually produce showers that hit multiple TT strips and deposit much more energy in the downstream TTs.

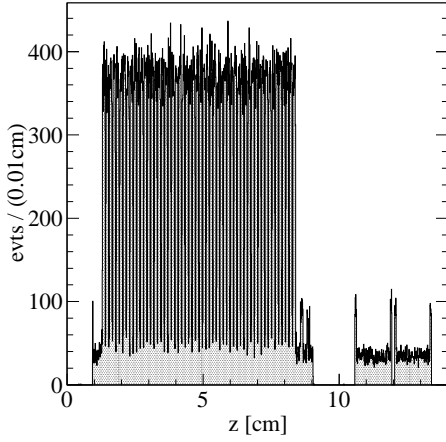


Figure 5.10: True vertex position (MC) within a target wall. The large structure on the left side is the ECC brick (including the CS), the smaller structure on the right side corresponds to the two aluminum-packed plastic scintillator planes of the TT. The average vertex position is at $z = 5.1$ cm.

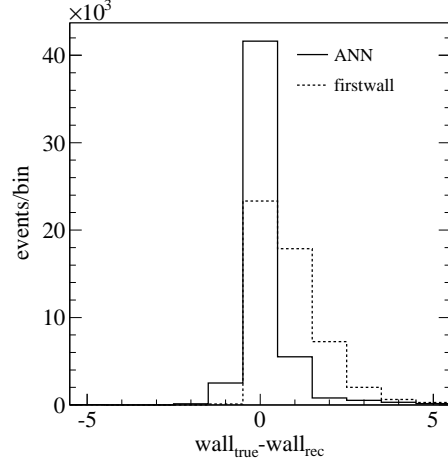
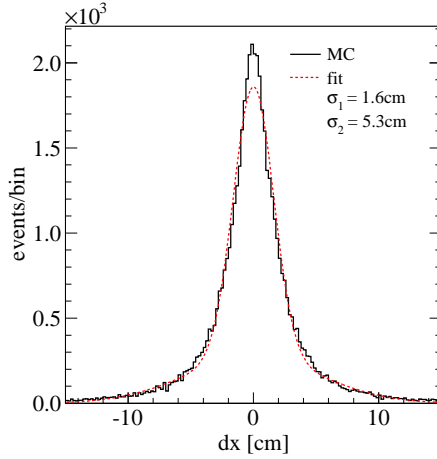
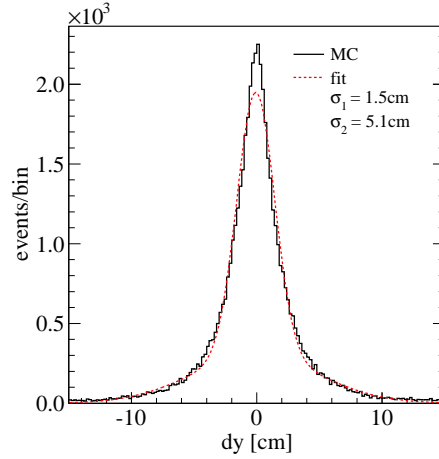


Figure 5.11: Difference between the true vertex wall and the electronic detector-reconstructed vertex wall, using either the first wall of an event (dashed line) or the ANN-reconstructed wall (solid line) for MC events reconstructed in the fiducial volume.



(a) Vertex residuals in x .



(b) Vertex residuals in y .

Figure 5.12: Vertex residuals $dx = x_{true} - x_{rec}$ in x and $dy = y_{true} - y_{rec}$ in y for MC events reconstructed in the fiducial volume, the Gaussian fit (see text for details) is shown as a red dashed line.

5.8 Event classification

In high-energy neutrino experiments like CCFR or NUTEV, the classification of events into NC-like or CC-like was performed by measuring the event-length in terms of the crossed passive target planes and applying a length-cut. For neutrino energies in the GeV-range, however, a single variable has not enough separation power and usually a multivariate classification is performed. If

not stated otherwise, only ν_μ interactions are used to train and validate the classification algorithm.

Within this thesis, all events without any reconstructed 3D-track are classified as being NC-like, without using an MVA algorithm. 1% of all true CC events and 37% of all true NC events are classified as NC-like by doing so. The following variables have been found to provide a good discrimination between the remaining true NC and true CC events in OPERA. Variables that show large differences between MC and data have been avoided in the event classification (compare Section 5.6).

ϕ_{KS} The first variable is the angle ϕ_{KS} between the hadron shower axis and the leading track in the plane perpendicular to the known neutrino direction (see Section 3.1). The angle between the true charged or neutral lepton direction and the hadronic shower is expected to be π rad, with corrections to account for Fermi motion of the target and intranuclear rescattering of the hadrons. Since the 3D-tracks reconstructed for true NC events cannot originate from the true lepton, the angle ϕ_{KS} for true NC events exhibits no excess for $\phi_{KS} = \pi$ rad.

$\theta_{K\nu}$ The second variable is the angle between the leading 3D-track and the neutrino direction, profiting from the very good angular resolution for true muon tracks. $\theta_{K\nu}$ is larger for true NC events than for true CC events.

Number of tracks The third variable is the number of reconstructed 3D-tracks. On average, this number is higher for true CC interactions than for true NC interactions.

Track length The 4th variable is the length L_t of the leading 3D-track¹⁶ in terms of crossed TT or RPC walls¹⁷, defined by $L_t = \sqrt{L_{t,hor}^2 + L_{t,vert}^2}$. Each crossed RPC wall is deweighted by 25% to account for the smaller muon energy loss per spectrometer iron wall compared to the target walls. To avoid possible technical issues with an integer input variable of the MVA method, a random jitter of $\pm 10^{-5}$ is applied to L_t . The average track length for true CC events is longer than for true NC events.

Transverse track profile The 5th variable is the transverse track profile R_t^{30} , defined by the ratio of the number of 3D-track digits D^{track} to the total number of digits D (i.e. also including the 3D-track itself) within ± 5 strips around the 3D-track: $R_t^{30} = \sum_j D_j^{track} / \sum_j D_j^{\pm 5}$. The separation power of this variable is further enhanced by excluding the first 30% of all planes of the event since they

¹⁶This variable is correlated with the muon energy which itself is correlated with the neutrino energy. A possible bias towards selecting events that are similar to the MC neutrino spectrum is reduced by the multivariate approach itself and the fact that the muon energy is a complicated function of the event kinematics.

¹⁷A similar variable is used to discriminate between NC-like and CC-like events in the nominal OPERA analysis, where all events with $L_t > 14$ are classified as CC-like.

contain the hadronic activity near the vertex¹⁸. The transverse track profile is approximately one for true muon tracks and smaller than one for hadron-induced ones.

Track extension The 6th variable is the track extension T_{ext} , defined by the difference between the shower length L_s and the track length L_t : $T_{ext} = L_t - L_s$. Each crossed RPC wall is deweighted by 10% when determining L_s (see above for L_t deweighting) to account for the reduced hadronic interaction length per spectrometer iron wall compared to the target walls. A random jitter of $\pm 10^{-5}$ is applied to T_{ext} . The average track extension is larger for true CC events than for true NC events.

TT and RPC walls and digits upstream of the reconstructed vertex are excluded from all variables. The different variables are shown in Figure 5.13 for true NC events and true CC events, respectively. The training sample is composed of about 2.2×10^5 ν_μ events (all interactions, both true NC and true CC) with a reconstructed vertex in the fiducial volume. The number of true CC events in the training sample is larger than the number of true NC events and would create a bias towards CC events. CC events are hence randomly removed from the training sample until parity of NC and CC events is reached.

Among the most often used MVA methods for classification in high-energy physics are ANNs (compare Section 5.7) and *k*-nearest neighbor (*k*-NN) algorithms [198, 199]. A *k*-NN algorithm finds the *k* closest events e_i ($i = 1, \dots, k$) in a *d*-dimensional parameter space for any queried event e_q . The closeness is given by the rescaled distance

$$D = \sqrt{\sum_{j=1}^d \frac{1}{w_j} |v_j^r - v_j^q|^2}, \quad (5.11)$$

where (v_j^q) are the parameters of the respective reference (query) event. w_j is a scale factor applied to each variable to account for different distribution widths of the variables¹⁹ and is calculated from the width of the distribution of events from the training sample, where the smallest and largest 10% of the events (both NC and CC combined) have been discarded. The relative probability, or so-called discriminant variable, that the query event is CC-like is given by

$$P_{CC} = \frac{k_{CC}}{k_{CC} + k_{NC}} = \frac{k_{CC}}{k}. \quad (5.12)$$

The *k*-NN classifier is a supervised learning algorithm: The neighbors are selected from a MC training sample where the true classification is known²⁰.

¹⁸Excluding the first 40% or 50% of all planes does not change the separation power of this variable.

¹⁹Without this weight factor, variables with a wider distribution would dominate the Euclidean metric.

²⁰The term *training* is a bit misleading here, since, unlike for e.g. ANNs, no explicit training step is required for *k*-NN classifiers.

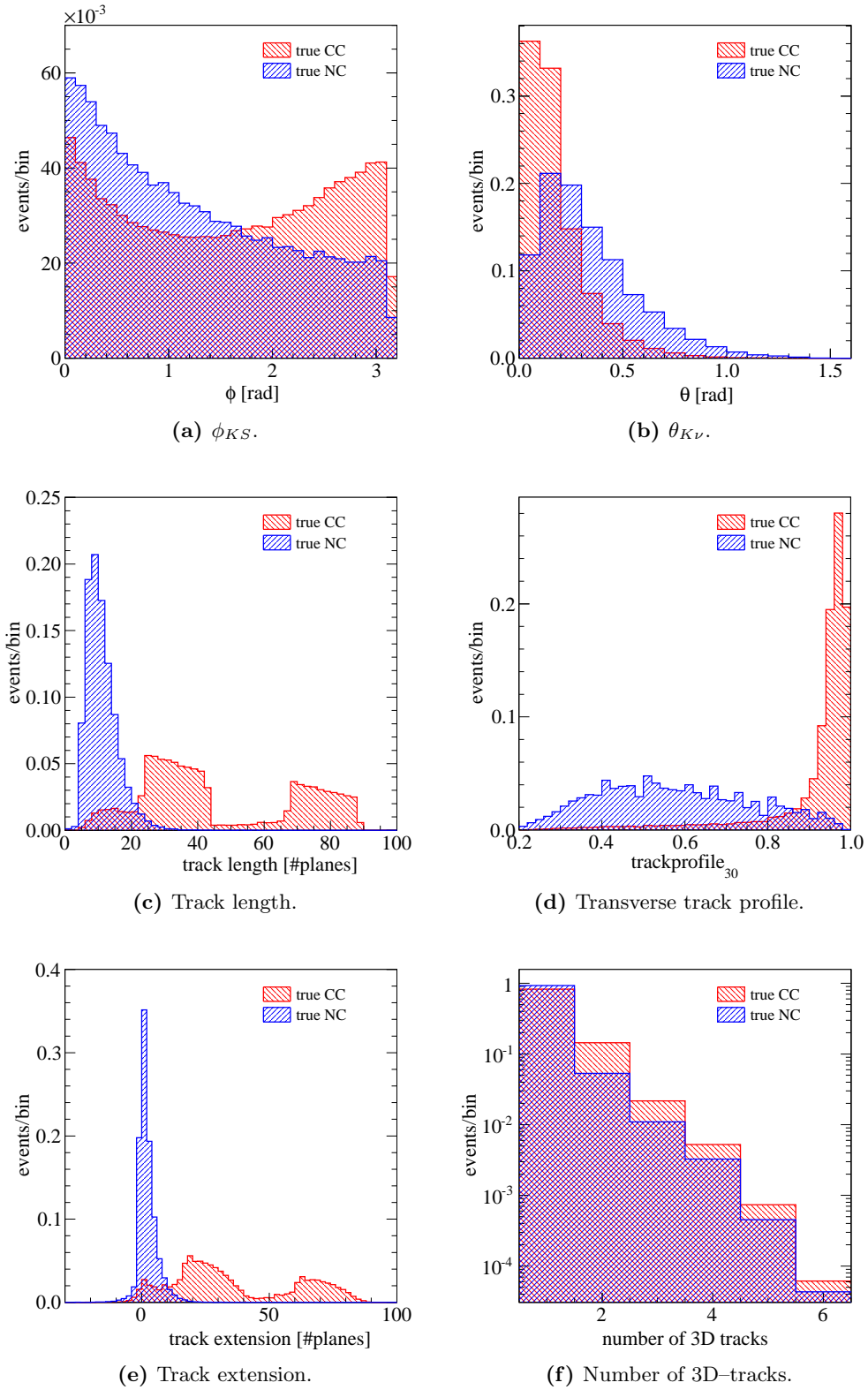


Figure 5.13: Separation variables (MC) used in the classification. All histograms are normalized to unity.

The choice of k , and hence the number of neighbors, determines the behavior of the k -NN: A large value of k produces statistically stable outputs but is not sensitive to local variations of the probability density function, whereas a small value of k probes local variations at the expense of large statistical fluctuations. A visualization of a $d = 2$ k -NN algorithm is shown in Figure 5.14. The classification step using a k -NN requires to calculate the d -dimensional distance from the query event to every event e_i ($i = 1, \dots, N$) in the training sample, where N is typically in the order of hundreds of thousands events and $d \lesssim 10$. The algorithm speed can be significantly increased by using a so-called *binary tree search*, which is implemented in TMVA. k -NN classifiers are quite transparent and have an intuitive interpretation in low dimensions (see Figure 5.14). They are quite robust against overtraining effects but are sensitive to weak input variables²¹.

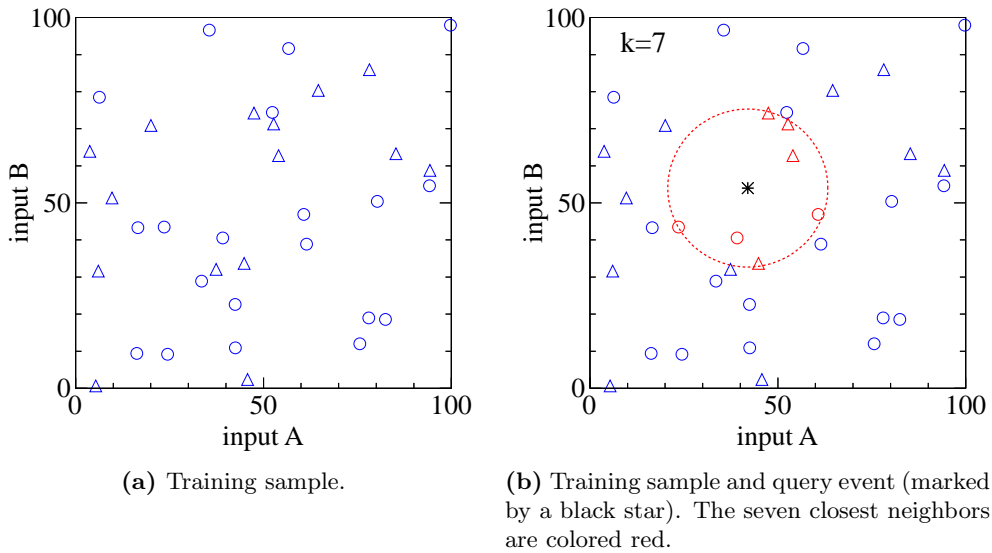


Figure 5.14: Example of a two-dimensional k -NN algorithm with $k = 7$ used for the classification. Events of signal type are displayed by a circle, events of background type by a triangle. The probability of the query event (indicated by a black star) to be a signal event is $P_s = 3/7$ in this example.

The performance of a classification algorithm can be assessed by introducing the variables efficiency and purity, which are typically defined for signal and background events. Within this section, CC events constitute the signal and NC events constitute the background. Using Monte Carlo event samples, the signal efficiency $\varepsilon_{sig,i}$ in the i -th bin is defined as the number of all true signal events $N_{rec\&true}$ that are reconstructed as signal events in the i -th bin, divided by the number of true signal events N_{true} in the i -th bin:

$$\varepsilon_{sig,i} = \left(\frac{N_{rec\&true}}{N_{true}} \right)_i. \quad (5.13)$$

²¹Input variables are weak if their separation power is small.

The background rejection efficiency $\varepsilon_{bkg,i}$ is calculated in full analogy, dividing correctly identified background events by the number of true background events in the i -th bin. Signal purity $\mathcal{P}_{sig,i}$ in the i -th bin is defined as the number of true signal events $N_{rec\&true}$ that are reconstructed as signal events in the i -th bin, divided by the number of all events N_{rec} reconstructed as signal in the i -th bin:

$$\mathcal{P}_{sig,i} = \left(\frac{N_{rec\&true}}{N_{rec}} \right)_i. \quad (5.14)$$

Signal efficiency and background rejection efficiency are usually combined in a *receiver operating characteristic (ROC)* curve to compare the overall separation power of different MVA classifiers. The ROC curves of different k-NN classifiers are shown in Figure 5.15. The optimal number k of neighbors has been found by testing different values of k between 10 and 200. For the same set of input variables, the integral below the ROC curve for a thus optimally tuned ANN²² is larger by about 1% than for k-NNs within this analysis and hence the separation power is slightly better. On the other hand, the classifier output distribution of the k-NN is very smooth (see Figure 5.19a) and a smaller impact for variations of the optimal cut value on this output is expected for k-NNs when applied to real data. In order to reduce the possible bias of the MVA output for real data²³, weak variables have been successively omitted from the MVA, and the training has been repeated. While omitting the number of 3D-tracks has been found to have almost no impact on the MVA performance, this is expected to improve the data/MC agreement of the classifier output, since this variable is poorly modeled by MC.

In order of their respective global separation power, the input variables can be ranked as follows: track length, track extension (very similiar power to track length), the transverse track profile, $\theta_{K\nu}$, ϕ_{KS} and the number of 3D-tracks. Note that the ranking order may vary in different regions of the phase space.

Correlations among the input variables, which are usually unavoidable for realistic problems, are not necessarily a fundamental problem for k-NNs (or most other MVA methods). However, the presence of such correlations may result in an underperformance of the MVA method. The linear correlation matrices for true CC events and true NC events are shown in Figure 5.17. Linear correlations can be removed at least partially by performing input variable transformations to reduce these correlations [198]. However, even linear correlations can usually not be removed completely for both signal and background events at the same time.

The final choice for this separation problem is a k-NN with five input variables, i.e. omitting the number of 3D-tracks from the k-NN, $k = 80$ and a decorrelation of the input variables. Smoothing the distance function (see

²²Using the same five input variables, two hidden layers of 15 and 5 neurons respectively, back-propagation training and sigmoid activation functions.

²³Usually, achieving a stable and unbiased output of the MVA method when applied to real data is preferred over the smallest achievable statistical error.

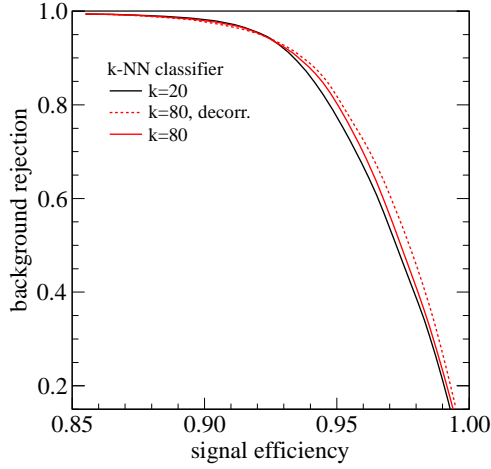


Figure 5.15: ROC curves for the different k -NN classifiers. For decorrelation (decorr.) see text.

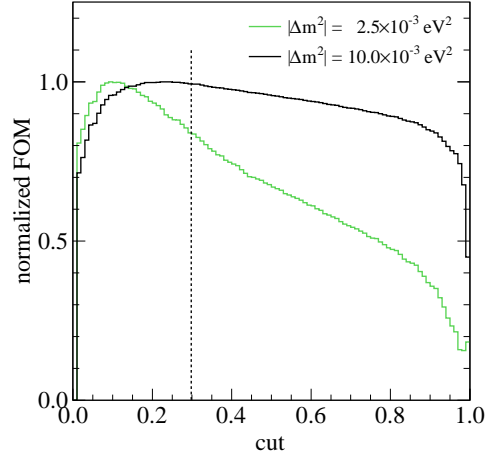


Figure 5.16: Figure of merit as a function of the classifier output cut for two different values of $|\Delta m_{23}^2|$. The final chosen cut value is shown as a vertical dashed line.

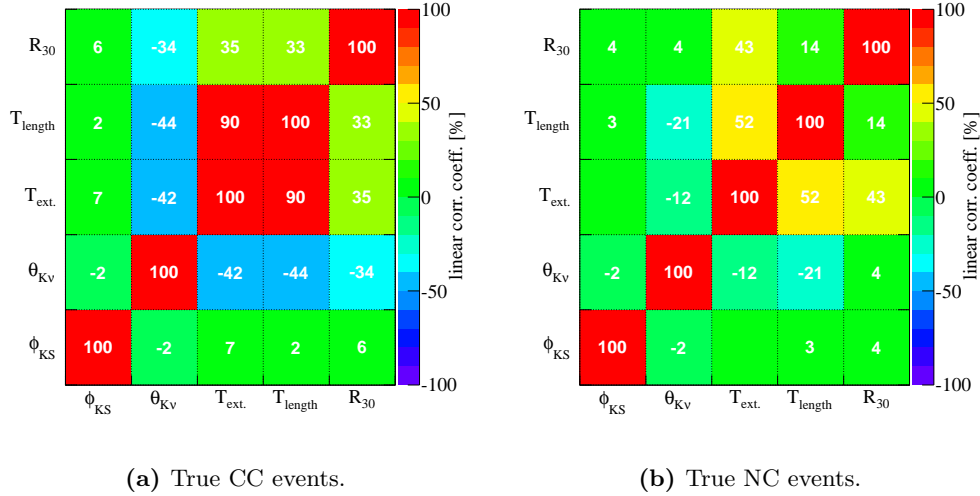


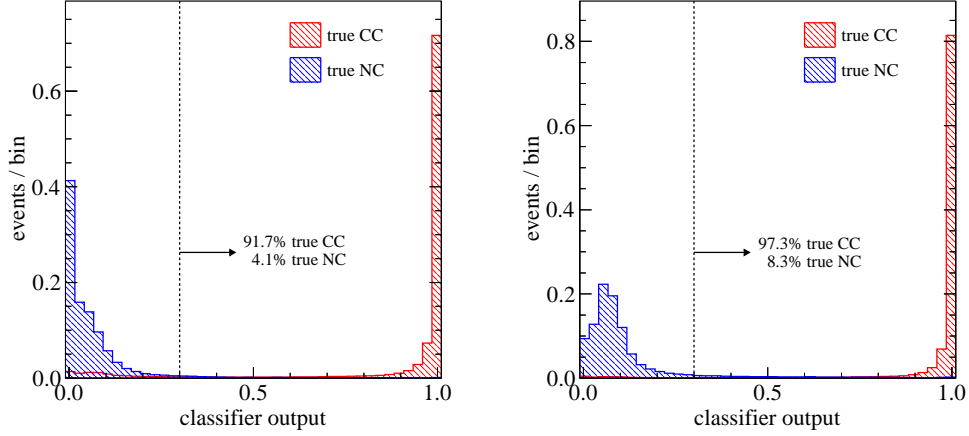
Figure 5.17: Linear correlation matrices for the k -NN classifier input variables using the training MC sample.

Equation 5.11) using a Gaussian kernel [198] did not improve the k -NN performance. The *figure of merit* (FOM) to determine the best cut Γ on the classifier output, scaled to an interval between 0 and 1, is given by the muon neutrino disappearance sensitivity for the ratio method described in Section 7.2. The distribution of the sensitivity, assuming two-flavor oscillations and muon neutrino disappearance only, as a function of Γ is shown in Figure 5.16. For small values of $|\Delta m_{23}^2|$, $\Gamma \approx 0.1$ maximizes the sensitivity by maximizing the CC selection efficiency at the cost of lower purity. For values of $|\Delta m_{23}^2| \gtrsim 5 \times 10^{-3} \text{ eV}^2$, cut values above 0.25 maximize the sensitivity. A higher cut value reduces the true

ν_μ NC contamination, as well as contaminations from true ν_e CC and true ν_τ CC to the ν_μ CC sample. In addition, the k-NN output probability distribution is very flat for $0.3 < \Gamma < 0.7$, which is a desired feature that makes the output less sensitive to variations of the exact cut value. Since the ratio method is statistically limited for small $|\Delta m_{23}^2| \lesssim 5 \times 10^{-3} \text{ eV}^2$ in OPERA anyway (see Section 7.2), the final cut value is set to $\Gamma = 0.3$. The classifier outputs for the different neutrino flavors and interactions are shown in Figure 5.18. Notice the large fraction of true ν_τ CC interactions that are identified as CC-like. These events originate almost completely from $\tau \rightarrow \mu$ decays that are almost not distinguishable from true ν_μ CC interactions.

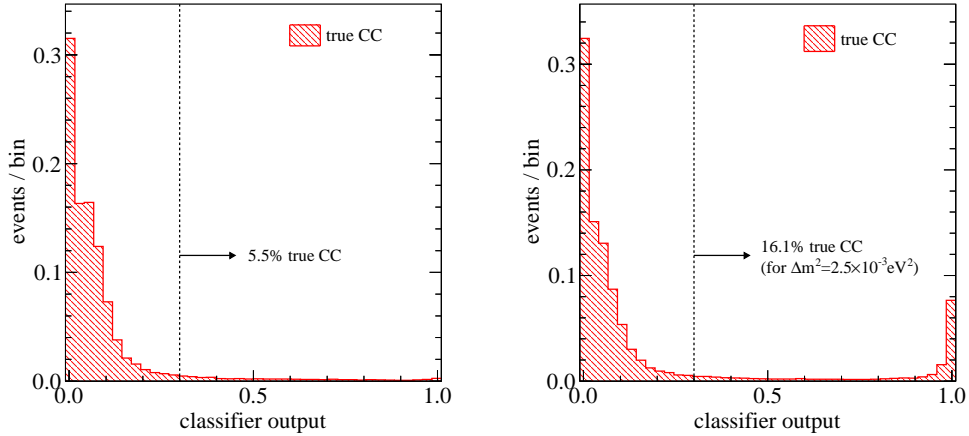
The efficiencies and purities for ν_μ and $\bar{\nu}_\mu$ interactions after event selection cuts (see Section 6.1) in the OPERA detector as functions of the true hadronic energy $E_{had}^{true} = (E_\nu^{true} - E_{lepton}^{true})$ and Bjorken- y (see Equation B.19), respectively, are shown in Figure 5.19. The efficiency distributions as functions of the hadronic energy depend in a complicated way on the initial neutrino flux and the different shapes of the ν_μ and $\bar{\nu}_\mu$ NC and CC cross sections. In general, it is not possible to remove the true CC background from an NC sample, since for high values of Bjorken- y , most of the neutrino energy is transferred to the hadronic system and the energy transferred to the lepton is too small to produce a reconstructable track. The drop of the ν_μ CC efficiency around $E_{had}^{true} \approx 20 \text{ GeV}$ is a result of the differential cross section $d\sigma/dy \sim 1$ for DIS neutrino interactions on quarks (see Equation 2.52) and the large decrease of $\varepsilon(y)$ for $y \gtrsim 0.8$ for CC events. Since the DIS differential cross section for antineutrino interactions on quarks decreases rapidly with y , $d\sigma/dy \sim (1-y)^2$, the low efficiency at high y does not change $\varepsilon(E_{had}^{true})$ for $\bar{\nu}_\mu$ much.

While within this thesis the sensitivity to muon neutrino disappearance is maximized, one major task of the OPERA electronic detector is to provide a CC efficiency of 95 % [137] that is needed for a sufficient particle identification. The remaining NC background in the default analysis is about 24 % in the pure NC sample and 6 % relative to the full sample [183]. Using the described k-NN classifier, the NC contamination for 95 % CC efficiency is much lower and amounts to only about 16 % for the pure NC sample and about 4 % relative to the full sample.



(a) ν_μ . The true NC fraction classified as CC-like in the full sample is 1.1%.

(b) $\bar{\nu}_\mu$. The true NC fraction classified as CC-like in the full sample is 3.2%.



(c) ν_e (intrinsic CNGS beam contamination). ν_e from $\nu_\mu \rightarrow \nu_e$ oscillations have a smaller energy and are even more rarely classified as CC-like. The NC classification output for true ν_e NC events is almost identical to the CC classification output.

(d) ν_τ (from $\nu_\mu \rightarrow \nu_\tau$ oscillations). The fraction of ν_τ events classified as CC-like increases slightly with $|\Delta m_{23}^2|$ and amounts to 16.5% for $|\Delta m_{23}^2| = 10 \times 10^{-3} \text{ eV}^2$.

Figure 5.18: k-NN classifier output for different neutrino flavors. Events without reconstructed 3D-tracks have a probability of zero. The fractions of true CC (true NC) events shown in the plots are calculated starting from pure samples of true CC (true NC) events. All distributions are normalized to unity.

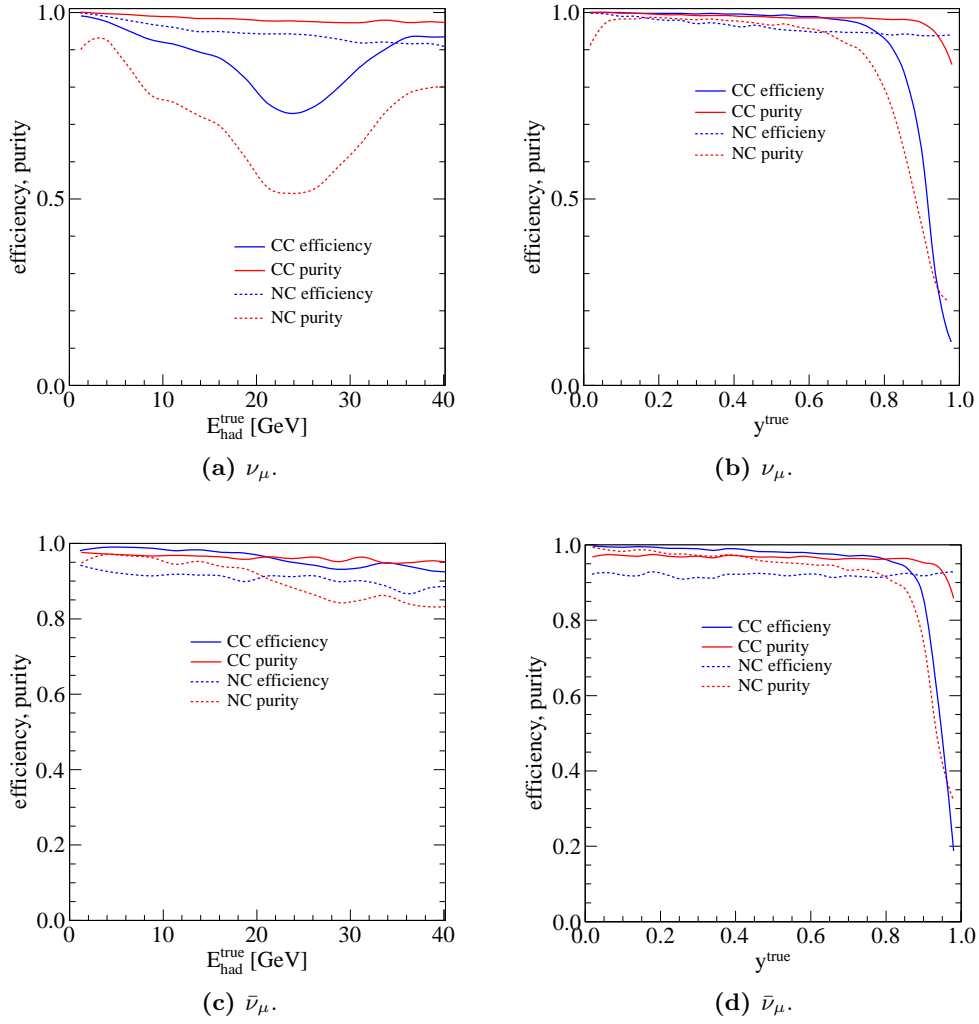


Figure 5.19: Efficiencies and purities (MC) of the optimal k-NN classification for different neutrino flavors as functions of the true hadronic energy and true Bjorken- y , respectively. The small wiggles visible on the curves are within the respective (not shown) statistical uncertainties of the used MC sample.

5.9 Energy reconstruction

The hadronic energy in the OPERA electronic detector is reconstructed using a calorimetric calibration function $f(E_{TT}, N_{RPC})$ that relates the deposited energy E_{TT} in the TTs and the number N_{RPC} of hit RPCs to the true hadronic energy. Based on a NEGN MC calibration, the resolution of the default algorithm is about 35% on average, worsening to about 100% for energies below 5 GeV [183]. In the following, the result of this default energy reconstruction is called E_{had}^{cal} .

An extension of this reconstruction, aiming to increase the energy resolution, to cross-check the existing algorithm, and to provide full consistency with the applied Monte Carlo modifications, is the usage of a multivariate analysis that combines various event information. Within this thesis, it is implemented as a multi-dimensional regression model based on a k-NN algorithm. Instead of a k-NN classification with a known target class (see Section 5.8), the k-NN target is the true hadronic energy E_{had}^{true} . The reconstructed hadronic energy E_{had}^{rec} is given by the inverse distance-weighted average of the k neighbors in the d -dimensional parameter space.

All events with reconstructed vertices inside the FV are divided into two different classes, while non-FV events are completely excluded. The first class contains all events where the shower is fully contained in the CTV, called the *high resolution sample (HRS)* in the following²⁴. The second class, called the *low resolution sample (LRS)*, contains all other events. The LRS mainly consists of events that longitudinally leak into a spectrometer. FV events that leak longitudinally out of the detector are limited to very large hadronic energies, whereas transverse leakage is mostly accounted for by the FV definition itself. All TT and RPC walls and digits upstream of the reconstructed vertex are not taken into account.

The following input variables are used for the k-NN:

Deposited energy The first variable is the total deposited energy E in the CTV after MR (see Section 5.4): $E = \sum_{strips} E_{strip}$.

Deposited energy within 75 cm (LRS only) The next variable is the total deposited energy E^{75} in the CTV within 0.75 m of the reconstructed event vertex²⁵.

Strip number The next variable is the total number N of TT and RPC strips. To reduce the systematic uncertainty due to PMT threshold modeling in MC, only strips with a combined number of $N_{PE} = N_{PE, left} + N_{PE, right} > 0.75$ of *photoelectrons (PE)* (before MR) are included²⁶.

²⁴Note that events in this sample only consists of TT digits.

²⁵These 75 cm correspond to about five brick walls, which is the minimum longitudinal distance (positive z direction) between a reconstructed FV vertex and the CTV border.

²⁶The resolution at low hadronic energies could be improved by energy de-weighting, where the hadronic energy is estimated from a de-weighted calorimetric variable

Shower length The last variable is the shower length L , as defined in Section 5.8. A random jitter of $\pm 10^{-5}$ is applied to L .

The training sample is composed from about 2.1×10^5 true ν_μ CC events with a true vertex in one of the target sections. If no hadronic shower is left after MR, the event is placed in the first bin of reconstructed hadronic energy.

The energy resolution σ_i and the mean value \bar{R}_i of the energy reconstruction per bin i of true hadronic energy is defined by the sigma and mean of a Gaussian fit to the distribution

$$R_i = \left(\frac{E_{had}^{rec} - E_{had}^{true}}{E_{had}^{true}} \right)_i. \quad (5.15)$$

The optimal number of neighbors is given by $k = 80$ ($k = 60$) for the LRS (HRS) k-NN, as was determined by minimization of σ_i for true hadronic energies of up to 10 GeV.

The raw output $E_{had}^{kNN,raw}$ of the k-NN algorithm is biased, i.e. $\langle E_{had}^{kNN,raw} / E_{had}^{true} \rangle \neq 1$, for two main reasons: Firstly, query events near the boundaries of the input parameter space are not isotropically surrounded by neighbors, which biases the output value towards events further away from the boundary. An example of this issue is illustrated in Figure 5.20. The second bias is introduced by the training sample itself, which is based on the default MC and the underlying CNGS neutrino spectrum and biases events towards the true neutrino energy spectrum.

The raw outputs of the two k-NN estimators are corrected using a polynomial fit to the respective the mean values \bar{R}_i , as a function of $(E_{had,i}^{true})$, of the HRS and the LRS separately, aiming at an unbiased estimator $\langle E_{had,i}^{kNN,corr} / E_{had,i}^{true} \rangle = 1$ for all i . However, the correction must be applied as a function of $(E_{had,i}^{kNN,raw})$ as an approximation. The remaining bias of $\langle E_{had}^{kNN,corr} / E_{had}^{true} \rangle$ is about 3% for $E_{had}^{true} = 2.5$ GeV and below 1.5% for $E_{had}^{true} \gtrsim 5.0$ GeV. The bias-corrected output of the k-NN estimator and the default output of the calorimetric method are shown in Figure 5.21.

The results of the bias-corrected k-NN-based energy reconstruction and of the default reconstruction for different ranges of true hadronic energy is shown in Figure 5.22.

$E_{had}^{dew} \propto \sum_{strips} (E_{strip})^{k(E)}$. $k(E) < 1$ is the de-weighting power that depends on an energy reconstruction obtained from, e.g., an un-de-weighted energy approximation. An un-de-weighted energy estimator suffers from large Landau fluctuations for low hadronic energies, which is thus better approximated by strip counting (i.e. $k = 0$). For large hadronic energies, the total fluctuations are smaller, and the hadronic energy is a linear function of the deposited energy (i.e. $k = 1$) until saturation effects of the PMTs occur. Finally, the de-weighted energy should then be used as an additional input parameter for an MVA method.

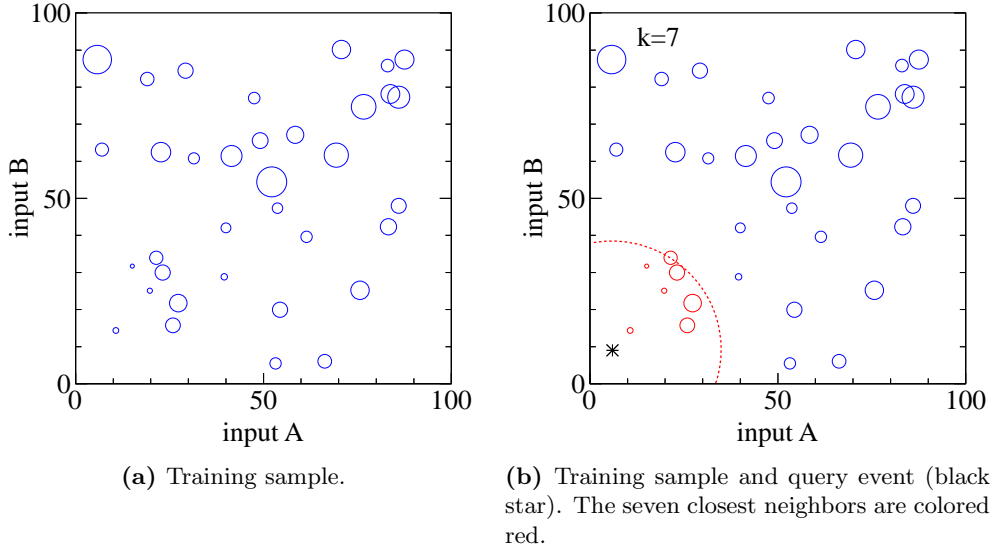


Figure 5.20: Example of a two-dimensional k -NN algorithm used for regression.

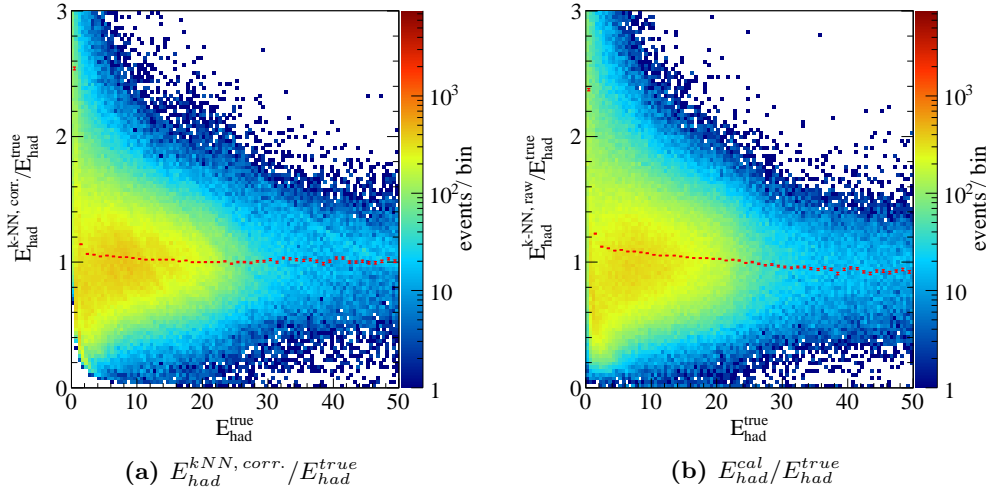


Figure 5.21: Distribution of $E_{had}^{rec} / E_{had}^{true}$ for the bias-corrected k -NN and the default reconstructed hadronic energy, respectively, for simulated true ν_μ CC events. The red markers show the means of the distributions per bin of E_{had}^{true} .

The energy resolution for true ν_μ CC events (compare Equation 5.15) using the k -NN estimator can be parameterized by

$$\frac{\sigma_E}{E_{had}^{true}} = \frac{48\%}{\sqrt{E_{had}^{true} [\text{GeV}]}} + 17\%. \quad (5.16)$$

The largest improvement of the energy reconstruction algorithm is given by the introduction of the FV: The improvement for energies below 5 GeV is about 50% (compare [183]), this also applies to the default energy reconstruction. The k -NN energy estimator yields a slightly better energy resolution for hadronic

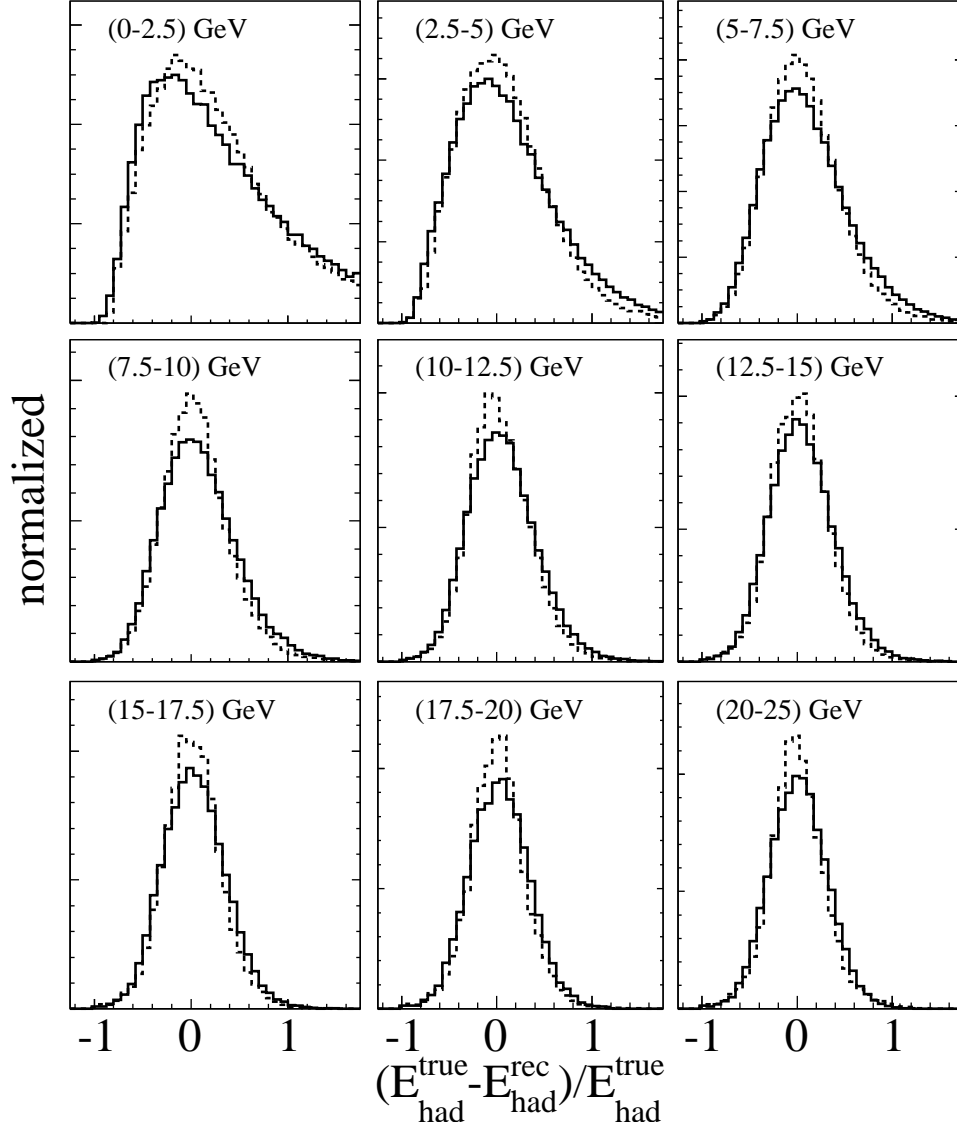


Figure 5.22: Distributions R_i for the k-NN based energy estimator (dashed) and the default algorithm (solid) for different ranges of true hadronic energy for simulated true ν_μ CC events.

energies between 5 GeV and 25 GeV, where the improvement of the resolution is about 2.5 %, while the performance at even higher hadronic energies is comparable for the k-NN and the default energy estimator. However, the significantly slower k-NN algorithm, the additional large bias-correction and the generally only small improvement compared to the default algorithm altogether do not justify the usage of the k-NN algorithm. In the following, the default estimator is thus used to reconstruct the hadronic energy E_{had}^{rec} for CC-like events with MR, and for NC-like events without MR.

The energy resolution could possibly be further improved by using energy de-weighting (see Footnote 26). If the electronic detector is used to reconstruct

the energy of ν_e CC or ν_τ CC events already identified as such in the emulsions, the energy reconstruction algorithm should be re-trained, using true ν_e CC and true ν_τ CC training events, respectively. Notice that it is normally not possible to separate the secondary electromagnetic shower (from ν_e CC interactions or ν_τ ($\tau \rightarrow e$) CC interactions) or hadronic shower (from ν_τ ($\tau \rightarrow h$) CC interactions) from the primary neutrino-induced hadronic shower in the OPERA electronic detector, even if the lepton flavor information is available from the emulsions. Within this thesis, these events are usually classified as being NC-like and are reconstructed with large hadronic energies that are the sum of the primary and the secondary shower energies.

Chapter 6

Analysis of CNGS beam events

The data used within this section is based on the CNGS runs of the years 2009, 2010 and 2011. The integrated number of POT is 3.59×10^{19} for 2009, 4.12×10^{19} for 2010 and 4.84×10^{19} for 2011, without any cuts. The total integrated POT amount to 12.542×10^{19} (see Section 3.1.3).

6.1 Event selection

The OPERA detector data is divided into so-called *extractions*, containing about eight hours of data each. The *data acquisition (DAQ)* is divided into *DAQ runs*, with fixed DAQ conditions during each of these DAQ runs. While some neutrino beam may be delivered during the commissioning phase predating the nominal runs, this analysis does not use the data of the beginning days or hours of the 2009 and 2010 runs with usually low overall detector performance. The run periods, the corresponding extractions and the DAQ runs are summarized in Table 6.1. Data from the 2008 run, corresponding to about 1.78×10^{19} POT before any cuts, is not included in the analysis, since the electronic detector conditions changed often and the target sections show much larger variations than during the other years.

The following selection cuts have been applied to all events recorded during the run periods given in Table 6.1 in order to select CNGS neutrino interactions.

Beam quality cut Both the CNGS atomic clock and the primary beam intensity monitoring system have to be active and their respective measurement values have to be stored in the CERN TIMBER data base¹.

CNGS timing cut The time difference between the first recorded hit timestamp t_{OPERA} in the OPERA detector and the nearest SPS kicker trigger timestamp t_{CERN} is required to be $-20 \mu s < (t_{OPERA} - t_{CERN} - \delta) < +20 \mu s$, where $\delta = +2394.4874 \mu s$ accounts for the time-of-flight, assuming $v_\nu = c$, and raw corrections for cable delays at CERN and LNGS [200]. The beam event selection

¹TIMBER is a logging system used at CERN, originally developed for the LHC.

Table 6.1: Run periods and corresponding extractions.

Year	first DAQ extr.	start time [GMT ^a] ([unix timestamp])	last DAQ extr.	stop time [GMT] ([unix timestamp])	DAQ runs
2009	9006	06/01/09, 08:00 (1243843200)	9353	11/23/09, 08:00 (1258963200)	583–865
2010	10214	04/29/10, 22:00 (1272578400)	10627	11/22/10, 08:00 (1290412800)	1109–1138
2011	11153	03/18/11, 14:00 (1300456800)	11637	11/16/11, 12:00 (1321444800)	1148–1167

^aGMT: Greenwich Mean Time.

efficiency using this cut is 100%. While this cut already produces comparable selections with very low backgrounds for 2009 and 2011, a large background remains for the 2010 data, as shown in Figure 6.1. Events passing this cut are called ontime with CNGS.

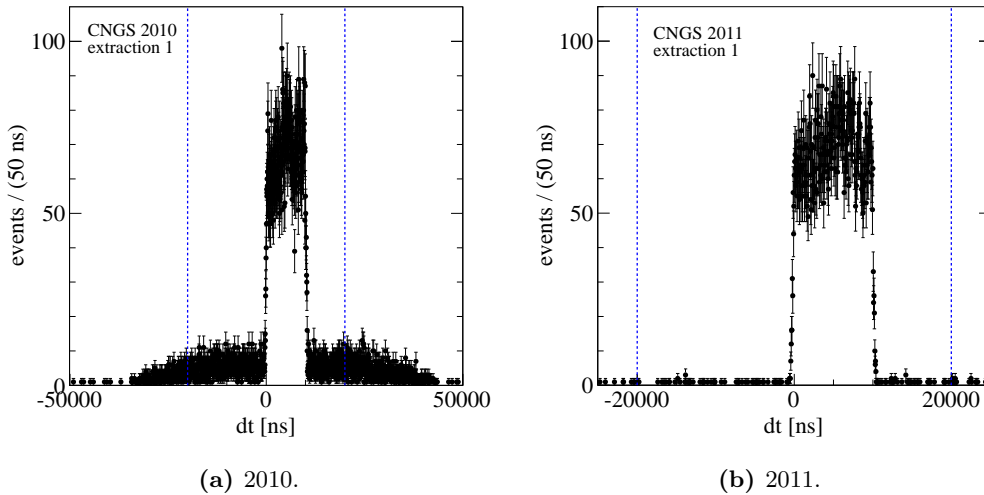


Figure 6.1: Relative time differences between OPERA neutrino events and the closest CNGS kicker trigger for the 2010 and 2011 runs (CNGS extraction 1). The CNGS timing cut is indicated by the blue dashed lines. Data from 2009 looks qualitatively equal to the 2011 data.

Minimum number of hits cut To reduce the background from cross-talk, noise and possible light leaks, events are required to have more than ten raw DAQ

hits². The number of hits per event is shown in Figure 6.2. The effect of this cut on the 2010 data is shown in Figure 6.3. This cut affects mainly the 2010 data, where the DAQ kept all events with at least four raw DAQ hits, while during the 2009 and 2011 runs, the DAQ kept only events with at least ten raw DAQ hits.

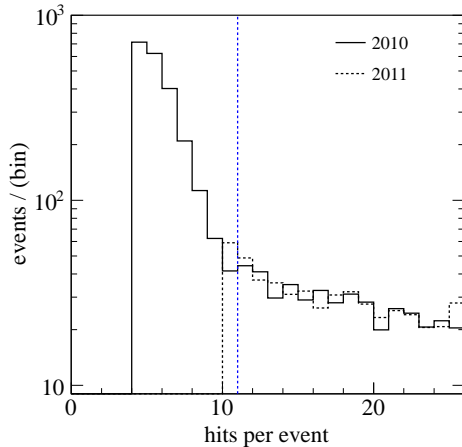


Figure 6.2: Distribution of number of raw hits per event for the 2010 and 2011 runs (both CNGS extractions, after CNGS timing cut). The selection cut is indicated by the blue dashed line. Data from 2009 looks qualitatively equal to the 2011 data.

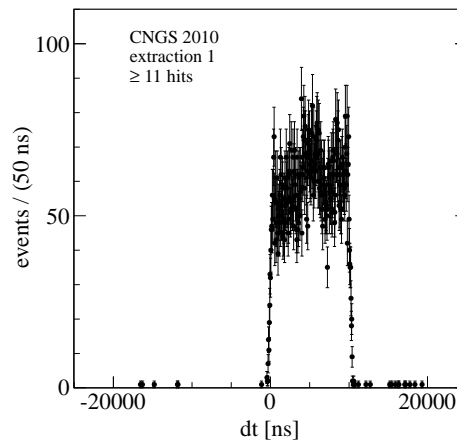


Figure 6.3: Relative time differences between OPERA neutrino events and the closest CNGS kicker trigger (after minimum number of hits cut) for the 2010 run (CNGS extraction 1) (compare Figure 6.1a).

Data quality cut The slow control of all electronic sub-detectors, the DAQ system and the GPS timing system must be operational and within their respective nominal values. In the absence of comprehensive logfiles including all the relevant information, all shift logs and weekly run reports have been checked for major detector problems. Based on these checks, the following extractions are considered bad and are thus excluded from the analysis as whole. The respective most severe problem and the corresponding linux timestamps are given in brackets:

- 9010 (overall unstable, 1243978437–1244026888),
- 10277–10279 (RPC off, 1275274800–1275404396),
- 10432–10433 (TT power supply, 1281970860–1282057259),
- 11226 (RPC gas, 1303570864–1303614058),
- 11339 (DAQ, 1308452461–1308495657),
- 11479–11483 (magnets, 1314500461–1314716460),

²This number sometimes includes timing board and trigger information (see Section 3.2.5) which have no associated detector hit. Note, that one TT digit is usually represented by two raw hits, one for each side of the TT strip.

- 11560 (partial)–end of 2011 run period (DAQ logs corrupt, 1318148940–end of 2011 run period)³.

In addition to the extractions given above removed as a whole, every event is checked against the available logfiles of the TT sub–DAQ⁴: The TT sub–DAQs of both super modules are required to be in acquisition without any pending problems, DAQ problems of single sensors are ignored.

If the charge or momentum of particle tracks are reconstructed, both magnets are required to be within 2% of their nominal current of 1600 A and both field polarities⁵ are included [201]. The magnet status is the only slow control information that is directly used during event reconstruction by the Kalman algorithm and its initialization.

Minimum number of digits cut Events with less than eleven digits after being processed by `OpRealIO` are excluded, where the left and right PMT signal of each TT strip is counted separately.

Minimum bias filter cut Events that fail the minimum bias filter conditions (see Section 3.2.5) after being processed by `OpRealIO` are excluded.

Multievents cuts To reduce the background from overlapping events, events with a duration of more than 1000 ns are excluded, as shown in Figure 6.4a. The effect of sensor dead time is reduced by rejecting events that have a distance of less than 2000 ns to the previous event (see Figure 6.4b), as explained in Section 6.2.

Fiducial volume cut The reconstructed event vertex is required to be within the fiducial volume of the target sections (see Section 5.6). The vertex distributions of neutrino events after all cuts are shown in Figure 6.5 on the example of the 2011 run. None of the vertex distributions show any suspicious behavior or non–isotropical vertex distributions, apart from some unfilled brick rows visible in the side view display. As a rule of thumb, about one half of all events recorded in the OPERA detector are interactions in the surrounding rock, about two thirds of the remaining half are interactions in the iron spectrometers, and the last third are interactions inside the target. The fiducial volume cut removes about one third of all true target events.

A summary of the cuts and the resulting event yield is given in Table 6.2.

³An additional GPS timing problem occurred in the course of extraction 11560–11563.

⁴The logfiles of the RPC sub–DAQs are corrupt and not usable for the entire runs of 2010 and 2011. The HPT and VETO sub–detectors are less important for this analysis and are thus neglected.

⁵The magnet polarity was inverted during a short neutrino beam period of the 2010 run only.

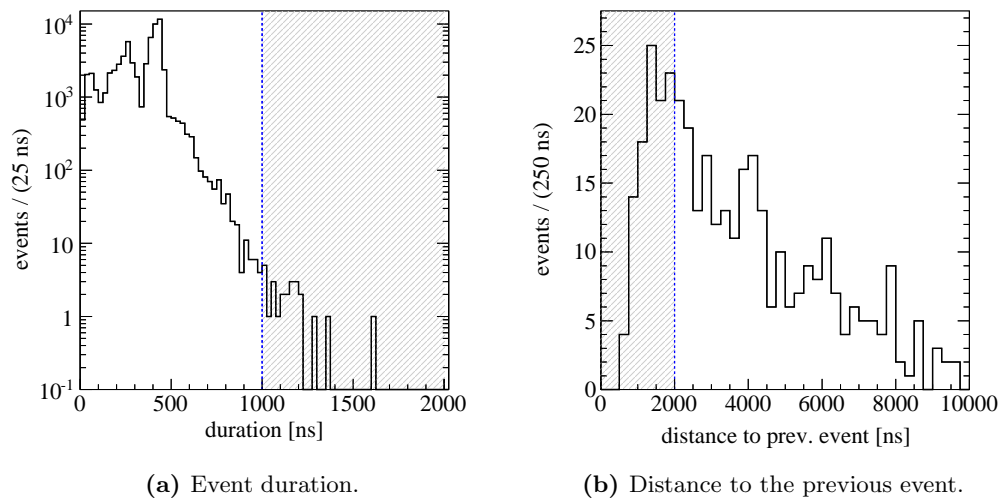


Figure 6.4: Event duration (left) and distance to the previous event for multievents (right). The selection cuts are shown by the blue dashed lines, the excluded areas are shaded gray.

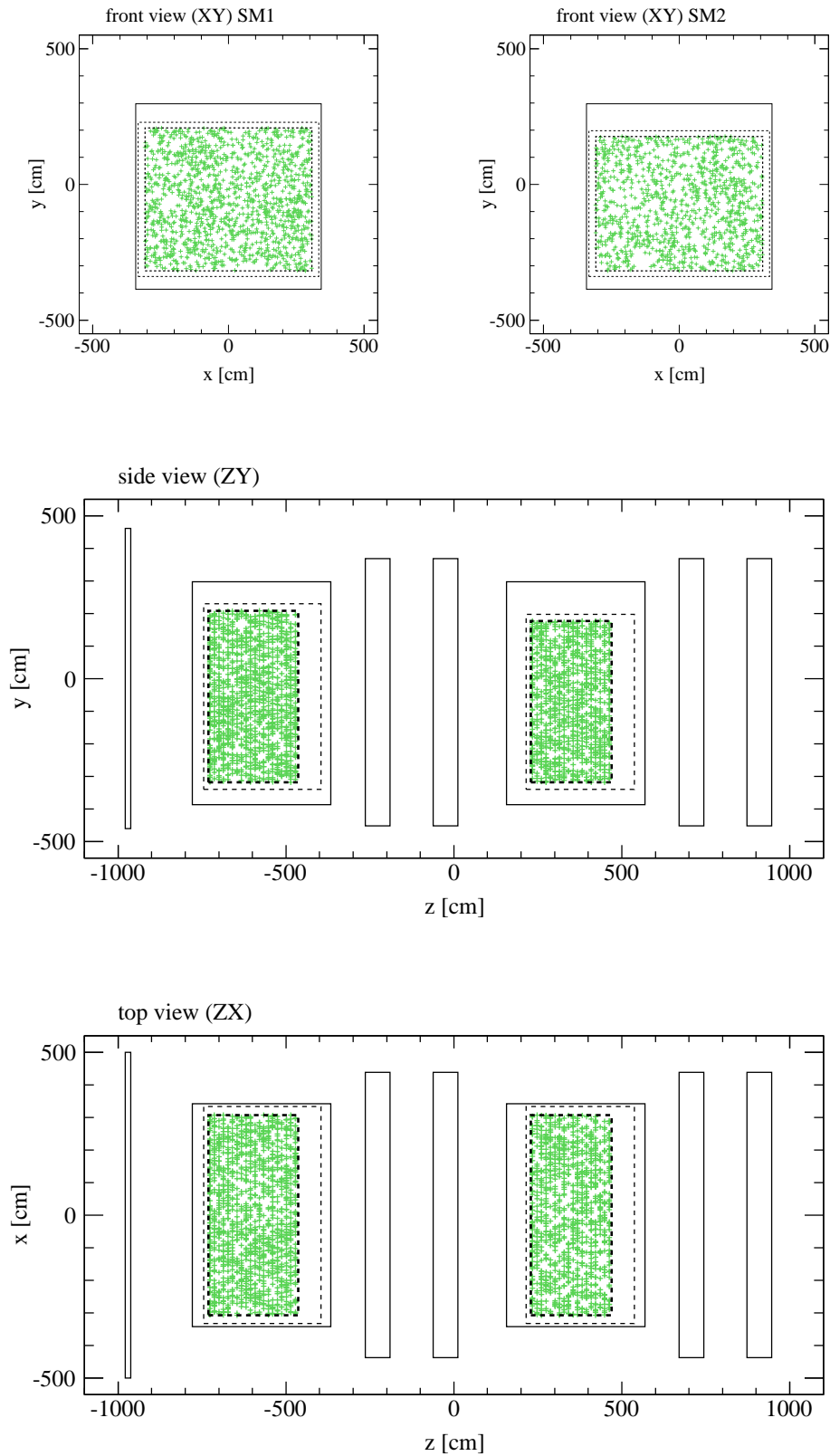


Figure 6.5: Reconstructed vertex positions in the fiducial volume for the 2011 run after all cuts. The inner thick dashed line indicates the fiducial volume, the outer thin dashed line indicates the compact target volume.

Table 6.2: Event yield after successive cuts for the different CNGS runs and the total event yield.

Cut	2009	2010	2011	total
CNGS timing and beam quality	21374	33439	28064	82877
Minimum number of hits	21307	24515	27783	73605
Detector quality				
Official run period	21198	24461	27783	73442
Bad extractions	21198	24264	26145	71607
TT sub-DAQ	19899	21463	25294	66656
<i>Magnet</i> ^a	<i>19432</i>	<i>20473</i> ^b	<i>25209</i>	<i>65114</i>
Minimum number of digits	19829	21328	25136	66293
Minimum bias filter	19828	21325	25135	66288
Multievents				
Event distance	19809	21289	25085	66183
Event duration	19803	21282	25075	66160
Fiducial volume ^c	2085	2110	2461	6656
SM1	1103	1180	1363	3644
SM2	982	930	1098	3010

^aThis cut is only applied if muon kinematics are reconstructed. 49 (1) events are removed in 2010 (2011) by the official software, even though the magnet status was good according to the magnet logfiles. This introduces a small normalization bias for 2010 (2011).

^bIncluding 384 events with inverted polarity.

^cUsing the default *contained* selection of the *OpCarac* algorithm, the event yields are 3247, 3362 and 4031 for the 2009, 2010 and 2011 run, respectively.

6.2 Background

Events recorded by OPERA that are ontime with the CNGS extractions comprise both neutrino interactions and contributions from the various background sources which are explained in the following. The MC expectation upon which this section is based, is composed from unoscillated CNGS neutrinos⁶ interacting inside the OPERA detector and the surrounding material (see Section 4.2). All events that do not originate from a true ν_μ interaction inside the fiducial volume are considered as background for the remaining part of this section. Within this section, background rates are given as numbers relative to each recorded non-background event⁷.

6.2.1 Beam-induced background

All beam-induced background events cannot be rejected by the CNGS timing cut, but only by fiducial volume cuts. Events in this background class can be divided into three main categories:

- High-energy muons from ν_μ or $\bar{\nu}_\mu$ CC interactions in the surrounding rock and other structures, so-called rock events, that result in a single straight track in the detector. If they pass the fiducial volume cut, these events are most likely identified as CC-like events with very low hadronic activity at the reconstructed vertex.
- Neutral particles, mostly neutrons and photons, originating from neutrino interactions in the surrounding material may generate an NC-like interaction, mainly in the border regions of the OPERA detector.
- Neutrino interactions in close proximity of the fiducial volume, particularly in the iron spectrometers, may be mistaken as fiducial volume events.

The true vertex positions of the simulated rock events from the first two categories are shown in Figure 6.6. The beam-induced background is included in this analysis by including all possible external target volumes in the MC simulation.

The full MC sample for this background study contains 4×10^7 ν_μ interactions, corresponding to an exposure of about 1.277×10^{20} POT. Of this sample, about 9.5×10^4 events result in an energy deposition in the detector (before any cuts). Most of these events are single muon tracks that are easily removed by the fiducial volume cut or very low energy depositions that do not pass the minimum bias filter. The remaining number of events, normalized to 1.0×10^{19} POT and the reference target filling, is 13.1 ± 1.7 (stat.) for the first SM and 3.2 ± 0.7 (stat.) for the second SM. The vertex distribution of all external events that pass all the aforementioned cuts is shown in Figure 6.7. Of these events, $(86 \pm 5)\%$ ($(59 \pm 20)\%$)

⁶ $\nu_\mu, \bar{\nu}_\mu, \nu_e$ and $\bar{\nu}_e$.

⁷A background of, e.g., 1×10^{-3} corresponds to one background event for 1000 non-background events.

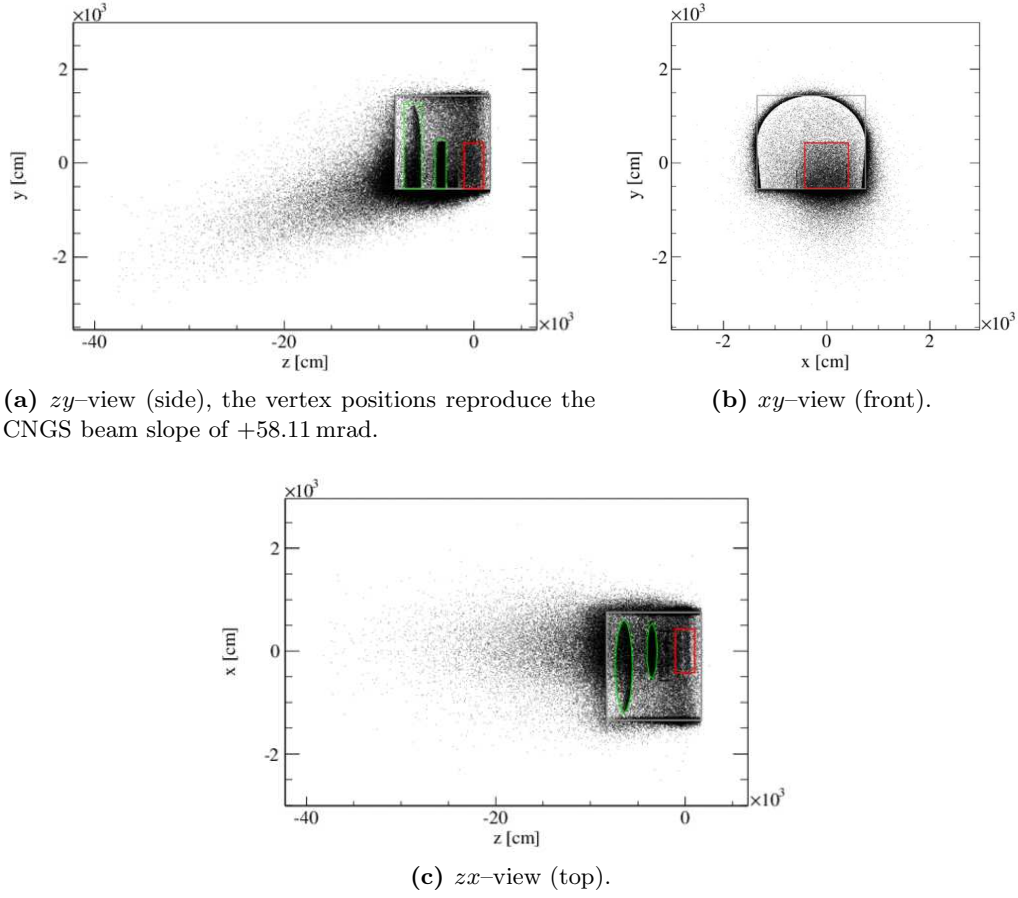


Figure 6.6: True vertex position of simulated ν_μ rock events (corresponding to 13.2×10^{19} POT), generated outside the OPDY volume that result in at least one hit in the OPERA detector (before any cuts). The BOREXINO main detector (left) and the BOREXINO Counting Test Facility (middle) are outlined in green, the OPERA detector is outlined in red, an approximate box surrounding LNGS hall C is outlined in gray. The aspect ratio in the zy - and the zx -views is not unity.

are classified as NC-like in SM1 (SM2). Most of the external background is produced by neutrons entering the detector from the front, yielding an observable asymmetry between the first and the second supermodule. The total number of CC-like background events is similar in the two supermodules and caused by true muons hitting the detector from the sides. Muons, but not neutrals, entering the detector from the front are rejected by requiring no veto hits for fiducial volume events.

6.2.2 Other background

Cosmics The only particles from secondary cosmic rays able to reach the OPERA detector are high-energy muons⁸. Cosmic rays are isotropically dis-

⁸The muon rate at the LNGS underground laboratory is reduced by a factor of about 10^6 compared to the surface rate, due to the rock overburden of about 3800 m.w.e.

tributed in time and thus effectively removed by the CNGS timing cut. The preferred direction of cosmic rays is vertical rather than horizontal, resulting in very characteristic event kinematics that can be used to reduce the cosmic contamination by rejecting tracks with large angles to the neutrino beam direction. The remaining background, including muon-induced neutral production in rock that may generate NC-like interactions in the detector without any visible muon hit, is found to be negligible. Using a detailed cosmic MC simulation (see Section 4.4), the expected cosmic background after all cuts is less than 1×10^{-3} (90 % C.L.) and hence is negligible.

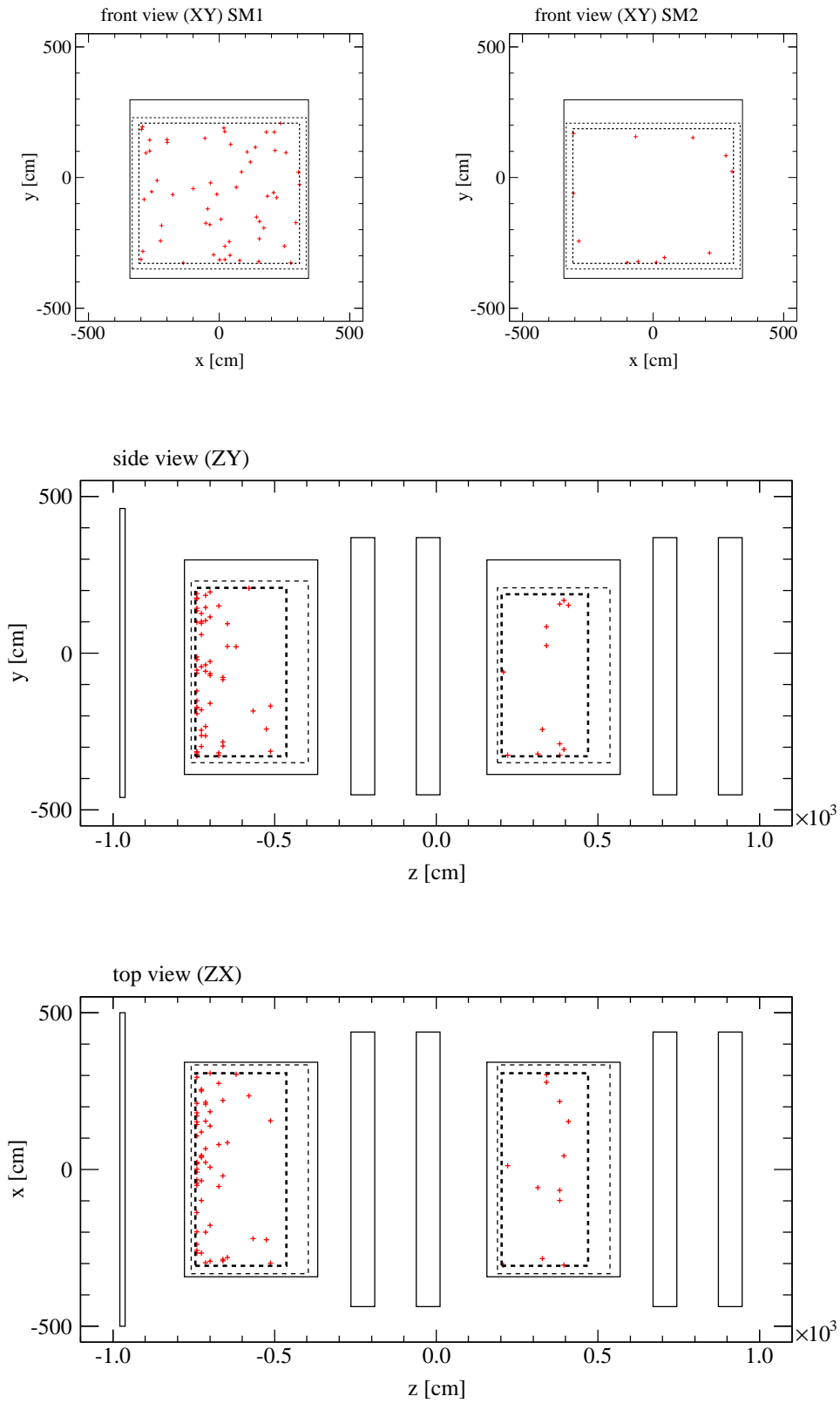


Figure 6.7: Reconstructed vertex positions in the fiducial volume for external MC events (corresponding to 1.277×10^{20} POT) after all cuts. The inner thick dashed line indicates the fiducial volume, the outer thin dashed line indicates the compact target volume.

Radioactivity The concrete walls of hall C and the lead inside the OPERA bricks are the main sources of MeV–photons from radioactive decays that generate energy depositions in the TTs. These events mainly exhibit low photo electron counts per PMT, already resulting in a suppression of this background by the nominal DAQ trigger settings. Events from radioactivity occur more often in the border regions of the detector, since events from outside the OPERA detector are shielded by the bricks inside the target and are hence partially removed by the fiducial volume cut. The discriminator threshold of the RPCs, on the other hand, is too high to record radioactivity events at all. Radioactivity is not included in the MC simulation as, after all event selection cuts, it is expected to have only negligible effect.

Noise and cross-talk The thermo-ionic noise of the TT photo cathodes is the dominant contribution to the single-PMT rate and is reduced by requiring a left/right coincidence of TT strip signals. Cross-talk in the 64-channel PMTs is mostly removed by a dedicated filter algorithm implemented within `OpRec`. Both target tracker noise and PMT cross-talk are included in the MC simulation [202].

Total other background The total non-beam-induced background can be determined from data by selecting events in proximity of the CNGS kicker trigger timestamps, but outside the $\pm 20 \mu\text{s}$ ontime selection window, as shown in Figure 6.8. This background is flat, as expected, and amounts to about 3×10^{-3} for the raw event rates for 2010 and 2011 and 6×10^{-3} for 2009. The higher background rate for 2009 is due to different DAQ settings. No deviations are visible between the two CNGS extractions. After all cuts, the remaining background is $< 1 \times 10^{-3}$ and hence is negligible.

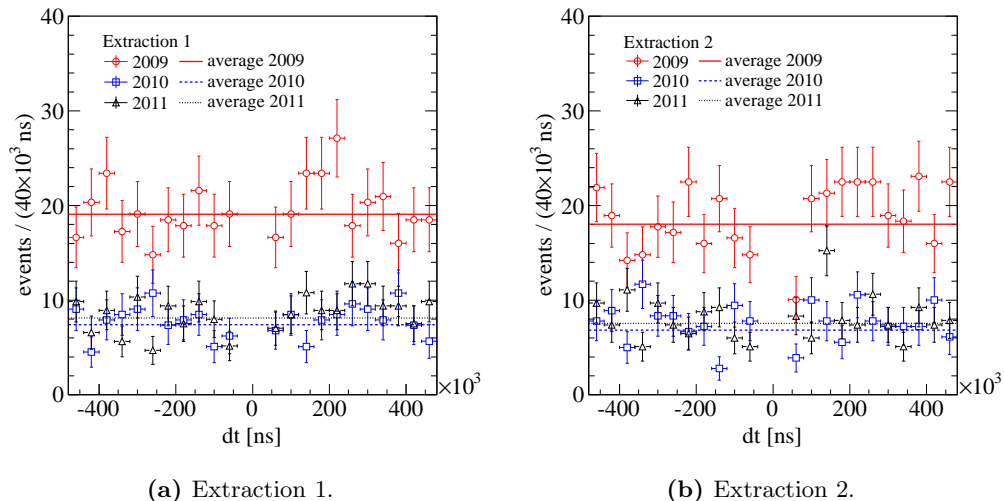


Figure 6.8: Relative time differences between OPERA events and the closest CNGS kicker trigger, where events with $-20 \mu\text{s} < dt < +20 \mu\text{s}$ have been excluded (same definition as in Section 6.1). Event rates are normalized to 10^{19} POT, data is not corrected for decreasing target mass, statistical errors only.

6.2.3 Multievents

The probability that a CNGS extraction results in at least one event in the OPERA detector is about 0.011, assuming an average beam intensity of 1.9×10^{13} POT/(CNGS extraction) and taking the event yield after the TT sub-DAQ cut from Table 6.2. The expected probability to observe two events from the same CNGS extraction therefore is about 6.4×10^{-5} /(CNGS extraction). The number of observed double-events is 102, 126 and 138 for the respective 2009, 2010 and 2011 run periods after the TT sub-DAQ cut, which is in perfect agreement with the expectations of 112, 121 and 140 events. The probability for triple-events is 2.5×10^{-7} /(CNGS extraction), which corresponds to about 0.5 expected triple-events per run period. None such triple-event has been found in the 2009 and 2010 data, three triple-events have been found in the 2011 data, compatible with the expectation. Multievents do not cause any problems in the analysis, as long as they are recorded as two different events by the DAQ. However, no default software exists to account for multiple events recorded as one event.

Two events are separated from each other by the DAQ event builder if the last hit of the first event is separated from the first hit of the second event by more than 500 ns. The maximal raw event duration is about 1000 ns, as shown in Figure 6.4a, while more than 99 % of all events have a duration of less than 500 ns. Assuming a maximum event duration of (1000+500) ns and a CNGS extraction length of $10.5 \mu\text{s}$, the overlap probability of two events is about 1.3×10^{-6} /(CNGS extraction), which corresponds to less than two overlapping events per run period. Naturally, overlapping events are expected to have a longer duration than single events.

If a DAQ sensor is hit again during its reset cycle of $1.4 \mu\text{s}$, the second hit is not recorded. Since the majority of events contain long horizontal muon tracks crossing many detector planes, this dead time can affect large areas of the target and spectrometer sections. The probability that, during a CNGS extraction, a second event falls into a (1000+1400) ns window is about 3.3×10^{-6} /(CNGS extraction), or about seven events per run period. For this analysis, the most important detector parts are the target sections and the TT sensors. Since TT hits typically are the first raw hits of an event, possibly affected events can be rejected by requiring a minimal distance of about $2 \mu\text{s}$ between the first hits of two different events from the same CNGS extraction.

6.3 Beam monitoring

As the selection cuts mentioned in the previous sections have to be applied to both data and MC events, the correspondingly integrated POTs depend on the same selection cuts. The expected integrated POT after the selection cuts are summarized in Table 6.3.

Table 6.3: Integrated POT after various cuts.

	2009	2010	2011	total
	[10^{19} POT]			
All	3.590	4.115	4.837	12.542
Beam quality	3.589	4.115	4.772	12.476
Detector quality				
Official run period	3.582	4.106	4.772	12.460
Bad extractions	3.581	4.076	4.446	12.103
TT sub-DAQ	3.312	3.568	4.296	11.176
Magnet	3.230	3.409	4.281	10.920

The integrated detector ontime, i.e. the uptime of the detector during all CNGS extractions, regardless of their respective intensity, is shown in Table 6.4 and can be used to estimate the non-beam-induced background rates.

Table 6.4: Integrated detector ontime after various cuts.

	2009	2010	2011	total
	[s]			
All	73.17	86.84	106.38	266.39
Beam quality	73.00	86.20	103.31	262.51
Detector quality				
Official run period	72.47	85.85	103.31	261.63
Bad extractions	72.46	85.28	93.71	251.45
TT sub-DAQ	67.11	75.05	90.57	232.73
Magnet	65.15	71.88	90.26	227.29

In order to calculate the expected event rates in OPERA, also the decreasing target mass of the OPERA detector has to be taken into account. According to the fiducial volume defined in Section 5.6, the average number of bricks in the target for the different run periods of 2009, 2010 and 2011 as well as that of the MC geometry are summarized in Table 6.5. Since no individual MC simulations for each run period are used, the existing MC simulations are weighted according to the average fiducial volume mass on a yearly basis. This introduces an additional total normalization uncertainty in the order of 1.5 %.

The total number of events in the fiducial volume per year, normalized to the reference target filling and an exposure of 10^{19} POT, is shown in Figure 6.9. The event numbers for the first and second SM separately agree within their statistical

Table 6.5: Average number of bricks in the target for the 2009 to 2011 run periods (see Table 6.1) for both the whole target and the fiducial volume, as defined in Table 5.3. The corresponding normalization factors for the fiducial volume are given in brackets.

Year	SM1	SM2	total
Whole target			
2009	77027.8	70552.6	147580.4
2010	75082.0	69139.9	144221.9
2011 ^a	72797.8	67339.9	140137.7
Reference ^b	77558.0	71214.0	148772.0
Fiducial volume only			
2009	49893.0 (0.981)	45552.0 (0.979)	95445.0
2010	49858.0 (0.980)	42236.3 (0.908)	92094.3
2011	46919.5 (0.923)	39759.9 (0.854)	86679.4
Reference	50856.0	46512.0	97368.0

^aIncluding 727 (494) iron fake bricks in row 3 of SM1 (SM2) with similar passive physical properties but without active emulsion sheets.

^bRealistic target configuration of 29-06-2009, also used for the MC simulations.

errors, as do the total numbers of events of all years. They also agree with the MC expectation within the systematic uncertainties from the CNGS beam, the cross section and the target variations, but the MC expectation is about 8% higher than the data. A similar normalization mismatch has been reported before for the 2008 and 2009 run periods [183]. Other LNGS experiments like ICARUS should observe a similar discrepancy if it is caused by the CNGS beam. The asymmetry between the first and the second SM in data is larger than in MC, where the asymmetry in MC is caused by external events (see Section 6.2.1). More data is required to detect possible asymmetries between the two super modules.

The relation between the CNGS extraction intensity and the interaction probability is shown in Figure 6.10. The data is compatible with a straight line fit through zero, as expected. The data from 2009 is higher than the average fitted line, while the 2011 data is lower, as was expected from the decreasing target mass. Data points at low CNGS extraction intensities mostly coincide with CNGS run (re-)starts with unstable detector performance.

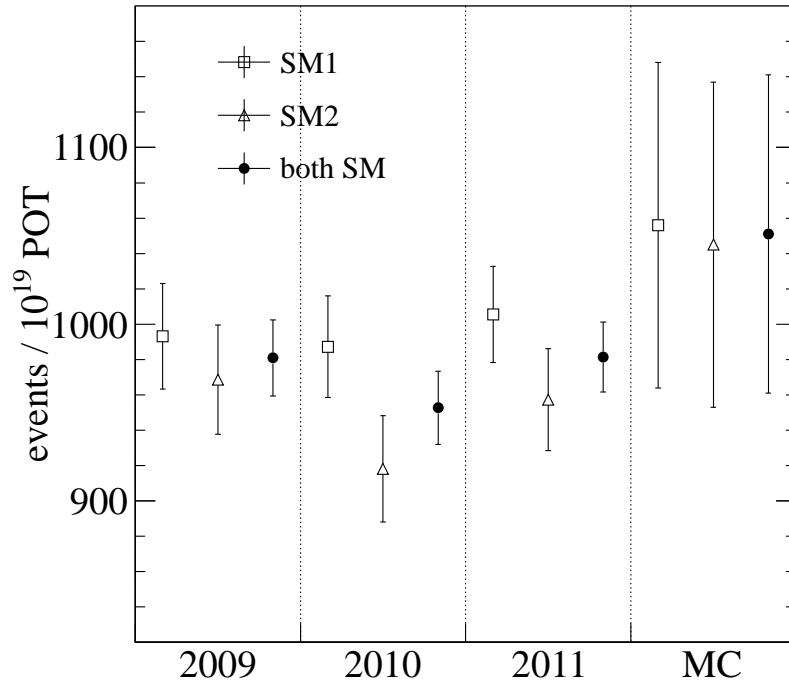


Figure 6.9: Total number of events in the fiducial volume per year, normalized to 10^{19} POT and the reference target filling (148,772 bricks). The data error bars represent the statistical uncertainty only, while the MC error bars include systematic uncertainties from the CNGS flux and cross sections. The MC statistical error alone is smaller than the marker size.

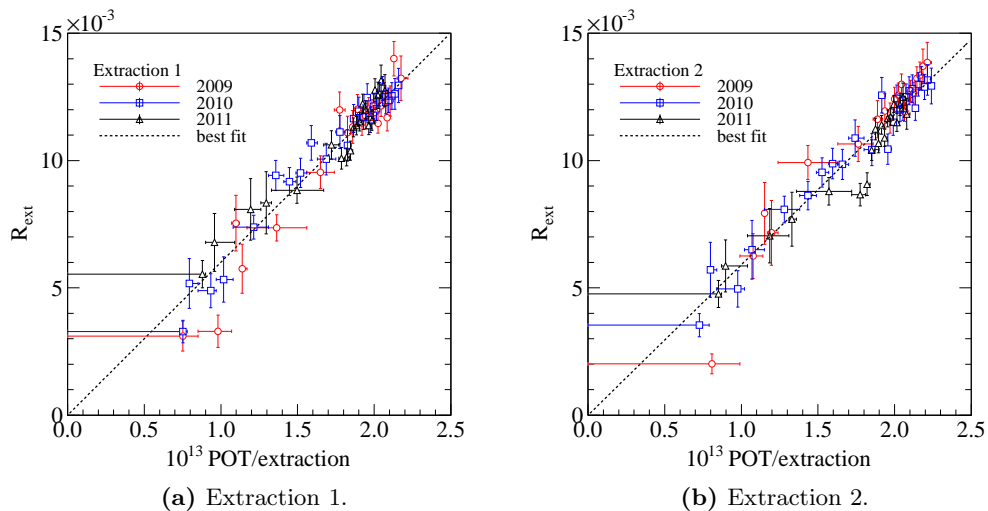


Figure 6.10: Ratio R_{ext} of event rates over extraction intensity (after cuts), data is not corrected for decreasing target mass, statistical errors only. The black dashed line is a linear fit to the combined data from all three run periods (forced through zero).

6.4 Data/Monte Carlo comparison

Within this section, the comparison between data and the unoscillated MC expectation for fiducial volume events is shown for some selected kinematic variables important for the muon disappearance analysis. A good understanding of these distributions is crucial for all higher-level analyses performed with the OPERA electronic detector.

The different MC contributions are stacked on top of each other and normalized to integrated number of POT given in Table 6.3 and the respective average fiducial target mass per year⁹ (see Table 6.5). The total MC normalization has been lowered by 8%, as determined in Section 6.3, which is still compatible with the systematic uncertainties from the CNGS beam. Unlike in [183], none of the MC distributions is normalized to data but to the respective POT and target mass and hence allows a better comparison of data and MC. This is especially important to detect a possible bias in the NC and CC classification which would be invisible if data and MC had been normalized to each other in every plot separately.

The bottom plots of all figures in this section show the data/MC ratio comparison. For data, only the statistical uncertainties are shown in both plots. For MC, statistical and systematic uncertainties are added in quadrature. The inner band in these ratio plots shows the, usually very small, statistical uncertainty of the MC only. The systematic uncertainty is dominated¹⁰ by the cross section and a 1.5% uncertainty from the average fiducial volume mass definition. The cross section uncertainty is taken to be 4% (6%) for neutrinos (antineutrinos), for simplicity (compare Section 2). Afterwards, the uncertainties from the cross sections, the fiducial volume, and the MC statistical error are added in quadrature. All distributions are shown after all cuts, called the basic cuts in the following, as described in the previous section.

All contributions that make up at least 0.1% of the events in at least one bin are shown. Notice that the external ν_μ MC sample is statistically limited and may lead to quite high statistical uncertainties in individual bins.

Event classification

The k-NN event classifier output (see Section 5.8) is shown in Figure 6.11. The event selection contains all events that pass the basic cuts. While the agreement for CC-like events is excellent, a small bias of NC-like events is visible, which are less NC-like in data than in MC for k-NN outputs < 0.15 . This kind of bias is not unexpected and the final cut value of $\Gamma = 0.3$ is chosen such that the influence of data/MC differences is reduced. The systematic uncertainty introduced by the cut

⁹In contrast to Figure 6.9, the data here is left unscaled, but the MC expectation is normalized accordingly.

¹⁰The largest uncertainty from the CNGS beam is already taken into account by the lowering of the global normalization.

value can be addressed by varying its value and checking the data/MC agreement for different CC-like-dependent distributions: Changing Γ by $\pm 10\%$ does not result in any worsening of the data/MC agreement of any of the distributions shown below.

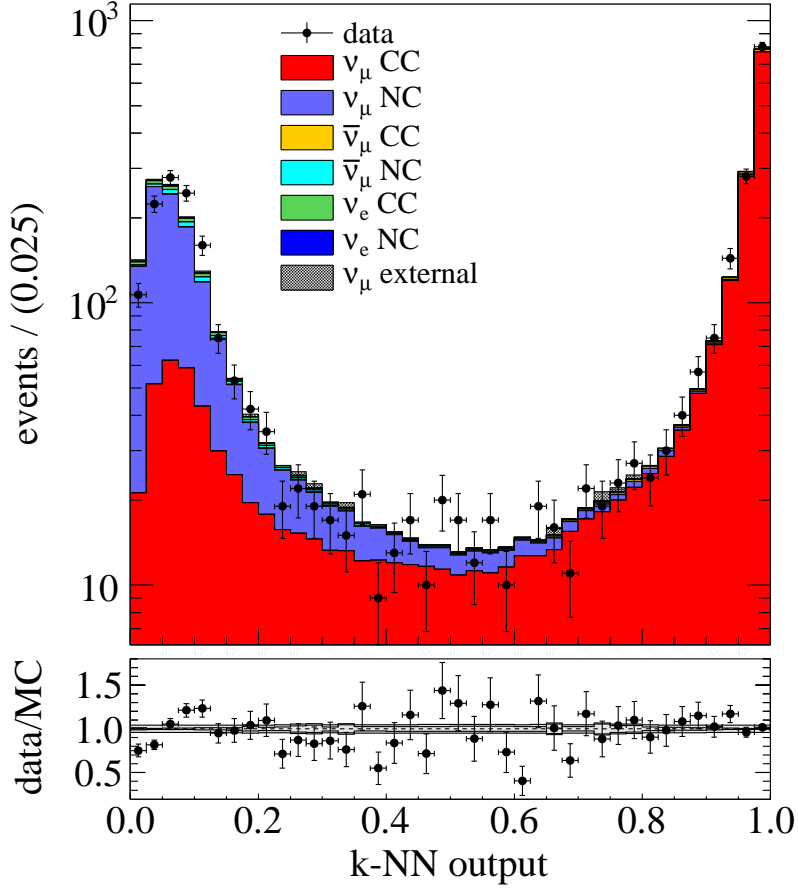


Figure 6.11: k-NN classifier output (logarithmic y -axis).

Muon kinematics

The OPERA electronic detector is optimized for the energy and charge reconstruction of muon tracks, with the goal of reducing the background from charm decays (see Section 3.2.7.1). The measurement of the antimuon spectrum is furthermore a tool for cross checking the CNGS beam simulation, since antimuons originate mainly from $\bar{\nu}_\mu$ CC interactions, with the $\bar{\nu}_\mu$ accounting for the largest part of the beam contamination. Additional systematic uncertainties of the muon momentum reconstruction are described in [183], but not included in the following plots.

The event selection contains CC-like events with at least one 3D-track and a good magnet status, where the MC normalization is adjusted according to the

magnet status. The reconstructed track charge is used to distinguish between μ^- and μ^+ , no further cut on the track quality is applied.

The reconstructed track angles θ with respect to the z -axis in the zy projection are shown in Figure 6.12a for muons and in Figure 6.12b for antimuons. The respective mean values of fitted Gaussians are $(+56.9 \pm 1.8 \text{ (stat.)})$ mrad for μ^- and $(+53.3 \pm 6.6 \text{ (stat.)})$ mrad for μ^+ are in very good agreement with the value of $\theta_{CNGS} = +58.11$ mrad expected from geodesy and earth curvature (see Section 3.1.2).

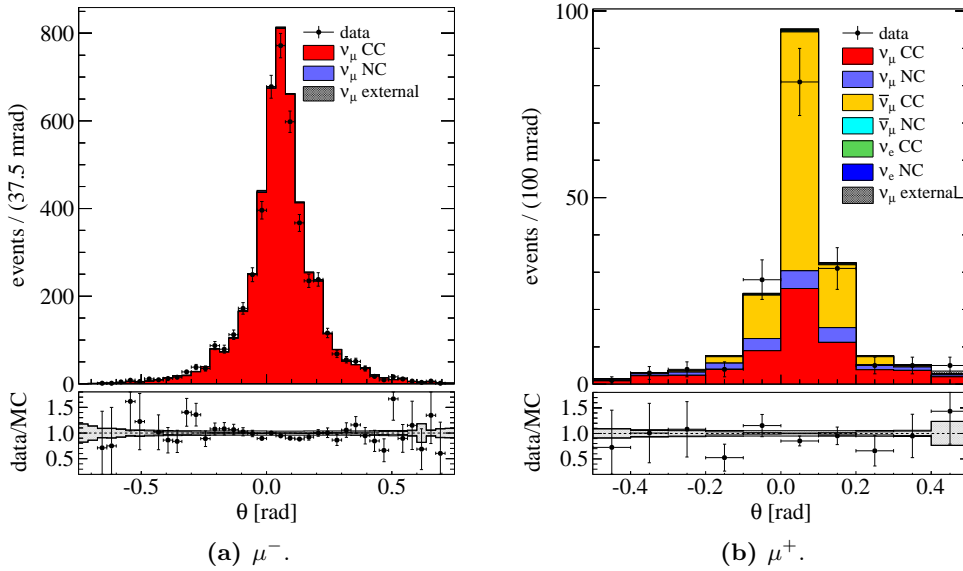


Figure 6.12: Reconstructed track angle θ in the zy projection.

The reconstructed muon angles ϕ with respect to the z -axis in the zx projection are shown in Figure 6.13a for muons and in Figure 6.13b for antimuons. The respective mean values of $(-6.7 \pm 1.8 \text{ (stat.)})$ mrad for μ^- and $(-11.3 \pm 6.5 \text{ (stat.)})$ mrad for μ^+ are in very good agreement with the value of $\theta_{CNGS} = -4.48$ mrad expected from geodesy and earth curvature.

The reconstructed (anti-)muon energy, multiplied by the reconstructed (anti-)muon charge, is shown in Figure 6.14. The agreement between MC and data within the uncertainties is very good, even for highest and lowest muon energies. While still compatible within the systematic uncertainties, a small deficit for muon energies around 15 GeV is visible.

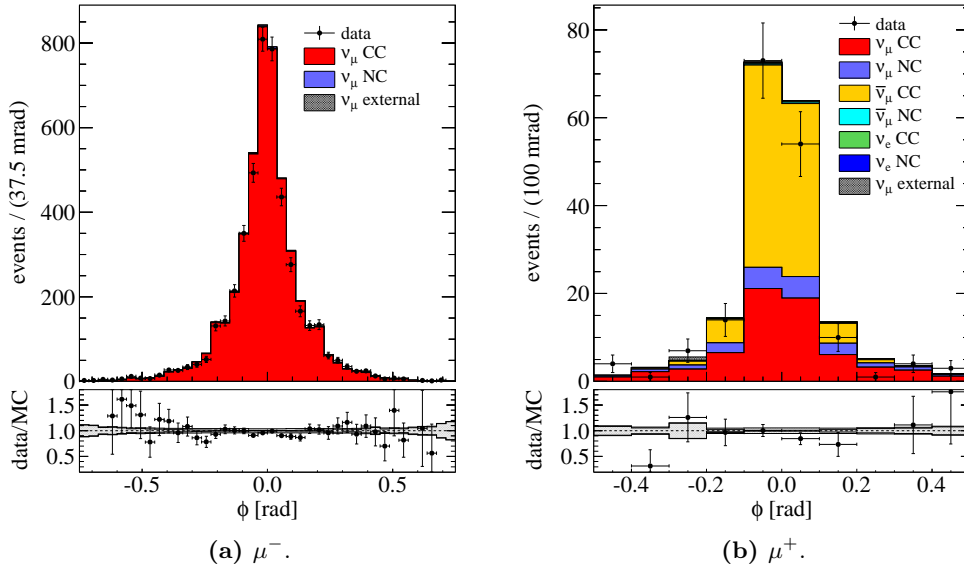


Figure 6.13: Reconstructed track angle ϕ in the zx projection.

Using all CC-like events, the muon charge ratio in the range $-200 \text{ GeV} < E_\mu \times \text{charge} < 100 \text{ GeV}$ can be determined. The selected CC-like data sample contains 162 μ^+ and 4523 μ^- events, yielding a ratio of

$$\left(\frac{N_{\mu^+}}{N_{\mu^+} + N_{\mu^-}} \right)_{data} = (3.46 \pm 0.28 \text{ (stat.)}) \%, \quad (6.1)$$

assuming binominal errors. The corresponding ratio expected from MC is given by

$$\left(\frac{N_{\mu^+}}{N_{\mu^+} + N_{\mu^-}} \right)_{MC} = (3.63 \pm 0.03 \text{ (stat.)}) \%. \quad (6.2)$$

The muon charge ratio for data and MC ratio are in agreement within their respective statistical uncertainties.

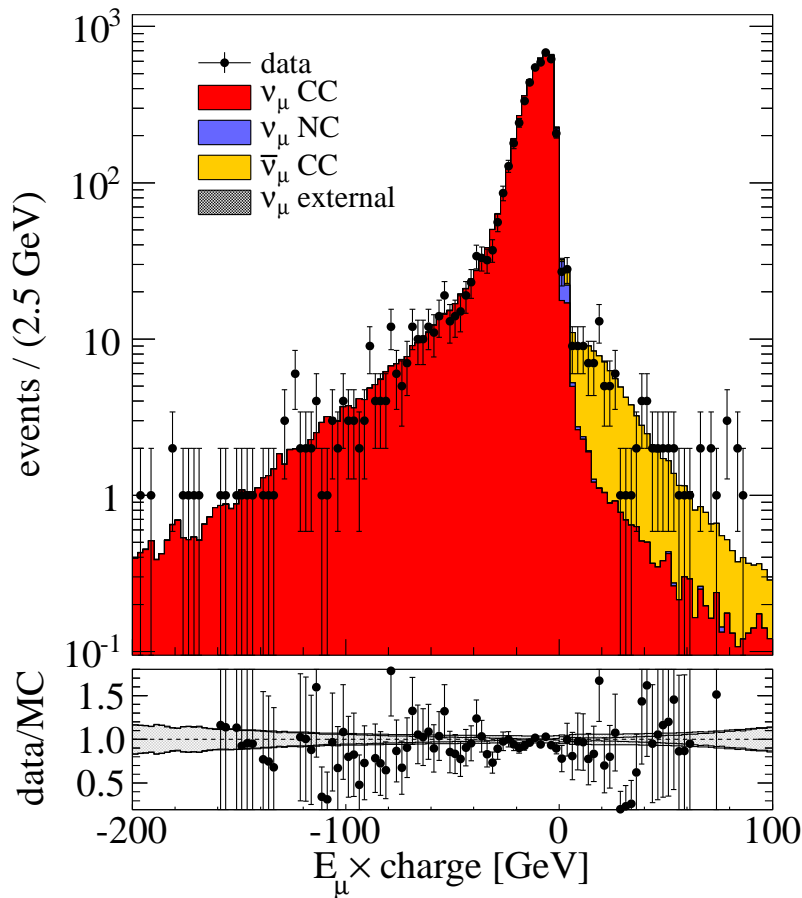


Figure 6.14: Reconstructed (anti-)muon energy spectrum, multiplied with the reconstructed (anti-)muon charge (logarithmic y-axis).

Hadronic energy

The reconstructed hadronic energy is a crucial input for the ratio measurement described in Section 7. The event selection contains CC-like events with at least one 3D-track that pass the basic cuts (see Figure 6.15a) and NC-like events or events with no 3D-track that pass the basic cuts (see Figure 6.15b).

The agreement of the CC-like data with MC is very good, with the deficit at low hadronic energies well within the respective uncertainties¹¹. For NC-like data, there is a large excess in the lowest energy bin: This bin contains all noise-like events and other events that may either be mismodeled or that are not included in the MC simulation at all. The largest uncertainty in this bin is expected to arise from the minimum bias filter (see Section 6.1), where the modeling of the trigger threshold has a large effect on the number of low-energy NC-like events. In addition, most of the external background, contributing almost 25% of all events

¹¹Notice that using the global cross section uncertainty underestimates the large uncertainties from CCQE and RESCC scattering for low hadronic energies.

in the MC simulation, is also included in this bin. For $E_{had} > 2.5$ GeV, the large true CC background in the NC-like sample is reproduced very well, both in shape and rate.

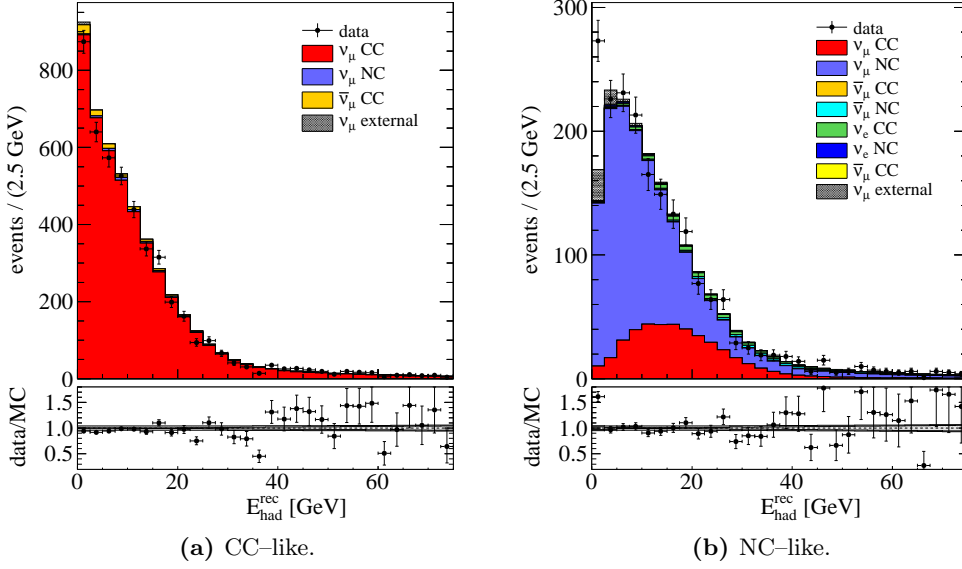


Figure 6.15: Reconstructed hadronic energy for CC-like and NC-like events.

Neutrino energy

The reconstructed hadronic energy E_{had}^{rec} and the reconstructed muon energy E_{μ}^{rec} can be combined into the total visible energy

$$E_{vis} = E_{had}^{rec} + E_{\mu}^{rec} \quad (6.3)$$

for CC-like events. The event selection contains CC-like events with at least one 3D-track and good magnet status. By dividing the sample into identified μ^- and μ^+ , the E_{vis} distribution are expected to be similar to the respective ν_{μ} and $\bar{\nu}_{\mu}$ energy spectra. The distributions are shown in Figure 6.16 and in Figure 6.17. The ν_{μ} energy spectrum shows a deficit at small values of $E_{vis} < 7.5$ GeV, which is related to the observed deficit for small values of E_{had}^{rec} shown in Figure 6.15a. The ν_{μ} energy spectrum in the energy range $20 \text{ GeV} < E_{vis} < 35 \text{ GeV}$ is below the MC expectation. This difference has also been observed in the 2008 and 2009 data periods in an independent analysis [183]. More data is needed to determine if this is a statistical fluctuation or a real issue.

The agreement of the ν_{μ} energy spectrum at low values of E_{vis} is improved if values with $E_{had}^{rec} < 2.5$ GeV are excluded (see Figure 6.18).

The respective mean values of the data and the MC distributions are in agreement within their respective uncertainties:

$$\langle E_{vis}^{\mu^-} \rangle_{MC} = (24.4 \pm 0.1 \text{ (stat.)} \pm 0.2 \text{ (syst.)}) \text{ GeV}, \quad (6.4)$$

$$\langle E_{vis}^{\mu^-} \rangle_{data} = (25.0 \pm 0.3 \text{ (stat.)}) \text{ GeV} \quad (6.5)$$

and

$$\langle E_{vis}^{\mu^+} \rangle_{MC} = (32.0 \pm 0.2 \text{ (stat.)} \pm 0.2 \text{ (syst.)}) \text{ GeV}, \quad (6.6)$$

$$\langle E_{vis}^{\mu^+} \rangle_{data} = (33.3 \pm 1.9 \text{ (stat.)}) \text{ GeV}. \quad (6.7)$$

The agreement persists if a cut at $E_{had} > 2.5 \text{ GeV}$ is applied, the respective mean values of $\langle E_{vis} \rangle$ are shifted to about 5% higher energies.

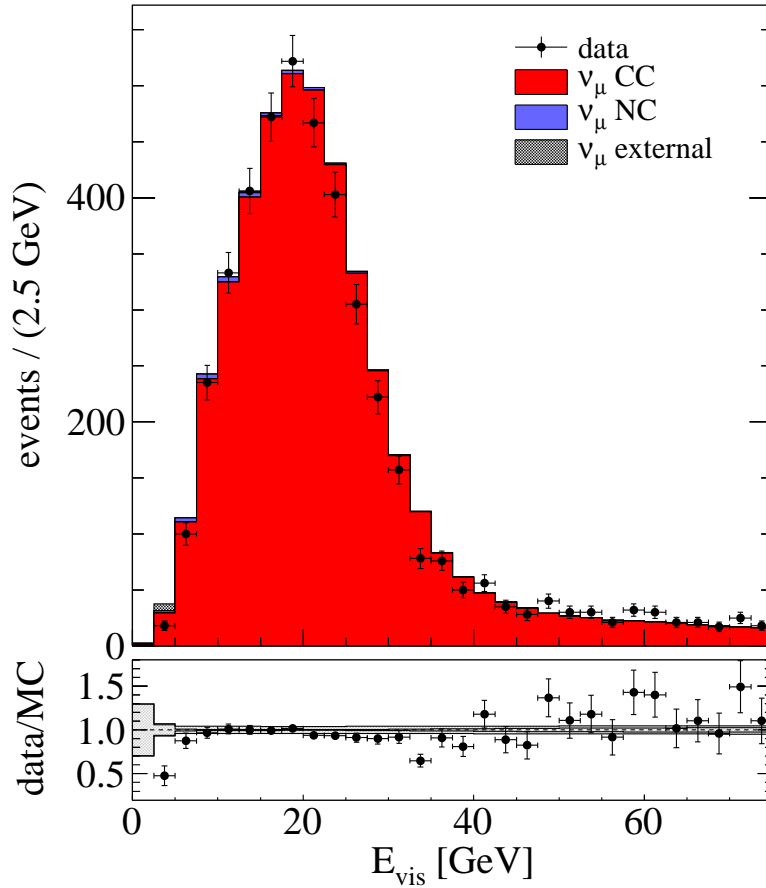


Figure 6.16: Total visible energy for CC-like events with a μ^- track.

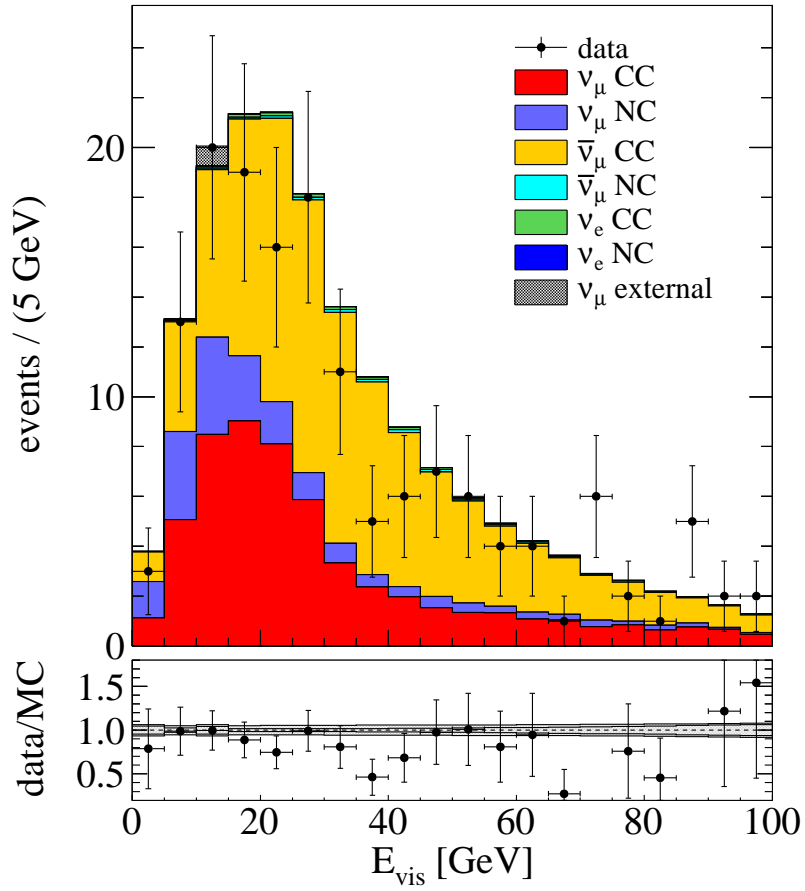


Figure 6.17: Total visible energy for CC-like events with a μ^+ track.

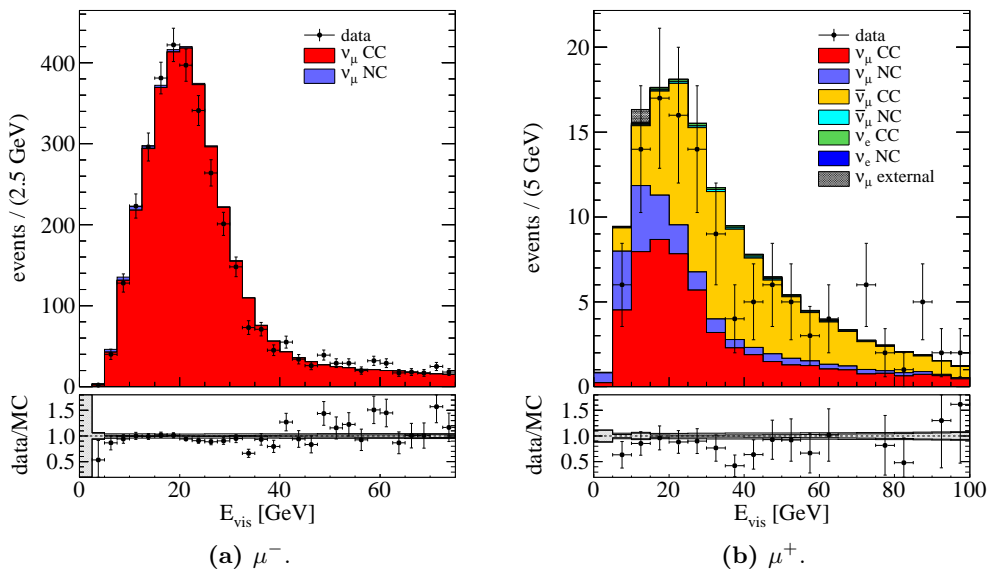


Figure 6.18: Total visible energy for CC-like events with $E_{\text{had}}^{\text{rec}} > 2.5$ GeV.

6.5 Comparison with emulsion data

The emulsion data of the OPERA experiment offers a unique opportunity for cross checking the electronic detector data with the data from reconstructed ECC bricks, without having to rely on MC simulations. However, the event selection is biased towards events where the correct brick has been successfully identified, extracted, developed and finally the vertex has been located.

The available number of events with a successfully located vertex in the brick in the analysed data from 2009 to 2011 amounts to 987 events. After electronic detector cuts, a sample of 873 events remains¹². The distance between the vertex reconstructed in the electronic detector using the algorithm described in Section 5.7, and the emulsion reconstruction is shown in Figure 6.19. The fit of a sum of two Gaussians yields $\sigma_{x1} = (1.7 \pm 0.2)$ cm and $\sigma_{x2} = (5.8 \pm 0.4)$ cm for the x vertex residuals and $\sigma_{y1} = (1.8 \pm 0.2)$ cm and $\sigma_{y2} = (5.0 \pm 0.5)$ cm for the y vertex residuals, which are in excellent agreement with the expectation from MC simulations (see Section 5.7). Both residual distributions are centered at $dx = dy = (0.0 \pm 0.1)$ cm. Note that for TT-CS matching, a higher precision $\mathcal{O}(1 \text{ mm})$ is required which makes TT alignment corrections necessary¹³.

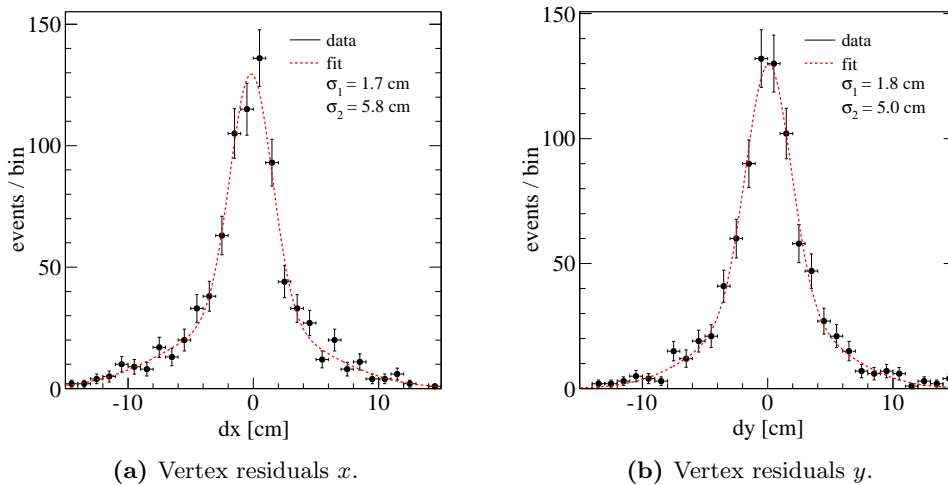


Figure 6.19: Vertex residuals $dx = x_{emulsion} - x_{electronic}$ and $dy = y_{emulsion} - y_{electronic}$ for events reconstructed in both the emulsions and the electronic detector. The Gaussian fit (see Section 5.7 for details) is shown as a red dashed line.

Out of these events, 757 events have a reconstructed muon track in the electronic detector that is also found in the emulsions¹⁴. This number is further reduced by the requirement of at least ten crossed lead plates by the track in the

¹²643 events from 2009, 203 events from 2010 and 29 events from 2011.

¹³The main contribution is a vertical shift of the loaded brick support structure relative to the TT planes.

¹⁴Using only the emulsions, the identification of muons is impossible, requiring the usage of the electronic detector predictions for this tasks.

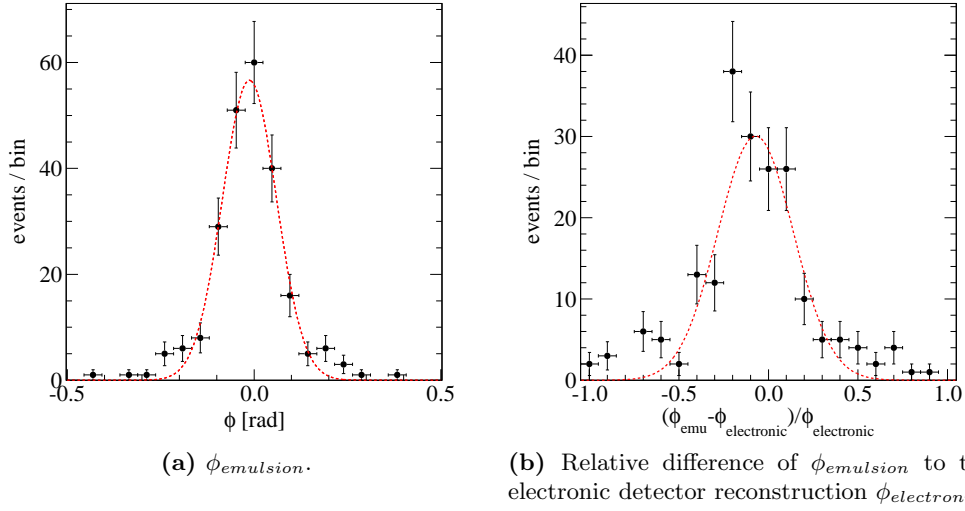


Figure 6.20: Reconstructed angle ϕ in the emulsions and relative difference to the electronic detector reconstruction. Gaussian fits are shown as red dashed lines.

respective vertex brick plus electronic detector cuts, resulting in 234 remaining events. These events can be used to reconstruct the CNGS beam angle using emulsions only, giving $\theta_{emulsion} = (49 \pm 5)$ mrad and $\phi_{emulsion} = (-12 \pm 5)$ mrad, which is in agreement with the expected values of $\theta_{CNGS} = +58.11$ mrad and $\phi_{CNGS} = -4.48$ mrad from geodesy and earth curvature (see Section 3.1.2). The respective distributions are shown in Figure 6.20a and Figure 6.21a. The relative difference between the track angles reconstructed in the emulsion and in the electronic detector with respect to the electronic detector measurements is shown in Figure 6.20b and Figure 6.21b. The means of Gaussian fits to these two distributions yield $(\phi_{emulsion} - \phi_{electronic})/\phi_{electronic} = (-7 \pm 2)\%$ and $(\theta_{emulsion} - \theta_{electronic})/\theta_{electronic} = (0 \pm 2)\%$. While the agreement for θ is excellent, the reconstructed angle ϕ in the emulsion gives a smaller values than both the electronic detector reconstruction and the expectation. Given the quite biased emulsion event selection, the reason for this discrepancy is yet unsolved¹⁵.

¹⁵Since ϕ is expected to be close to zero, changing the definition of this angle could be used to define a more stable expression by avoiding a vanishing denominator in $(\phi_{emulsion} - \phi_{electronic})/\phi_{electronic}$.

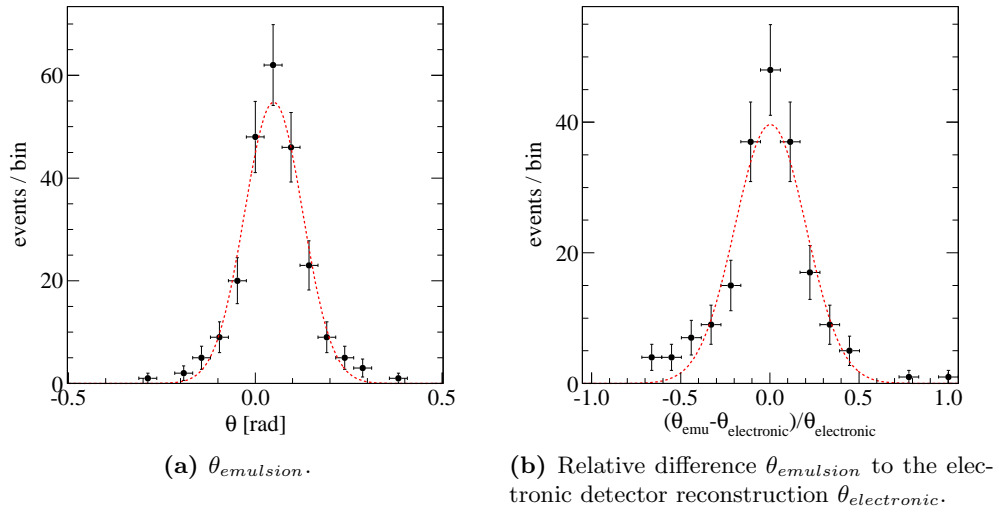


Figure 6.21: Reconstructed angle θ in the emulsions and relative difference to the electronic detector reconstruction. Gaussian fits are shown as red dashed lines.

Chapter 7

Oscillation analysis

The neutrino event rate for a neutrino flavor β at the OPERA location is given by

$$N_{\nu\beta} = \sum_{\alpha} K \int_0^{\infty} \Phi_{\nu\beta}(E) \times \sigma_{\nu\beta}(E) \times \epsilon_{\nu\beta}(E) dE, \quad (7.1)$$

with the neutrino flux

$$\Phi_{\nu\beta}(E) = \Phi_{\nu\alpha}(E) \times P(\nu_{\alpha} \rightarrow \nu_{\beta})(E), \quad (7.2)$$

the initial neutrino flux $\Phi_{\nu\alpha}$, the oscillation probability $P(\nu_{\alpha} \rightarrow \nu_{\beta})(E)$ (see Section 1.3), the total neutrino cross section $\sigma_{\nu\beta}(E)$ (see Section 2), the integrated CNGS neutrino flux $\Phi(E)$ (see Section 4.1), and the overall detection efficiency $\epsilon(E)$. K is a factor to account for a proper normalization in physical units¹. In the following, event rates are normalized to a nominal total exposure of 22.5×10^{19} POT and an average fiducial target mass² of 1.3 kt (including non lead dead material), if not stated otherwise.

The unoscillated event rates for the different neutrino flavors ν_{β} and interactions in the OPERA experiment are given in Table 7.1, calculated using Equation 7.1 with $\epsilon_{\nu\beta}(E) = 1$, $\alpha = \beta$ and $P(\nu_{\alpha} \rightarrow \nu_{\beta})(E) = 1$.

¹For Φ given in $1/\text{cm}^2/10^{19}$ POT and $\sigma_{\nu\alpha}$ given in $\text{cm}^2/\text{nucleon}$, the factor is $K = M[\text{kt}]/10^9/A$ where M is the target mass in kt and A is atomic number of the target.

²Calculated for pure lead isotope ^{208}Pb , difference to event rates for other lead isotopes are negligible though, total event rates for iron are smaller (larger) for neutrinos (antineutrinos) by about 1 % compared to lead.

Table 7.1: Default OPERA event rates for unoscillated CNGS beam flux, normalized to 10^{19} POT and 1kton lead. The raw total number of neutrino-induced events (NC and CC, all flavors) in OPERA amounts to $841.0/10^{19}$ POT/kton. The uncertainties of these rates are dominated by the CNGS normalization (about 5%) and the total cross sections (about 4% for neutrinos and 6% for antineutrinos).

	ν_e	$\bar{\nu}_e$	ν_μ	$\bar{\nu}_\mu$
CC	5.5	0.3	623.7	12.1
NC	1.7	0.1	192.7	4.9
total	7.2	0.4	816.4	17.0

7.1 Neutrino appearance

The OPERA experiment offers the unique opportunity to measure both appearance channels, $\nu_\mu \rightarrow \nu_\tau$ and $\nu_\mu \rightarrow \nu_e$, in one experiment in the same neutrino beam. The general requirements for the two channels are different: $\nu_\mu \rightarrow \nu_\tau$ oscillation experiments need a high neutrino energy above the τ threshold whereas specialized $\nu_\mu \rightarrow \nu_e$ oscillation experiments like NOVA or T2K are operated at much lower energies around 1 GeV in off-axis beams to reduce the high-energy tails of the neutrino energy distributions and hence the background from mis-identified π^0 produced in ν_μ DIS NC interactions.

In this section, the distance from the average secondary meson decay point at CERN to the OPERA detector center is taken to be 730.085 km, the default oscillation parameters are taken from Table 1.1 and the definitions given by Equation 1.39 ff. are used.

7.1.1 ν_τ appearance

The OPERA detector is capable of detecting τ leptons from ν_τ CC interactions on an event-by-event basis with a very low background. Within the three-flavor oscillation model, the most general expression describing ν_τ appearance in a ν_μ beam is given by Equation A.4 for neutrino propagation in vacuum. For propagation in matter, the Hamiltonian in the equation of motion has to be augmented by matter potentials as described in Section 1.3.3. The numbers of expected CNGS beam-induced ν_τ CC events in OPERA for different values of θ_{13} and δ_{CP} for normal mass hierarchy are shown in Table 7.2 assuming an overall ν_τ detection efficiency of 7%.

The neutrino mass hierarchy, a possible CP-violation and matter effects are small effects for the τ appearance search in the OPERA experiment: Matter effects only act on electron neutrinos and hence are a sub-leading effect for $\nu_\mu \rightarrow \nu_\tau$ oscillations at the OPERA baseline. Their impact grows for larger θ_{13} , but never changes the expected τ event rates by more than $\pm 0.25\%$, where the sign of the difference depends on the mass hierarchy. CP-violation in ν_τ appearance is a small effect, where the τ event rate in OPERA gets maximal for $\delta_{CP} = \pi/2$ and minimal

for $\delta_{CP} = 3\pi/2$. The event rate change is less than $\pm 0.25\%$ for all possible values of δ_{CP} . A value of $\theta_{13} = 8.8^\circ$ as measured by the Daya Bay experiment [20] reduces the expected τ event rates by about 5% compared to $\theta_{13} = 0^\circ$. The ν_τ appearance probability for different values of θ_{13} and different values of the CP-violating phase is shown in Figure 7.1.

Table 7.2: ν_τ CC event rates in OPERA for propagation in vacuum and matter (given in brackets) for different values of θ_{13} with the approximate 1σ range from Daya Bay [20], δ_{CP} and normal mass hierarchy. The numbers are given explicitly to show the smallness of the variations. Matter effects and CP violation are not observable for $\theta_{13} = 0^\circ$.

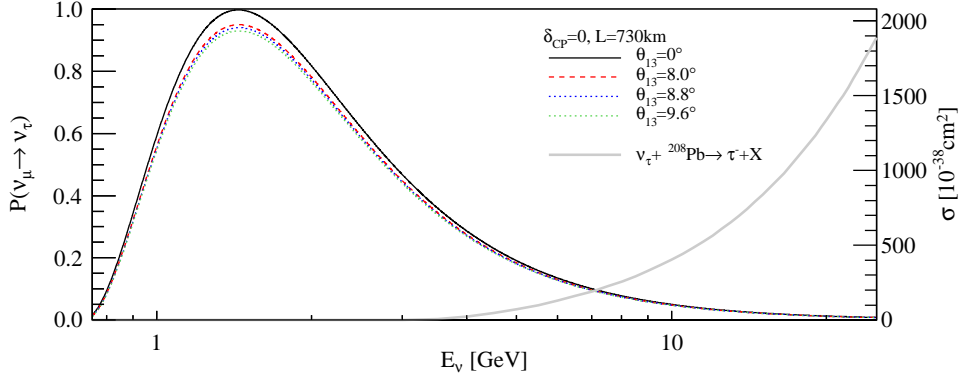
	θ_{13}	
	0°	$8.0^\circ - 9.6^\circ$
$\delta_{CP} = 0$	7.54 (7.54)	7.25–7.12 (7.24–7.11)
$\delta_{CP} = \pi/2$	7.54 (7.54)	7.25–7.13 (7.25–7.12)
$\delta_{CP} = \pi$	7.54 (7.54)	7.24–7.11 (7.23–7.11)
$\delta_{CP} = 3\pi/2$	7.54 (7.54)	7.23–7.11 (7.23–7.10)

In the two-flavor approximation, however, the number N_τ of τ events does neither depend on θ_{13} nor δ_{CP} , and is calculated to be $N_\tau \approx 7.81$ ($N_\tau \approx 7.88$ for maximal mixing). These numbers are about 3% higher than the official expectation [162], most likely due to different cross section models and rounding issues when using the total efficiency instead of the decay channel-based ones.

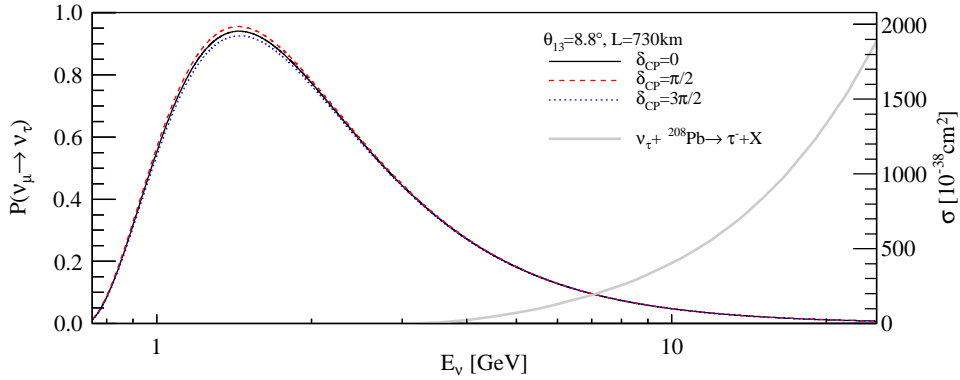
If the τ event rates are evaluated in a “3+1” oscillation model (see Section 1.3.2) and the extended normal mass hierarchy $m_1 < m_2 < m_3 < m_4$ with one additional sterile neutrino that is separated by about $\Delta m_{41}^2 = \mathcal{O}(1 \text{ eV}^2)$, the event rates change significantly for certain combinations of mixing angles and CP-violating phases. Within this model, N_τ depends mainly on θ_{23} , θ_{24} , θ_{34} and the CP-violating phase δ_{24} . N_τ is almost unaffected by θ_{12} and the two other CP-violating phases³ δ_{12} and δ_{13} , whereas θ_{14} may introduce small corrections in the percent range. Compared to three-flavor oscillations, N_τ is depleted for $\delta_{24} = 3\pi/2$ and the expected event rates drop by up to 60% for small values of θ_{24} , whereas the signal is enhanced for $\delta_{24} = \pi/2$ for $\theta_{24} \geq 3^\circ$. The expected event rates are shown in Figure 7.2. These values depend only weakly on the exact value of Δm_{41}^2 since the corresponding high oscillation frequency is washed out at the long OPERA baseline.

The expected number of background events in OPERA is $N_{bkgd,\tau} = 0.73 \pm 0.15$ for 22.5×10^{19} POT. The higher-energy ν_μ -dominated background rate is almost unaffected by neutrino oscillations, both in the

³Within the used notation, δ_{13} is equivalent to δ_{CP} in the three-flavor oscillation model.



(a) ν_τ appearance probability for OPERA for different values of θ_{13} . The CP-violating phase has been fixed to $\delta_{CP} = 0$.



(b) ν_τ appearance probability in OPERA for different values of δ_{13} . The mixing angle θ_{13} has been fixed to $\theta_{13} = 8.8^\circ$.

Figure 7.1: ν_τ appearance probability in OPERA as a function of true neutrino energy assuming three-flavor oscillations in matter and for different values of θ_{13} and δ_{13} (normal mass hierarchy). The total $\nu_\tau + {}^{208}\text{Pb}$ CC cross section is superimposed (gray line).

standard three-flavor and in “3+1” oscillation schemes.

With one ν_τ event observed by OPERA and an expected background of (0.16 ± 0.03) events ((0.05 ± 0.01) events for the $\tau \rightarrow h$ channel) (see Section 3.3), the background-only hypothesis (no oscillation) is rejected with a probability of 85% (95% for the $\tau \rightarrow h$ channel). The one-sided upper limits on N_τ in the analysed sample are calculated to be 2.18, 3.71 and 4.56 for the 68%, 90% and 95% C.L. assuming an overall ν_τ detection efficiency of 7%. These values can be used to exclude parts of the $(\sin^2(2\theta_{23}), \Delta m_{23}^2)$ parameter space as shown in Figure 7.3, including a systematic uncertainty of 25% on the τ rate from cross section and efficiency uncertainties. For maximal mixing, $\Delta m_{23}^2 > 4.5 \times 10^{-3} \text{ eV}^2$ is excluded at 90% C.L..

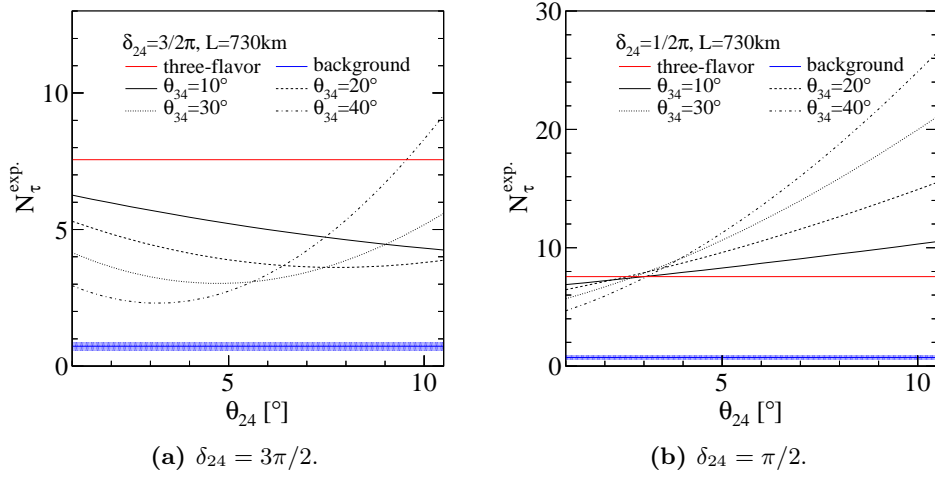


Figure 7.2: Number of expected τ events in OPERA for different values of θ_{24} , θ_{34} and δ_{24} with $\theta_{13} = \theta_{14} = 10^\circ$ and $\Delta m_{41}^2 = 1 \text{ eV}^2$. All other parameters have been taken from Table 1.1.

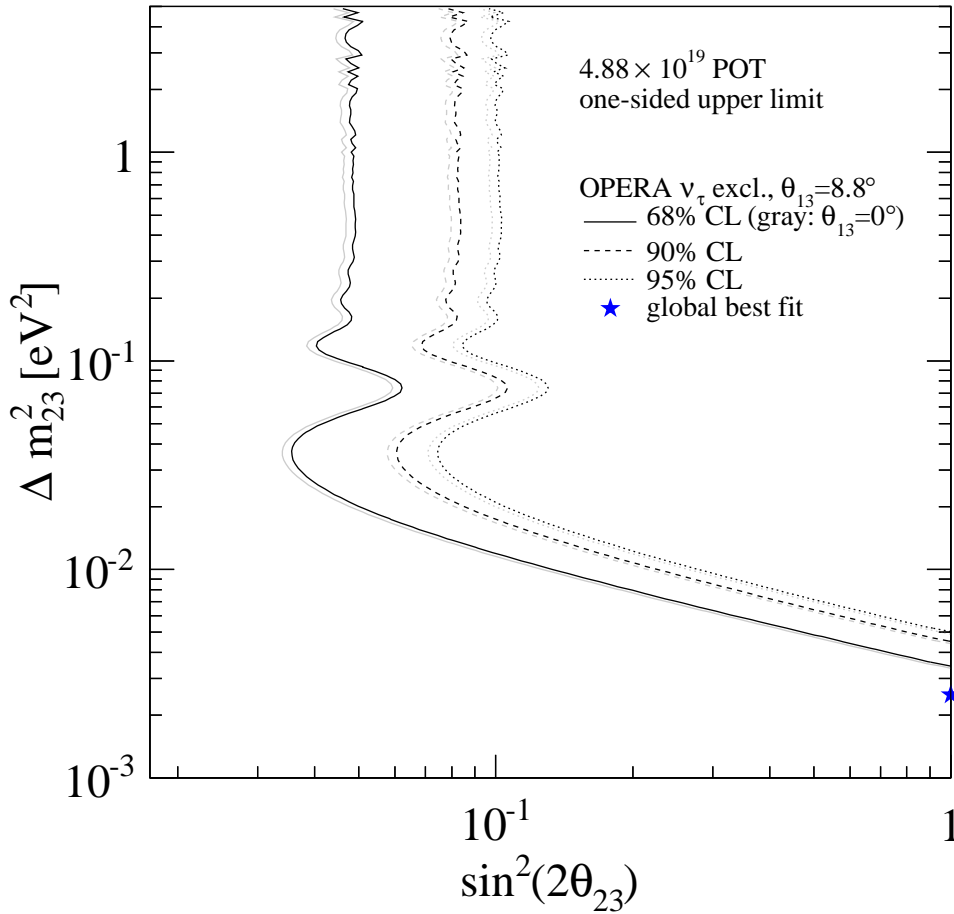


Figure 7.3: Excluded parameter region for $\sin^2(2\theta_{23})$ and $|\Delta m_{23}^2|$ from ν_{τ} appearance assuming 3-flavor oscillations in vacuum with $\theta_{13} = 8.8^\circ$ and $\delta_{CP} = 0$. The contours correspond to the 68%, 90% and 95% confidence levels. The exclusion region for $\theta_{13} = 0^\circ$ is shown for comparison.

7.1.2 ν_e appearance

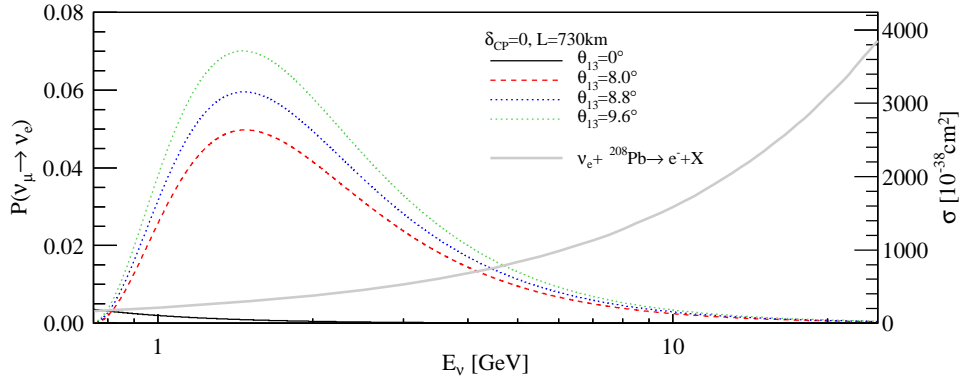
ν_e appearance in a long-baseline accelerator ν_μ experiment is a sub-leading oscillation and a three-flavor effect that cannot be described within a two-flavor approximation. The dominant term in the oscillation probability in vacuum (compare Equation A.1) is given by

$$P_{\mu e} \approx \sin^2(2\theta_{13}) \sin^2(\theta_{23}) \sin^2 \left(1.267 \frac{\Delta m_{23}^2 [\text{eV}^2] L [\text{km}]}{E [\text{GeV}]} \right). \quad (7.3)$$

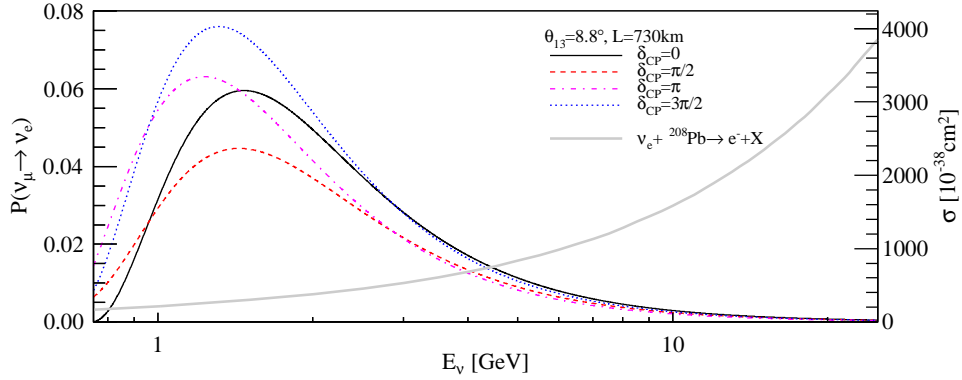
The ν_e appearance probability in OPERA for different values of θ_{13} , different values of δ_{CP} and either the normal or the inverted mass hierarchy are shown in Figure 7.4. As can be seen in Figure 7.4b, the ν_e appearance probability is maximized for $\delta_{CP} = 3\pi/2$ (normal mass hierarchy). Due to the high neutrino energies in OPERA, the expected electron neutrino flux from oscillation is small compared to the background. The latter is composed (in order of importance) of the intrinsic ν_e contamination of the CNGS beam, mis-identified decays of π^0 produced in ν_μ NC interactions, $\tau \rightarrow e$ decays from $\nu_\mu \rightarrow \nu_\tau$ oscillations, and mis-identified ν_μ CC interactions. Since $\nu_\mu \rightarrow \nu_e$ oscillations occur mainly at low neutrino energies $\mathcal{O}(\text{GeV})$, the signal-to-background ratio can be enhanced by applying an energy cut at about $E_{\nu_e}^{rec, cut} = 20 \text{ GeV}$.

The expected number of ν_e events for normal mass hierarchy, $\theta_{13} = 8.8^\circ$ and $\delta_{CP} = 0$, including a total ν_e detection efficiency of about 50 %, is of the order of five events from oscillations and about 20 background events for $E_{\nu_e}^{rec} < 20 \text{ GeV}$ [203, 204].

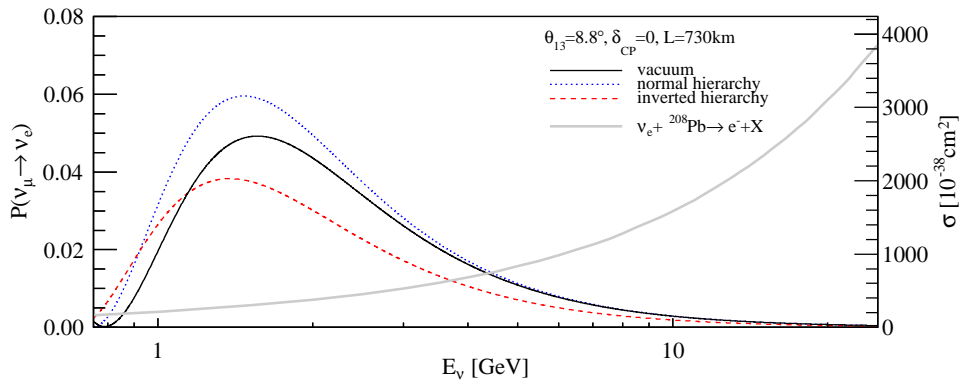
In a “3+1” scenario, the number of expected ν_e events from $\nu_\mu \rightarrow \nu_e$ oscillations changes, too. The explicit values depend on the exact and not yet fixed decay search procedures and selection efficiencies. However, the effect is not as large as for $\nu_\mu \rightarrow \nu_\tau$ oscillations, and the limited statistics of the OPERA will make it difficult to constrain the sterile neutrino parameter space using ν_e appearance [204].



(a) ν_e appearance probability for different values of θ_{13} (normal mass hierarchy). The CP-violating phase has been fixed to $\delta_{CP} = 0$. For $\theta_{13} = 0^\circ$, the ν_e appearance happens entirely due to θ_{12} .



(b) ν_e appearance probability for different values of δ_{CP} (normal mass hierarchy). The mixing angle θ_{13} has been fixed to $\theta_{13} = 8.8^\circ$.



(c) ν_e appearance probability for different mass hierarchies. The mixing angle θ_{13} has been fixed to $\theta_{13} = 8.8^\circ$ and the CP-violating phase has been fixed to $\delta_{CP} = 0$, the oscillation probability in vacuum is shown for comparison.

Figure 7.4: ν_e appearance probability in OPERA as a function of true neutrino energy assuming three-flavor oscillations in matter for different values of θ_{13} , δ_{CP} and different mass hierarchies. The total $\nu_e + {}^{208}\text{Pb}$ CC cross section is superimposed (grey line).

7.2 Neutrino disappearance

The measurement of ν_μ disappearance in a long-baseline accelerator neutrino beam experiment is usually performed by comparing the ν_μ CC energy spectra at two different detector positions: A near detector, located at $\Delta m_{23}^2 L/4E \ll 1$, measures the unoscillated spectrum, and a far detector, located at about $\Delta m_{23}^2 L/4E \sim 1$, measures the distorted spectrum due to oscillations. Usually, the design of the near and far detectors is similar, thus cancelling out systematic uncertainties related to the cross section models, beam normalization and composition and detector design. An example of such an experiment is MINOS [140, 205].

7.2.1 ν_μ disappearance

Another way to measure ν_μ disappearance is based on a method that was used to measure the Weinberg angle $\sin^2(\theta_W)$ in neutrino DIS⁴. Assuming only isospin symmetry, the *Llewellyn-Smith (LS)* relation

$$R^{LS} = \frac{\sigma_\nu^{NC}}{\sigma_\nu^{CC}} = \frac{1}{2} - \sin^2(\theta_W) + \frac{5}{9} \left(1 + \frac{\sigma_\nu^{CC}}{\sigma_{\bar{\nu}}^{CC}} \right) \sin^4(\theta_W) \quad (7.4)$$

is exact in lowest-order QCD and electroweak theory for DIS on isoscalar targets composed of first-generation light quarks [207]. Measuring the ratio of “short events”, predominantly ν_μ NC interactions without any reconstructed muon track, to “long events”, mainly ν_μ CC interactions, and using MC simulations to correct this measured ratio

$$R^{exp} = \frac{N_{short}}{N_{long}} \quad (7.5)$$

for detector efficiency and acceptance, thus yielding $R^{exp,corr}$, tracking calorimeter detectors like CHARM, CDHS or CCFR have measured the Weinberg angle $\sin^2(\theta_W)$. “Short” and “long” are typically expressed in terms of crossed absorber plates in the calorimeters.

If, on the other hand, an external measurement of $\sin^2(\theta_W)$ is used to calculate R^{LS} , any deviation of

$$t = \frac{R^{exp,corr}}{R^{LS}} \quad (7.6)$$

from unity⁵ can be interpreted in the framework of neutrino oscillations: $\nu_\mu \rightarrow \nu_\tau$ oscillations reduce the number of “long” events, since ν_τ CC interactions produce a τ , where only $\tau \rightarrow \mu$ decays will result in “long” events while the other τ decay modes, namely $\tau \rightarrow e$ and $\tau \rightarrow hadrons$, will appear as “short” events. In addition, the ν_τ CC cross section $\sigma_{\nu_\tau}^{CC}$ is significantly lower than the ν_μ CC

⁴The NUTEV experiment employed the Paschos–Wolfenstein relation using both neutrino and antineutrino beams [206].

⁵This approach is sometimes simply called the *t-test*, referring to a student’s t-test, where the zero hypothesis is given by the assumption of no oscillations.

cross section $\sigma_{\nu_\mu}^{CC}$ for neutrino energies in the GeV-range (compare Figure 2.32 and Figure 2.34). $\nu_\mu \rightarrow \nu_e$ oscillations further reduce the number of “long” events, since all ν_e CC interactions produce “short” events with a cross section $\sigma_{\nu_e}^{CC} \approx \sigma_{\nu_\mu}^{CC}$. The same arguments apply to the charge-conjugated channels.

For high neutrino energies, typically above about 30 GeV, and high hadronic energies, typically about above 10 GeV, the “short” sample contains mainly true NC events, while the “long” sample contains mainly true CC events. The “short” sample will contain an unavoidable contamination of very inelastic, i.e. $y \approx 1$, true CC interactions, where most of the neutrino energy is transferred to the hadronic system. The “long” sample is contaminated with true NC events, where single hadrons, mostly charged pions, can fake a long muon track. This method has been applied at the high-energy accelerator experiments CDHS and CHARM to place limits on neutrino oscillations [208].

If the method is extended to lower neutrino and hadronic energies, the classification using only the variable “short” and “long” is not sufficient to produce sufficiently pure event selections but requires the use of multivariate approaches (see Section 5.8). In the following, *NC-like* instead of “short” and *CC-like* instead of “long” will be used to denote the two different event classes.

Instead of using the ratio defined by Equation 7.5, the ratio

$$R^{exp} = \frac{N_{CC}}{N_{NC} + N_{CC}} = \frac{N_{CC}}{N}, \quad (7.7)$$

will be used. This definition avoids complications due to the correlations of N_{CC} and N_{NC} drawn from the same population N .

To extend the sensitivity of this method down to $\Delta m^2 \lesssim 5 \times 10^{-3}$, in OPERA, the ratio R must be measured for neutrino energies below about 10 GeV. Since the neutrino energy in NC interactions is unknown, one can either apply a cut on E_{had}^{rec} at some low value in the GeV-range and recover the original idea of a single-number t-test, or extend the measurement to an E_{had}^{rec} -dependent shape analysis

$$R(E_{had}^{rec}) = \frac{N_{CC}(E_{had}^{rec})}{N(E_{had}^{rec})}. \quad (7.8)$$

Such an energy-dependent measurement of $R(E_{had}^{rec})$, albeit at high hadronic energies, was performed by the CCFR short-baseline experiment and excluded $\Delta m_{23}^2 \gtrsim 1.4 \text{ eV}^2$ (90 % C.L.) for $\sin^2(2\theta_{23}) = 1$, using a cut of $E_{had}^{rec} > 30 \text{ GeV}$ [209].

Since the measurement of $R(E_{had}^{rec})$ is statistically dominated by the NC event rate, which is naturally much smaller than the corresponding CC event rate, the sensitivity of the $R(E_{had}^{rec})$ method is statistically worse than that of CC spectrum measurements. On the other hand, the $R(E_{had}^{rec})$ method is less affected by systematic uncertainties of the neutrino beam, the hadronization model and parts

of the cross section model (e.g. PDF uncertainties in DIS) that cancel in the ratio.

Lacking a near detector to measure the flux normalization, the $R(E_{had}^{rec})$ method is the only way for OPERA to measure ν_μ disappearance. It is complementary to CC disappearance measurements, since it is insensitive to possible admixtures of oscillations into sterile neutrinos or neutrino decays that would equally affect the NC and the CC event rates and hence leave $R(E_{had}^{rec})$ unchanged. Notice that at low hadronic energies, the ratio is not dominated by DIS anymore, but has large contributions from resonant and (quasi-)elastic scattering (see Section 2). Instead of using the Llewellyn-Smith relation and correcting the data accordingly, the full cross section and hadronization model as described in Section 2 is used to build a MC prediction of $R^{MC}(E_{had}^{rec})$ for OPERA which is then directly compared to the measured $R^{data}(E_{had}^{rec})$, as described below.

7.2.2 Systematic uncertainties

Most systematic uncertainties that affect both the NC and the CC components cancel out in the ratio. The remaining systematic uncertainties arise from those parameters that mainly affect either only the NC or only the CC component or that affect the energy reconstruction. All parameters and models of the event generator, the detector simulation, the event selection and the reconstruction have been considered as possible sources of systematic uncertainties. The included systematic uncertainties are summarized in Table 7.3 and in Table 7.4.

Uncertainties in the cross section models of quasi-elastic and resonant neutrino scattering are dominated by the variation of the axial mass parameters m_A (see Section 2.1.1 and Section 2.1.2). Almost no elastic NC events pass the trigger conditions in OPERA, thus these have negligible influence on the ratio. The axial mass parameters for resonant NC and resonant CC scattering are varied separately.

Uncertainties of the radiative corrections are estimated by using the CCFR LO PDFs (as provided together with the modified NUDIS2 code [77]) in comparison to the GRV98LO PDFs (default). The differences between these corrections for ν_μ interactions are below 15% for all regions of the parameter space covered by OPERA and below 5% for intermediate x and y . For all neutrino flavors and interactions (DIS NC or DIS CC), the 1σ uncertainty is conservatively set to $\pm 15\%$ for all values of x , y and E_ν (see Section 2.1.3.7).

At higher neutrino energies, the modeling of charm production becomes important since it mostly affects N_{CC} (see Section 2.1.3.5).

Uncertainties of the cross section in the inelastic transition region between RES and DIS scattering (see Section 2.1.4) are included by tweaking the weight

factors for the 1π and 2π final states.

The modeling of neutrino interactions itself includes uncertainties in the final state particle selection, the final state kinematics, resonance decays and intranuclear re-interactions (see Section 2.2). All varied parameters are summarized in Table 7.4. They are used to produce an overall hadronization uncertainty by quadratically adding up all contributions obtained via reweighting, as described in Appendix E, and using the resulting value as the combined 1σ uncertainty in the fit. These uncertainties are largest for low neutrino energies, as the produced hadrons also have low energies and thus are more strongly affected by intranuclear rescattering and uncertainties in the formation zone modeling.

CNGS-related uncertainties are included for ν_μ and ν_e only, as uncertainties of $\bar{\nu}_\mu$ and $\bar{\nu}_e$ are negligible for the ratio measurement. Despite the smallness of the ν_e contamination in the CNGS beam, uncertainties in the intrinsic ν_e contamination (see Section 4.1) have an effect on the ratio, since ν_e -induced events are almost always identified as being NC-like. For ν_e from $\nu_\mu \rightarrow \nu_e$ oscillations, the experimental uncertainty on θ_{13} is already small enough to be negligible within the scope of this thesis.

The systematic uncertainty of external background events (see Section 6.2) can be estimated from variations of the FV definitions and the respective change in the data/MC agreement. While the cut on $E_{had}^{rec} > 2.5\text{ GeV}$ and the tight FV definition already removes most of this background, the remaining external background events are assigned a $\pm 25\%$ uncertainty [183].

The minimum bias filter and the minimum number of digits cut (see Section 6.1) are the largest systematic uncertainties for very low-energy NC-like events. By varying the filter conditions and the cut values within a reasonable range, for $E_{had}^{rec} > 2.5\text{ GeV}$ their impact is found to be negligible.

The fractional systematic uncertainties of the ratio $R(E_{had}^{rec})$ are summarized in Table 7.5 and Table 7.6. The technical implementation of the systematic uncertainties is summarized in Appendix E.

Many other parameters of the MC simulation and the event reconstruction have been considered as sources of systematic uncertainties but turned out to have negligible impact on this ratio measurement. They are briefly summarized below:

- Apart from m_A , other systematic parameters of the CCQE and RES cross section model are negligible for neutrino energies $\gtrsim 1\text{ GeV}$ as in OPERA.
- Contributions from QE charm production (see Section 2.1.1) and from those interactions summarized in Section 2.1.5 are too small to have any significant impact on the ratio, the same applies to their systematic uncertainties.
- TT calibration uncertainties and possible TT-PMT gain variations have been checked by varying the MVA input variables (see Section 5.8 and

Table 7.3: Summary of systematic uncertainties for the ν_μ disappearance analysis. The respective 1σ parameter uncertainties are shown in the second column.

Systematic uncertainty	1σ range
m_A^{CCQE} in quasi-elastic scattering	$+25$ -15 %
$m_A^{RES\text{CC}}$ in resonant scattering	± 20 %
$m_A^{RES\text{NC}}$ in resonant scattering	± 20 %
Radiative corrections	± 15 %
Charm production ^a	–
$1\pi/2\pi$ final states weight factors	± 50 %
GENIE hadronization ^b	–
ν_μ CNGS flux ^c	–
ν_e CNGS flux ^c	–
External background	± 25 %

^aThe combined variation of the charm quark mass m_c (± 10 %) and the CKM matrix elements V_{cd} (± 5 %) and V_{cs} (± 10 %) is taken as $\pm 1\sigma$.

^bThe combined variation of all input parameters of the hadronization model (apart from pion final states) is taken as $\pm 1\sigma$ (see Table 7.4).

^cSee Section 4.1.

Section 5.9) within reasonable bounds: Tweaking the *deposited energy* by $\pm 5\%$ or changing the photo electron threshold of the input variable *strip number* by ± 0.5 units have no effect.

- Missing and not-accounted for TT sensors result in more events identified as NC-like and reconstructed with a lower hadronic energy. This is taken into account by the very careful event selection described in Section 6.1.
- Variations of the magnetic field were found to have minor effects on the track-finding, but none on the measured ratio. Notice that the track charge is not used in the ratio analysis.
- The normalization uncertainty of $\pm 1.5\%$ introduced by using the average FV definitions (see Section 5.6) cancels in the ratio.
- The uncertainty of the Weinberg angle (see Section 2.1.3) translates into a ratio uncertainty of less than 0.15% and hence is negligible within this analysis.
- The uncertainty of the low- Q^2 correction parameters $C_u^{val,1}$ and $C_u^{val,2}$, as well as the uncertainties of the BY higher twist correction factors A and B are negligible for all values of E_{had}^{rec} .
- The modeling of hadronic interactions within GEANT3 has been evaluated as described in Appendix E. Within the available MC statistics, no change of the ratio was observed.

Table 7.4: Summary of systematic uncertainties for the GENIE hadronization model. The propagation inside the nucleus is different for nucleons and pions.

Systematic uncertainty	1σ range
Hadron kinematics x_F	$\pm 20\%$
Hadron kinematics p_T^2	$\pm 3\%$
Formation time τ_0	$\pm 50\%$
Nucleon <i>mean free path (MFP)</i>	$\pm 20\%$
Nucleon charge exchange	$\pm 50\%$
Nucleon elastic scattering	$\pm 30\%$
Nucleon inelastic scattering	$\pm 40\%$
Nucleon absorption	$\pm 20\%$
Nucleon π production	$\pm 20\%$
π MFP	$\pm 20\%$
π charge exchange	$\pm 50\%$
π elastic scattering	$\pm 10\%$
π inelastic scattering	$\pm 40\%$
π absorption	$\pm 30\%$
π π production	$\pm 20\%$

- Uncertainties of the ν_τ CC cross section are in the order of 25 %, but their impact is small due to the small ν_τ CC cross section. Neglecting this uncertainty may result in a small underestimation of systematic uncertainties for very large values of $|\Delta m_{23}^2|$.

Furthermore, three possible effects, namely DIS nuclear corrections, strange sea asymmetry and non-isoscalarity of the neutrino target, have received special attention in the context of the interpretation of the NUTEV result [77] which used a similar ratio in the analysis, but was aimed at a much higher precision at higher neutrino energies than the OPERA disappearance search. These effects are not included as systematic uncertainties, but their impact on the ratio measurement at OPERA is discussed below:

- In the absence of a conclusive theoretical model for nuclear corrections in neutrino–nucleon interactions (see Section 2.1.3.8), an extreme position is to assume the complete absence of nuclear effects in neutrino DIS. For the ratio measurement, an even more extreme assumption is to assume full nuclear effects for CC (or NC) interactions and no nuclear effects for NC (CC) interactions. By assuming the same or very similar nuclear effects for NC and CC interactions, the uncertainty cancels in the ratio.

Table 7.5: Fractional systematic uncertainties of the ratio $R(E_{had}^{rec})$ from a variation of the input parameters as given in Table 7.3.

Parameter	energy bin					
	2.5 GeV	5 GeV	7.5 GeV	12.5 GeV	25 GeV	40 GeV
	-5 GeV	-7.5 GeV	-12.5 GeV	-25 GeV	-40 GeV	-70 GeV
	fractional uncertainty [%]					
m_A^{CCQE}	-0.059	-0.010	-0.001	-0.000	-0.000	-0.000
	0.168	0.036	0.007	0.000	0.000	0.000
m_A^{RESCC}	-0.539	-0.153	-0.032	-0.005	-0.000	-0.000
	0.823	0.292	0.073	0.011	0.001	0.000
m_A^{RESNC}	-0.770	-0.271	-0.057	-0.006	-0.000	-0.000
	0.429	0.128	0.023	0.002	0.000	0.000
Radiative corrections	-0.040	-0.063	-0.075	-0.076	-0.063	-0.078
	0.040	0.062	0.074	0.075	0.062	0.077
Charm production	-0.0216	-0.0383	-0.0518	-0.0581	-0.1002	-0.1751
	0.0435	0.1098	0.1826	0.2222	0.1319	0.1288
m_c	-0.018	-0.032	-0.044	-0.043	-0.041	-0.062
	0.030	0.075	0.119	0.135	0.054	0.027
V_{cd}	-0.011	-0.020	-0.028	-0.036	-0.068	-0.110
	0.026	0.068	0.108	0.133	0.087	0.079
V_{cs}	-0.002	-0.003	-0.004	-0.015	-0.061	-0.122
	0.017	0.044	0.086	0.115	0.083	0.098
Combined $1\pi/2\pi$ FS weight factors	-1.1893	-0.3887	-0.0828	-0.0090	-0.0027	-0.0000
	1.1516	0.3847	0.0826	0.0090	0.0027	0.0000
$\nu + p$ (NC) 1π	-0.106	-0.038	-0.008	-0.002	-0.000	-0.000
	0.106	0.038	0.008	0.002	0.000	0.000
$\nu + p$ (NC) 2π	-0.221	-0.065	-0.014	-0.001	-0.000	-0.000
	0.222	0.065	0.014	0.001	0.000	0.000
$\nu + n$ (NC) 1π	-0.477	-0.161	-0.034	-0.003	-0.000	-0.000
	0.481	0.161	0.034	0.003	0.000	0.000
$\nu + n$ (NC) 2π	-0.321	-0.103	-0.020	-0.003	-0.000	-0.000
	0.323	0.103	0.020	0.003	0.000	0.000
$\nu + p$ (CC) 1π	-0.103	-0.035	-0.004	-0.000	-0.001	-0.000
	0.103	0.035	0.004	0.000	0.001	0.000
$\nu + p$ (CC) 2π	-0.186	-0.053	-0.009	-0.002	-0.000	-0.000
	0.184	0.053	0.009	0.002	0.000	0.000
$\nu + n$ (CC) 1π	-0.861	-0.283	-0.063	-0.006	-0.001	-0.000
	0.814	0.278	0.063	0.006	0.001	0.000
$\nu + n$ (CC) 2π	-0.488	-0.158	-0.031	-0.004	-0.002	-0.000
	0.473	0.156	0.031	0.004	0.002	0.000
ν_μ CNGS flux	-0.014	-0.006	-0.003	-0.083	-0.432	-0.285
	0.015	0.006	0.003	0.074	0.370	0.226
ν_e CNGS flux	-0.018	-0.024	-0.036	-0.077	-0.241	-0.434
	0.018	0.024	0.036	0.077	0.242	0.438
External background	-0.336	-0.071	-0.032	-0.011	-0.045	-0.000
	0.338	0.071	0.032	0.011	0.045	0.000
MC statistical	-0.196	-0.221	-0.178	-0.174	-0.355	-0.414
	0.196	0.221	0.178	0.174	0.355	0.414

- A possible small strange sea asymmetry $[S^-] \neq 0$ is not fully excluded by external data but would, in any case, be negligible for OPERA due to the overall smallness of the effect (see Section 2.1.3.6).
- The excess of d quarks over u quarks in the OPERA target is corrected by modeling the complicated ECC brick geometry in detail and using the experimentally measured isotope compositions of the emulsions and lead plates that contribute to the largest fraction of events in the FV. Possibly uncorrected non-isoscalarity may arise from extracted bricks not accounted for in MC, geometry structures missing in the MC, or wrongly measured

Table 7.6: Fractional systematic uncertainties of the ratio $R(E_{had}^{rec})$ from a variation of the GENIE hadronization model input parameters as given in Table 7.4.

Parameter	energy bin					
	2.5 GeV	5 GeV	7.5 GeV	12.5 GeV	25 GeV	40 GeV
	-5 GeV	-7.5 GeV	-12.5 GeV	-25 GeV	-40 GeV	-70 GeV
	fractional uncertainty [%]					
Comb. GENIE hadr.	-0.6230	-0.3183	-0.1945	-0.4590	-0.3948	-0.3506
	0.7745	0.6537	0.3865	0.7454	0.4583	0.3470
Comb. GENIE hadr. (w/o form. time)	-0.4913	-0.2331	-0.1945	-0.2559	-0.2171	-0.3317
	0.4928	0.3236	0.2072	0.2395	0.3526	0.2629
p_T^2	-0.048	-0.040	-0.002	-0.001	-0.001	-0.000
	0.066	0.066	0.012	0.004	0.000	0.000
x_F	-0.021	-0.001	-0.004	-0.000	-0.001	-0.000
	0.153	0.123	0.018	0.004	0.000	0.000
Formation time ^a	-0.383	-0.217	-0.001	-0.381	-0.330	-0.113
	0.597	0.568	0.326	0.706	0.293	0.226
Nucleon MFP	-0.013	-0.026	-0.006	-0.045	-0.054	-0.023
	0.024	0.016	0.003	0.046	0.047	0.032
Nucleon charge exchange	-0.073	-0.017	-0.080	-0.016	-0.016	-0.040
	0.073	0.017	0.078	0.014	0.014	0.035
Nucleon elastic scattering	-0.001	-0.002	-0.007	-0.006	-0.005	-0.003
	0.001	0.002	0.007	0.007	0.005	0.003
Nucleon inelastic scattering	-0.099	-0.070	-0.109	-0.040	-0.041	-0.092
	0.099	0.071	0.107	0.037	0.025	0.080
Nucleon absorption	-0.004	-0.004	-0.005	-0.004	-0.009	-0.004
	0.004	0.004	0.005	0.004	0.009	0.004
Nucleon π production	-0.004	-0.024	-0.007	-0.004	-0.023	-0.009
	0.004	0.024	0.007	0.004	0.021	0.009
π MFP	-0.080	-0.072	-0.004	-0.045	-0.027	-0.025
	0.080	0.064	0.008	0.052	0.075	0.060
π charge exchange	-0.337	-0.158	-0.060	-0.167	-0.187	-0.252
	0.326	0.204	0.092	0.162	0.210	0.091
π elastic scattering	-0.048	-0.036	-0.011	-0.016	-0.049	-0.076
	0.052	0.032	0.010	0.024	0.048	0.075
π inelastic scattering	-0.015	-0.020	-0.004	-0.015	-0.002	-0.014
	0.015	0.017	0.007	0.017	0.009	0.018
π absorption	-0.318	-0.119	-0.125	-0.176	-0.058	-0.158
	0.290	0.179	0.127	0.153	0.262	0.194
π π production	-0.006	-0.009	-0.008	-0.007	-0.001	-0.063
	0.006	0.008	0.014	0.011	0.001	0.069

^aThe formation time reweighting scheme does not produce stable results for high hadronic energies, since the introduced bug-fix (see Section 2.3) violates the overall normalization. This uncertainty is expected to be largest for small hadronic energies, where other uncertainties (like $1\pi/2\pi$ final state weight factors) dominate the total uncertainty anyhow. Consequently, the formation time reweighting is not used in the overall systematic uncertainty evaluation.

and implemented isotope and atomic compositions. Tweaking the neutron fraction⁶ by $\pm 0.2\%$ only has negligible effect on R .

7.2.3 Oscillation fit

The events are selected as described in Section 6.1 and both data and MC samples are divided into $N_{bins} = 6$ bins i of reconstructed hadronic energy E_{had}^{rec} .

⁶Variations of the target inside the FV are below 3% in mass and less than 0.1% in terms of consequently changed isoscalarity. Missing or mis-modeled geometry structures, such as the aluminum brick support, lower the neutron fraction by less than 0.1%.

This binning has been optimized using MC for maximizing the muon neutrino disappearance sensitivity. For each bin i , the ratio

$$R_i = \frac{N_{i,CC}}{N_{i,NC} + N_{i,CC}} = \frac{N_{i,CC}}{N_i} \quad (7.9)$$

is determined for both data and MC, where $N_{i,CC}$ ($N_{i,NC}$) are the numbers of events classified as CC-like (NC-like) by the k-NN algorithm described in Section 5.8. The hadronic energy E_{had}^{rec} is reconstructed using the default algorithm as described in Section 5.9.

The shape of R_i is dominated by the ν_μ component of the CNGS beam, but various different effects contribute to the distribution. The main contributions to the CC sample are: Correctly identified ν_μ and $\bar{\nu}_\mu$ CC interactions, wrongly identified NC interactions and ν_τ CC interactions with $\tau \rightarrow \mu$. The NC sample is mainly composed of: Correctly identified ν_μ and $\bar{\nu}_\mu$ NC interactions, wrongly identified ν_μ and $\bar{\nu}_\mu$ CC interactions, ν_e interactions from the beam contamination, ν_e interactions from $\nu_\mu \rightarrow \nu_e$ oscillations, and ν_τ CC interactions with $\tau \rightarrow e$ or $\tau \rightarrow hadrons$.

The data is fitted using a χ^2 function

$$\chi^2(\sin^2(2\theta_{23}), \Delta m_{23}^2, \varepsilon_j) = \sum_{i=1}^{N_{bins}} \frac{\left(R_i^{data} - R_i^{MC} \left(1 + \sum_{j=1}^{N_{syst}} f_j^i \varepsilon_j \right) \right)^2}{(\sigma_i^{data})^2 + (\sigma_i^{MC})^2} + \sum_{j=1}^{N_{syst}} \frac{\varepsilon_j^2}{\sigma_j^2} \quad (7.10)$$

where the $N_{syst} = 10$ systematic uncertainties (see Table 7.3) are included as nuisance parameters [209, 210]. R_i^{data} is the ratio of observed events in the i -th bin and $R_i^{MC}(\sin^2(2\theta_{23}), \Delta m_{23}^2)$ is the expected ratio from MC. $\sigma_i^{data/MC}$ denote the corresponding statistical uncertainties, calculated assuming binomial errors. f_j^i describes the fractional change of R_i^{MC} due to a variation of the j -th nuisance parameter by $1\sigma_j$ and ε_j is the deviation from the respective default parameter value in terms of σ_j . The second sum in Equation 7.10 is called penalty term.

A scan over a $(\sin^2(2\theta_{23}), \Delta m_{23}^2)$ grid is made, and χ^2 is minimized with respect to all nuisance parameters using MINUIT. For each combination of $\sin^2(2\theta_{23})$ and Δm_{23}^2 , the MC expectation R_i^{MC} is recalculated, assuming a linear dependency of R_i^{MC} on each of the nuisance parameters. The MC expectation includes the disappearance of both ν_μ and $\bar{\nu}_\mu$, the appearance of ν_τ (from $\nu_\mu \rightarrow \nu_\tau$), the appearance of $\bar{\nu}_\tau$ (from $\bar{\nu}_\mu \rightarrow \bar{\nu}_\tau$) and the appearance of ν_e (from $\nu_\mu \rightarrow \nu_e$). The beam contamination with ν_e and $\bar{\nu}_e$ is included in the MC expectation calculation, but oscillations of these are negligible as is the appearance of $\bar{\nu}_e$ (from $\bar{\nu}_\mu \rightarrow \bar{\nu}_e$). Assuming CPT invariance⁷, the oscillation probabilities of neutrinos and antineu-

⁷This analysis does not distinguish between μ^- and μ^+ . The $\bar{\nu}_\mu$ contribution is too small to perform a muon antineutrino oscillation analysis with OPERA.

trinos are set equal. The values for $\nu_\mu \rightarrow \nu_e$ oscillations are calculated assuming $\theta_{13} = 8.8^\circ$ and $\delta_{CP} = 0$. Other values of δ_{CP} , matter effects and different mass hierarchies should be addressed in different fits once external data is available. Notice that ν_e appearance also depends on the values of $\sin^2(\theta_{23})$ and Δm_{23}^2 .

The measured ratio R^{data} and the Monte Carlo prediction R^{MC} are shown as double ratio R^{data}/R^{MC} in Figure 7.5 for no oscillations and different oscillation scenarios.

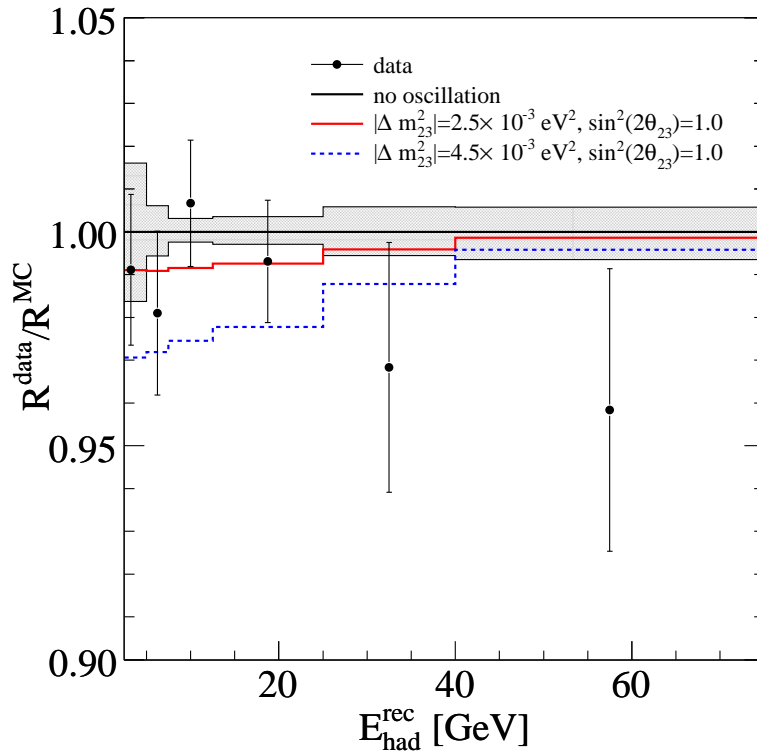


Figure 7.5: Double ratio R^{data}/R^{MC} of CC-like events to all events for data and MC. The total systematic uncertainty is shown as gray band on the no oscillation ratio. The expected ratio for two different oscillation scenarios are superimposed.

The minimum χ^2 value, $\chi_{min}^2/NDOF = 2.52/4$, is found for $\sin^2(2\theta_{23}) = 1.0$ and $\Delta m_{23}^2 = 2.5 \times 10^{-3} \text{ eV}^2$. The *number of degrees of freedom (NDOF)* is given by the number of bins, plus the number of nuisance constraints (penalty terms), minus the number of nuisance parameters⁸, minus the two fit parameters $\sin^2(2\theta_{23})$ and Δm_{23}^2 . The χ^2 value for no oscillations is given by $\chi_{no\,osc.}^2/NDOF = 2.96/4$, thus the data is consistent with no oscillations. For fixed $\sin^2(2\theta_{23}) = 1$, $|\Delta m_{23}^2| > 4.4 \times 10^{-3} \text{ eV}^2$ is excluded at 90% C.L. (estimation of one parameter, double-sided limit).

⁸The number of nuisance penalty terms and nuisance parameters need not be the same.

The excluded parameter region corresponding to 68 % C.L. and 90 % C.L. are given by $\chi_{min}^2 + 2.31$ and $\chi_{min}^2 + 4.60$ for the joint estimation of two fit parameters [94] and are shown in Figure 7.6. The regions excluded by ν_τ appearance (see Section 7.1) and ν_μ disappearance are compatible. The ν_τ appearance exclusion is slightly stronger for small values of $\sin^2(2\theta_{23})$. The general shape of the excluded regions is dominated by the CNGS beam spectrum and hence similar for both methods. The projection of $\Delta\chi^2 = \chi^2 - \chi_{min}^2$ for fixed $\sin^2(2\theta_{23}) = 1$ as a function of $|\Delta m_{23}^2|$ is shown in Figure 7.7.

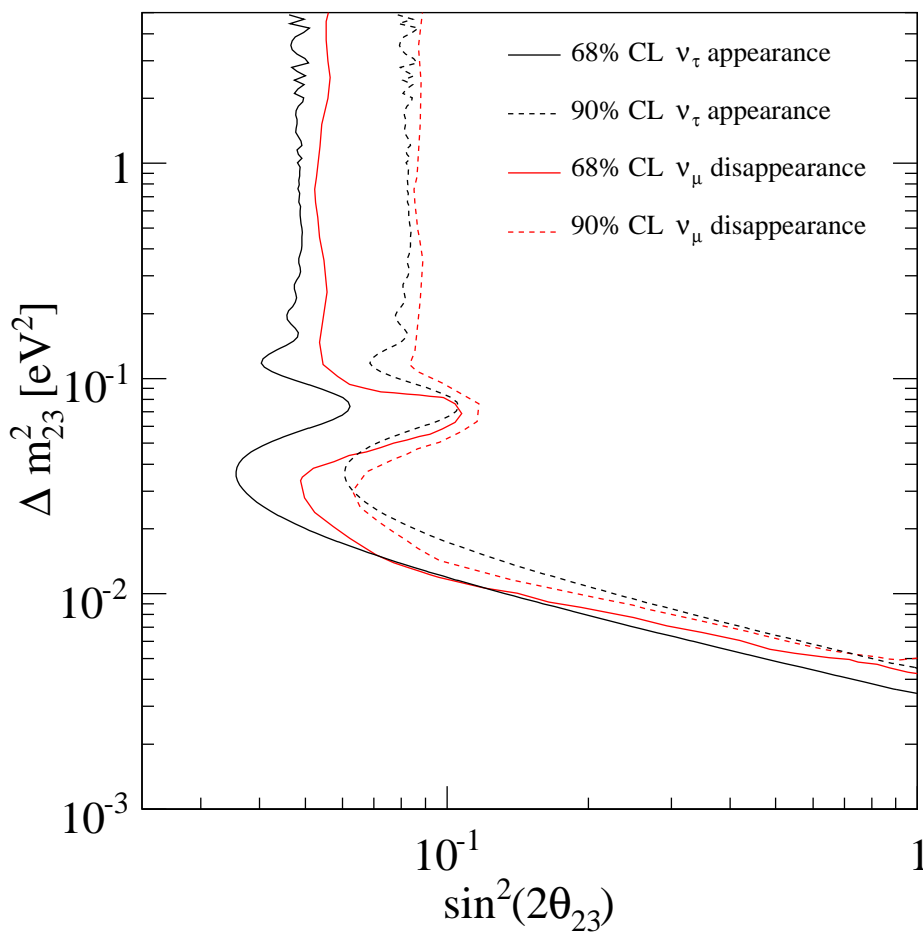


Figure 7.6: Excluded parameter region for $\sin^2(2\theta_{23})$ and $|\Delta m_{23}^2|$ from ν_μ disappearance and ν_τ appearance (see Section 7.1). The contours correspond to the 68 % and 90 % confidence levels. The ν_μ disappearance exclusion curves show less details since the fitting procedure is too time-consuming to generate more than about 20 grid points per decade, while the ν_τ appearance exclusion curves are based on 1000 grid points per decade.

Furthermore, the total data sample has been split into three different subsamples with data from the run periods of 2009, 2010 and 2011 on the one hand and in two different subsamples with data from the first and the second super module, on the other hand. All different data samples are compatible with

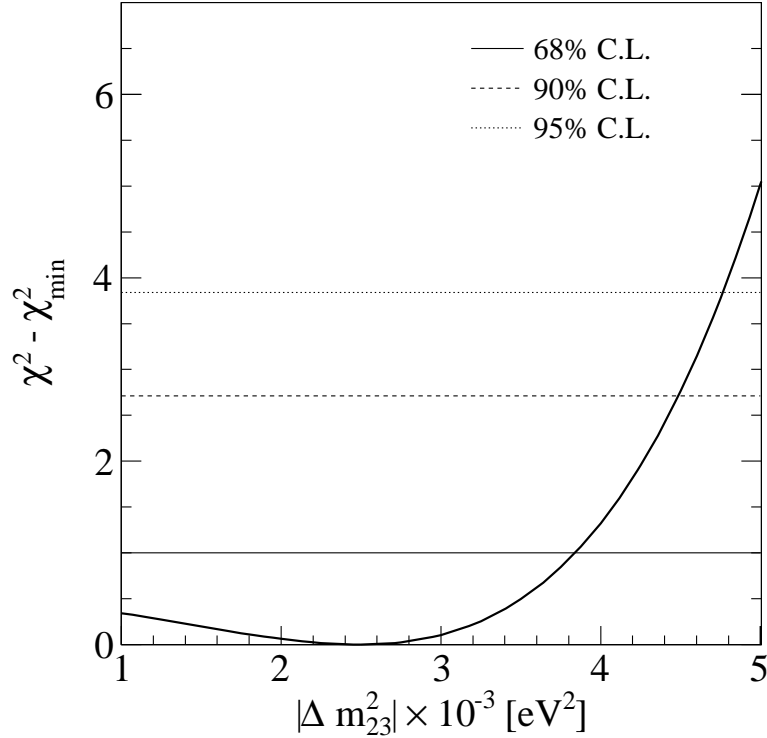


Figure 7.7: Projection of $\Delta\chi^2$ for fixed $\sin^2(2\theta_{23}) = 1$ as a function of $|\Delta m_{23}^2|$. $|\Delta m_{23}^2| > 4.4 \times 10^{-3} \text{ eV}^2$ is excluded at 90 % C.L..

each other within their respective statistical uncertainties and do not indicate any systematic bias.

The effect of neutrino oscillations on the ratio N_{CC}/N is negligible for $E_{had}^{rec} > 12.5 \text{ GeV}$ when using the world best fit values of the neutrino oscillation parameters given in Table 1.1. For $12.5 \text{ GeV} < E_{had}^{rec} < 70 \text{ GeV}$, the ratio for data and for the unoscillated MC are in agreement within their respective uncertainties:

$$R^{MC} = \left(\frac{N_{CC}}{N} \right)^{MC} = 0.672 \pm 0.001 \text{ (stat.)} \pm 0.002 \text{ (syst.)}, \quad (7.11)$$

$$R^{data} = \left(\frac{N_{CC}}{N} \right)^{data} = 0.663 \pm 0.010 \text{ (stat.)}. \quad (7.12)$$

The largest systematic uncertainties in this hadronic energy range are the charm production, the neutrino flux and the hadronization model, while external background is negligible. Notice that these ratios are intentionally not corrected for selection and trigger efficiencies and must not be used as cross section ratios without appropriate corrections.

7.3 Accelerator oscillation summary

OPERA is the only experiment that has observed ν_τ appearance on an event-by-event basis [163]. Up to now, the significance of this observation is about 2σ but this may improve to up to 4σ once the full event sample is analysed. Using a statistical analysis, Super-Kamiokande excludes the no-tau-appearance hypothesis with about 3.8σ [211].

While OPERA can also detect electron neutrinos on an event-by-event basis, the expected performance in the ν_e appearance channel cannot compete with dedicated accelerator ν_e appearance experiments such as T2K and NOVA. A contemporary OPERA result on $\nu_\mu \rightarrow \nu_e$ oscillations together with the ν_τ appearance data, would help to form a consistent three-flavor picture, though.

Observing ν_e appearance in long-baseline accelerator experiments opens up the possibility to determine the neutrino mass hierarchy and to measure CP violation in the neutrino sector, and is hence complementary to reactor neutrino experiments measuring θ_{13} in the $\bar{\nu}_e \rightarrow \bar{\nu}_e$ disappearance mode. The first accelerator neutrino result was presented by the MINOS experiment, which disfavored the $\theta_{13} = 0^\circ$ hypothesis at 89% C.L. [212]. T2K observed a ν_e signal, deriving $0.03(0.04) < \sin^2(2\theta_{13}) < 0.28(0.34)$ for $\delta_{CP} = 0$ and normal (inverted) mass hierarchy [16].

Using the ratio R as defined within this chapter, it was possible to measure $\nu_\mu \rightarrow \nu_\mu$ disappearance with OPERA and provide a measurement of the two oscillation parameters $\sin^2(2\theta_{23})$ and $|\Delta m_{23}^2|$, complementary to the CC disappearance analysis of the MINOS experiment. For maximal mixing ($\sin^2(2\theta_{23}) = 1$), $(|\Delta m_{23}^2|)_{OPERA} > 4.4 \times 10^{-3} \text{ eV}^2$ is excluded at 90% C.L., which is compatible with the latest MINOS results $(\sin^2(2\theta_{23}))_{MINOS} > 0.9$ (90% C.L.) and $(|\Delta m_{23}^2|)_{MINOS} = (2.32^{+0.12}_{-0.08}) \times 10^{-3} \text{ eV}^2$ [205]. This OPERA disappearance result is also consistent with the atmospheric neutrino oscillation results $(\sin^2(2\theta_{23}))_{SK} = 1.0$ and $(|\Delta m_{23}^2|)_{SK} = 2.1 \times 10^{-3} \text{ eV}^2$ obtained by Super-Kamiokande [213].

Using muon antineutrinos, MINOS [214] and Super-Kamiokande [213] have published results for the antineutrino oscillation parameters $\sin^2(2\bar{\theta}_{23})$ and $\Delta\bar{m}_{23}^2$ that are compatible with their respective results obtained using muon neutrinos and thus show no indication of, e.g., CPT violation.

The possible existence of sterile neutrinos is one of the open questions in neutrinos physics (see Section 1.3.2). However, OPERA will not be able confirm or exclude sterile neutrinos in the LSND-preferred parameter space [25], given the expected event statistics of about seven detected ν_τ CC interactions. Since ν_τ appearance is very sensitive to sterile neutrinos (see Section 7.1.1), dedicated experiments able to identify ν_τ CC reactions using high-power, high-energy neu-

trino beams and a larger target mass than OPERA could be the definite tool to determine the associated parameters.

Chapter 8

Conclusion

This thesis describes a measurement of muon neutrino disappearance in the OPERA experiment. Using the data taken with the OPERA electronic detectors between June 2009 and November 2011, a determination of the neutrino mixing parameters $|\Delta m_{23}^2|$ and $\sin^2(2\theta_{23})$ has been performed. The used method is based on a flux normalization-independent ratio measurement making use of a decrease of CC events in case of neutrino oscillations. For $\sin^2(2\theta_{23}) = 1$, $|\Delta m_{23}^2| > 4.4 \times 10^{-3} \text{ eV}^2$ is excluded at 90 % C.L..

To achieve that result, a consistent framework including the theory of neutrino interactions, Monte Carlo simulations, reconstruction tools and fitting methods including systematic uncertainties has been provided. The result is limited by statistics and hence can be improved with more data from the 2012 run once the OPERA experiment is completed. Upcoming data from dedicated cross section experiments like MINERVA will help to reduce the systematic uncertainties at low energies, while high energy effects like nuclear effects in deep inelastic scattering are unlikely to be resolved in the near future. Data driven methods based on muon removal could be used to generate fake NC-like hadronic showers from identified CC events to reduce systematic uncertainties from hadronic interaction modeling in OPERA.

OPERA is the only experiment that has observed ν_τ appearance in a pure ν_μ neutrino beam on an event-by-event basis. So far, OPERA has detected one ν_τ event, which corresponds to a significance of about 2σ . Given the recently measured large value of θ_{13} by various reactor neutrino experiments, OPERA is also sensitive to $\nu_\mu \rightarrow \nu_e$ appearance. Due to the strong competition from dedicated beam experiments, a contemporary ν_e analysis is crucial for OPERA. In combination with the muon neutrino disappearance analysis described within this thesis, OPERA would be the first experiment to measure all possible muon neutrino oscillation channels, $\nu_\mu \rightarrow \nu_\mu$, $\nu_\mu \rightarrow \nu_\tau$ and $\nu_\mu \rightarrow \nu_e$, within the same experiment in the same neutrino beam. The disappearance analysis will become especially important if the ν_τ appearance search yields results incompatible with three-active neutrino oscillations.

In addition to neutrino oscillation physics, OPERA has provided a measurement of the muon neutrino velocity, which is compatible with the speed of light within 1σ . Within this thesis, a subsample of antimuon events has been used to determine the muon antineutrino velocity. The result $(v_{\bar{\nu}} - c)/c = (7.1 \pm 13.5) \times 10^{-6}$ (68% C.L.) is compatible with the speed of light within 1σ and is the first measurement of the muon antineutrino velocity.

Appendix A

Neutrino oscillation

Three-flavor oscillations in vacuum

The three-flavor oscillation probabilities $P(\nu_\mu \rightarrow \nu_e, L) \equiv P_{\mu e}$, $P(\nu_\mu \rightarrow \nu_\mu, L) \equiv P_{\mu\mu}$ and $P(\nu_\mu \rightarrow \nu_\tau, L) \equiv P_{\mu\tau}$ of an initial muon neutrino in vacuum using the three-flavor parametrization 1.26 are given below.

$$\begin{aligned} P_{\mu e} = & \left\{ \sin(2\theta_{12}) \cos^2(\theta_{13}) [\sin^2(2\theta_{12}) (\cos^2(\theta_{23}) - \sin^2(\theta_{23}) \sin^2(\theta_{13})) \right. \\ & \left. + \cos(2\theta_{12}) \sin(2\theta_{23}) \sin(\theta_{13}) \cos(\delta)] \right\} \sin^2 \left(\frac{\Delta m_{21}^2 L}{4E} \right) \\ & + 4 \left\{ \sin(\theta_{12}) \sin(\theta_{23}) \sin(\theta_{13}) \cos^2(\theta_{13}) [\sin(\theta_{12}) \sin(\theta_{23}) \sin(\theta_{13}) \right. \\ & \left. - \cos(\theta_{12}) \cos(\theta_{23}) \cos(\delta)] \right\} \sin^2 \left(\frac{\Delta m_{32}^2 L}{4E} \right) \\ & + 4 \left\{ \cos(\theta_{12}) \sin(\theta_{23}) \sin(\theta_{13}) \cos^2(\theta_{13}) [\cos(\theta_{12}) \sin(\theta_{23}) \sin(\theta_{13}) \right. \\ & \left. + \sin(\theta_{12}) \cos(\theta_{23}) \cos(\delta)] \right\} \sin^2 \left(\frac{\Delta m_{31}^2 L}{4E} \right) \\ & \pm 2J \sin \left(\frac{\Delta m_{21}^2 L}{2E} \right) \pm 2J \sin \left(\frac{\Delta m_{32}^2 L}{2E} \right) \mp 2J \sin \left(\frac{\Delta m_{31}^2 L}{2E} \right) \quad (\text{A.1}) \end{aligned}$$

where J is the so-called Jarlskog invariant

$$J = \frac{1}{8} \sin(2\theta_{12}) \sin(2\theta_{23}) \cos(\theta_{13}) \sin(2\theta_{13}) \sin(\delta). \quad (\text{A.2})$$

The upper signs in the last line refer to neutrinos, the lower signs to antineutrinos.

$$\begin{aligned}
P_{\mu\mu} = 1 - 4 & \left\{ -\frac{1}{4} \sin^2(2\theta_{12}) \sin^2(2\theta_{23}) \sin^2(\theta_{13}) \cos^2(\delta) \right. \\
& + \frac{1}{4} \sin(4\theta_{12}) \sin(2\theta_{23}) \sin(\theta_{13}) [\cos^2(\theta_{23}) - \sin^2(\theta_{23}) \sin^2(\theta_{13})] \cos(\delta) \\
& + \frac{1}{4} \left[1 - \frac{1}{2} \sin^2(2\theta_{12}) \right] \sin^2(2\theta_{23}) \sin^2(\theta_{13}) \\
& \left. + \frac{1}{4} \sin^2(2\theta_{12}) [\cos^4(\theta_{23}) + \sin^4(\theta_{23}) \sin^2(\theta_{13})] \right\} \sin^2 \left(\frac{\Delta m_{21}^2 L}{4E} \right) \\
- 4 & \left\{ \sin^2(\theta_{23}) \cos^2(\theta_{13}) \left[\cos^2(\theta_{12}) \cos^2(\theta_{23}) + \sin^2(\theta_{12}) \sin^2(\theta_{23}) \sin^2(\theta_{13}) \right. \right. \\
& \left. \left. - \frac{1}{2} \sin(2\theta_{12}) \sin(2\theta_{23}) \sin^2(\theta_{13}) \cos^2(\delta) \right] \right\} \sin^2 \left(\frac{\Delta m_{32}^2 L}{4E} \right) \\
- 4 & \left\{ \sin^2(\theta_{23}) \cos^2(\theta_{13}) \left[\sin^2(\theta_{12}) \cos^2(\theta_{23}) + \cos^2(\theta_{12}) \sin^2(\theta_{23}) \sin^2(\theta_{13}) \right. \right. \\
& \left. \left. + \frac{1}{2} \sin(2\theta_{12}) \sin(2\theta_{23}) \sin^2(\theta_{13}) \cos^2(\delta) \right] \right\} \sin^2 \left(\frac{\Delta m_{31}^2 L}{4E} \right). \quad (\text{A.3})
\end{aligned}$$

$$\begin{aligned}
P_{\mu\tau} = & \left\{ -\frac{1}{4} \sin^2(2\theta_{12}) \sin^2(2\theta_{23}) (1 + \sin^2(\theta_{13}))^2 \right. \\
& + \sin^2(\theta_{13}) (\sin^2(2\theta_{12}) + \sin^2(2\theta_{23})) \\
& + \frac{1}{4} \sin(4\theta_{12}) \sin(4\theta_{23}) (1 + \sin^2(\theta_{13})) \sin(\theta_{13}) \cos(\delta) \\
& \left. - \sin^2(2\theta_{12}) \sin^2(2\theta_{23}) \sin^2(\theta_{13}) \cos^2(\delta) \right\} \sin^2 \left(\frac{\Delta m_{21}^2 L}{4E} \right) \\
& \left\{ + \sin(2\theta_{23}) \cos^2(\theta_{13}) [\sin(2\theta_{23}) (\cos^2(\theta_{12}) - \sin^2(\theta_{12}) \sin^2(\theta_{13}))] \right. \\
& \left. - \sin(2\theta_{12}) \cos(2\theta_{23}) \sin(\theta_{13}) \cos(\delta) \right\} \sin^2 \left(\frac{\Delta m_{32}^2 L}{4E} \right) \\
& \left\{ - \sin(2\theta_{23}) \cos^2(\theta_{13}) [\sin(2\theta_{23}) (\cos^2(\theta_{12}) \sin^2(\theta_{13}) - \sin^2(\theta_{12}))] \right. \\
& \left. - \sin(2\theta_{12}) \cos(2\theta_{23}) \sin(\theta_{13}) \cos(\delta) \right\} \sin^2 \left(\frac{\Delta m_{31}^2 L}{4E} \right) \quad (\text{A.4})
\end{aligned}$$

$$\pm 2J \sin \left(\frac{\Delta m_{21}^2 L}{2E} \right) \pm 2J \sin \left(\frac{\Delta m_{32}^2 L}{2E} \right) \mp 2J \sin \left(\frac{\Delta m_{31}^2 L}{2E} \right). \quad (\text{A.5})$$

The upper signs in the last line refer to neutrinos, the lower signs to antineutrinos.

Four–neutrino mixing matrix

The entries of the 4×4 mixing matrix

$$U = \begin{pmatrix} U_{e1} & U_{e2} & U_{e3} & U_{e4} \\ U_{\mu1} & U_{\mu2} & U_{\mu3} & U_{\mu4} \\ U_{\tau1} & U_{\tau2} & U_{\tau3} & U_{\tau4} \\ U_{s1} & U_{s2} & U_{s3} & U_{s4} \end{pmatrix} \quad (\text{A.6})$$

defined by Equation 1.43 are given below, where $s_{ij} = \sin(\theta_{ij})$ and $c_{ij} = \cos(\theta_{ij})$.

$$U_{e1} = c_{12}c_{13}c_{14} \quad (\text{A.7})$$

$$U_{e2} = e^{-i\delta_{12}}c_{13}c_{14}s_{12} \quad (\text{A.8})$$

$$U_{e3} = e^{-i\delta_{13}}c_{14}s_{13} \quad (\text{A.9})$$

$$U_{e4} = s_{14} \quad (\text{A.10})$$

$$U_{\mu1} = -e^{i\delta_{12}}c_{23}c_{24}s_{12} - e^{-i\delta_{24}}c_{12}(e^{i(\delta_{13}+\delta_{24})}c_{24}s_{13}s_{23} + c_{13}s_{14}s_{24}) \quad (\text{A.11})$$

$$U_{\mu2} = c_{12}c_{23}c_{24} - e^{-i(\delta_{12}+\delta_{24})}s_{12}(e^{i(\delta_{13}+\delta_{24})}c_{24}s_{13}s_{23} + c_{13}s_{14}s_{24}) \quad (\text{A.12})$$

$$U_{\mu3} = c_{13}c_{24}s_{23} - e^{-i(\delta_{13}+\delta_{24})}s_{13}s_{14}s_{24} \quad (\text{A.13})$$

$$U_{\mu4} = e^{-i\delta_{24}}c_{14}s_{24} \quad (\text{A.14})$$

$$U_{\tau1} = e^{i\delta_{12}}s_{12}(c_{34}s_{23} + e^{i\delta_{24}}c_{23}s_{24}s_{34}) - c_{12} \left[e^{i\delta_{13}}c_{23}c_{34}s_{13} + (c_{13}c_{24}s_{14} - e^{i(\delta_{13}+\delta_{24})}s_{13}s_{23}s_{24})s_{34} \right] \quad (\text{A.15})$$

$$U_{\tau2} = -c_{12}(c_{34}s_{23} + e^{i\delta_{24}}c_{23}s_{24}s_{34}) + e^{-i\delta_{12}}s_{12} \left[-e^{i\delta_{13}}c_{23}c_{34}s_{13} + (-c_{13}c_{24}s_{14} + e^{i(\delta_{13}+\delta_{24})}s_{13}s_{23}s_{24})s_{34} \right] \quad (\text{A.16})$$

$$U_{\tau3} = -e^{-i\delta_{13}}c_{24}s_{13}s_{14}s_{34} + c_{13}(c_{23}c_{34} - e^{i\delta_{24}}s_{23}s_{24}s_{34}) \quad (\text{A.17})$$

$$U_{\tau4} = c_{14}c_{24}s_{34} \quad (\text{A.18})$$

$$(\text{A.19})$$

$$\begin{aligned}
U_{s1} = & e^{i\delta_{12}} s_{12} (e^{i\delta_{24}} c_{23} c_{34} s_{24} - s_{23} s_{34}) \\
& + c_{12} \left[-c_{13} c_{24} c_{34} s_{14} + e^{i\delta_{13}} s_{13} (e^{i\delta_{24}} c_{34} s_{23} s_{24} + c_{23} s_{34}) \right] \quad (\text{A.20})
\end{aligned}$$

$$\begin{aligned}
U_{s2} = & c_{12} (-e^{i\delta_{24}} c_{23} c_{34} s_{24} + s_{23} s_{34}) \\
& + e^{-i\delta_{12}} s_{12} \left[-c_{13} c_{24} c_{34} s_{14} + e^{i\delta_{13}} s_{13} (e^{i\delta_{24}} c_{34} s_{23} s_{24} + c_{23} s_{34}) \right] \quad (\text{A.21})
\end{aligned}$$

$$U_{s3} = -e^{-i\delta_{13}} c_{24} c_{34} s_{13} s_{14} - c_{13} (e^{i\delta_{24}} c_{34} s_{23} s_{24} + c_{23} s_{34}) \quad (\text{A.22})$$

$$U_{s4} = c_{14} c_{24} c_{34} \quad (\text{A.23})$$

Appendix B

Relativistic kinematics for neutrino interactions

The descriptions of cross sections and various other equations are usually based on Lorentz-invariant quantities. The definitions (preceded by $:=$) and corresponding expressions in the laboratory frame (preceded by \equiv) are given below (see also Figure B.1 and Figure B.2). Neglecting the neutrino mass ($m_\nu = 0$), but keeping the final state lepton mass, the four-vectors in the laboratory frame are given by

$$k_1 = (E_\nu, \vec{p}_\nu) = (E_\nu, 0, 0, E_\nu), \quad (\text{B.1})$$

$$k_2 = (E_l, \vec{p}_l) = (E_l, 0, |\vec{p}_l| \sin \theta_{\nu l}, |\vec{p}_l| \cos \theta_{\nu l}), \quad (\text{B.2})$$

$$p_1 = (E_N, \vec{p}_N) = (M, 0, 0, 0), \quad (\text{B.3})$$

$$p_2 = (E_X, \vec{p}_X), \quad (\text{B.4})$$

where, without loss of generality, the incident neutrino direction is chosen along the positive z -axis, and $\theta_{\nu l}$ is the angle between the incoming neutrino and the outgoing lepton. The definitions are also valid for neutral current scattering (by replacing the outgoing charged lepton with a neutrino as well as the exchanged W with a Z^0), for other lepton flavors and for incoming anti-neutrinos (with reversed time axis and charge-conjugated leptons in Feynman diagrams).

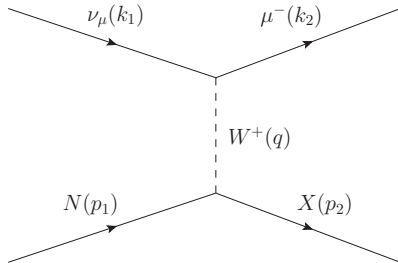


Figure B.1: Feynman diagram for ν_μ -N deep inelastic scattering, charged current.

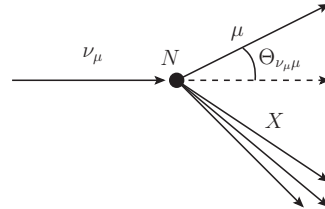


Figure B.2: ν_μ -N deep inelastic scattering in the laboratory system, charged current.

The Lorentz-invariant quantities are given by:

- The negative squared four-momentum transfer Q^2 between the incident neutrino and the target:

$$Q^2 = -q^2 := -(k_1 - k_2)^2 \quad (\text{B.5})$$

$$\stackrel{(\text{B.16})}{\equiv} 2xp_1q \quad (\text{B.6})$$

$$\stackrel{(\text{B.19})}{\equiv} 2xyp_1k_1 \quad (\text{B.7})$$

$$\stackrel{(\text{B.13})}{\equiv} 2xy\frac{1}{2}(s - k_1^2 - p_1^2) \quad (\text{B.8})$$

$$\stackrel{(\text{B.15})}{\equiv} 2E_\nu Mxy \quad (\text{B.9})$$

$$= m_l^2 + 2E_\nu(E_l - p_l \cos \theta_{\nu l}), \quad (\text{B.10})$$

where

$$q = (E_{W/Z}, \vec{q}) \quad (\text{B.11})$$

$$\equiv (\nu, \vec{q}_{LAB}). \quad (\text{B.12})$$

- The squared center-of-mass energy s :

$$s := (k_1 + p_1)^2 \quad (\text{B.13})$$

$$= E_\nu^2 - \vec{p}_\nu^2 + 2(E_\nu E_N - \vec{p}_\nu \vec{p}_N) + E_N^2 - \vec{p}_N^2 \quad (\text{B.14})$$

$$\equiv 2E_\nu M + M^2. \quad (\text{B.15})$$

- The Bjorken scaling variable x (the fraction of target momentum carried by the struck quark in the DIS limit ($Q^2 \gg M$)):

$$x := \frac{Q^2}{2p_1q} \quad (\text{B.16})$$

$$\equiv \frac{Q^2}{2M\nu} \quad (\text{B.17})$$

$$= \frac{Q^2}{2ME_\nu y}. \quad (\text{B.18})$$

- The inelasticity y :

$$y := \frac{p_1q}{p_1k_1} \quad (\text{B.19})$$

$$\equiv \frac{E_{had}}{E_\nu}. \quad (\text{B.20})$$

- The transferred energy ν from the incident neutrino to the target in the laboratory frame (equal to the energy of the exchanged boson in the laboratory frame, see Equation B.12):

$$\nu := \frac{qp_1}{M} \quad (\text{B.21})$$

$$\equiv \frac{M(E_\nu - E_l)}{M} \quad (\text{B.22})$$

$$= E_\nu - E_l \quad (\text{B.23})$$

$$= E_{had}. \quad (\text{B.24})$$

- The squared center-of-mass energy W^2 of the outgoing hadron system:

$$W^2 := (p_1 + q)^2 \quad (\text{B.25})$$

$$\equiv -Q^2 + \frac{Q^2}{x} + M^2 \quad (\text{B.26})$$

$$= M^2 + 2M\nu - Q^2. \quad (\text{B.27})$$

The threshold energy E_t for a reaction can be calculated using these laboratory frame variables. In general, a reaction is energetically possible if

$$\sqrt{s} \geq m_l + W \quad (\text{B.28})$$

where m_l is the mass of the outgoing (charged) lepton l and W the mass of the outgoing hadrons. The simplest charged current neutrino–nucleon interaction is the CCQE scattering 2.1.1 of neutrinos on neutrons. Using (B.15) with $M = m_n$ and $W = m_p$, the threshold energy of the incoming neutrino for a CCQE reaction is given by

$$E_t = \frac{(m_p + m_l)^2 - (m_n)^2}{2m_n}. \quad (\text{B.29})$$

Appendix C

Integration limits for neutrino interactions

The integration limits for neutrino interactions are given by the kinematic of the process and can be derived from relativistic kinematics [215]. To include a non-zero lepton mass and an arbitrary cut on W^2 , it is useful to rewrite Q^2 and W^2 with variables in the center-of-mass system, defined by

$$\vec{p}_\nu^* + \vec{p}_N^* = 0. \quad (\text{C.1})$$

which are denoted by an asterisk (*) in this chapter. The momentum transfer Q^2 in terms of center-of-mass variables is given by

$$\begin{aligned} Q^2 &= -(k_1^2 - 2k_1k_2 + k_2^2) \\ &= -(-2(E_\nu^*E_l^* - \vec{p}_\nu^*\vec{p}_l^*) + E_l^{*2} - \vec{p}_l^{*2}) \\ &= 2E_\nu^*(E_l^* - p_l^* \cos \theta_{\nu l}^*) - m_l^2 \end{aligned} \quad (\text{C.2})$$

with $m_\nu = 0$ and $p_{l,\nu}^* = |p_{l,\nu}^*|$. By using the center-of-mass energy

$$s = (E_\nu^* + E_N^*)^2 = (E_l^* + E_X^*)^2 \quad (\text{C.3})$$

and by exploiting the equality of momenta in the center-of-mass system the following way

$$\begin{aligned} E_l^{*2} - E_X^{*2} &= (E_l^* + E_X^*)(E_l^* - E_X^*) \\ &= p_l^{*2} + m_l^2 - p_X^{*2} - m_X^2 \\ &= m_l^2 - m_X^2, \end{aligned} \quad (\text{C.4})$$

one can calculate the invariant squared mass W^2 of the outgoing hadron system X :

$$\begin{aligned}
W^2 &= m_X^2 \\
&= m_l^2 - (E_l^* + E_X^*)(E_l^* - E_X^*) \\
&= m_l^2 - \sqrt{s}(E_l^* - E_X^*) \\
&= m_l^2 - \sqrt{s}(E_l^* - \sqrt{s} + E_l^*) \\
&= s + m_l^2 - 2\sqrt{s}E_l^*. \tag{C.5}
\end{aligned}$$

Using (B.15), (B.25) and (C.5), the center-of-mass energy E_l^* of the outgoing lepton is given by

$$E_l^* = \frac{m_l^2 + (s - M^2)(1 + xy - y)}{2\sqrt{s}}. \tag{C.6}$$

With $|\cos \theta_{\nu l}^*| \leq 1$, (B.9) and (C.2) give

$$2p_l^* E_\nu^* \geq |xy(s - M^2) + m_l - 2E_l^* E_\nu^*|. \tag{C.7}$$

Replacing $E_\nu^* = \frac{s - M^2}{2\sqrt{s}}$ in (C.7) leads to

$$\frac{p_l^*}{\sqrt{s}} \geq |xy + \frac{m_l^2}{s - M^2} - \frac{E_l^*}{\sqrt{s}}|. \tag{C.8}$$

Inserting

$$A \equiv xy + \frac{m_l^2}{s - M^2} \tag{C.9}$$

in (C.8) and squaring it results in

$$A^2 - 2A \frac{E_l^*}{\sqrt{s}} + \frac{m_l^2}{s} \leq 0. \tag{C.10}$$

Using (C.6) and the dimensionless ratios $r_l \equiv \frac{m_l^2}{s - M^2}$ and $r_N \equiv \frac{M^2}{s - M^2}$ in (C.10) give

$$\begin{aligned}
0 &\geq A^2 - 2A \frac{m_l^2 + (s - M^2)(1 + xy - y)}{2\sqrt{s}\sqrt{s}} + \frac{m_l^2}{s} \\
\stackrel{(C.9)}{\Rightarrow} 0 &\geq \frac{sA^2}{s - M^2} - Ar_l - A + Ay - A^2 + Ar_l + r_l \\
&= A^2 \left(\frac{s}{s - M^2} - 1 \right) - A(1 - y) + r_l \\
&= A^2 r_N - A(1 - y) + r_l \tag{C.11}
\end{aligned}$$

$$\begin{aligned}
&= A^2 r_N - A + \frac{A^2}{x} - \frac{Ar_l}{x} + r_l \\
\Rightarrow 0 &\geq A^2(r_N x + 1) - A(x + r_l) + r_l x. \tag{C.12}
\end{aligned}$$

A lower limit on x can be derived by expanding (C.12) the following way. The inequality

$$0 \geq A^2(r_N x + 1) - A(x + r_l) + r_l x \quad (\text{C.13})$$

$$\begin{aligned} \Rightarrow 0 &\geq A^2 - A \frac{x + r_l}{r_N x + 1} + \frac{r_l x}{r_N x + 1} \\ &= (A - c)^2 - c^2 + \frac{r_l x}{r_N x + 1}. \end{aligned} \quad (\text{C.14})$$

with $c = \frac{x+r_l}{2(r_N x+1)}$ can only be fulfilled if

$$c^2 \geq \frac{r_l x}{r_N x + 1} \quad (\text{C.15})$$

$$\Rightarrow (x + r_l)^2 - 4(r_N x + 1)r_l x \geq 0 \quad (\text{C.16})$$

$$\Rightarrow (x - r_l)^2 - 4r_N r_l x^2 \geq 0. \quad (\text{C.17})$$

Deep inelastic charged current

Taking the square root of (C.17), the lower limit on x is then given by

$$\begin{aligned} x &\geq \frac{r_l}{1 - 2\sqrt{r_l r_N}} \\ &= \frac{m_l^2}{(s - M^2) \left(1 - 2\frac{m_l M}{(s - M^2)}\right)} \\ &\stackrel{(\text{B.15})}{=} \frac{m_l^2}{2M(E_\nu - m_l)}. \end{aligned} \quad (\text{C.18})$$

The upper limit on x depends on the choice of $W \geq W_{DIS}$ and can be derived from (B.9), (B.15) and (B.26):

$$x \leq 1 - \frac{W_{DIS}^2 - M^2}{y(s - M^2)} \quad (\text{C.19})$$

$$= 1 - \frac{W_{DIS}^2 - M^2}{2ME_\nu y} \quad (\text{C.20})$$

$$= \frac{Q^2}{Q^2 - M^2 + W_{DIS}^2}. \quad (\text{C.21})$$

Solving the quadratic equation (C.13) for A and using $A = xy + r_l$ again, results in the kinematic limits for y :

$$\frac{x - r_l - 2r_l r_N x - \sqrt{\alpha}}{2(1 + r_N x)x} \leq y \leq \frac{x - r_l - 2r_l r_N x + \sqrt{\alpha}}{2(1 + r_N x)x} \quad (\text{C.22})$$

with $\alpha = (x - r_l)^2 - 4x^2 r_l r_N$. These limits agree with those given by [76] in the case of $W_{DIS} = M$.

Deep inelastic neutral current

Since $m_l \approx 0$ in NC scattering, the integration limits (C.18), (C.19) and (C.22) simplify to

$$0 \leq y \leq 1 \quad (\text{C.23})$$

and

$$0 \leq x \leq 1 - \frac{W_{DIS}^2 - M^2}{y(s - M^2)}. \quad (\text{C.24})$$

Note that the available data of the structure functions F_i does not extend to infinitely small x . One has to use extrapolation or a cutoff to avoid integration problems.

Quasi elastic charged current

In contrast to DIS scattering, the kinematical constraint $W = M$ reduces the number of invariant variables to describe the scattering process by one since $x = 1$ in CCQE scattering. The differential CCQE cross section is given in terms of Q^2 , the integration limit follows from (C.22) and (B.9):

$$\frac{2ME_\nu^2 - m_l^2(E_\nu + M) - \sqrt{\beta}}{2E_\nu + M} \leq Q^2 \leq \frac{2ME_\nu^2 - m_l^2(E_\nu + M) + \sqrt{\beta}}{2E_\nu + M} \quad (\text{C.25})$$

$$\text{with } \beta = (2ME_\nu^2 - m_l^2 E_\nu)^2 - 4m_l^2 M^2 E_\nu^2.$$

Elastic neutral current

Neglecting the neutrino mass in Equation C.25 ($m_l \approx 0$), the full kinematic range

$$0 \leq Q^2 \leq \frac{4ME_\nu^2}{2E_\nu + M} \quad (\text{C.26})$$

is accessible in elastic neutral current scattering.

Appendix D

Kinematics of neutrino beams

Without loss of generality, this section describes the decay kinematics and results for neutrino beams from two-body pion decays

$$\pi^+ \rightarrow \mu^+ + \nu_\mu. \quad (\text{D.1})$$

For kaon decays, the respective results can easily be obtained by replacing m_π with m_K in the following equations. The neutrino is taken to be massless ($m_\nu = 0$).

The two-body decay can be evaluated in the pion rest-frame, which is defined by $\vec{p}_\mu' = -\vec{p}_\nu'$ and $m_\pi = E'_\mu + E'_\nu$. The variables in the pion rest-frame are denoted by a prime. Using energy and momentum conservation, the neutrino energy can thus be calculated via

$$\begin{aligned} m_\pi &= E'_\nu + E'_\mu \\ \Leftrightarrow m_\pi &= E'_\nu + \sqrt{m_\mu^2 + \vec{p}_\mu'^2} \\ \Leftrightarrow m_\pi &= E'_\nu + \sqrt{m_\mu^2 + \vec{p}_\nu'^2} \\ \Leftrightarrow m_\pi &= E'_\nu + \sqrt{m_\mu^2 + E_\nu'^2} \\ \Leftrightarrow m_\pi^2 - 2m_\pi E'_\nu + E_\nu'^2 &= m_\mu^2 + E_\nu'^2 \end{aligned} \quad (\text{D.2})$$

$$\Leftrightarrow E'_\nu = \frac{m_\pi^2 - m_\mu^2}{2m_\pi}. \quad (\text{D.3})$$

This gives $E'_\nu = 29.8$ MeV for pions and $E'_\nu = 235.5$ MeV for kaons, respectively.

In the following, the beam axis will be chosen as z and the decay angle Θ' between the outgoing neutrino and the pion is going to be measured in the xz -plane. These choices are completely arbitrary. By doing so, the problem is

effectively reduced to a two-dimensional one. In the pion rest-frame, the neutrino four vector \vec{P}' can be written as

$$\vec{P}' = \begin{pmatrix} E'_\nu \\ p'_{\nu,x} \\ p'_{\nu,y} \\ p'_{\nu,z} \end{pmatrix} = \begin{pmatrix} E'_\nu \\ p'_\nu \sin \Theta' \\ 0 \\ p'_\nu \cos \Theta' \end{pmatrix} = \begin{pmatrix} E'_\nu \\ E'_\nu \sin \Theta' \\ 0 \\ E'_\nu \cos \Theta' \end{pmatrix}. \quad (\text{D.4})$$

The neutrino four vector \vec{P} in the lab-frame is given by a Lorentz transformation of the quantities D.4:

$$\vec{P} = \begin{pmatrix} E_\nu \\ p_{\nu,x} \\ p_{\nu,y} \\ p_{\nu,z} \end{pmatrix} = \begin{pmatrix} E_\nu \\ p_\nu \sin \Theta \\ 0 \\ p_\nu \cos \Theta \end{pmatrix} = \begin{pmatrix} \gamma E'_\nu (1 + \beta \cos \Theta') \\ E'_\nu \sin \Theta' \\ 0 \\ \gamma E'_\nu (\cos \Theta' + \beta) \end{pmatrix}. \quad (\text{D.5})$$

The inverse transformation from the lab-frame to the pion rest-frame is given by:

$$\vec{P}' = \begin{pmatrix} \gamma E_\nu (1 - \beta \cos \Theta) \\ E_\nu \sin \Theta \\ 0 \\ \gamma E_\nu (\cos \Theta - \beta) \end{pmatrix}. \quad (\text{D.6})$$

A rich variety of consequences arises from these rather simple equations, some of which will be derived below.

Since $\cos \Theta' \leq 1$, the first component of Equation D.5 can be written as

$$\begin{aligned} E_\nu^{\max} &= E'_\nu \frac{E_\pi}{m_\pi} \left(1 + \frac{p_\pi}{E_\pi} \right) \\ &= \frac{(m_\pi^2 - m_\mu^2)}{2m_\pi} \frac{E_\pi}{m_\pi} \frac{(E_\pi + p_\pi)}{E_\pi} \\ &= \frac{1}{2} \left(1 - \frac{m_\mu^2}{m_\pi^2} \right) (E_\pi + p_\pi), \end{aligned} \quad (\text{D.7})$$

yielding an upper limit on the neutrino energy of

$$E_\nu^{\max} \approx 0.427 E_\pi, \quad (\text{D.8})$$

where $m_\mu^2/m_\pi^2 \approx 0.573$ and $E_\pi \approx p_\pi$ for high pion energies ($\beta \approx 1$). Analogously, the upper limit for kaon decays is given by $E_\nu^{\max} \approx 0.954 E_K$.

In the lab-frame, the maximum angle under which a neutrino of an energy E may be emitted by a pion can be directly obtained from the comparison of the p_x component of Equation D.5 and Equation D.6:

$$\begin{aligned} E_\nu \sin \Theta &= E'_\nu \sin \Theta' \\ \Leftrightarrow \sin \Theta &\leq \frac{E'_\nu}{E_\nu} \\ \Rightarrow \Theta_{\max} &= \arcsin \frac{E'_\nu}{E_\nu} \approx \frac{E'_\nu}{E_\nu}. \end{aligned} \quad (\text{D.9})$$

The angle Θ in the lab-frame is quite small: A cone with an opening angle of $2 \times 0.17^\circ$ will contain all neutrinos with energies of 10 GeV or above, independent of the pion energy. At a typical distance for a narrow-band neutrino beam experiment of about $s = 1000$ m, this corresponds to a radial spread of $r \approx 3$ m.

The ratios of the z and x components of Equation D.4 and Equation D.6 results in

$$\cos \Theta = \frac{\cos \Theta' + \beta}{1 + \beta \cos \Theta'}, \quad (\text{D.10})$$

$$\cos \Theta' = \frac{\cos \Theta - \beta}{1 - \beta \cos \Theta}, \quad (\text{D.11})$$

$$\sin \Theta = \frac{\sin \Theta'}{\gamma(1 + \beta \cos \Theta)} \quad (\text{D.12})$$

and

$$\sin \Theta' = \frac{\sin \Theta}{\gamma(1 - \beta \cos \Theta)}. \quad (\text{D.13})$$

Inserting Equation D.13 in Equation D.12 gives the relation

$$(1 + \beta \cos \Theta')(1 - \beta \cos \Theta) = \frac{1}{\gamma^2}, \quad (\text{D.14})$$

which can be used for an expression of the neutrino energy in the lab-frame:

$$E_\nu = E'_\nu \gamma(1 + \beta \cos \Theta') \quad (\text{D.15})$$

$$= E'_\nu \gamma \frac{1}{\gamma^2(1 - \beta \cos \Theta)} \quad (\text{D.16})$$

$$= \frac{m_\pi^2 - m_\mu^2}{2(E_\pi - p_\pi \cos \Theta)}. \quad (\text{D.17})$$

An upper limit for the maximum neutrino energy $E_\nu(\Theta)$ for a fixed angle Θ and a given pion energy E_π can be derived by differentiation of Equation D.17 with respect to the pion energy:

$$\frac{\partial E_\nu}{\partial E_\pi} = - \frac{m_\pi^2 - m_\mu^2}{2(E_\pi - p_\pi \cos \Theta)^2}. \quad (\text{D.18})$$

Equation D.18 gets maximal for

$$E_\pi = \frac{m_\pi}{\sin \Theta}. \quad (\text{D.19})$$

Thus, the maximum neutrino energy for a fixed angle Θ is given by

$$E_\nu(\Theta) = \frac{m_\pi^2 - m_\mu^2}{2 \left(\frac{m_\pi}{\sin \Theta} - \cos \Theta \sqrt{\frac{m_\pi^2}{\sin^2 \Theta} - m_\pi^2} \right)}. \quad (\text{D.20})$$

The double differential neutrino spectrum $\frac{d^2 N}{d\Omega dE}$ is necessary for describing the off-axis properties of a neutrino beam. For the assumption of a simple pion spectrum, a valuable discussion is given by [216, 217].

For some applications, it is sufficient to know the integrated neutrino flux at given distance l for a detector surface A , instead of the differential spectrum. According to [218], for highly relativistic particles ($\beta \approx 1$), the flux is given by

$$\Phi_\nu = \frac{A}{4\pi l^2} \left(\frac{2\gamma}{1 + \gamma^2 \Theta^2} \right)^2 \quad (\text{D.21})$$

if $\tan \Theta \ll 1$, as is the case for most experimental situations (see Equation D.9). The resulting total and relative fluxes for pions and kaons with different energies are shown in Figure D.1 and Figure D.2.

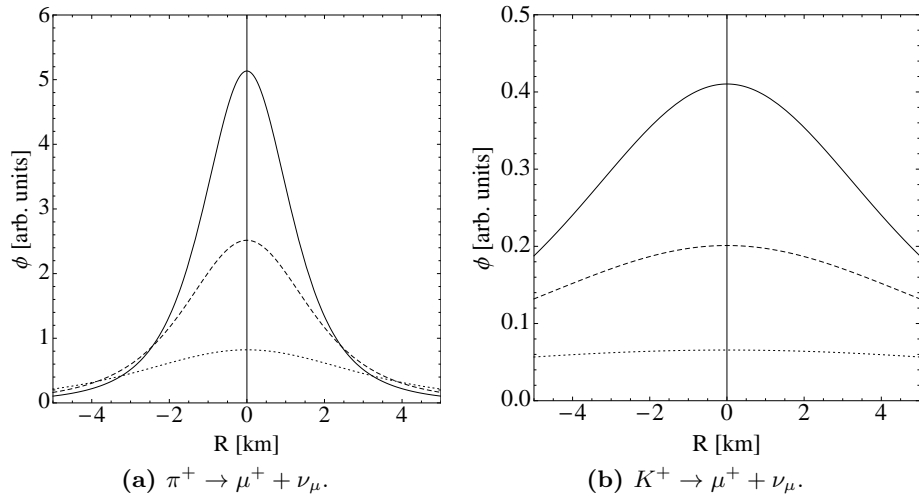


Figure D.1: Idealized neutrino flux Φ from mono-energetic, perfectly aligned parent particles with energies of 20 GeV (dotted), 35 GeV (dashed) and 50 GeV (solid), according to Equation D.21. R is the lateral displacement from the on-axis position at a distance of 732 km.

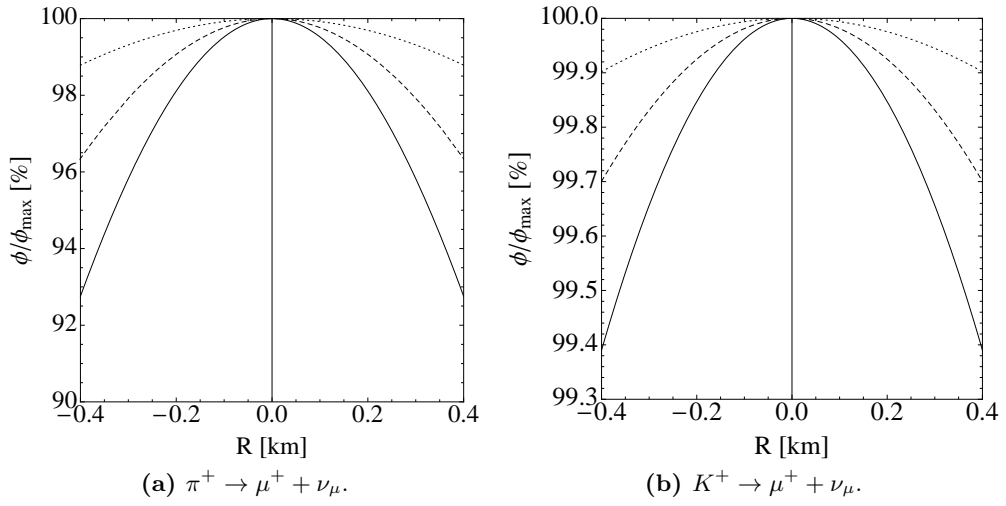


Figure D.2: Flux ratio Φ/Φ_{max} of neutrinos from mono-energetic, perfectly aligned parent particles with energies of 20 GeV (dotted), 35 GeV (dashed) and 50 GeV (solid) according to Equation D.21. R is the lateral displacement from the on-axis position at a distance of 732 km, Φ_{max} is the on-axis flux.

Appendix E

Systematic uncertainties for the disappearance fit

The oscillation fit using nuisance parameters incorporates systematic uncertainties via the fractional change f_i^j of $R_i^{MC}(E_{had}^{rec})$ in each bin i , resulting from a variation of the j -th systematic parameter. The systematic parameters affect different parts of the phase space and usually depend on the neutrino flavor and the simulated event kinematics.

Event reweighting

If possible, systematic uncertainties are included via event reweighting to the need for reduce time-consuming re-generation of MC samples. Reweighting is used for all of the systematic parameters included in the oscillation fit apart from the **GEANT4** hadronization model and the fiducial volume selection (see below).

Each systematic parameter j is varied in nine equidistant steps s between $-1\sigma_j$ and $+1\sigma_j$, and the individual event weight is calculated via

$$w_j(s) = \frac{\text{event probability with varied parameter } j \text{ by } s}{\text{event probability with nominal parameter } j}. \quad (\text{E.1})$$

The variation by $0\sigma_j$ must result in $w_j = 1$ if the MC model has not changed between generation and reweighting. This is checked explicitly for every event and every reweighted parameter to exclude possible errors arising from different software installations or undetected code changes.

Apart from the systematic parameters, radiative corrections to DIS and neutrino oscillations are included via event weights, resulting in a total event weight of

$$w_{total}(\sin^2(2\theta), \Delta m^2, j, s) = w_j(s) \times w_{RAD} \times w_{osc}(\sin^2(2\theta), \Delta m^2) \times w_{norm}, \quad (\text{E.2})$$

where the nominal value $R_i^{MC}(E_{had}^{rec})$ is given by $w_j(s) = 1$ and $w_{osc} = 1$ ($\nu_\mu, \bar{\nu}_\mu, \nu_e$ or $\bar{\nu}_e$) or $w_{osc} = 0$ ($\nu_\tau, \bar{\nu}_\tau$ or ν_e). w_{norm} is used to normalize all MC subsamples

to the same beam exposure.

For each systematic parameter j , nine histograms for the ratio $R_i^{MC}(E_{had}^{rec})$ were constructed. One of the histograms holds the nominal value, while the others hold the ratio after weighting each event with its respective weight w_{total} . For each bin i of the histogram, the positive total error was taken to be the largest positive difference between the eight weighted histograms and the default histogram and the negative total error is taken to be the largest negative difference. The fractional systematic uncertainty f_i^j per bin is obtained by dividing the absolute errors by the nominal histogram value.

GEANT3 hadronic interactions

The simulation of hadronic interactions (see Section 4.5.3) depends on non-parameterized functions and is too complex to be included via reweighting. Thus, 100k events have been generated using the same GENIE-simulated interactions and vertex positions, but with two different detector simulations: One simulation uses GHEISHA and the other the default GFLUKA, both with the same cut-off energies and the same geometry model. For both simulations, one histogram of each ratio $R_i^{MC}(E_{had}^{rec})$ was constructed. For each bin i of the histograms, the absolute difference of the two histograms contents is taken as conservative approximation of the absolute error. The fractional systematic uncertainty f_i per bin i is obtained by dividing these absolute errors by the GFLUKA (default) histogram value. Within the available MC statistics, no change of the ratio was observed.

Fiducial volume selection

Systematic uncertainties associated with the fiducial volume selection, which mostly affect the fraction of NC-like background events, are evaluated by comparing MC and real data for a modified FV definition. The maximal difference between MC and data for a variation of the FV as given in Section 7.2 is used as a 1σ -equivalent uncertainty.

List of tables

1.1	Neutrino oscillation parameters from global data for normal hierarchy	12
1.2	Leading-order neutrino matter potentials	19
2.1	Parameters used for the low- Q^2 corrections within the BY model . .	47
2.2	GENIE transition region weight factors for 1π and 2π final states . .	60
2.3	Showers charge and final state baryon selection probabilities in the AGKY-KNO model	68
2.4	Parameters used in the AGKY-KNO model	69
3.1	CNGS performance	87
4.1	Average CNGS beam composition	112
4.2	Decay parent contribution of the various neutrino flavors in the CNGS beam.	114
4.3	Material composition of the OPDY geometry	125
4.4	Rock muon rate for different Monte Carlo codes	130
5.1	Comparison of different shower axis reconstruction methods	148
5.2	Compact target definitions during the different CNGS run periods	150
5.3	Fiducial volume definitions during the different run periods	150
6.1	Run periods and corresponding extractions	170
6.2	Event yield after successive cuts for the different CNGS runs and the total event yield	175
6.3	Integrated POT after various cuts	182
6.4	Integrated detector ontime after various cuts	182
6.5	Average number of bricks in the target for the 2009 to 2011 run periods	183
7.1	Default OPERA event rates for unoscillated CNGS beam flux	197
7.2	ν_τ CC event rates in vacuum and matter for different values of θ_{13} and δ_{CP}	198
7.3	Summary of systematic uncertainties for the ν_μ disappearance anal- ysis	207
7.4	Summary of systematic uncertainties for the GENIE hadronization model	208
7.5	Fractional systematic uncertainties of the ratio $R(E_{had}^{rec})$	209

7.6	Fractional systematic uncertainties of the ratio $R(E_{had}^{rec})$ from a variation of the GENIE hadronization model input parameters	210
-----	---	-----

List of figures

1.1	β -decay electron energy spectrum measured by Chadwick 1914. . .	4
1.2	Three-neutrino mass spectra (schematic) and flavor composition for normal and inverted mass hierarchy	12
1.3	Sensitivity and exclusion plots from various electron-(anti)neutrino appearance experiments	14
1.4	Different four-neutrino mass spectra	15
1.5	Four-neutrino mass spectra and flavor composition for the normal mass hierarchy	17
1.6	Mixing angle $\sin^2(2\theta^M)$ in matter	22
1.7	Three-flavor oscillation probability $P_{\mu e}$ including matter effects . .	22
2.1	Kinematical coverage of the CNGS neutrino beam	25
2.2	$\nu+n$ quasi-elastic scattering, charged current	26
2.3	Differential CCQE cross section	30
2.4	Fractional uncertainty of the CCQE cross section	30
2.5	Fraction of CCQE events to the total number of CC events	31
2.6	Total cross sections for $\nu+^{208}\text{Pb}$ NCE and CCQE scattering	31
2.7	Total $\nu_\mu + n \rightarrow \mu^- + p$ CCQE cross section, comparison of the calculation with data	32
2.8	Total $\bar{\nu}_\mu + p \rightarrow \mu^+ + n$ CCQE cross section, comparison of the calculation with data	33
2.9	$\nu+p$ resonant scattering	35
2.10	Total RESCC cross section	37
2.11	Fractional uncertainty of the RESCC cross section	38
2.12	Fraction of RESCC events to the total number of CC events	38
2.13	$\nu-N$ deep inelastic scattering, charged current	39
2.14	Uncorrected GRV98LO parton distributions	40
2.15	Example diagrams contributing to higher twist corrections	43
2.16	Longitudinal structure function, comparison of the calculation with data	46
2.17	Up and down quark distributions from the GRV98LO PDF without and with BY corrections	48
2.18	Simulated Q^2 distribution of $\nu_\mu + ^{208}\text{Pb}$ CC interactions	48
2.19	Neutrino structure functions, comparison of the GENIE model with data	51

2.20	Charm mass, comparison of GENIE value with data from neutrino experiments	53
2.21	DIS CC charm cross section uncertainty	53
2.22	NC charm production in boson–gluon fusion	53
2.23	CC charm production in boson–gluon fusion	53
2.24	QED radiative corrections diagrams, initial and final state quark radiation	55
2.25	QED radiative corrections diagrams, final state lepton radiation	55
2.26	Some of the weak corrections diagrams for NC (Z exchange) and CC (W exchange) scattering	55
2.27	Total radiative corrections (QED only) for ν_μ scattering off an isoscalar nucleon	56
2.28	Radiative corrections to the total DIS cross sections	57
2.29	Nuclear corrections to F_2 , comparison of the calculation with data	59
2.30	Fraction of events with 1π or 2π final hadronic states	61
2.31	Cross sections of ν_μ scattering off lead nuclei for COH scattering, IMD and elastic $\nu + e$ scattering	62
2.32	Total $\nu_\mu + N$ cross section, comparison of the calculation with data	63
2.33	Total $\bar{\nu}_\mu + N$ cross section, comparison of the calculation with data	64
2.34	Total average $((\nu_\tau + N) + (\bar{\nu}_\tau + N))/2$ cross section, comparison of the calculation with data	65
2.35	W distribution for CNGS beam–induced $\nu_\mu + {}^{208}\text{Pb}$ CC DIS events	66
2.36	Fraction of DIS CC $\nu_\mu + {}^{208}\text{Pb}$ events hadronized by KNO to all DIS CC events	66
2.37	Average charged hadron multiplicity comparison of the parametrization with data	69
2.38	KNO–based probability distribution, comparison of the parametrization with data	70
2.39	Normalized x_F distribution for protons, comparison of the AGKY–KNO model with data	71
2.40	Normalized transverse momentum distribution for protons, comparison of the AGKY–KNO model with data	71
2.41	Comparison of hadronic final states before and after intranuclear rescattering	73
3.1	Schematic earth profile and neutrino flight path from CERN to Gran Sasso	75
3.2	$\sigma_{\nu_\tau n}(E)/E^2$ and $\sigma_{\nu_\mu n}(E)/E^2$	76
3.3	$P_{\nu_\mu \rightarrow \nu_\tau}(E) \times \sigma_{\nu_\tau n CC}(E)$ for different values of Δm_{23}^2	76
3.4	Original drawing of a cone–shaped horn	80
3.5	Trajectories of charged pions inside a cone–shaped horn	80
3.6	Neutrino energy E_ν for different off–axis angles with respect to the pion energy	82
3.7	Pion energy and maximum neutrino energy with respect to the off–axis angle θ	82
3.8	Secondary CNGS beamline layout.	84

3.9	OPERA coordinate system	85
3.10	LNGS laboratory (schematic, top view)	86
3.11	Integrated POT over date	87
3.12	Protons on target per extraction over date	88
3.13	Photograph of the OPERA detector	90
3.14	Photograph of a partially opened OPERA ECC brick	91
3.15	Photograph of the empty OPERA brick support structure	91
3.16	Brick status on 29-06-2009	91
3.17	Total number of bricks in the OPERA detector	92
3.18	Schematic drawing of an OPERA spectrometer	94
3.19	Photograph of the OPERA spectrometer of SM 1	94
3.20	Schematic drawing of an OPERA magnet	94
3.21	Schematic drawing of an OPERA RPC	94
3.22	Schematic drawing of a PT module	97
3.23	Photograph of a European photo emulsion scanning station	99
3.24	Scanned photo emulsion	99
3.25	τ decay topology (schematic)	100
3.26	Scanning result of the first τ candidate event	104
3.27	BCT measurements of the proton time distributions	105
3.28	Comparison of the neutrino arrival time distributions and the average proton waveform	105
3.29	NLL distribution for the alternative method	107
4.1	$\Phi_{\nu_\mu}(r)$ at LNGS.	111
4.2	Comparison of $\Phi_{\nu_\mu}(E)$ for three concentric 100 m-wide rings	111
4.3	$\Phi_{\bar{\nu}}(r)$ at LNGS.	111
4.4	Comparison of $\Phi_{\bar{\nu}_\mu}(E)$ for three concentric 100 m-wide rings	111
4.5	$\Phi_{\nu_e}(r)$ at LNGS.	117
4.6	$\Phi_{\bar{\nu}_e}(r)$ at LNGS.	117
4.7	Comparison of default and revised neutrino flux at LNGS.	117
4.8	ν_μ flux $\Phi_{\nu_\mu}(E)$ at LNGS, $r < 120$ m	118
4.9	Decay position of the ν_μ parent.	118
4.10	$\bar{\nu}_\mu$ flux $\Phi_{\bar{\nu}_\mu}(E)$ at LNGS, $r < 120$ m.	119
4.11	Decay position of the $\bar{\nu}_\mu$ parent.	119
4.12	ν_e flux $\Phi_{\nu_e}(E)$ at LNGS.	120
4.13	$\bar{\nu}_e$ flux $\Phi_{\bar{\nu}_e}$ at LNGS.	120
4.14	Systematic energy dependent uncertainty of the FLUKA neutrino beam simulation	121
4.15	Statistical uncertainty of the FLUKA ν_μ and $\bar{\nu}_\mu$ neutrino beam simulation.	121
4.16	Statistical uncertainty of the FLUKA ν_e and $\bar{\nu}_e$ neutrino beam simulation.	122
4.17	3D view of the OPERA detector	123
4.18	3D view of the total geometry	124
4.19	GENIE flux driver geometry used by <code>gevgen_opera</code>	126
4.20	Comparison of different rock muon simulations	130

4.21	Distance between production vertex and exit plane for rock muons	132
4.22	Lateral displacement of rock muons due to the neutrino beam angle and multiple Coulomb scattering	132
4.23	Momentum distributions of different outgoing hadrons (after final state interactions) from $\nu_\mu + {}^{208}\text{Pb}$ NC interactions	133
4.24	Detector response to π^+ with $p = 3$ GeV in the OPERA target . .	134
4.25	Energy distributions of outgoing π^0 and γ (after FSI) from $\nu_\mu + {}^{208}\text{Pb}$ NC interactions	135
4.26	Detector response to π^0 with $p = 3$ GeV in the OPERA target . . .	136
5.1	Monte Carlo and real data flow in the OPERA experiment.	138
5.2	Example of a ν_μ CC interaction (MC) in the electronic detector. . .	139
5.3	Different neighbor definitions	141
5.4	Example of a ν_μ CC interaction (MC) in the electronic detector after clustering.	142
5.5	Example of a ν_μ CC interaction (MC) in the electronic detector after preprocessing.	143
5.6	Example of a ν_μ CC interaction (MC) in the electronic detector after muon removal.	145
5.7	Distance between the reconstructed shower axis and the leading track to the true vertex	147
5.8	Angle between the reconstructed shower axis and the true hadron direction and angle between the leading track and the true muon direction	148
5.9	Example of a ν_μ CC interaction (MC) with backscattering in the electronic detector	151
5.10	True vertex position within a target wall	154
5.11	Difference between the true vertex wall and the electronic detector–reconstructed vertexwall	154
5.12	Vertex residuals in x and y	154
5.13	Separation variables used in the classification	157
5.14	Example of a two–dimensional k–NN algorithm used for classification	158
5.15	ROC curves for the different k–NN classifiers	160
5.16	Figure of merit as a function of the classifier output cut.	160
5.17	Linear correlation matrices for the k–NN classifier input variables .	160
5.18	k–NN classifier output for different neutrino flavors	162
5.19	Efficiencies and purities of the optimal k–NN classification for different neutrino flavors	163
5.20	Example of a two–dimensional k–NN algorithm used for the regression	166
5.21	Distribution of $E_{had}^{rec}/E_{had}^{true}$ for the bias–corrected k–NN and the default reconstructed hadronic energy	166
5.22	Distributions R_i for different ranges of true hadronic energy	167
6.1	Relative time differences between OPERA neutrino events and the closest CNGS kicker trigger	170
6.2	Distribution of number of raw hits per event for the 2010 and 2011 runs	171

6.3	Relative time differences between OPERA neutrino events and the closest CNGS kicker trigger after minimum hits cut	171
6.4	Event duration and distance the to previous event for multievents	173
6.5	Reconstructed vertex positions in the fiducial volume after all cuts	174
6.6	True vertex position of simulated ν_μ rock events	177
6.7	Reconstructed vertex positions in the fiducial volume for external MC events	179
6.8	Relative time differences between OPERA events and the closest CNGS kicker trigger, where events outside of the ontime selection cut have been excluded	180
6.9	Total number of events in the fiducial volume per year	184
6.10	Ratio of event rates after cuts over extraction intensity	184
6.11	k-NN classifier output	186
6.12	Reconstructed track angle θ in the zy projection	187
6.13	Reconstructed track angle ϕ in the zx projection	188
6.14	Reconstructed (anti-)muon energy spectrum, multiplied with the reconstructed (anti-)muon charge	189
6.15	Reconstructed hadronic energy for CC-like and NC-like events . .	190
6.16	Total visible energy for CC-like events with a μ^- track	191
6.17	Total visible energy for CC-like events with a μ^+ track.	192
6.18	Total visible energy for CC-like events with $E_{had}^{rec} > 2.5$ GeV	192
6.19	Vertex residuals for events reconstructed in both the emulsions and the electronic detector	193
6.20	Reconstructed angle ϕ in the emulsions and its relative difference to the electronic detector reconstruction	194
6.21	Reconstructed angle θ in the emulsions and its relative difference to the electronic detector reconstruction	195
7.1	ν_τ appearance probability in OPERA as a function of true neutrino energy assuming three-flavor oscillations in matter for different values of θ_{13} and δ_{13}	199
7.2	Number of expected τ events in OPERA for different values of θ_{24} , θ_{34} and δ_{24}	200
7.3	Excluded parameter region for $\sin^2(2\theta_{23})$ and $ \Delta m_{23}^2 $ from ν_τ appearance	200
7.4	ν_e appearance probability in OPERA as a function of true neutrino energy assuming three-flavor oscillations in matter for different values of θ_{13} , δ_{CP} and mass hierarchies	202
7.5	Double ratio R^{data}/R^{MC} of CC-like events to all events for data and MC	212
7.6	Excluded parameter region for $\sin^2(2\theta_{23})$ and Δm_{23}^2 from ν_μ disappearance	213
7.7	Projection of $\Delta\chi^2$ for fixed $\sin^2(2\theta_{23}) = 1$ as a function of $ \Delta m_{23}^2 $.	214
B.1	Feynman diagram for ν_μ -N deep inelastic scattering, charged current	223
B.2	ν_μ -N deep inelastic scattering in the laboratory system, charged current	223

- D.1 Idealized neutrino flux from mono-energetic parent particles 233
- D.2 Flux ratio Φ/Φ_{max} of neutrinos from mono-energetic parent particles 234

Bibliography

- [1] C. Amsler and others. The Review of Particle Physics and 2009 partial update for the 2010 edition. *Phys. Lett. B*, 667:1, 2008.
- [2] W. Pauli. Offener Brief an die Gruppe der Radioaktiven bei der Gauvereins-Tagung zu Tübingen. Unpublished, 1930.
- [3] J. Chadwick. Intensitätsverteilung im magnetischen Spektrum der β -Strahlen von Radium B + C. *Verhandl. Dtsch. phys. Ges.*, 16:383, 1914.
- [4] C. L. Cowan, F. Reines, et al. Detection of the free neutrino: A confirmation. *Science*, 124:103–104, 1956.
- [5] R. Davis Jr. Attempt to detect the antineutrinos from a nuclear reactor by the $\text{Cl}^{37}(\bar{\nu}, e^-)\text{A}^{37}$ reaction. *Phys. Rev.*, 97:766–769, 1955.
- [6] W. Pauli. Zur älteren und neueren Geschichte des Neutrinos. 1957. [talk given in Zuerich, 21.01.1957].
- [7] D. J. Griffith. *Introduction to Elementary Particles*. John Wiley & Sons, 1987.
- [8] R. E. Marshak. *Theory of weak interactions in particle physics*. Wiley-Interscience, 1969.
- [9] C. Giunti and C. W. Kim. *Fundamentals of neutrino physics and astrophysics*. Oxford University Press, 2007.
- [10] S. L. Glashow. Partial symmetries of weak interactions. *Nucl. Phys.*, 22:579–588, 1961.
- [11] S. Weinberg. A model of leptons. *Phys. Rev. Lett.*, 19:1264–1266, 1967.
- [12] A. Salam. Weak and Electromagnetic Interactions. 1968. [originally printed in Svartholm: Elementary Particle Theory, Proceedings Of The Nobel Symposium held 1968 at Lerum (Sweden), Stockholm, 367-377, 1968].
- [13] N. Cabibbo. Unitary Symmetry and Leptonic Decays. *Phys. Rev. Lett.*, 10:531–533, 1963.
- [14] M. Kobayashi and T. Maskawa. CP Violation in the Renormalizable Theory of Weak Interaction. *Prog. Theor. Phys.*, 49:652–657, 1973.

-
- [15] N. Schmitz. *Neutrino Physik (in German)*. Teubner Studienbücher, 1997.
- [16] K. Abe et al. Indication of electron neutrino appearance from an accelerator-produced off-axis muon neutrino beam. *Phys.Rev.Lett.*, 107:041801, 2011.
- [17] P. Adamson et al. Improved search for muon-neutrino to electron-neutrino oscillations in MINOS. *Phys.Rev.Lett.*, 107:181802, 2011.
- [18] Y. Abe et al. Indication for the disappearance of reactor electron antineutrinos in the Double Chooz experiment. 2011, arxiv:1112.6353.
- [19] S.-B. Kim et al. Observation of reactor electron-antineutrino disappearance in the RENO experiment. 2012, arxiv:1204.0626v2.
- [20] F. P. An et al. Observation of electron-antineutrino disappearance at Daya Bay. 2012, arxiv:1203.1669v2.
- [21] J. Schechter and J. W. F. Valle. Neutrinoless double beta decay in $SU(2) \times U(1)$ theories. *Phys. Rev. D*, 25:2951–2954, 1982.
- [22] T. Schwetz et al. Global neutrino data and recent reactor fluxes: status of three-flavour oscillation parameters. *New J. Phys.*, 13:063004, 2011.
- [23] T. Schwetz et al. Where we are on θ_{13} : addendum to 'Global neutrino data and recent reactor fluxes: status of three-flavour oscillation parameters'. 2011, arxiv:1108.1376.
- [24] N. Jarosik et al. Seven-year Wilkinson Microwave Anisotropy Probe (WMAP) observations: Sky maps, systematic errors, and basic results. *Astrophys.J.Suppl.*, 192:14, 2011.
- [25] A. Aguilar et al. Evidence for neutrino oscillations from the observation of anti-neutrino(electron) appearance in a anti-neutrino(muon) beam. *Phys.Rev.*, D64:112007, 2001.
- [26] B. Armbruster et al. Upper limits for neutrino oscillations $\bar{\nu}_\mu \rightarrow \bar{\nu}_e$ from muon decay at rest. *Phys.Rev.*, D65:112001, 2002.
- [27] A.A. Aguilar-Arevalo et al. Event excess in the MiniBooNE search for $\bar{\nu}_\mu \rightarrow \bar{\nu}_e$ oscillations. *Phys.Rev.Lett.*, 105:181801, 2010.
- [28] A.A. Aguilar-Arevalo et al. A Search for electron neutrino appearance at the $\Delta m^2 \sim 1\text{eV}^2$ scale. *Phys.Rev.Lett.*, 98:231801, 2007.
- [29] P. Astier et al. Search for $\nu_\mu \rightarrow \nu_e$ oscillations in the NOMAD experiment. *Phys.Lett.*, B570:19–31, 2003.
- [30] B. Baibussinov et al. A new search for anomalous neutrino oscillations at the CERN-PS. 2009, arxiv:0909.0355.
- [31] G. Mention et al. The Reactor Antineutrino Anomaly. *Phys.Rev.*, D83:073006, 2011.

- [32] J. Kopp et al. Are there sterile neutrinos at the eV scale? *Phys.Rev.Lett.*, 107:091801, 2011.
- [33] P. Adamson et al. Search for sterile neutrino mixing in the MINOS long-baseline experiment. *Phys. Rev. D*, 81:052004, 2010.
- [34] K. N. Abazajian et al. Light Sterile Neutrinos: A White Paper. 2012, arxiv:1204.5379v1.
- [35] J. Linder. Neutrino matter potentials induced by earth. 2006, arxiv:hep-ph/0504264v4.
- [36] Q.R. Ahmad et al. Measurement of the rate of $\nu_e + d \rightarrow p + p + e^-$ interactions produced by ^8B solar neutrinos at the Sudbury Neutrino Observatory. *Phys.Rev.Lett.*, 87:071301, 2001.
- [37] C. Andreopoulos et al. The GENIE Neutrino Monte Carlo Generator. *Nucl. Instrum. Meth.*, A614:87–104, 2010.
- [38] C. Andreopoulos. personal communication, 2011.
- [39] C. Andreopoulos et al. *GENIE – Physics and user manual*, 2010.
- [40] T. Yang. *A study of muon neutrino to electron neutrino oscillations in the MINOS experiment*. PhD thesis, Stanford University, 2009.
- [41] D. Bhattacharya. *Neutrino and antineutrino inclusive charged-current cross section measurement with the MINOS near detector*. PhD thesis, Pittsburgh University, 2009.
- [42] M. Kordosky. Hadronic interaction modelling in MINOS. *AIP Conf.Proc.*, 896:185–194, 2007.
- [43] J. Dobson and C. Andreopoulos. Propagating ν -interaction uncertainties via event reweighting. *Acta Phys.Polon.*, B40:2613–2620, 2009.
- [44] C. H. Llewellyn Smith. Neutrino reactions at accelerator energies. *Phys. Rep.*, 3:261–379, June 1972.
- [45] R. Bradford et al. A new parameterization of the nucleon elastic form factors. *Nucl. Phys. B - Proc. Sup.*, 159, 2006.
- [46] L. A. Ahrens et al. Measurement of neutrino-proton and antineutrino-proton elastic scattering. *Phys. Rev. D*, 35(3):785–809, 1987.
- [47] A. Bodek and J. L. Ritchie. Further studies of fermi-motion effects in lepton scattering from nuclear targets. *Phys. Rev. D*, 24, 1981.
- [48] E. C. M. Young. High energy neutrino interactions. (CERN-67-12), 1967.
- [49] R. L. Kustom et al. Quasielastic neutrino scattering. *Phys. Rev. Lett.*, 22(19), 1969.

- [50] W. A. Mann et al. Study of the reaction $\nu + n \rightarrow \mu^- + p$. *Phys. Rev. Lett.*, 31:844–847, 1973.
- [51] S. J. Barish et al. Study of Neutrino Interactions in Hydrogen and Deuterium. 1. Description of the Experiment and Study of the Reaction $\nu + d \rightarrow \mu^- + p + p'_s$. *Phys. Rev.*, D16, 1977.
- [52] S. Bonetti et al. Study of Quasielastic Reactions of Neutrino and anti-neutrino in Gargamelle. *Nuovo Cim.*, A38:260–270, 1977.
- [53] M. Pohl et al. Experimental study of the reaction $\nu + n \rightarrow \mu^- + p$. *Lett. Nuovo Cim.*, 26:332–336, 1979.
- [54] N. J. Baker et al. Quasielastic Neutrino Scattering: A Measurement of the Weak Nucleon Axial Vector Form-Factor. *Phys. Rev.*, D23:2499–2505, 1981.
- [55] S. V. Belikov et al. Quasielastic $\nu_\mu + n$ scattering at 3 GeV to 30 GeV energy. *Yad. Fiz.*, 35, 1982.
- [56] T. Kitagaki et al. High-Energy Quasielastic $\nu_\mu + n \rightarrow \mu^- + p$ Scattering in Deuterium. *Phys. Rev.*, D28:436–442, 1983.
- [57] S. V. Belikov et al. Quasielastic neutrino and anti-neutrino scattering: Total cross-sections, axial vector form-factors. *Z. Phys.*, A320, 1985.
- [58] D. Allasia et al. Investigation of exclusive channels in neutrino/anti-neutrino deuteron charged current interactions. *Nucl. Phys.*, B343:285–309, 1990.
- [59] J. Brunner et al. Quasielastic nucleon and hyperon production by neutrinos and anti-neutrinos with energies below 30 GeV. *Z. Phys.*, C45, 1990.
- [60] L. B. Auerbach et al. Measurements of charged current reactions of ν_μ on ^{12}C . *Phys. Rev. C*, 66(1), 2002.
- [61] N. Suwonjandee. *The measurement of the quasi-elastic neutrino-nucleon scattering cross section at the Tevatron*. PhD thesis, FERMILAB-THESIS-2004-67, 2004.
- [62] V. Lyubushkin et al. A study of quasi-elastic muon neutrino and antineutrino scattering in the NOMAD experiment. *Eur. Phys. J. C*, 63:355–381, 2009.
- [63] J. L. Alcaraz-Aunion and J. Walding. Measurement of the muon-neutrino charged-current quasielastic cross-section in the SciBooNE experiment. *AIP Conf. Proc.*, 1189:145–150, 2009.
- [64] A. A. Aguilar-Arevalo et al. First measurement of the muon neutrino charged current quasielastic double differential cross section. *Phys. Rev. D*, 81(9), 2010.
- [65] G. Fanourakis et al. Study of low-energy antineutrino interactions on protons. *Phys. Rev. D*, 21(3):562–568, 1980.

- [66] S.G. Kovalenko. Quasielastic neutrino production of charmed baryons from the point of view of local duality. *Sov.J.Nucl.Phys.*, 52:934–936, 1990.
- [67] M. Bischofberger. *Quasi elastic charm production in neutrino nucleon scattering*. PhD thesis, ETH Zurich, 2005.
- [68] D. Rein and L. M. Sehgal. Neutrino–excitation of baryon resonances and single pion production. *Annals of Physics*, 133(1):79 – 153, 1981.
- [69] R. P. Feynman et al. Current matrix elements from a relativistic quark model. *Phys. Rev. D*, 3(11):2706–2732, 1971.
- [70] F. Ravndal. Weak production of nuclear resonances in a relativistic quark model. *Nuovo Cim.*, A18:385–415, 1973.
- [71] O. Lalakulich and E. A. Paschos. Resonance production by neutrinos: $j = 3/2$ resonances. *Phys. Rev. D*, 71(7), 2005.
- [72] S. Kretzer and M. H. Reno. Tau neutrino deep inelastic charged current interactions. *Phys. Rev. D*, 66(11):113007, 2002.
- [73] E. Derman. Tests for a weak neutral current in $(l^\pm + n) \rightarrow (l^\pm + \text{anything})$ at high energy. *Phys. Rev. D*, 7(9):2755–2775, May 1973.
- [74] M. Glueck et al. Dynamical parton distributions revisited. *Eur. Phys. J.*, C5:461–470, 1998.
- [75] C. G. Callan and D. J. Gross. High–energy electroproduction and the constitution of the electric current. *Phys. Rev. Lett.*, 22(4):156–159, 1969.
- [76] C. H. Albright and C. Jarlskog. Neutrino production of m^+ and e^+ heavy leptons (i). *Nucl. Phys. B*, 84(2):467–492, 1975.
- [77] G. P. Zeller. *A precise measurement of the weak mixing angle in neutrino–nucleon scattering*. PhD thesis, FERMILAB-THESIS-2002-34, 2002.
- [78] A. Bodek and U Yang. Improved low q^2 model for neutrino and electron nucleon cross sections in few gev region. *Nucl. Phys. B - Proc. Sup.*, 139:113 – 118, 2005.
- [79] M. Arneodo et al. Accurate measurement of $F_2(d)/F_2(p)$ and $R^d - R^p$. *Nucl.Phys.*, B487:3–26, 1997.
- [80] R.S. Towell et al. Improved measurement of the \bar{d}/\bar{u} asymmetry in the nucleon sea. *Phys. Rev.*, D64:052002, 2001.
- [81] I. Schienbein and others. A Review of target mass corrections. 2008, arxiv:0709.1775.
- [82] L. W. Whitlow. *Deep inelastic structure functions from electron scattering on hydrogen, deuterium and iron at $0.6 \text{ GeV}^2 < Q^2 < 30 \text{ GeV}^2$* . PhD thesis, SLAC-357-UC-414, 1990.

- [83] G. Onengut et al. Measurement of nucleon structure functions in neutrino scattering. *Phys. Lett. B*, 632(1):65 – 75, 2006.
- [84] V. Tvaskis. *Longitudinal–transverse separation of deep–inelastic scattering at low Q^2 on nucleons and nuclei*. PhD thesis, Vrije University, 2004.
- [85] A. Bodek and U Yang. Axial and vector structure functions for electron– and neutrino–nucleon scattering cross sections at all Q^2 using effective leading order parton distribution functions. 2010, arxiv:1011.6592.
- [86] W. G. Seligman. *A next–to–leading order QCD analysis of neutrino–iron structure functions at the Tevatron*. PhD thesis, Columbia University, 1997.
- [87] J.P. Berge et al. A Measurement of Differential Cross–Sections and Nucleon Structure Functions in Charged Current Neutrino Interactions on Iron. *Z.Phys.*, C49:187–224, 1991.
- [88] M. Tzanov et al. Precise measurement of neutrino and anti–neutrino differential cross sections. *Phys. Rev.*, D74:012008, 2006.
- [89] H. Gallagher. Event generator tuning in the resonance region for the MINOS experiment. *Nucl.Phys.Proc.Suppl.*, 159:229–234, 2006.
- [90] D. J. Gross and C. H. Llewellyn Smith. High–energy neutrino–nucleon scattering, current algebra and partons. *Nucl.Phys.*, B14:337–347, 1969.
- [91] J. D. Bjorken. Asymptotic sum rules at infinite momentum. *Phys. Rev.*, 179(5):1547–1553, 1969.
- [92] S. L. Adler. Sum rules giving tests of local current commutation relations in high–energy neutrino reactions. *Phys.Rev.*, 143:1144–1155, 1966.
- [93] M. A. G. Aivazis et al. Leptoproduction of heavy quarks. I. General formalism and kinematics of charged current and neutral current production processes. *Phys. Rev. D*, 50(5):3085–3101, 1994.
- [94] W. M. Yao et al. Review of Particle Physics. *J. Phys. G*, 33:1, 2006.
- [95] G. De Lellis et al. Charm physics with neutrinos. *Physics Reports*, 399(5–6):227 – 320, 2004.
- [96] A. Kayis-Topaksu et al. Associated charm production in neutrino–nucleus interactions. *Eur. Phys. J.*, C52:543–552, 2007.
- [97] Glueck, M. et al. Heavy flavor production at high–energy e–p colliders. *Z.Phys.*, C38:441, 1988.
- [98] A. Alton et al. Observation of neutral current charm production in ν_μ –Fe scattering at the Fermilab Tevatron. *Phys.Rev.*, D64:012002, 2001.
- [99] G.P. Zeller et al. On the effect of asymmetric strange seas and isospin violating parton distribution functions on $\sin^2 \theta_W$ measured in the NuTeV experiment. *Phys.Rev.*, D65:111103, 2002.

-
- [100] D. Bardin and V.A. Dokuchaeva. On the radiative corrections to the neutrino deep inelastic scattering. *JINR-E2-86-260*, 1986.
- [101] D. Bardin et al. ZFITTER v.6.21: A semi-analytical program for fermion pair production in e^+e^- -annihilation. *Comp. Phys. Comm.*, 133(2-3):229–395, 2001.
- [102] J. E. Kari et al. EPS09–Global NLO analysis of nuclear PDFs and their uncertainties. *Nucl. Phys. A*, 830, 2009.
- [103] U. K. Yang. *A measurement of differential cross-sections in charged-current neutrino interactions on iron and a global structure functions analysis*. PhD thesis, Rochester University, 2001.
- [104] K. Kovarik et al. Nuclear corrections in neutrino-nucleus DIS and their compatibility with global NPDF analyses. *Phys.Rev.Lett.*, 106:122301, 2011.
- [105] K. Kovarik. Personal communication, 2011.
- [106] M. Botje. A QCD analysis of HERA and fixed target structure function data. *Eur. Phys. J.*, C14:285–297, 2000.
- [107] J. Gomez et al. Measurement of the A-dependence of deep inelastic electron scattering. *Phys.Rev.*, D49:4348–4372, 1994.
- [108] A. Bodek et al. Electron scattering from nuclear targets and quark distributions in nuclei. *Phys.Rev.Lett.*, 50:1431, 1983.
- [109] G. Bari et al. A measurement of nuclear effects in deep inelastic muon scattering on deuterium, nitrogen and iron Targets. *Phys.Lett.*, B163:282, 1985.
- [110] A.C. Benvenuti et al. Nuclear effects in deep inelastic muon scattering on deuterium and iron targets. *Phys.Lett.*, B189:483, 1987.
- [111] P. Amaudruz et al. A reevaluation of the nuclear structure function ratios for D, He, Li-6, C and Ca. *Nucl.Phys.*, B441:3–11, 1995.
- [112] M.R. Adams et al. Shadowing in inelastic scattering of muons on carbon, calcium and lead at low $x(Bj)$. *Z.Phys.*, C67:403–410, 1995.
- [113] D. Rein and L. M. Sehgal. Coherent π^0 production in neutrino reactions. *Nucl.Phys.*, B223:29, 1983.
- [114] D. Rein and L.M. Sehgal. PCAC and the deficit of forward muons in π^+ production by neutrinos. *Phys.Lett.*, B657:207–209, 2007.
- [115] D. Bardin and V.A. Dokuchaeva. Muon energy spectrum in inverse muon decay. *Nucl.Phys.*, B287:839, 1987.
- [116] W. J. Marciano and Z. Parsa. Neutrino electron scattering theory. *J.Phys.G*, G29:2629–2645, 2003.

- [117] Q. Wu. *Neutrino–nucleon cross section measurements in NOMAD*. PhD thesis, UMI-32-45445, 2006.
- [118] S. Mishra. Personal communication, 2011.
- [119] Hepdata reaction database. <http://durpdg.dur.ac.uk/HEPDATA/REAC>. [online; accessed 05-May-2011].
- [120] Q. Wu et al. A precise measurement of the muon neutrino–nucleon inclusive charged current cross–section off an isoscalar target in the energy range $2.5 < E_\nu < 40$ GeV by NOMAD. *Phys. Lett.*, B660:19–25, 2008.
- [121] K. Kodama et al. Final tau–neutrino results from the donut experiment. *Phys. Rev. D.*, 78(5), 2008.
- [122] T. Yang et al. A hadronization model for the MINOS experiment. *AIP Conf.Proc.*, 967:269–275, 2007.
- [123] T. Yang et al. A hadronization model for few–GeV neutrino interactions. *Eur.Phys.J.*, C63:1–10, 2009.
- [124] T. Sjostrand et al. PYTHIA 6.4 Physics and Manual. *JHEP*, 0605:026, 2006.
- [125] Z. Koba et al. Scaling of multiplicity distributions in high–energy hadron collisions. *Nucl.Phys.*, B40:317–334, 1972.
- [126] P.D.B. Collins and T.P. Spiller. The fragmentation of heavy quarks. *J.Phys.G*, G11:1289, 1985.
- [127] W. Wittek et al. Production of π^0 mesons and charged hadrons in anti–neutrino neon and neutrino neon charged current interactions. *Z.Phys.*, C40:231, 1988.
- [128] R. Bruns et al. ROOT–TGenPhaseSpace. <http://root.cern.ch/root/html/TGenPhaseSpace.html>, 2011. [online; accessed 12-July-2011].
- [129] D. Zieminska et al. Charged particle multiplicity distributions in $\nu + n$ and $\nu + p$ charged current interactions. *Phys.Rev.*, D27:47–57, 1983.
- [130] S. Barlag et al. Charged hadron multiplicities in high–energy $\nu_\mu n$ and $\bar{\nu}_\mu p$ interactions. *Z.Phys.*, C11:283, 1982.
- [131] A. M. Cooper-Sarkar. Hadron final state results from BEBC. In *Neutrino 1982*, 1982.
- [132] M. Derrick et al. Properties of the hadronic system resulting from $\bar{\nu}_\mu p$ interactions. *Phys.Rev.*, D17:1, 1978.
- [133] A. B. Clegg and A. Donnachie. A description of jet structure by p_t limited phase space. *Z.Phys.*, C13:71, 1982.
- [134] A. Rubbia. NUX–Neutrino generator. [talk given at NuInt01], December 2001.

- [135] S. Dytman. Neutrino Event Generators. *AIP Conf. Proc.*, 896, 2007.
- [136] D.S. Baranov et al. An estimate for the formation length of hadrons in neutrino interactions. Technical Report PHE 84-04, 1984.
- [137] M. Guler et al. An appearance experiment to search for $\nu_\mu \rightarrow \nu_\tau$ oscillations in the CNGS beam: experimental proposal. Technical Report CERN-SPSC-2000-028. LNGS-2000-25. SPSC-P-318, CERN, Geneva, Jul 2000.
- [138] CNGS homepage. <http://proj-cngs.web.cern.ch/proj-cngs/Download/Download.htm>. [online; accessed 28-December-2009].
- [139] P. Astier et al. Prediction of neutrino fluxes in the NOMAD experiment. *Nucl. Instrum. Meth.*, A515, 2003.
- [140] D. G. Michael et al. Observation of muon neutrino disappearance with the MINOS detectors and the NuMI neutrino beam. *Phys. Rev. Lett.*, 97, 2006.
- [141] B. Pontecorvo. Electron and muon neutrinos. *Sov. Phys. JETP*, 10, 1960. [original in russian: Pontecorvo, B., *Zh. Eksp. Teor.Fiz.* (37), 1959].
- [142] M. Schwartz. Feasibility of using high-energy neutrinos to study the weak interactions. *Phys. Rev. Lett.*, 4(6):306–307, 1960.
- [143] S. E. Kopp. Accelerator neutrino beams. *Physics Reports*, 439(3):101 – 159, 2007.
- [144] G. Danby et al. Observation of high-energy neutrino reactions and the existence of two kinds of neutrinos. *Phys. Rev. Lett.*, 9(1):36–44, 1962.
- [145] J. Yu et al. NuTeV SSQT performance. *FERMILAB-TM-2040*, 1998.
- [146] S. Van Der Meer. A directive device for charged particles and its use in an enhanced neutrino beam. *CERN-61-07*, 1961.
- [147] D. Beavis et al. Long baseline neutrino oscillation experiment at the AGS. Technical Report BNL-52459, 1995.
- [148] D. S. Ayres et al. NOvA proposal to build a 30-kiloton off-axis detector to study neutrino oscillations in the Fermilab NuMI beamline. 2004, hep-ex/0503053.
- [149] D. Drakoulakos et al. Proposal to perform a highstatistics neutrino scattering experiment using a fine-grained detector in the NuMI beam. 2004, hep-ex/0405002.
- [150] P. Adamson et al. First measurement of ν_μ and ν_e events in an off-axis horn-focused neutrino beam. *Phys. Rev. Lett.*, 102, 2009.
- [151] Y. Hayato. T2K at J-PARC. *Nucl. Phys. Proc. Suppl.*, 143, 2005.
- [152] A. Ferrari et al. An updated Monte Carlo calculation of the CNGS neutrino beam. Technical Report CERN-AB-Note-2006-038, CERN, Geneva, 2007.

-
- [153] Brunetti, G. *Neutrino velocity measurement with the OPERA experiment in the CNGS beam*. PhD thesis, Bologna University, 2011.
- [154] T. Adam et al. Measurement of the neutrino velocity with the OPERA detector in the CNGS beam. 2011, arxiv:1109.4897v1.
- [155] E. Eskut et al. The CHORUS experiment to search for $\nu_\mu \rightarrow \nu_\tau$ oscillation. *Nucl. Instrum. Meth.*, A401:7–44, 1997.
- [156] T. Adam et al. The OPERA experiment target tracker. *Nucl. Instrum. Meth.*, A577:523–539, 2007.
- [157] N. Chon-Sen et al. Target tracker efficiency survey. *OPERA internal note 113*, 2010.
- [158] F. Terranova et al. Electromagnetic characterization of the 990 ton gapless magnets for the opera experiment. *J. Instrum.*, 2:T03001, 2007.
- [159] A. Paoloni. Cluster size studies on OPERA RPCs. *OPERA internal note 109*, 2010.
- [160] G. Felici et al. The trigger system of the OPERA precision tracker. *OPERA public note 71*, 2009.
- [161] T. Ferber et al. The gas system of the drift tube detector of the neutrino experiment OPERA. *Nucl. Instrum. Meth. A*, 592(3):493–497, 2008.
- [162] N. Agafonova et al. Observation of a first ν_τ candidate in the OPERA experiment in the CNGS beam. *Phys. Lett.*, B691:138–145, 2010.
- [163] N. Agafonova et al. Search for $\nu_\mu \rightarrow \nu_\tau$ oscillation with the OPERA experiment in the CNGS beam. *New J.Phys.*, 14:033017, 2012.
- [164] N. Agafonova et al. Determination of a time-shift in the OPERA set-up using high energy horizontal muons in the LVD and OPERA detectors. 2012, arxiv:1206.2488.
- [165] A. Ferrari et al. FLUKA: A multi-particle transport code (program version 2005). *CERN-2005-010*, 2005.
- [166] G. Battistoni et al. The FLUKA code: Description and benchmarking. *AIP Conf. Proc.*, 896, 2007.
- [167] G. Ambrosini et al. Measurement of charged particle production from 450 GeV/c protons on beryllium. *Eur. Phys. J.*, C10:605–627, 1999.
- [168] C. F. J. Wu. Jackknife, bootstrap and other resampling methods in regression analysis. *Annals of Statistics*, 14:1261–1295, 1986.
- [169] P. Sala. Personal communication, 2010.
- [170] A. Ferrari et al. CNGS neutrino beam systematics for Θ_{13} . *Nucl. Phys. Proc. Suppl.*, 145, 2005.

-
- [171] L. Chaussard. OpGeom, software model of the OPERA detector. *OPERA internal note 69*, 2005.
- [172] A. Cazes et al. Electromagnetic characterization of the 990-ton gapless magnets for the OPERA experiment. *JINST*, 2:T03001, 2007.
- [173] A. Anokhina et al. Study of the effects induced by lead on the emulsion films of the OPERA experiment. *JINST*, 3, 2008.
- [174] M. Ambrosio et al. Vertical muon intensity measured with MACRO at the Gran Sasso Laboratory. *Phys.Rev.*, D52:3793–3802, 1995.
- [175] P.G Catalano et al. Analisi strutturale nei laboratori dell’ I.N.F.N. del Gran Sasso d’Italia. *Mem.Soc.Geol.It.*, 35:647–655, 1986.
- [176] P. Capuano et al. The density of the rock covering gran sasso laboratories in central apennines, italy by underground gravity measurements. *J. App. Geophys.*, 39(1):25–33, 1998.
- [177] H. Wulandari et al. Neutron flux at the gran sasso underground laboratory revisited. *Astropart. Phys.*, 22(3-4):313–322, 2004.
- [178] J. Stanislaw et al. TAUOLA: A Library of Monte Carlo programs to simulate decays of polarized tau leptons. *Comp. Phys. Comm.*, 64:275–299, 1990.
- [179] L. Lipari et al. A Monte Carlo generator of multimMuon events. *MACRO internal note*, 1988.
- [180] L. Lipari et al. A monte carlo program for the generation of multiple-muon events in an underground detector. *MACRO internal note*, 1991.
- [181] Agafonova N. et al. Measurement of the atmospheric muon charge ratio with the OPERA detector. *Eur. Phys. J.*, C67:25–37, 2010.
- [182] *GEANT - Detector Description and Simulation Tool*, 1993.
- [183] N. Agafonova et al. Study of neutrino interactions with the electronic detectors of the OPERA experiment. *New J. Phys.*, 13:053051, 2011.
- [184] M. Aglietta et al. CNGS beam monitor with the LVD detector. *Nucl. Instrum. Meth.*, A516:96–103, 2004.
- [185] M. Selvi. LVD and the CNGS beam. http://www.lngs.infn.it/lngs_infn/contents/lngs_en/research/experiments_scientific_info/conferences_seminars/seminars/LVD-CNGS-Run1e2_GSJan07.ppt, 2007. [online; accessed 28-December-2009].
- [186] P. Sala. Muons at gran sasso. <http://lxmi.mi.infn.it/~psala/Icarus/muatgs2006/muatgs2006.pdf>, 2006. [online; accessed 28-December-2009].
- [187] S. Dusini. MC study of rock muon flux. [talk given at OPERA Coll. Meeting], 2009.

- [188] V. A. Kudryavtsev. Muon simulation codes MUSIC and MUSUN for underground physics. *Comput. Phys. Commun.*, 180:339–346, 2009.
- [189] D. E. Groom et al. Muon stopping power and range tables 10–MeV to 100–TeV. *Atom. Data Nucl. Data Tabl.*, 78:183–356, 2001.
- [190] V. A. Kudryavtsev. Personal communication, 2010.
- [191] H. S. Fesefeldt. The simulation of hadronic showers: physics and applications. Technical Report PITHA-85-02, 1985.
- [192] A Ferrari and P. R. Sala. GEANT Hadronic Event Generators: a comparison at the single interaction level. Technical Report ATL-PHYS-96-086. ATL-GE-PN-86, CERN, 1996.
- [193] C. Zeitnitz and T.A. Gabriel. The GEANT–CALOR interface and benchmark calculations of ZEUS test calorimeters. *Nucl.Instrum.Meth.*, A349:106–111, 1994.
- [194] J. E. Campagne. Muon tracking in heterogeneous structure. *OPERA internal note 61*, 1999.
- [195] A. Bertolin et al. OpCarac: An algorithm for the classification of the neutrino interactions recorded by the OPERA experiment. *OPERA public note 100*, 2009.
- [196] D. E. Groom. Atomic and nuclear properties of materials for more than 300 materials. <http://pdg.lbl.gov/2009/AtomicNuclearProperties/>, 2009. [online; accessed 01-January-2010].
- [197] P. J. Huber. *Robust statistics*. Wiley, 1981.
- [198] A. Hoecker et al. TMVA: Toolkit for Multivariate Data Analysis. *PoS, ACAT:040*, 2007.
- [199] T. Hastie et al. *The elements of statistical learning*. Springer, 2001.
- [200] A. Hollnagel and T. Ferber. OPERA Event – Proton Waveform Matching. *OPERA internal note 146*, 2012.
- [201] T. Ferber. Monte Carlo studies on different magnetic field polarities of the OPERA spectrometers. *OPERA internal note 117*, 2010.
- [202] C. Jollet and A. Meregaglia. Cross talk optimisation. *OPERA internal note 130*, 2011.
- [203] M. Komatsu et al. Sensitivity to θ_{13} of the CERN to Gran Sasso neutrino beam. *J.Phys.G*, G29:443, 2003.
- [204] A. Donini and other. 3+1 sterile neutrinos at the CNGS. *JHEP*, 0712:013, 2007.

-
- [205] P. Adamson et al. Measurement of the neutrino mass splitting and flavor mixing by MINOS. *Phys.Rev.Lett.*, 106:181801, 2011.
- [206] E.A. Paschos and L. Wolfenstein. Tests for neutral currents in neutrino reactions. *Phys.Rev.*, D7:91–95, 1973.
- [207] C.H. Llewellyn Smith. On the determination of $\sin^2(\theta_W)$ in semileptonic neutrino interactions. *Nucl.Phys.*, B228:205, 1983.
- [208] P.F. Loverre. Limits on neutrino oscillations derived from the ratio of neutral to charged current cross-sections of neutrinos measured at the CERN SPS NBB. *Phys.Lett.*, B206:711, 1988.
- [209] K.S. McFarland et al. A limit on $\nu_\mu(\bar{\nu}_\mu) \rightarrow \nu_\tau(\bar{\nu}_\tau)$ oscillations from a precision measurement of neutrino–nucleon neutral current interactions. *Phys.Rev.Lett.*, 75:3993–3996, 1995.
- [210] Y. Ashie et al. A measurement of atmospheric neutrino oscillation parameters by super–kamiokande i. *Phys.Rev.D*, 71:112005, 2005.
- [211] K. Abe et al. A measurement of the appearance of atmospheric tau neutrinos by Super–Kamiokande. 2012, arxiv:1206.0328.
- [212] P. Adamson et al. Improved search for muon–neutrino to electron–neutrino oscillations in MINOS. *Phys.Rev.Lett.*, 107:181802, 2011.
- [213] K. Abe et al. Search for differences in oscillation parameters for atmospheric neutrinos and antineutrinos at Super–Kamiokande. *Phys.Rev.Lett.*, 107:241801, 2011.
- [214] P. Adamson et al. An improved measurement of muon antineutrino disappearance in MINOS. *Phys.Rev.Lett.*, 108:191801, 2012, 1202.2772.
- [215] J-M. Levy. Cross section and polarization of neutrino–produced τ 's made simple. *J. Phys. G*, 36(055002), 2009.
- [216] K. T. McDonald. An off–axis neutrino beam. 2001, arxiv:hep-ex/0111033.
- [217] J.-M. Levy. Kinematics of an off axis neutrino beam. 2010, arxiv:hep-ex/1005.0574v2.
- [218] C. A. Ramm. Neutrino spectra from the two–body decay of relativistic parents. In *The 1963 NPA seminars – The neutrino experiment, CERN-61-07*. 1963.